Alma Mater Studiorum – Università di Bologna
Dottorato di Ricerca in Geofisica
XXIV ciclo

The bursting behavior of gas slugs: laboratory and analytical insights into Strombolian volcanic eruptions.

Settore concorsuale di afferenza: 04/A4: Geofisica

Candidata

Elisabetta Del Bello

_____

Coordinatore scuola Dottorato

Michele Dragoni

_____

Relatore

Piergiorgio Scarlato

_____

Esame finale Anno 2012

Abstract

The aim of this thesis is to study how explosive behavior and geophysical signals in a volcanic conduit are related to the development of overpressure in slug-driven eruptions.

A first suite of laboratory experiments of gas slugs ascending in analogue conduits was performed. Slugs ascended into a range of analogue liquids and conduit diameters to allow proper scaling to the natural volcanoes. The geometrical variation of the slug in response to the explored variables was parameterised. Volume of gas slug and rheology of the liquid phase revealed the key parameters in controlling slug overpressure at bursting.

Founded on these results, a theoretical model to calculate burst overpressure for slug-driven eruptions was developed. The dimensionless approach adopted allowed to apply the model to predict bursting pressure of slugs at Stromboli. Comparison of predicted values with measured data from Stromboli volcano showed that the model can explain the entire spectrum of observed eruptive styles at Stromboli – from low-energy puffing, through normal Strombolian eruptions, up to paroxysmal explosions – as manifestations of a single underlying physical process.

Finally, another suite of laboratory experiments was performed to observe oscillatory pressure and forces variations generated during the expansion and bursting of gas slugs ascending in a conduit. Two end-member boundary conditions were imposed at the base of the pipe, simulating slug ascent in closed base (zero magma flux) and open base (constant flux) conduit. At the top of the pipe, a range of boundary conditions that are relevant at a volcanic vent were imposed, going from open to plugged vent. The results obtained illustrate that a change in boundary conditions in the conduit concur to affect the dynamic

of slug expansion and burst: an upward flux at the base of the conduit attenuates the magnitude of the pressure transients, while a rheological stiffening in the top-most region of conduit changes dramatically the magnitude of the observed pressure transients, favoring a sudden, and more energetic pressure release into the overlying atmosphere. Finally, a discussion on the implication of changing boundary on the oscillatory processes generated at the volcanic scale is also given.

Table of contents

Acknowledgements

First of all, I would like to thank Piergiorgio Scarlato. I have been privileged to have him as PhD supervisor. He carefully accomplished is role, guaranteeing funding for my project and for travelling abroad, and putting me in the conditions to work in a stimulating, comfortable and relaxed environment. Besides on a professional level, I really owe much to him on a personal level, since, he has been very thoughtful and kind throughout these years of collaboration.

I am greatly indebted to my 'informal' supervisor, Jacopo Taddeucci, for the stimulating scientific interaction, and for giving me the opportunity to collaborate with a number of reputable colleagues with different expertise. I am grateful to him for being a mentor and a friend; I really enjoyed spending working and hilarious time with him.

My heartfelt thanks go to Ed Llewellin, who came to be my second 'informal' supervisor. I really appreciate his tireless commitment to teaching and research. He has been an inspiring example and I am grateful to him for his supervision.

I am much obliged to Steve Lane and Mike James for being supportive during my time at the University of Lancaster, and for insightful discussion in many other activities.

My special recognitions go to my colleagues Valeria, Silvio, Andrea, and Antonio. Thanks to you all for providing very insightful NON-scientific break-time sessions in our room. It has been very nice spending time with you all guys. I am also grateful to Salvatore. Thanks to Valeria for her superlative present.

My special thank goes to 'i ragazzi del muretto', Cesaroni and Gianfi.

This thesis is dedicated to my beautiful family, Mamma, Papà, Riccardo, Giulia and Nonna Vera. Monia and Magico. I couldn't have done it without you. To my much-loved brothers and sisters Valerio, Fabietto, Mannino, Stella, Vale, Andrea, Peppe, goes my warmest embrace.

1. Introduction

1.1 Aim of the study

Magmatic systems characterised by a low viscosity of the erupting magma usually exhibit a variety of eruption styles, ranging from passive degassing, through lava fountaining, mildly explosive Strombolian eruptions, up to Plinian eruptions, that are explained in terms of different regimes of gas liberation dynamics at the surface [*Parfitt and Wilson,* 1995; *Houghton and Gonnermann,* 2008]. Impulsive Strombolian activity is driven by the explosive liberation of pressurized pockets of gas, named 'slugs', which have risen through an almost stagnant column of low-viscosity magma [e.g*., Blackburn et al.,* 1976; *Parfitt,* 2004; *Houghton and Gonnermann,* 2008 and references therein].

The ascent, expansion and bursting of gas slugs can cause pressure changes on interaction with the conduit system that are detectable as seismic activity [e.g., *Chouet et al.,* 2003; 2010]. Acoustic signals measured from Strombolian eruptions at different volcanoes world-wide appear similar suggesting a robust mechanism related to the bursting behaviour of such large overpressured bubbles [*Vergniolle & Brandeis*, 1994; 1996; *Johnson et al*., 2004; *Vergniolle et al.*, 2004].

Hence, the dynamics of slugs expansion/pressurization in the conduit system is crucial to understand which factors determine the transition between eruptive regimes and a variation in associated pressure changes.

The goal of this study is to investigate the physical processes governing the explosive behaviour of slug-driven Strombolian eruptions. The main interest is to explore the mechanisms that cause a change of the degree gas overpressure in the slug, and consequently, the range of burst processes observed at the surface. This is motivated by

the ultimate necessity of improving forecasting of volcanic events by founding a link between conduit processes and detectable precursory signals.

Various physical parameters in the conduit are expected to control explosive behaviour of volcanic slugs, such as rheological properties of the surrounding magma, volume of gas slug, geometry of the conduit, and in-conduit flow regime. In this thesis, these aspects have investigated with a twofold purpose:

i) determining volcanic gas overpressure during Strombolian eruptions and linking it to the range of burst processes observed at the surface.
ii) correlating the degree of overpressure in the slug to measured pressure changes in the system.

The problem is approached by performing analogue laboratory simulations that are scaled to conditions appropriate to a low-magma viscosity volcanic system. In the recent years laboratory models have had significant assessment in the study of low magma-viscosity volcanic systems [*Jaupart and Vergniolle* 1988, 1989; *Ripepe et al.,* 2001; *Seyfried and Freundt*, 2000; *James et al.*, 2004; 2006; 2008; 2009; *Corder*, 2008]. Although representing simplification of the real systems, these models rely on established scaling terms that revealed appropriate to low-viscosity volcanic systems [*White and Beardmore*, 1962; *Seyfried and Freundt*, 2000], and have the advantage of direct observation of the process.

In the first part of the work, a very simple laboratory set up is used to investigate the physical parameters controlling slug behaviour in the conduit. Experimental observations on the ascent of slugs in vertical cylindrical conduits of various diameters, filled with liquids with a range of viscosities, are used to build a model that predict the

thickness of the liquid film draining down the conduit around the rising slug and as a function of the physical parameters explored. This allows to determine the width of the slug, and, if the volume is known, its length.

Based on these results, an analytical model is presented that describes the conditions under which a gas slug rising in a cylindrical conduit becomes overpressured, and which predicts the overpressure when the slug bursts. Also, a new framework for estimating relevant geometrical parameters for volcanic slugs over the range of plausible conduit conditions is given. The model is applied to predict the overpressure of Strombolian eruptions using appropriate volcano-scale parameters and is validated against previously published estimates of bursting overpressure derived from a broad dataset of eruptions at Stromboli. Further, it is discussed whether the range of volcanic eruptions observed at Stromboli can be explained in terms of the ascent and burst of gas slugs.

In the second part of the work, a second series of laboratory experiments is presented, that investigate pressure changes and forces resulting from gas slug expansion and bursting in different flow boundary conditions at the top and at the base of the conduit. The experimental set up is equipped with a high speed camera and pressure sensors, and the system is scaled for the potential expansion of the slug by reducing the pressure at the top of the liquid filled pipe with a vacuum pump. In previous experiments the same experimental facility has been used to exploring the effect of conduit geometrical features [*James et al*, 2004; 2006], and potential expansion [*Corder*, 2008; *James et al*., 2009] on pressure oscillations in the conduit, but they always considered the simplest scenario of a slug ascending in closed-base and in a homogenous liquid. Here the more geologically-sound condition of a constant flux at the base of the conduit is investigated.

Further, at the top of the pipe, a range of boundary conditions that are relevant at a volcanic vent were imposed, going from open to plugged vent. Measured pressure variations were interpreted using high speed imagery of expanding/bursting slugs, and implications for the bursting dynamic of volcanic slug in relation with the change in boundary conditions are discussed.

1.2 Slugs (Taylor bubbles)

In this work, two-phase flow analogue laboratory experiments are used to model the behavior of slugs ascending in low-viscosity volcanic systems. The analogue approach has been previously adopted in a number of studies applied to basaltic volcanoes [*Jaupart and Vergniolle* 1988, 1989, *Seyfried and Freundt*, 2000; *James et al.*, 2004; 2006; 2008; 2009; *Corder*, 2008] providing useful insights into first-order conduit dynamics that are not accessible with other methods of investigation.

All these previous studies drew inspiration from the chemical engineering literature, where the study of large bubbles, named Taylor bubbles (section 1.2.1), in liquid-filled tubes had become established over the last 80 years, and applied well-established scaling parameters to a basaltic magma (section 1.2.2).

1.2.1 Definition

Taylor bubbles - as gas slugs are called in the engineering literature - are bubbles that almost fill the cross section of a pipe such that their buoyant ascent causes a film of liquid to fall around them, down the walls of the pipe. The morphology of Taylor bubbles has been described in detail by previous workers [e.g. *Goldsmith & Mason* 1962; *Brown* 1965; *Batchelor* 1967; *Campos & Guedes de Carvalho* 1988; *Bugg et al.* 1998, *Viana et al.* 2003, *Nogueira et al.* 2006; *Feng* 2008, *Kang et al*, 2010] and is summarized in Figure 1-1. The bubble can be divided into four regions: i) an approximately hemispherical, or prolate nose, ii) a body region surrounded by a falling liquid film of thickness λ, iii) a tail region of variable morphology, which may be hemispheroidal, flat or concave, and iv) a wake, which may be open and laminar, closed or turbulent. The

body region can be subdivided in an upper part, where the developing film is accelerating and thinning; and in a lower part, where the forces acting on the film are in equilibrium and the film has constant thickness λ.

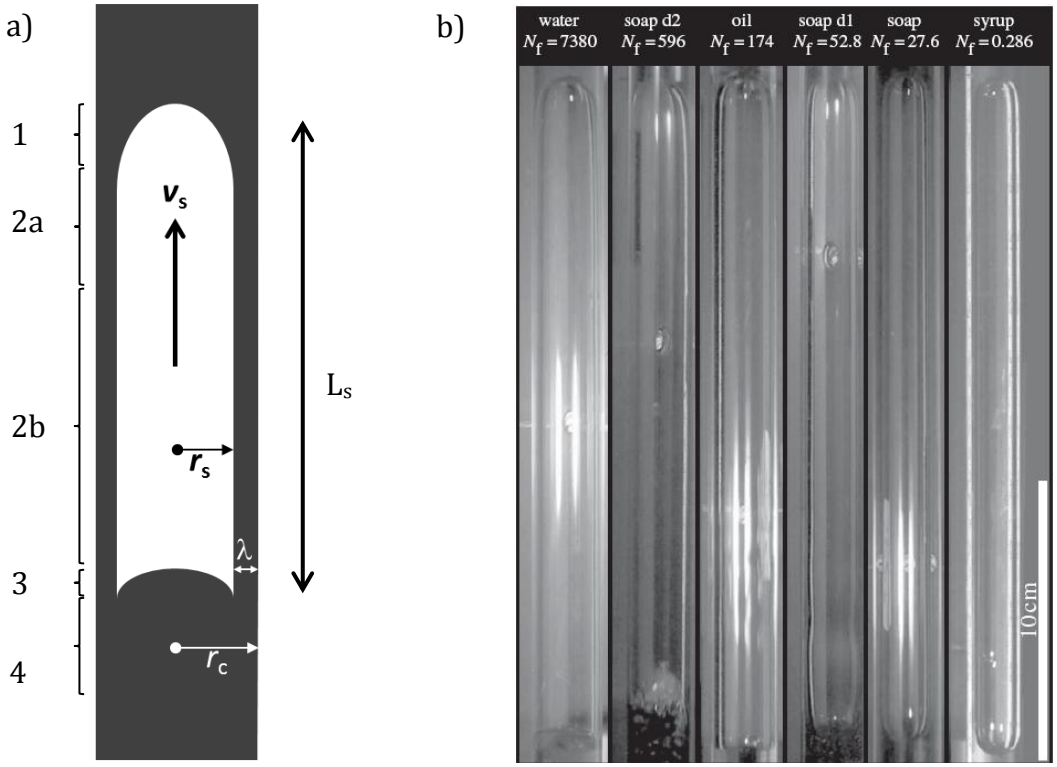

Figure 1-1. a) A schematic representation of a Taylor bubble of length L_s and radius r_s ascending a cylindrical pipe of internal diameter D = $2r_c$. The bubble can be divided into four distinct regions: 1) nose, 2) body, 3) tail, and 4) wake. Around the lower part of the body region (2b), the film has achieved its equilibrium thickness λ. b) Examples of Taylor bubbles rising through various liquids in a pipe with r_c =0.01 m; images are taken from the experiments performed in this work (section 2), and arranged with N_f decreasing from left to right. Physical properties of the liquids are given in Table 2.1.

The behavior of the slugs during ascent influences the nature of the eruptions they cause and the associated geophysical signals [*Vergniolle & Brandesis* 1996; *Chouet et al.* 2003, 2010, *James et al.* 2006; 2008; 2009]. In particular, the thickness of the falling

magma film influences the shape the slug acquires prior bursting, hence has a role on the development of overpressure during a slug's ascent. Several theoretical models exist for the thickness of the falling film around a rising Taylor bubble [*Goldsmith & Mason* 1962; *Brown* 1965; *Batchelor* 1967; *Campos & Guedes de Carvalho* 1988; *Bugg et al.* 1998, *Viana et al.* 2003, *Nogueira et al.* 2006; *Feng* 2008, *Kang et al*, 2010], but there has been no systematic experimental validation of these models over the wide range of dimensionless parameters appropriate for the volcanic range.

1.2.2 Non dimensional parameters

Taylor bubbles are dependent on fundamental physical parameters of the conduit system. These are dynamic viscosity of the liquid filling the pipe μ, its density ρ, the liquid–gas interfacial tension σ, the internal diameter of the pipe D and the gravitational acceleration g. These quantities are re-casted in various dimensionless groups to scale slugs in the laboratory to the conditions appropriate to a volcanic conduit filled with low viscosity magma [*White & Beardmore* 1962; *Wallis* 1969; *Seyfried & Freundt* 2000].

The Morton number, *Mo* represents the ratio of viscous and surface tension forces,

$$Mo = \frac{g\mu^4}{\rho\sigma^3} \tag{1-1}$$

the Eötvös number *Eo*, which represents the ratio of buoyancy and surface tension forces,

$$Eo = \frac{4\rho g r_c^2}{\sigma}. \quad (1\text{-}2)$$

Surface tension plays a negligible role in determining slug behavior when $Mo > 10^{-6}$ [*Seyfried and Freundt*, 2000] and $Eo > 40$ [*Viana et al.*, 2003]. The inverse viscosity is given by [*Wallis,* 1969]:

$$N_f = \frac{\rho}{\mu}\sqrt{8 g r_c^3}. \quad (1\text{-}3)$$

In this case, *Mo* and *Eo* can be combined to eliminate surface tension, forming the inverse viscosity as $N_f = \sqrt[4]{Eo^3 / Mo}$.

Appropriate parameter values for Stromboli are discussed in section 1.4.2 and summarized in Table 1-2. With these values we find that for volcanic slugs, $10^2 < Mo < 10^{15}$, $10^5 < Eo < 10^6$, and $10^0 < Eo < 10^4$. In a recent work *Llewellin et al* [2011], show that the inverse viscosity is related to the slug Reynolds number (*Re*) which is sometimes used to characterize volcanic slugs [*Vergniolle and Brandeis*, 1996; *Harris and Ripepe*, 2007], via:

$$Re = \frac{2\rho v_s r_c}{\mu} = Fr N_f; \quad (1\text{-}4)$$

where v_s is the ascent velocity of the slug and *Fr* is the Froude number, which is a dimensionless measure of slug ascent velocity:

$$Fr = \frac{v_s}{\sqrt{2 g r_c}}. \quad (1\text{-}5)$$

1.2.3 Thickness of the falling film

Several previous theoretical and experimental studies have investigated the physical controls on the thickness $\lambda = r_c - r_s$ of the falling film around a rising gas slug. This work is summarized by *Llewellin et al.* [2011] who show that, in the case where surface tension effects are unimportant, all of the published expressions for film thickness can be recast as relationships between two dimensionless parameters, λ', the dimensionless film thickness ($\lambda' = \lambda - r_c$), and N_f, the 'inverse viscosity'. In this thesis we express the film thickness in terms of the dimensionless film cross-sectional area of the conduit that is occupied by the falling film in the slug region, $A' = 1 - \frac{r_s^2}{r_c^2}$. This is a more useful convention, as it allows immediate scaling in terms of volumes (see section 3). The dimensionless film thickness is given by $\lambda' = \lambda / r_c$, which is related to the dimensionless film cross section by:

$$A' = \lambda'(2 - \lambda'). \qquad (1\text{-}6)$$

Seyfried and Freundt [2000] consider a gas slug rising in a conduit filled with basaltic magma and predict the thickness of the falling film of magma as a function of magma viscosity using an expression derived by *Brown* [1965]. *Llewellin et al.* [2011] show that this theoretical expression can be written in terms of the dimensionless quantities λ' and N_f:

$$\lambda' = 2\frac{\sqrt{1+N}-1}{N}, \quad \text{where} \quad N = \sqrt[3]{14.5 N_f{}^2}\,. \qquad (1\text{-}7)$$

The derivation of this relationship depends on the assumption of potential flow around the nose of the slug, which breaks down for $N_f < 30$ [*Llewellin et al.,* 2011].

James et al. [2008] compare the *Brown* [1965] model with an alternative expression for film thickness derived by *Batchelor* [1967] in their investigation of the behavior of gas slugs at low viscosity basaltic volcanoes. The analysis of *Batchelor* [1967] is based on a balance between viscous and gravitational forces acting on the film, and involves the assumption that the falling film is thin compared with the pipe radius ($\lambda << r_c$), yielding:

$$\lambda = \left(\frac{3\mu r_c v_s}{2\rho g} \right)^{\frac{1}{3}}, \tag{1-8}$$

This expression can also be derived, from *Brown* [1965], under the assumption of a thin film. Equation 1-8 can be written in terms of dimensionless quantities as:

$$\lambda' = \left(6\frac{Fr}{N_f} \right)^{\frac{1}{3}}, \tag{1-9}$$

Prediction of the film thickness from equations 1-8 and 1-9 require that, respectively, the slug ascent velocity, or the Froude number, can be measured or estimated. *James et al.* [2008] measure ascent velocity directly for their experiments and find that the *Batchelor* [1967] model gives better agreement with their experimental observations than the *Brown* [1965] model. Consequently, they apply the *Batchelor* [1967] model to the volcanic case [*James et al.*, 2008; 2009], and use an expression for $Fr(N_f)$ from *Wallis* [1969]. We note that a more recent study [*Viana et al.*, 2003] proposes an alternative expression for $Fr(N_f)$ that is derived from an empirical fit to a much more extensive experimental dataset. *Llewellin et al.* [2011] present a simplified form of this expression that is valid in the inertial–viscous regime:

$$Fr = 0.34\left[1+\left(\frac{31.08}{N_f}\right)^{1.45}\right]^{-0.71}. \qquad (1\text{-}10)$$

By combining equations 1-8 and 1-9 we have a second expression for $\lambda'(N_f)$.

Batchelor [1967] also presents a simplified version of equation 1.8 predicated on the additional assumption of constant Froude number $Fr = 0.34$, giving:

$$\lambda' = 0.9\left(\frac{\mu^2}{\rho^2 r_c^3 g}\right)^{\frac{1}{6}} = \left(\frac{2.04}{N_f}\right)^{\frac{1}{3}}. \qquad (1\text{-}11)$$

This expression is used by *Vergniolle et al.* [2004] to estimate conduit diameter from acoustic measurements of slug burst during Strombolian activity at Shishaldin volcano (Alaska, USA).

Kang et al. [2010] perform numerical simulations in the range $10 < N_f < 450$ and propose an empirical fit to their data:

$$\lambda' = 0.64 N_f^{-0.2}. \qquad (1\text{-}12)$$

Very recently, *Llewellin et al.* [2011] use experimental data presented in this thesis (described in section 2) to develop a semi-empirical relationship:

$$\lambda' = 0.204 + 0.123\tanh\left(2.66 - 1.15\log_{10} N_f\right) \qquad (1\text{-}13)$$

for which validity over the inverse viscosity range $0.1 < N_f < 10^5$ is demonstrated.

1.3 Volcanic slugs

1.3.1 Strombolian eruptions

The discrete, often jet-like bursting of meter-sized, conduit-filling gas bubbles at the surface of a column of magma, commonly defined as 'Strombolian' activity, has been widely studied at Stromboli [*Chouet et al.,* 1974; *Blackburn et al.,* 1976; *Rosi et al,* 2000] and at several other persistently active volcanoes with low viscosity magma, such as Mount Etna, Sicily [e.g., Gresta et al., 2004], Erebus, Antarctica [e.g. *Jones et al.,* 2008; *De Lauro et al.,* 2009], Halema`uma`u vent [e.g. *Chouet et al.,* 2010] and Pu`u`Ō`ō crater at Kīlauea, Hawai`i, USA [e.g. *Edmonds and Gerlach,* 2007], and Nyiragongo, DRC [*Sawyer et al.,* 2008].

Strombolian activity occurs when overpressured gas, transported as discrete pockets, or slugs, disrupts the surface of an almost stagnant magma column, ejecting magma fragments as pyroclasts [e.g., *Chouet et al.,* 1974, *Blackburn*, 1976, *Vergniolle and Brandeis*, 1996; *Ripepe and Marchetti*, 2002].

This intermittent style of activity is typical of volcanoes where the viscosity of the magma is low enough to permit a relatively easy separation of the exsolved volatile phase from the parent magma. Such systems are often in a persistent state of activity, displaying a variety of other low-level degassing mechanisms, ranging from passive degassing, through low-level bubble bursting not associated with seismic activity [*Ripepe et al.*, 1996; *Ripepe et al.*, 2002; *Harris and Ripepe*, 2007], up to more plinian-style eruptions [*Parfitt and Wilson,* 1995, *Houghton and Gonnermann*, 2008].

Such variations in intensity and style often occur within a short time span and have been explained in terms of either outgassing processes, i.e. how exsolved gas separates from the magma [*Parfitt,* 2004; *Houghton and Gonnermann,* 2008; *Namiki and Manga,* 2008], or variations in the mechanical-rheological properties of magma in the shallow conduit [*Taddeucci et al*., 2004a, b; *Valentine et al*., 2005; *Andronico et al.,* 2009; *Cimarelli et al*., 2010].

1.3.2 Origin of slugs in volcanoes

Within a volcanic system, gas slugs are believed to form by coalescence of smaller bubbles at depth, either by accumulation and collapse of a foam layer at geometrical discontinuities within the plumbing system [*Vergniolle and Jaupart,* 1986; *Jaupart and Vergniolle,* 1988*,* 1989], or by differential ascent rate of gas with respect to the surrounding magma [*Parfitt and Wilson,* 1995; *Parfitt,* 2004].

The first conceptual model, known as collapsing foam model (CF, Figure 1-2a), supported by a series of two-phase flow laboratory experiments [*Jaupart and Vergniolle*, 1988; 1989] suggests that bubble nucleation and growth within a magma chamber might lead to the formation of a foam layer at its roof. Periodic collapses cause the formation of large bubbles that rises within the volcanic conduit as a gas slug.

According to the second mechanism, known as rise speed dependent model (RSD, Figure 1-2b), if the magma ascent speed is relatively low, gas bubbles within the magma are able to rise relative to the magma before eruption. The rise speed of large bubbles is quicker than smaller bubbles, hence they are able to reach and coalesce with smaller bubbles, increasing their volume as they approach the surface.

In either case, once the amount of gas has reached some critical value, a slug decouples from the magma and rises as a separate phase, potentially reaching the surface with a pressure significantly higher than atmospheric (i.e. with an overpressure). The density and viscosity ratios between the surrounding magma and the gas in the slugs are such that the composition of the volatile phase can be neglected [*James et al.,* 2008].

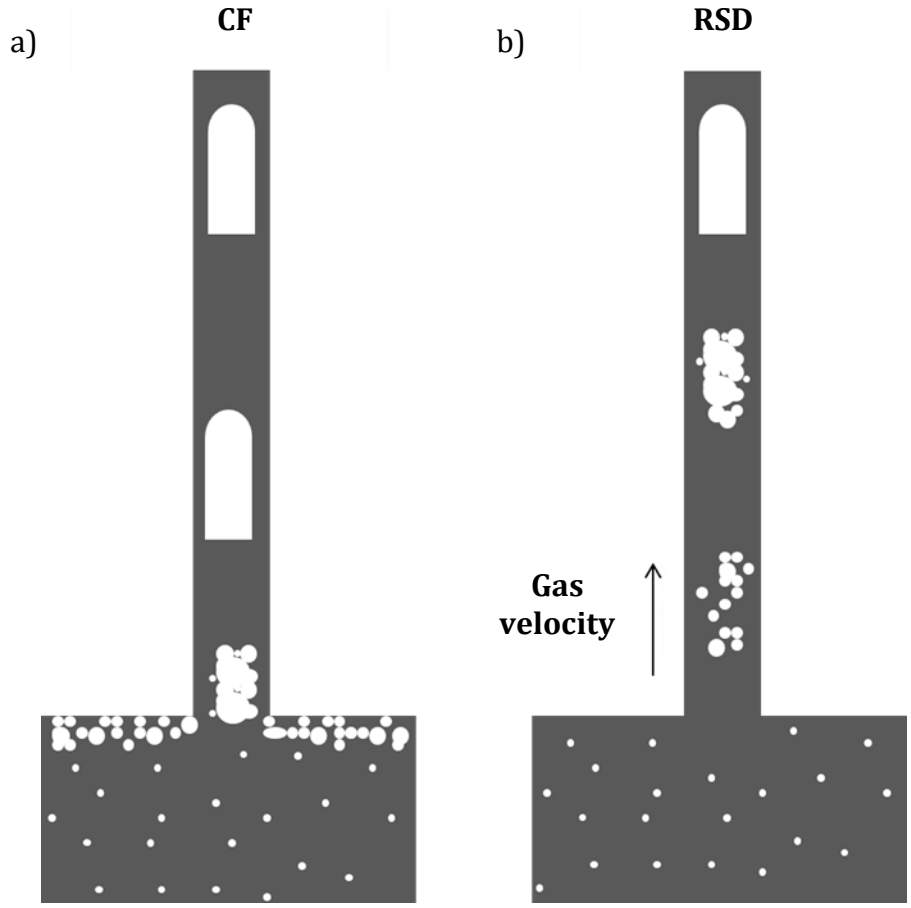

Figure 1-2 Conceptual models for the orgin of slugs in basaltic volcanic conduits. a) Collapsing foam model [Jaupart and Vergniolle, 1988; 1989]; b) Rise speed dependent model [Parfitt and Wilson, 1995; Parfitt, 2004]. The key difference between the two models is that the CF model requires a change in geometry to form gas slugs, whereas the RSD model requires differential ascent velocity between the volatile and the liquid phase.

1.3.3 Measurements

A wealth of evidence exists at basaltic volcanoes to support the bursting of large bubbles within a magma-filled conduit. Some are based upon direct observations of the eruption and their products, such as, e.g., i) the launch velocity of ballistic blocks, [*Chouet et al.*, 1974; *Blackburn et al.*, 1976], ii) micro-textural observation of scoriae, [*Lautze and Houghton,* 2007], or iii) spectroscopic composition of erupted gases [e.g, *Allard et al.,* 1994; 2010; *Burton et al.,* 2007a, b; *Aiuppa et al,* 2010], while others rely on indirect observations of the pressure variations (mainly seismic and acoustic) induced by fluid-related processes within the volcanic conduit.

Infrasound and other geophysical signals are generated by changes in the pressure distribution within the conduit during the ascent and burst of gas slugs. The intensity of the pressure change is strongly dependent on the size of the slug and on the viscosity of the conduit-filling magma [*James et al.,* 2004; 2006; 2008; 2009; *Corder*, 2008; *Chouet et al.,* 2003; *Vergniolle and Ripepe,* 2008], and several studies yield constraints on the interpretation of geophysical signals using models that rely on geometrical parameters of the slugs (size, radius and thickness of the surrounding magma layer). These parameters have been inferred from acoustic [*Vergniolle and Brandeis,* 1996] and seismic [*Chouet et al.,* 2003; *O'Brien and Bean*, 2008] measurements, or estimated from visual observation [*Chouet et al.,* 1974; *Vergniolle et al.,* 1996; 2004], and the maximum size of ejecta [*Blackburn et al.,* 1976; *Wilson,* 1980].

Acoustic studies revealed that Strombolian-style eruptions worldwide share similar infrasonic signatures, suggesting a robust mechanism related to the bursting of large overpressured bubbles. The current physical model for the generation of acoustic

signals from Strombolian bursts is based around the formation and oscillation of a meniscus of magma [*Vergniolle & Brandeis*, 1994; 1996*; Johnson et al.*, 2004; *Vergniolle et al.*, 2004]. These signals are characterized by initial high amplitude, low frequency (infrasonic) impulse followed by higher frequency signals (Figure 1-3). At Stromboli, different vents have characteristic infrasonic signals [*Ripepe et al.,* 2001; *Ripepe and Marchetti,* 2002; *McGregor and Lees*, 2004, Figure 1-4], and different eruption styles can be identified on the basis of bursting pressure [*Harris and Ripepe*, 2007; *Colò et al.*, 2010]. *Colò et al*. [2010] relate the amplitude of infrasonic signals to bursting overpressure of 'puffing' and Strombolian activity, and indicate that, for puffers, infrasonic amplitude is <5 Pa, whilst for 'explosive' events it is >5 Pa.

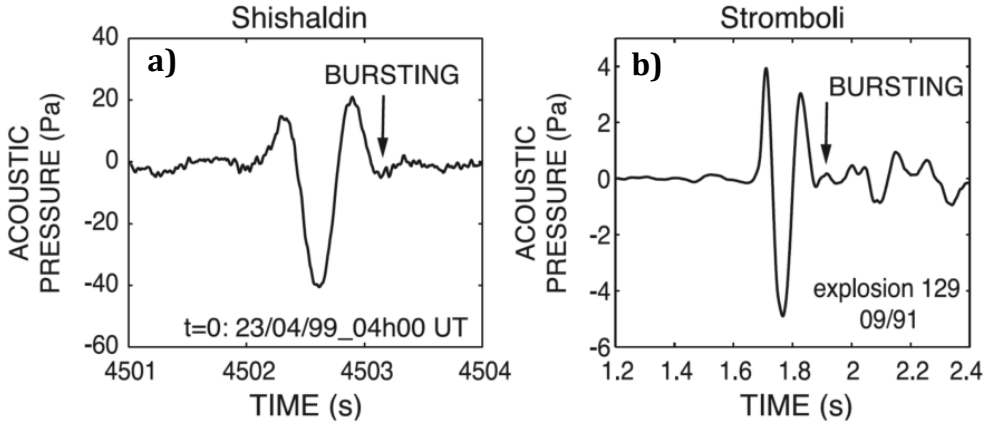

Figure 1-3. Similar acoustic signals recorded at a) Shishaldin volcano (Alaska, USA), and b) at Stromboli and associated bubble meniscus bursting time [Vergniolle et al., 2004].

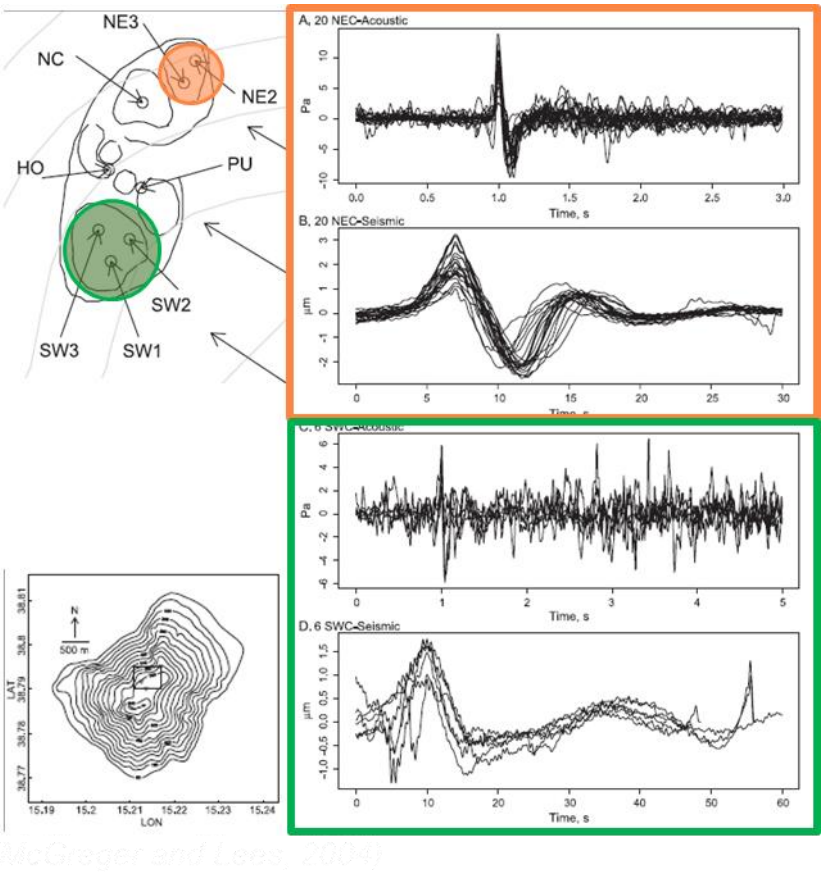

Figure 1-4. Sketch map of Stromboli summit area, showing different groups of craters (SouthWest, SW, an NorthEast, NE) and associated stacked acoustic and seismic signals from a series of eruption, revealing a repetitive nature of the waveforms. Inset shows Stromboli Island with the location of the crater terrace terrace [modified after McGreger and Lees, 2004].

Seismic studies show that VLP (2 - 30 s) seismic signals detected at Stromboli have two highly repeatable waveforms that could be ascribed to differing eruptive styles observed from different vents [*Chouet et al.* 1999; 2003*; McGreger and Lees*, 2004; *Marchetti and Ripepe*, 2005]. *Chouet et al* [2003], suggest that the repeatability of the waveforms (Figure 1-5a) indicate a non-destructive source mechanism, where fluid dynamic rather than shear fracture processes are responsible. Waveform inversion of the seismic signals locates the source mechanisms to a depth comprised between 220 and 260 m beneath of the active vents (480-520 m a.s.l, Figure 1-5b) that is attributed to

a change in the conduit geometry from a dyke to a pipe, or alternatively, from a change in dyke slope. This change might be able to induce a sudden expansion of a gas slug responsible for the vertical single-force components.

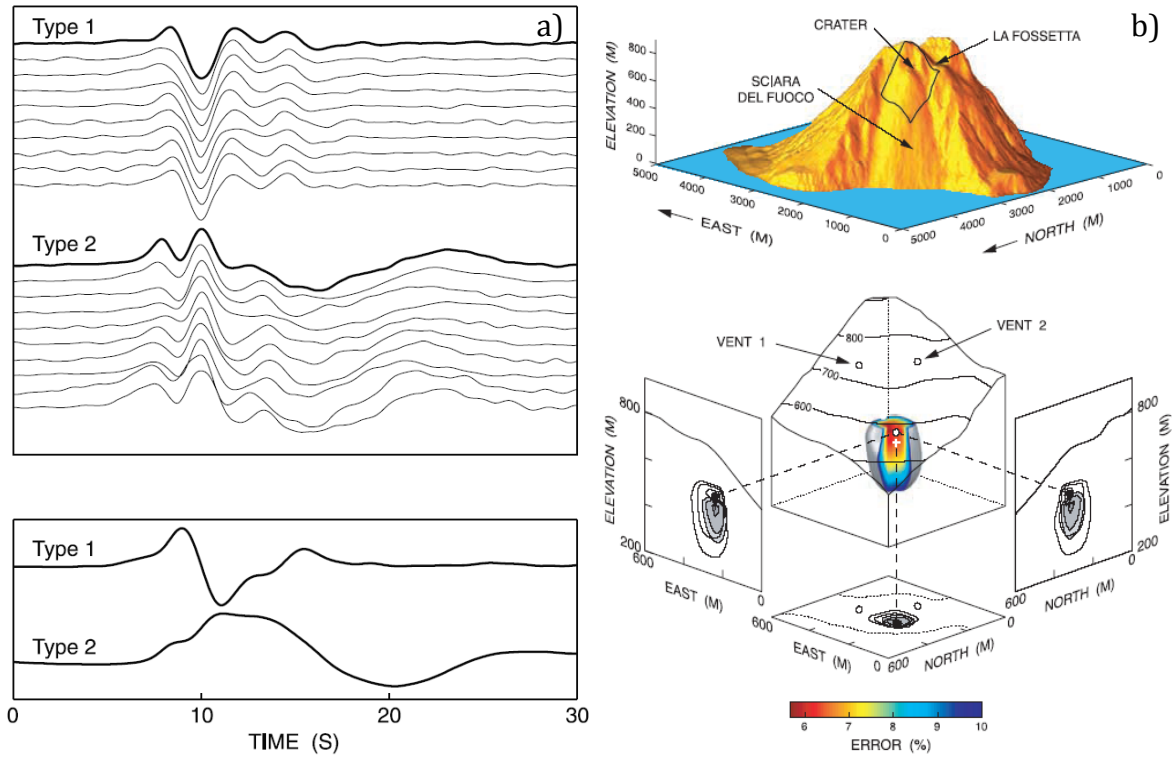

Figure 1-5. a) Normalized components of velocity (upper diagrams) and displacement (lower diagrams) seismograms from two types of events (Type 1 and 2) recorded at Stromboli, showing similarity of waveforms between events. b) Source location of the Type 1 and Type 2 events determined from waveform inversion of seismic data indicating depths of 220 m and 260 m beneath the vents [from Chouet et al., 2003].

1.3.4 Laboratory Models

The first studies applied to low-viscosity volcanic systems were aimed at investigating the dynamics of separated two-phase flow within a conduit [*Jaupart and Vergniolle*, 1988; 1989; *Seyfried and Freundt*, 2000]. More recent studies expanded the former field of investigation, by examining the pressure and force changes recorded during single

gas slug rise in cylindrical conduits [*James et al.*, 2004; 2006; 2008; 2009; *Corder*, 2008]. Here the experiments were conducted in an apparatus equipped with pressure and displacement transducers, in order to record the pressure changes associated with i) the rise of the gas slug in vertical, inclined [*James et al.*, 2004], narrowing or flaring conduits [*James et al.*, 2006], or ii) with the near-surface expansion of gas slugs within a conduit [*Corder,* 2008; *James et al.,* 2008; 2009].

In all previous applications, the main assumptions of the laboratory models regard i) the geometry of the conduit, which is assumed cylindrical and with no asperities at the wall margins, ii) the rheological properties of the magma, that is usually regarded as a single liquid phase of constant density, rather than a three-phase system of solid crystals, liquid melt and volatile gases [e.g., *Ishibashi*, 2009; *Mueller et al.,* 2010, 2011; *Vona et al.,* 2011], iii) interfacial tension, that is generally considered to play a negligible role.

Jaupart and Vergniolle [1988;1989] performed experiments using a cylindrical tank connected to a vertical pipe (Figure 1-6). They observed the ascent of numerous small nitrogen bubbles rising from a series of holes drilled at the bottom of the tank. Bubbles rose in a silicon oil of viscosity of ~ 1 Pa s until encountering the top of the experimental tank, where they collided and coalesced to emerge up the narrow exit pipe as large bubbles. They envisaged that this mechanism was plausible for the production of slugs at some depth beneath the vent at Stromboli volcano.

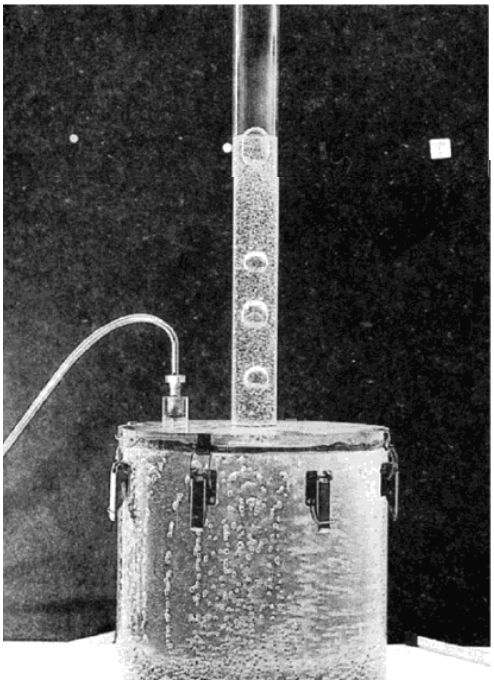

Figure 1-6. Experimental set up of Vergniolle and Jaupart [1989]. Small bubbles form after collision and coalescence at the tank roof, travelling rapidly within the liquid-filled pipe.

Later, *Seyfried and Freundt* [2000], investigated multiphase flow in basaltic volcanic conduits scaled to basaltic conditions over Morton, Eotvös, Reynolds, and Froude numbers (see section 1.2.2), using analogue experiments and theoretical approaches. They found that, depending on gas supply, gas slugs may rise through basaltic magmas in regimes of distinct fluid dynamical behavior: ascent of single slugs, supplied and periodic slug flow. In a first set of experiments they demonstrate that the growth of gas slugs due to hydrostatic decompression does not affect their ascent velocity and that excess pressure in the slugs remain negligible. They apply their theoretical formulation describing slug ascent velocity as a function of liquid and conduit properties in a second set of experiments (see section 1.2.3). In a third set of experiments with continuous gas supply into a cylindrical conduit, gas flow rate and liquid viscosity were varied over the whole range of flow regimes to observe flow dynamics and to measure gas and liquid

eruption rates. They found that at the transition from slug to annular flow, when the liquid bridges between the gas slugs disappear, pressure at the conduit entrance dropped by ~ 60% from the hydrostatic value to the dynamic-flow resistance of the annular flow, which could trigger further degassing in a stored magma to maintain the annular flow regime until the gas supply is exhausted and the eruption ends abruptly. In a fourth set of experiments they uses a conduit partially blocked by built-in obstacles providing traps for gas pockets (Figure 1-7). Once gas pockets were filled, rising gas slugs deformed but remained intact as they moved around obstacles without coalescence or significant velocity changes. They also monitored the bursting of bubbles coalescing with trapped gas pockets, measuring pressure signals at least 3 orders of magnitude more powerful than gas pocket oscillation induced by passing liquid.

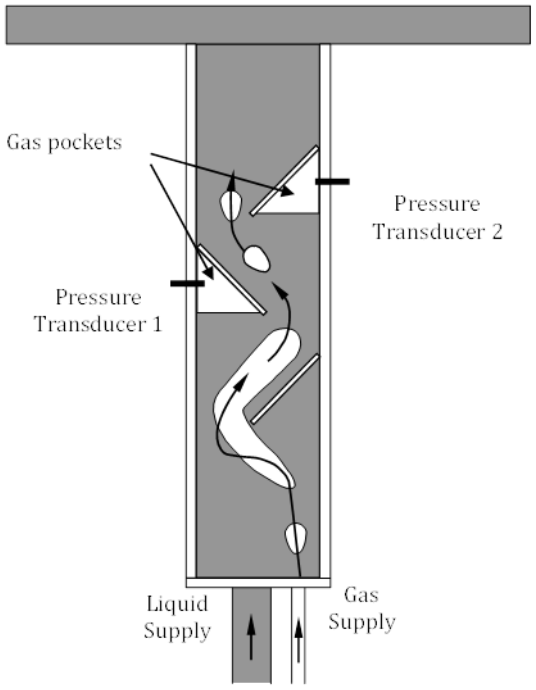

Figure 1-7. Experimental set-up of Seyfried and Freundt, [2000] for gas slug ascent in a partially obstructed liquid-filled tube [picture redrawn from Corder, 2008].

These latter experiments showed that coalescence of the slugs results in significant pressure oscillations that may be a source of volcanic tremor; revealing that linking volcano-seismic signals to fluid flow can be a powerful method of scaling inaccessible conduit processes. Motivated by the new imaging of the conduit at Stromboli, as illustrated by *Chouet et al.* [2003] from inversion of seismic waveforms measured at Stromboli volcano (section 1.3.3), showing that stable and repeatable seismic sources are located at conduit discontinuities, *James et al*. [2004] focused on pressure oscillation resulting from the ascent of single gas slugs in a vertical or inclined tube. They carried out experiments of both single gas slugs and continuously supplied gas phase ascending in pure water (μ = 0.001 Pa s) and sugar-water solutions (μ = 0.09 and 0.9 Pa s) at atmospheric pressure. The apparatus comprised a 2.5 m long tube of 38 mm internal diameter with six pressure transducers (active strain gauges) attached at various heights in order to record the pressure changes associated with the rise of the gas slug (Figure 1-8). They found that ascent of individual gas slugs is accompanied by strong dynamic pressure variations resulting from the flow of liquid around the slug. These transient pressure variations are associated to slugs approaching the surface and bursting, and are also observed during the release of gas slugs and in their wake region. Also, they observed that conduit inclination promotes a change of regime from bubbly to slug flow and favors an increase in size and velocity of the slugs at the expense of their frequency of occurrence during continuously supplied two-phase flow.

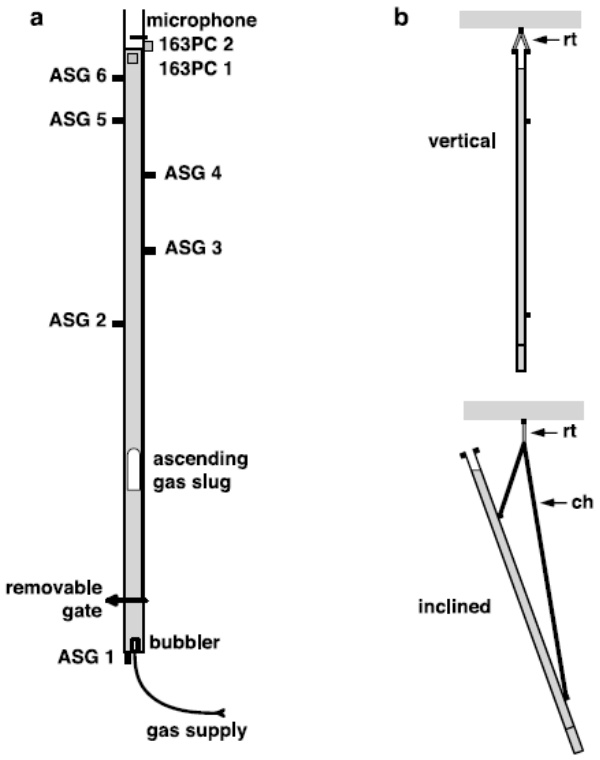

Figure 1-8. a) Experimental apparatus used by James et al [2004]; pressure sensors (ASG transducers) are located along the tube, and 163 differential pressure transducers are set up close to or just above the liquid surface. A removable gate is used for slug generation during single slug experiments. For continuous gas-supply experiments, gas enters the liquid column from a bubbler set in the base of the tube. In b) vertical and inclined tube mounting configurations are shown.

Improving their previous work, *James et al.* [2006] carried out new experiments to study pressure changes and forces associated with the passage of gas slugs through discontinuities comprising either a constriction (narrowing of tube diameter) or flare (increase in tube diameter). They used the same experimental set up (Figure 1-9), performing runs in vertical pipes with three geometry change ratios (38, 50 and 80 mm) and water (μ = 0.001 Pa s), white cane sugar solution (μ = 0.1 Pa s) or dilute Golden Syrup (μ = 30 Pa s) as experimental liquids. They observed that gas slugs undergoing an abrupt flow pattern change upon entering a section of significantly increased tube diameter induce a transient pressure decrease in and above the flare and

an associated pressure increase below it, which stimulates acoustic and inertial resonant oscillations. Systematic pressure changes varying with slug size, liquid depth, tube diameter, and liquid were observed. Further, they reported that when the liquid flow is not dominantly controlled by viscosity, net vertical forces on the apparatus are also detected, and the magnitude of the pressure transients is a function of the tube geometry. They concluded that their experiments suggest that significant downward forces can result from the rapid deceleration of relatively small volumes of downward-moving liquid, in contrast to interpretations of related volcano-seismic data, where a single downward force is assumed to result from an upward acceleration of the center of mass in the conduit.

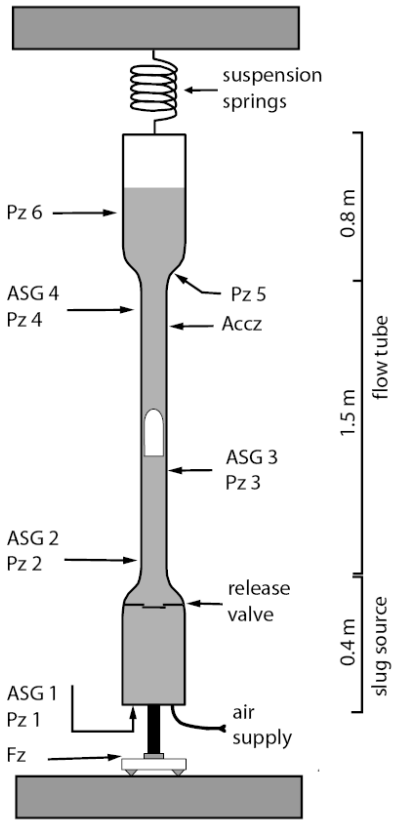

Figure 1-9. Experimental setup of James et al. [2006] to study expansion and burst of gas slugs rising into flared sections. Pressure (ASG) and Piezo (Pz) transducers are used, and a force sensor (Fz) to detect vertical motion of the apparatus.

In a following series of experiments, Corder [*2008*] investigated pressure changes and forces resulting from gas slug expansion in the late stage of slug ascent in a conduit. The static pressure experienced by the gas slug is given by

$$P = P_{amb} + \rho g h, \tag{1-14}$$

where P is the static pressure at a depth, h in a liquid of density ρ, g is the acceleration due to gravity and P_{amb} is the ambient pressure [*Corder*, 2008]. The ratio of the static pressure at any point within volcanic conduit to the ambient pressure at the surface defines the potential expansion of the slug P*:

$$P^* = \frac{P_{amb} + \rho g h}{P_{amb}}. \tag{1-15}$$

To achieve potential expansions comparable with those calculated for Stromboli, *Corder* [2008] carried out experiments across a range of values for P* from approximately 1.1, to 15500. The laboratory setup comprised a c. 2-m-long vertical borosilicate glass tube of internal diameter ~25 mm, sealed at the base (with the exception of a syringe for gas injection), and connected to a vacuum pump at the top (Figure 1-10). The tube was filled at depth of ~ 1.7 m with three vacuum oils (with viscosities 0.08, 0.16, 0.28 Pa s, respectively) and equipped with pressure (ASG, 163 and Piezo), displacement transducers, and normal and high speed camcorders to record the ascent and rapid expansion of the slug. The experiments demonstrated that rapid near-surface expansion imparts an upward directed viscous shear within the liquid piston preceding the gas slug, exerting a net upward directed force on the apparatus which scales to ~ 4.5×10^6 N for a basaltic volcanic system. Video data obtained from the experiments showed that

burst of the gas slug exhibits a transition in behaviour from a passive to a dynamic burst mechanism, which was also detected in pressure and displacement signals.

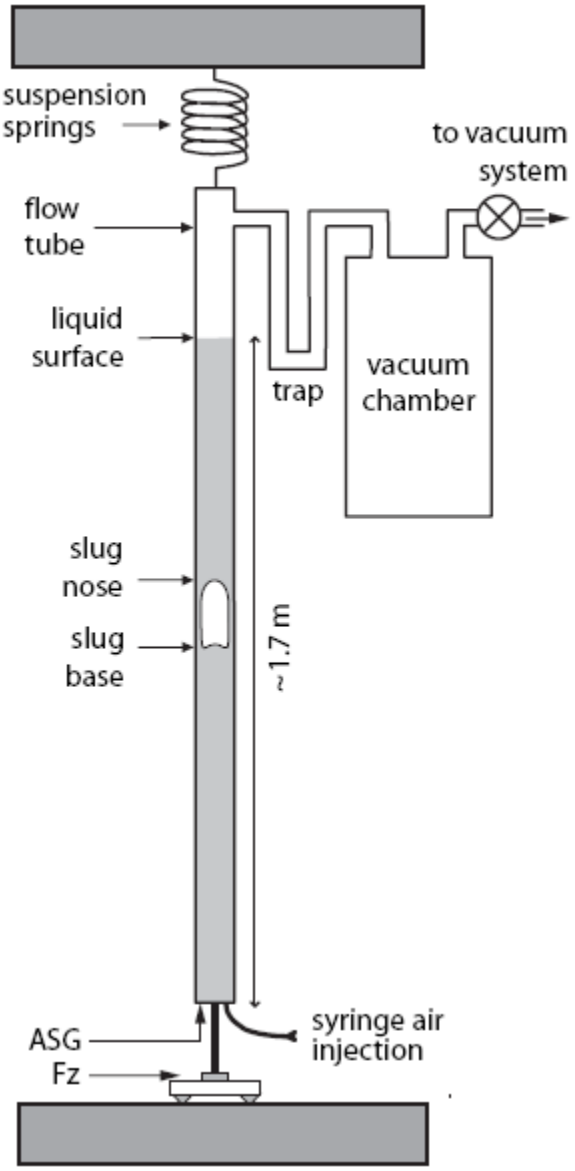

Figure 1-10. (a) Experimental apparatus used by Corder [2008] and James et al. [2008]. During experiments, pressures were measured at the base of the apparatus by a pressure sensor (ASG) and apparatus vertical motion was measured by a force sensor (Fz). In Corder [2008] pressure are also measured at the top of liquid surface by meancs of differential pressure transducers [163].

The data obtained from these experiments were compared with two one-dimensional models in order to test the validity of the models for application at the volcanic scale. Firstly, a static pressure, constant liquid-volume model, provided an upper boundary for the expansions obtained during the experiments and secondly, a dynamic model developed by *James et al.* [2008]. The results of the study carried out here were then compared with a three-dimensional computational fluid dynamic model [CFD model in *James et al.* 2008] that was applied to the volcanic situation. The change in burst behavior recorded at the laboratory scale is supported by CFD modeling, indicating a possible transition in behavior may take place with infrasonic data collected at Stromboli.

1.4 Stromboli Volcano

In this thesis, Stromboli volcano (Aeolian Islands, Italy) is chosen as case study. Strombolian eruptions are named after this small volcano-island, located in south-eastern Tyrrhenian Sea, between Sicily and south-western Italian Peninsula. This volcano has been in an almost uninterrupted state of activity for at least the past 1700 years [*Rosi et al.*, 2000]. Its persistent activity, and an easily accessible observational spot – safely located above the crater terrace – have made Stromboli an ideal location for a range of multi-parametric studies.

1.4.1 Styles of activity

The most common type of activity at Stromboli, usually classified as 'normal' [*Barberi et al.,* 1993] is characterized by intermittent, mildly explosive activity and continuous degassing, occurring simultaneously at multiple craters, on a crater terrace, located at ~

800 m a.s.l. (Figure 1-11). Two main types of explosions characterize normal activity: i) 'puffers', defined as non-passive degassing phenomena, where the gas is erupted with an overpressure, but is not associated with ejection of pyroclasts (Figure 1-11a), and ii) 'Strombolian' activity, where the explosive liberation of gas is accompanied by the ejection of disrupted magma fragments (Figure 1-11b). Normal activity is occasionally interrupted by more violent 'major explosions' and 'paroxysms' (Figure 1-11c), and by lava flow activity [*Barberi et al.,* 1993]. During normal activity, the rise and bursting of large gas slugs at the surface of the magma column causes recurring explosive events, which last tens of seconds and have a return interval of a few minutes [5-20 events per hour, *Ripepe et al.,* 2002; *Chouet et al*., 2003 and references therein]. These explosions result in the emission of jets of gas and incandescent magma fragments to heights of 100–200 m above the vents (Figure 1-11b).

The depth of formation of gas slugs at Stromboli has been estimated from the composition of erupted gases. The pressure dependence of gas solubility in the melt varies with gas species [see e.g., *Anderson*, 1995; *Bottinga and Javoy*, 1989; 1990; 1991]; consequently, the ratio of the abundances of the various gas species erupted during a slug burst event indicates the depth at which the gas in the slug was in equilibrium with the melt. At Stromboli, OP-FTIR spectroscopy of erupting volatiles reveal that the gases erupted during Strombolian explosions have mean CO_2/SO_2, SO_2/HCl, and CO/CO_2 ratios that are three to five times higher than those measured during continuous passive degassing [*Burton et al.*, 2007a]. This indicates that Strombolian eruptions are driven by CO_2 rich, water poor gas slugs in equilibrium with a hot magma source (~1100°C) under confining pressures of ~70-80 MPa (corresponding to a depth range ~ 0.8-2.7 km). This depth corresponds to a region where structural discontinuities in the crust [*Chouet et*

al., 2008] and differential bubble rise speed, may promote bubble coalescence and separation from the melt.

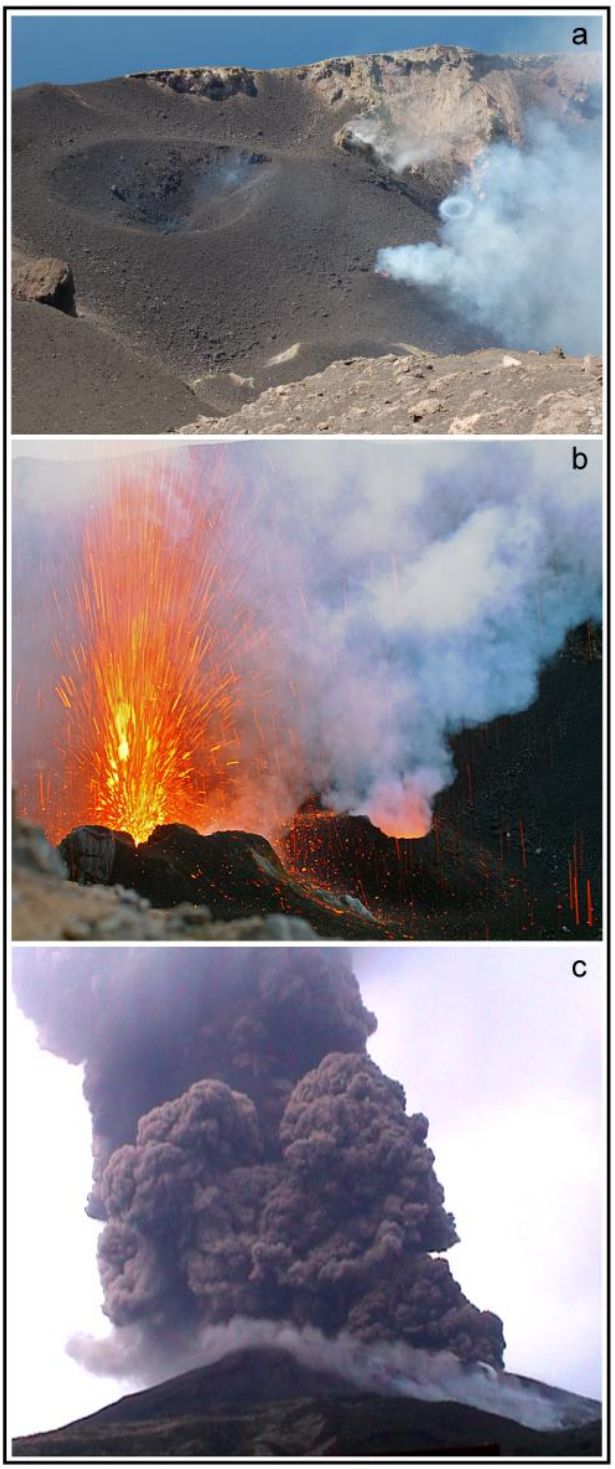

Figure 1-11. Main eruption types at Stromboli. a) A panoramic view of part of Stromboli crater terrace. 'gas puffing' is taking place at a glowing vent on the right hand side on the

image; note the 'smoke ring' (picture taken in May 2009, courtesy of M. Rosi). b) A typical Strombolian explosion from a vent (on the left hand side) with simultaneous degassing at an adjacent vent (on the right hand side) in the SW crater (picture taken in June 2008, copyright: M. Fulle) .Vents diameters range approximately 2-5 m. c) A still image of the 5th April 2003 paroxysmal explosive event captured ~ 1 sec after the beginning of the eruption (09h13m local time, photograph taken by P. Scarlato). Vertical height of the picture is ~ 2 km.

Paroxysms are characterized by violent, higher-magnitude explosions that occasionally interrupt normal Strombolian activity [*Barberi et al*., 1993; *Rosi et al*., 2006; *Bertagnini et al.,* 2008]. There have been twenty-five paroxysmal events in the last two centuries, [*Barberi et al.,* 1993]. Such events generate plumes up to 4 km high and produce greater volumes of ejecta than normal activity [*Rosi et al* 2006; *Barberi et al*., 2009].

There are two leading models to explain the origin of paroxysms: i) a 'gas-trigger' model [*Allard*, 2010]; and ii) a 'magma-trigger' model [*Métrich et al.,* 2010]. The gas trigger model proposes that highly-energetic, paroxysmal eruptions at Stromboli are also caused by gas slugs, but that they originate from much greater depths than for normal activity. The gas slugs driving paroxysmal eruptions show even greater enrichment in CO_2 with respect to normal Strombolian eruptions, corresponding to equilibrium with a magma source more than 4 km deep [*Allard*, 2010; *Aiuppa et al.,* 2010]. This has been proposed by *Allard et al.* [2008; 2010] and *Aiuppa et al.* [2010], based on geochemical composition of the gas emitted during, respectively, the 5th April 2003 and 15th March 2007 paroxysms, and by *Pino et al*. [2011] based on geochemical data and precursory seismic signals for the April 2003 explosion. The contrasting 'magma-trigger' model hypothesizes that paroxysms are triggered by the rapid ascent (in a few hours or days) of pockets of volatile-rich basaltic magma from a 7–10 km deep reservoir; this model was proposed by *Bertagnini et al.* [2003] and *Métrich et al.* [2010], on the basis of the

texture and chemistry of pyroclasts. A third model has recently been proposed by *Calvari et al.,* [2011], who have suggested that intense effusive activity and associated magma-static load removal may trigger paroxysmal eruptions by decompression of the plumbing system.

1.4.2 Physical parameters

In this section we introduce a set of parameters and data distilled from previous works on Stromboli. We use these to derive ranges for various dimensionless parameters that are appropriate for volcano scale-conditions and to calculate burst overpressure at Stromboli.

A summary of parameters presented in this section is given in Table 1-1 at the end of this section. Table 1-2 reports dimensionless parameters for volcanic slugs calculated assuming typical Stromboli parameters given in Table 1-1. Their values are such that surface tension plays a negligible role for volcanic slugs, hence their morphology and ascent velocity are predominantly controlled by inertial and viscous forces [*Seyfried and Freundt*, 2000].

1.4.2.1 Magma viscosity, density and melt–gas surface tension

The *in situ* viscosity of the magma filling the conduit system at Stromboli cannot be measured directly, but may be estimated from laboratory rheometry of natural samples, or using published rheological models, in which case appropriate values for temperature, pressure, magmatic composition, and crystal and bubble contents must be assumed. All of these quantities may vary dramatically with position in the conduit, and

between periods of normal and paroxysmal activity, hence there is a very broad range of plausible values for the magma viscosity.

For bubble-free, primitive melts at depths greater than 3 km, the empirically-derived equation of *Misiti et al*. [2009] gives a viscosity of approximately 5 Pa s for a Stromboli potassium-rich (HK) basalt with a 3.36 wt.% added water content (representative of the more primitive basaltic melts, following *Métrich et al*. [2001] and *Bertagnini et al.* [2003] who found 2–3.4 wt% H_2O in trapped melt inclusions in olivine crystals basalts) at a temperature of 1150°C. This is much lower than the pure melt viscosity of ~350 Pa s at 1157°C reported by *Vona et al.* [2011] for Stromboli HK samples. This discrepancy is probably due to loss of water during the sample preparation procedure employed by *Vona et al.* [2011].

The presence of crystals at sub-liquidus temperatures has a strong impact on the rheology of the magma, introducing shear thinning behavior and other non-Newtonian phenomena [*Ishibashi,* 2009; *Mueller et al.,* 2010]. An important manifestation of this impact is a dramatic increase in magma viscosity with increasing crystal content; this is most pronounced for elongate crystals [*Mueller et al.,* 2011], which are typical of Stromboli basalts [mean aspect ratio ~ 7; *Vona et al.,* 2011]. *Vona et al.* [2011] measured the viscosity of Stromboli HK-basalts in the subliquidus temperature range T = 1187.5–1156.7°C, corresponding to crystal volume fractions in the range ~10% to ~30%; they found that the crystals increased the magma viscosity by a factor of ~1.5 (~270 Pa s) for the lowest crystal content, rising to a factor of ~13 (~4400 Pa s) for the highest crystal content.

The presence of bubbles may also have a strong impact on magma rheology and viscosity [*Stein and Spera*, 2002; *Llewellin et al.,* 2002]. The viscosity of bubbly magma at

3 km is computed as 100 Pa s by *Allard* [2010] based on the viscosity of bubble-free melt derived from the equation of *Hui and Zhang* [2007]. Shallower than this depth, the magma starts crystallizing and mingles with a more viscous ($\sim 10^4$ Pa s), crystal-rich, partially-degassed magma residing in the conduit and/or recycled from the uppermost portion of the plumbing system [*Landi et al.,* 2004 and references therein]; hence, estimates of the viscosity of the magma filling the portion of the conduit system at Stromboli that is shallower than 3 km vary from around 10^2 to 10^4 Pa s.

The density of the magma varies according to its vesicularity. Various textural studies [*Métrich et al.,* 2001; *Bertagnini et al.,* 2003; *Lautze and Houghton*, 2005; 2007; *Polacci et al*., 2009] have shown the presence of both high-density (low vesicularity) and low-density (40-50% vesicularity) magmas in the uppermost part of the conduit. For a pure basaltic melt we use a typical density value of 2600 kg/m^3 [*Murase and McBirney*, 1973], which gives a density of 1300 kg/m^3 for the most vesicular magma.

Murase and McBirney [1973] provide surface tension data for several silicate liquids in an Argon atmosphere. Their data for basaltic liquids fall in the range 0.25 – 0.4 N/m. A value of 0.4 N/m was previously applied by *Seyfried and Freundt* [2000] and *James et al.* [2008] for slugs in basaltic magma. We are not aware of any direct measurements of surface tension for Stromboli basalts, so we adopt this value.

1.4.2.2 Conduit geometry and dimensions

In common with most other physical and numerical models of volcanic eruptions, we assume that the volcanic conduit is a vertical, cylindrical pipe. Since this geometry minimizes heat loss, a stable plumbing system might be expected to evolve towards cylindrical morphology over time; given the unusually long-lived stability of eruptive

behavior at Stromboli [*Rosi et al.*, 2000] this assumption is perhaps more valid here than at most other volcanoes. The diameter of the conduit has not been measured directly, but may be inferred from visual estimates of the dimensions of the exploding slugs and the diameter of the vents at Stromboli, which are of the order of 2 to 5 meters [*Chouet et al.*, 1974; *Vergniolle and Brandeis*, 1996]. *Burton et al.*, [2007b] have inferred the conduit radius (r_c) as a function of pressure by applying mass conservation to magma flow rate, obtaining $r_c \sim$ 1.5 m at 200 MPa and 1.3 m at 50 MPa. We follow *James et al.* [2008; 2009] and choose as a reference value r_c = 1.5 m for all calculations in section 5. We further explored the effect of r_c = 3 m when calculating overpressure as a function of volume (section 3).

1.4.2.3 Slug volumes

At Stromboli the typical volume of gas emitted during a single, short lived explosion, characteristic of normal activity has been estimated by several field methods. *Harris and Ripepe* [2007a] report volumes for gas 'puffers' (non-passive degassing phenomena, where the gas is erupted with an overpressure, but is not associated with ejection of pyroclasts) of around of 50–190 m^3, that correspond to gas masses around 10 to 30 kg. *Vergniolle and Brandeis* [1996] estimate the radius, length and overpressure of slugs by matching synthetic acoustic pressure waveforms to recorded signals from 36 eruptions at Stromboli. They estimate slug volumes in the range 10-100 m^3, with the volume depending strongly on the value chosen for the thickness of the liquid film above the slug at the point of burst. Following this approach, *Ripepe and Marchetti* [2002] find volumes of 20-35 m^3 from infrasound measurements of a series of eruptions during September 1999. Photo-ballistic determination of gas emission reported by *Chouet et al.* [1974] yields typical volumes of 10^3 m^3. Volume estimates inferred by *Chouet et al.*

[2003] from seismic measurements range from 7 x 10^3 to 2 x 10^4 m^3. UV-measurements of SO_2 fluxes from a series of eruptions in October 2006 indicated volumes in the range 1.5-4 x 10^3 m^3 [*Burton et al.*, 2007a; *Mori and Burton*, 2009].

Paroxysmal eruptions are associated with slugs of much larger volume; *Ripepe and Harris* [2008] inferred the ejection velocity of the gas particle-mixture erupted by the paroxysm of the 5th April 2003 using multi-modal data obtained from a thermal-seismic-infrasonic array. They then used the velocity data to estimate that a gas volume of 6 x 10^5 m^3 was erupted during the paroxysmal eruption.

1.4.2.4 Slug ascent velocity

In previous models of slug flow at Stromboli [*Vergniolle and Brandeis*, 1996; *James et al*., 2004; 2008; *O'Brien and Bean,* 2008; *Allard*, 2010; *Pino et al.,* 2011] slug ascent velocity has been evaluated using the empirical correlation of *Wallis* [1969]. *Viana et al.* [2003] present a thorough, and more up-to-date, review of available slug velocity data and use it to derive a well-validated empirical correlation (presented in section 1.2.3); this can be used to calculate ascent velocity from magma viscosity and density, and conduit radius. Both correlations yield slug-base ascent velocities v_s (or likewise, in the absence of expansion, slug nose ascent velocities) in the range 0.11-2.6 m/s for Stromboli parameters. These theoretical values differ significantly from the ascent velocities of 10–70 m/s inferred by *Harris and Ripepe* [2007b] from the delay between seismic and infrasonic signal arrival times. Their measurements reflect slug behavior only in the uppermost portion of the conduit (~250 m below the crater terrace) and may be influenced by the rapid expansion of the slugs in that region [*James et al.*, 2008]. Consequently, we follow *Viana et al.* [2003] when deriving slug ascent velocities.

Physical Property		Volcano-scale range
g (m/s^2)	Gravitational acceleration	9.81
μ (Pa s)	Magma dynamic viscosity	10-10000
ρ (kg m^{-3})	Density of magma	1300-2600
σ (N m^{-1})	Surface Tension	0.07
r_c (m)	Conduit radius	1.5 - 3
V_a (m^3)	Slug volume	10^2 -10^6

Table 1-1. Summary of parameters and their ranges used for modelling to the eruptions of Stromboli volcano.

Dimensionless group	Volcano-scale conditions
$Mo = \frac{g\eta^4}{\rho\sigma^3}$	5.9×10^2 - 1.2×10^{15}
$Eo = \frac{4\rho g r_c^2}{\sigma}$	2.9×10^5 - 2.3×10^6
$N_f = \frac{\rho}{\eta}\sqrt{8g r_c^3}$	2.1 - 1.2×10^4
$Fr = \frac{v_s}{\sqrt{2g r_c}}$	0.02 - 0.34
$Re = N_f Fr$	0.04 – 4×10^3

Table 1-2. Dimensionless parameters for volcanic-scale slugs, calculated using physical parameters discussed in section 1.4.2 and summarized in Table 1-1.

2. An experimental model of liquid film thickness around gas slugs

In this section we report new experimental data describing the behavior for the thickness of the liquid film around a rising slug. The results of these experiments have been tested, in a recent work by *Llewellin et al.* [2011], against the existing models presented in previous section. In previous volcanological applications *James et al*. [2006; 2008; 2009] considered a thickness of liquid film $\lambda \sim 0.5$ m ($A' \sim 0.5$) as suitable to represent an average viscosity of a bubble free basaltic magma of 10^3 Pa s. However, as previously reported in section 1.2.3, a variation in the thickness of the falling magma film strongly affects the shape of the slug, and consequently, its expansion capability. Determining this parameter carefully is then crucial to estimate the development of overpressure during a slug's ascent.

2.1 Materials and methods

Quantitative experimental data for the equilibrium thickness of the falling film around a rising Taylor bubble are scarce, and only one systematic work [*Nogueira et al.,* 2006] studied air slugs rising through vertical columns of stagnant and flowing Newtonian liquids in a pipe with $r_c = 0.016$ m, filled with liquids with viscosities in the range $10^{-3} < \mu < 1.5$ Pa s, and with densities close to that of water. Their experiments span the range $15 < N_f < 18 \times 10^3$ and $140 < Eo < 200$. While their experiments cover a wide range of inverse viscosity, they do not collect data for sufficiently low values of N_f to constrain behavior in the viscous, thick-film regime. Therefore we performed laboratory experiments to explore a range of A' values accounting for such viscosity variability.

2.1.1 Experimental set up

We conducted laboratory experiments in which Taylor bubbles were formed by introducing air into cylindrical, transparent acrylic pipes of three different internal radii (r_c = 0.01, 0.02, 0.04 m) and of length 2 m. A schematic representation of the experimental set up is reported in Figure 2-1. The pipes were filled with a variety of Newtonian liquids (golden syrup, cooking oil, liquid soap, water and mixtures prepared by diluting syrup or soap with water) in order to cover a range of values of viscosity and interfacial tension. Taylor bubbles were formed by partially filling the pipes with liquid to leave an air pocket of length L_0, then sealing and inverting the pipe. The Taylor bubble's ascent was recorded in the upper part of the pipe using high-definition videography (Casio Exilim EX-F1). After each ascent, liquid was added and the experiment was re-run; between 8 and 16 different values of L_0 were used for each liquid/pipe combination (typically covering the range $0.01 < L_0 < 0.3$ m), thus producing a suite of n data points for each value of N_f.

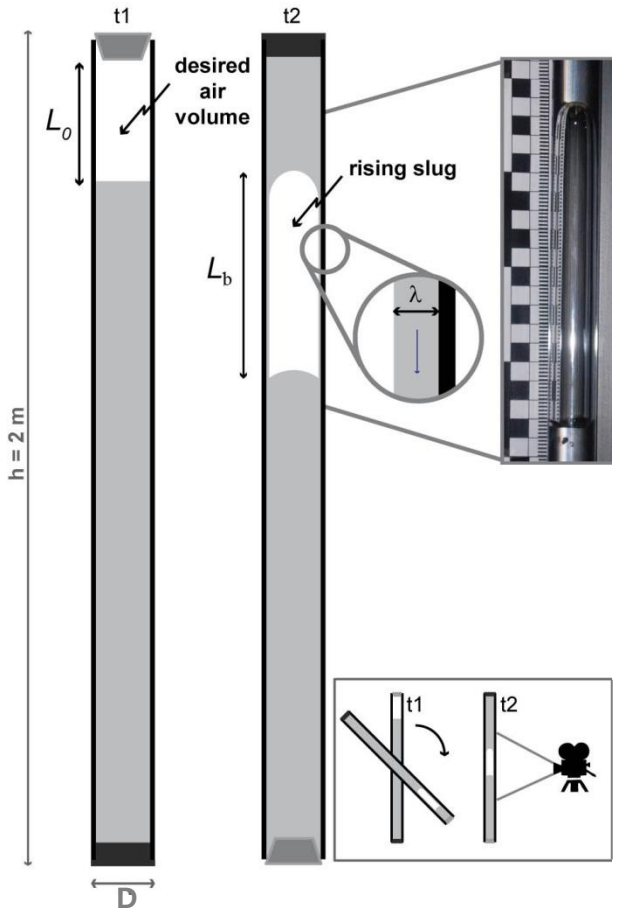

Figure 2-1. Experimental setup. For each experimental run a progressively decreasing amount of air was left in the pipe by adding fixed volumes of liquid (t1). Turning the tube upside down around a pivot results in the formation of slugs with variable initial L_0 (t2). Slug motion and length (L_b) was captured using full high-definition videos.

2.1.2 Properties characterization and scaling

Stress–strain rate flow curves were determined with a rotational rheometer (Physica MCR 301, Anton Paar), using both parallel plate and concentric cylinder geometries. Rotational tests have been performed at room temperature for a range of shear strain rate ($1 < \varepsilon < 10^2$ s^{-1}), in a linear ramp profile. To ensure an accurate temperature control within the sample a Peltier element coupled with Peltier hood has been used during the tests. All liquids were found to have Newtonian rheology. Data from five repeat runs were used to determine viscosity μ with a typical error of less than 0.5%; however,

owing to small temperature fluctuations during experiments, we put a conservative uncertainty of 5 % on viscosity. The density of each liquid was measured by weighing a known volume at controlled ambient temperature with error of less than 1 %. The interfacial tension of cooking oil, soap and soap solutions was measured using the drop shape method [*Woodward*, 2008] with an error of less than 10 %. The interfacial tension of pure and diluted golden syrup was taken from *Llewellin et al.* [2002]. Measured physical properties of the liquids are presented in Table 2-1. Raw data of viscosity measurements are given in Appendix A.

Table 2-1 reports dimensionless parameters for our experimental conditions and for volcanic slugs calculated assuming typical Stromboli parameters given in Table 1-1. Our experimental conditions are scaled to the inertia/viscous-dominated regime inferred for a basaltic conduit with associated dimensionless numbers $5.2 \times 10^{-11} < Mo < 3.6 \times 10^{7}$, $54 < Eo < 3.2 \times 10^{3}$., $2.9 \times 10^{-1} < N_f < 5.9 \times 10^{4}$, $2.7 \times 10^{-4} < Fr < 0.37$, and $7.7 \times 10^{-4}. < Re < 2 \times 10^{4}$.

Dimensionless group	**Experimental conditions**	**Volcano-scale conditions**
$Mo = \frac{g\eta^4}{\rho\sigma^3}$	5.2×10^{-11} – 3.6×10^{7}	5.9×10^{2} - 1.2×10^{15}
$Eo = \frac{4\rho g r_c^2}{\sigma}$	54 – 3.2×10^{3}	2.9×10^{5} - 2.3×10^{6}
$N_f = \frac{\rho}{\eta}\sqrt{8gr_c^3}$	2.9×10^{-1}- 5.9×10^{4}	2.1 - 1.2×10^{4}

$Fr = \frac{v_s}{\sqrt{2gr_c}}$	2.7×10^{-4} - 0.37	0.02 - 0.34
$Re = N_f Fr$	7.7×10^{-4} – 2×10^{4}	0.04 – 4×10^{3}

Table 2-1. Dimensionless parameters for scaling experiments to the natural system.

	Experimental data									Derived values				
Quantity	μ	ρ	σ	D	r_c	n	v_b	σ_{vb}	%error v_s	β	$\sigma\beta$	λ'	$\Delta\lambda'+$	$\Delta\lambda'-$
Units	Pa s	kg/m^3	N/m	m	m		m/s	m/s						
glucose syrup	40.3	1390	0.08	0.01912	0.00956	8	0.0012	0.00003	4.8	2.126	0.023	0.314	0.009	0.009
7% glucose s.	3.7	1370	0.08	0.01912	0.00956	8	0.0124	0.00084	13.6	2.179	0.023	0.323	0.009	0.009
10% glucose s.	1.15	1360	0.08	0.01912	0.00956	8	0.0380	0.00059	3.1	2.158	0.020	0.319	0.008	0.008
soap	0.33	1027.4	0.02	0.02	0.01	14	0.0944	0.00306	6.5	2.070	0.021	0.305	0.007	0.008
25% soap	0.171	1019	0.035	0.02	0.01	14	0.1362	0.00117	1.7	1.861	0.029	0.267	0.012	0.013
soap	0.33	1027.4	0.02	0.04	0.02	10	0.1870	0.00196	2.1	1.855	0.023	0.266	0.010	0.011
25% soap	0.171	1019	0.035	0.04	0.02	8	0.2052	0.00128	1.2	1.663	0.046	0.225	0.025	0.028
seed oil	0.0456	894.7	0.032	0.02	0.01	11	0.1419	0.00108	1.5	1.589	0.014	0.207	0.008	0.008
soap	0.33	1027.4	0.02	0.08	0.04	13	0.2855	0.00280	2.0	1.501	0.014	0.184	0.008	0.008

25% soap	0.171	1019	0.035	0.08	0.04	11	0.3128	0.00219	1.4	1.410	0.009	0.158	0.006	0.006
seed oil	0.0456	894.7	0.032	0.04	0.02	12	0.2062	0.00245	2.4	1.428	0.026	0.163	0.016	0.017
33% soap	0.015	1008.9	0.045	0.02	0.01	15	0.1480	0.00075	1.0	1.360	0.016	0.142	0.011	0.011
seed oil	0.0456	894.7	0.032	0.08	0.04	14	0.3242	0.00669	4.1	1.336	0.017	0.135	0.012	0.012
33% soap	0.015	1008.9	0.045	0.04	0.02	8	0.2265	0.00193	1.7	1.186	0.023	0.082	0.021	0.023
33% soap	0.015	1008.9	0.045	0.08	0.04	12	0.2932	0.00290	2.0	1.171	0.035	0.076	0.029	0.032
tap water	0.0012	999.7	0.073	0.02	0.01	15	0.1494	0.00156	2.1	1.165	0.012	0.074	0.010	0.011
tap water	0.0012	999.7	0.073	0.04	0.02	12	0.2161	0.00222	2.1	1.191	0.010	0.084	0.009	0.009
tap water	0.0012	999.7	0.073	0.08	0.04	16	0.3050	0.00177	1.2	1.197	0.012	0.086	0.010	0.010

Table 2-2. Measured properties of materials and experimental results. Dilutions of syrup and soap are indicated.

2.2 Results

Consistent with previous studies,[e.g., *Campos & Guedes de Carvalho*, 1988], we find that the shapes of the nose and body of the bubble are qualitatively the same for all bubbles, and are independent of bubble length and other experimental parameters.

The morphology of the tail and the nature of the wake that follows it vary systematically with inverse viscosity, as previously shown in both laboratory experiments [*Campos & Guedes de Carvalho,* 1988; *Viana et al*., 2003] and numerical simulations [*Kang et al.,* 2010]. We find that the shape of the tail is stable for $N_f < 600$ and unstable for $N_f > 600$, as reported by *Campos & Guedes de Carvalho* [1988].

Video images were analysed using the freely available IMAGEJ software, and the ascent velocity v_b and the length of the bubble L_b were recorded. The velocity was determined by measuring the position of the bubble's nose in two frames of the video (near the bottom and top of the measurement section, respectively) and noting the elapsed time. For each value of N_f, velocity was determined for all of the bubbles in the suite of data, and was found to be independent of bubble length. The mean value of v_b was calculated for each suite, along with the standard deviation σ_{vb} . The length of each bubble from nose to tail, L_b, was measured from a single video frame and was plotted against L_0 for each suite of data (Figure 2-2a). All measurements performed from video data are reported in Appendix B. A linear relationship between L_b, and L_0 was found for each suite,

$$L_b = \alpha + \beta L_0, \qquad (2\text{-}1)$$

where $\beta = (1 - \lambda')^{-2}$, and α is a constant related to the length of the nose and tail regions. This linearity indicates that only the cylindrical part of the body of the bubble changes length as gas volume changes, the nose, upper body and tail remaining unchanged; hence, the thickness of the falling film in the cylindrical part of the body region is, indeed, independent of bubble length.

For each data suite (i.e. for each value of N_f), the best-fit value of β was found by linear regression of equation 2-1. The standard deviation σ_β was then calculated (assuming that errors in the residual are normally distributed) and, from these data, 95% confidence limits on b were computed. Two examples, for the best and for the worst fitting-series respectively, are shown in Figure 2-2b. These values were used to determine λ' and upper and lower bounds on λ'. Results are summarized in Table 2-2. Results are also plotted in Figure 2-3. The figure shows that film thickness is a strong function of inverse viscosity; it also demonstrates that all the data collapse to a single curve, indicating that the non-dimensionalization is appropriate, and is sufficient to characterize the system when surface tension can be neglected ($Eo > 40$; see section 1.2.2).

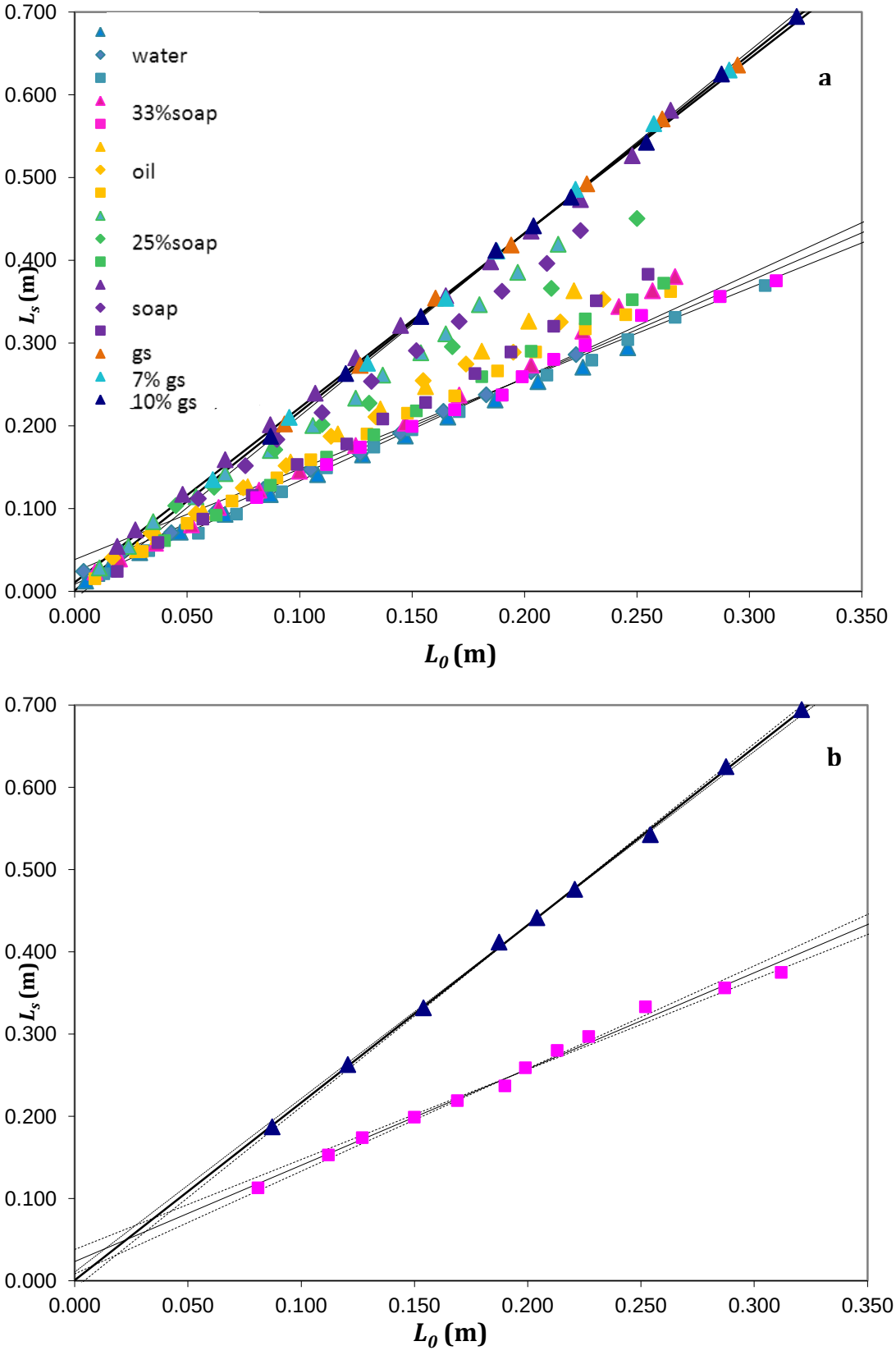

Figure 2-2. a) Experimentally measured bubble length L_s and initial length of the air pocket L_0 for all the experiments performed in this work. Triangles, diamonds and squares

represent suites performed in pipes with radius r_c= 0.01, 0.02, and 0.04, respectively. b) two selected data suites representing the best (syrup solution) and worst (soap solution) fit to regression. Best-fit values of β (solid lines) and 95% confidence limits (dashed lines) are shown.

2.3 Comparison with previous models

The experimental data presented here are used to examine the validity of each of the three models for film thickness that have been applied to the volcanic system: the *Brown* [1965] model (equation 1-7); the combined *Batchelor* [1967]–*Viana et al.* [2003] expression (equations 1-9 and 1-10); and the simple *Batchelor* [1967] model (equation 1-11). We also test the *Kang et al.* [2010] model (equation 1-12). Experimental data of *Nogueira et al.* [2006] are also included.

The comparison between data and models is shown in Figure 2-3a. Note that, since the parameter of interest in the present study is the dimensionless film cross section *A'*, rather than the dimensionless film thickness *λ*', we recast the experimental data presented in *Llewellin et al.* [2011], and each of the models for film thickness, as $A'(N_f)$ using equation 1-6:

$$A' = 0.351 + 0.197 \tanh(2.71 - 1.14 \log_{10} N_f). \quad (2\text{-}2)$$

This expression has an advantage over equation 1-13 for the current application because it expresses *A*' as a function of N_f directly and does not require conversion via equation 1-6, whilst retaining the same excellent fit to data.

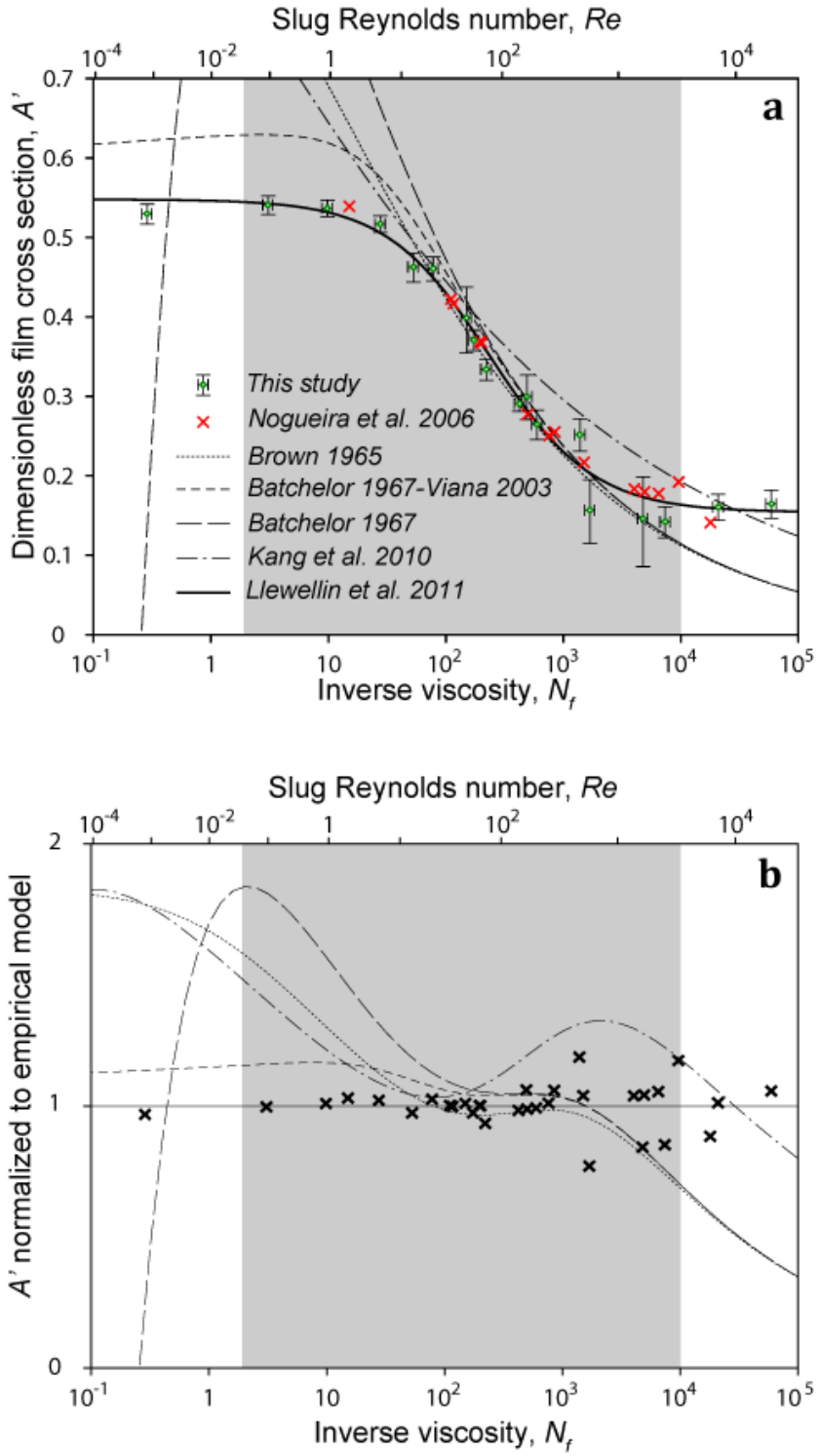

Figure 2-3. Comparison of models for dimensionless film cross section A′ as a function of dimensionless inverse viscosity N_f (or related Reynolds number Re) with experimental data from Llewellin et al. [2011] and Nogueira et al. [2006]. The shaded area shows the range of values of N_f that is relevant to gas slugs at Stromboli Table 2-1). a) Lines show the predictions of various models for A′ (N_f). The published models show good agreement with

the data at intermediate values of N_f but perform poorly at the extremes. The new model (solid line) of Llewellin et al. [2011] is the best fit solution to data across the volcanologically-relevant range of N_f, and beyond. b) The data and models presented in (a) are shown normalized to the new empirical model to give a clearer demonstration of the quality of fit provided by each model across the range of N_f.

The data in Figure 2-3a describe a clear sigmoidal shape, with well-defined asymptotic regions at low and high N_f, where film thickness is independent of inverse viscosity. In the low N_f asymptotic region ($N_f < 10$), the film occupies around 55% of the conduit cross section ($A' = 0.55$); in the high N_f asymptotic region ($N_f > 10^4$), the film occupies only 15% of the conduit cross section ($A' = 0.15$). In the region between these two asymptotes ($0.1 < N_f < 10^5$), the film thickness shows a logarithmic dependence on inverse viscosity; it is notable that this region coincides with the range of inverse viscosity expected for Stromboli (shaded in Figure 2-3), indicating that A' may assume any value in the range $0.15 < A' < 0.55$, depending on the physical properties of the magma, and the dimensions of the conduit. in Figure 2-3b, all of the models presented are normalized to equation 2-2, allowing the quality of fit provided by each model to be directly compared.

Of the three models for film thickness that have previously been adopted for volcanological applications, *Brown*'s model (equation 1-7) and the combined *Batchelor* – *Viana* model (equations 1-9 and 1-10) perform fairly well in the volcanically-relevant range of N_f; however, both overpredict film thickness at low end of the range, and underpredict at the high end (although we note that the data scatter is greatest in the range $10^3 < N_f < 10^4$). *Nogueira et al.* [2006] noted that the *Brown* model underpredicts film thickness at high *Re*, and attributed this to the onset of flow transition in the film. By combining equations 1-5 and 1-10, we can see that *Re* is a function of N_f only. *Re* is

plotted as a secondary axis in Figure 2-3. Supposing *Nogueira*'s hypothesis is correct, the data show that flow transition occurs at $N_f > 10^3$, which is within the volcanically-relevant range.

The simple *Batchelor* model (equation 1-11) performs poorly for $N_f < 100$. The *Kang* model (equation 1-12), which has not yet found volcanological application, generally performs poorly, except over a very limited range of N_f. The semi-empirical model for $\lambda'(N_f)$ proposed by *Llewellin et al.* [2011] (equation 1-13), provides excellent fit to data when combined with equation 1-6 and expressed as $A'(N_f)$ (equation 2-2).

Therefore, in the following section, equation 2-2 is applied to calculate A' for the range of volcanic conditions appropriate to Stromboli and used in our model of overpressure.

3. A model for gas overpressure in slug-driven eruptions

In this section we propose a new solution to the problem of determining volcanic gas overpressure during Strombolian eruptions.

The degree of gas overpressure a slug acquires prior to bursting depends on the balance of the magmastatic, viscous and inertial forces acting on the slug during its ascent of the conduit. As previously reported in section 1.3, analytical [*Vergniolle and Brandeis,* 1994; *Seyfried and Freundt,* 2000; *James et al.,* 2008; 2009], numerical [*D'Auria,* 2006; *James et al.,* 2008] and laboratory models [*Jaupart and Vergniolle,* 1988; *Seyfried and Freundt,* 2000; *James et al.,* 2004; 2006; 2008] have explored in detail the formation, ascent and expansion of slugs in vertical and inclined conduits, but have focused largely on slug formation and motion, rather than explosion. However, *James et al.* [2009] qualitatively correlated overpressure in the slug with different regimes of 'burst vigour', linking the magnitude of the measurable geophysical effects of overpressure, e.g., pressure transients and acoustic signals, to the surface style of an eruption.

We adopt and expand previous analysis of *James et al.* [2009] to build a simple analytical model that describes the conditions under which a gas slug rising in a cylindrical conduit becomes overpressured, and which predicts the overpressure when the slug bursts. Using this model, we identify and quantitatively explore two key parameters that control pressure inside a slug at the time of explosion: 1) the amount of gas in the slug; and 2) the thickness of the liquid film draining down the conduit around the rising slug. Then, using the model of *Llewellin et al.*, [2011, equation 2-2], based on analogue experimental data presented in section 2, we also develop a new framework for estimating relevant geometrical parameters for volcanic slugs over the range of plausible conduit conditions. We then apply our model to predict the overpressure of Strombolian eruptions using appropriate volcano-scale parameters. Model outputs are

validated against previously published estimates of bursting overpressure derived from a broad dataset of eruptions at Stromboli. Finally, we discuss whether the range of volcanic eruptions observed at Stromboli can be explained in terms of the ascent and burst of gas slugs.

Gas overpressure is the key parameter in determining explosion vigour of Strombolian eruptions and the nature of associated hazards such as the range of ballistically-transported volcanic bombs [e.g. *McGetchin and Chouet,* 1979; *Self et al.,* 1979; *Wilson,* 1980; *Alatorre et al.,* 2010; *Vidal et al.,* 2010]. Overpressure has been determined from estimates of the initial velocity of gas–pyroclast mixtures [*Blackburn et al.,* 1976], from gas/ash velocity derived from thermal imagery [*Ripepe and Harris,* 2008], and from synthetic oscillating-bubble waveforms [*Vergniolle and Brandeis,* 1996; *Ripepe and Marchetti,* 2002]. Attention has also been paid to the role of overpressured gas slugs as a source of infrasonic and seismic signals at Stromboli [e.g. *Vergniolle and Brandeis,* 1996; *Ripepe and Gordeev,* 1999; *Ripepe and Marchetti,* 2002; *Vergniolle et al.,* 2004; *Ripepe and Harris,* 2008], which has permitted quantitative determination of overpressure during explosive eruptions.

Infrasound and other geophysical signals are generated by changes in the pressure distribution within the conduit during the ascent and burst of gas slugs. The intensity of the pressure change is strongly dependent on the size of the slug and on the viscosity of the conduit-filling magma [*James et al.,* 2004; 2006; 2008; 2009; *Corder*, 2008; *Chouet et al.,* 2003; *Vergniolle and Ripepe,* 2008], and several studies yield constraints on the interpretation of geophysical signals using models that rely on geometrical parameters of the slugs (size, radius and thickness of the surrounding magma layer). These parameters have been inferred from seismic [*Chouet et al.,* 2003; *O'Brien and Bean*,

2008], acoustic [*Vergniolle and Brandeis,* 1996], thermal [*Harris and Ripepe,* 2007a] and Doppler [*Gerst et al*., 2008] measurements, and estimated from visual observation [*Chouet et al.,* 1974; *Vergniolle et al.,* 1996; 2004], and the maximum size of *ejecta* [*Blackburn et al.,* 1976; *Wilson,* 1980].

3.1 Slug overpressure model

In this section, we develop two models for the development of overpressure in a gas slug during its ascent of a magma-filled conduit. The main aim is to quantify the pressure inside the slug at the moment of burst, when the gas is liberated to the atmosphere. In the first model – the 'standard model' – we assume that the magma is confined to the conduit, and does not overflow during the slug's ascent; this is consistent with observations of normal Strombolian activity. In the second model – the 'overflow model' – we assume that the expansion of the slug during ascent causes the magma above it to overflow; this is consistent with observations of paroxysmal activity.

3.1.1 Development of slug overpressure in the absence of magma effusion (standard model)

To quantify the pressure evolution inside a rising slug when magma is confined to the conduit, we develop a model that builds on the "static pressure limit approach" developed in *James et al.* [2009] (their sections 2 and 3). In that model, the rising slug is treated as a cylinder of length L_s and constant radius r_s, rising along the axis of a cylindrical pipe of radius r_c (Figure 3-1). As the slug ascends, it grows in response to the decrease in the magma-static head. Inertial and viscous forces acting on slug expansion at the conduit scale are neglected in the formulation of the model.

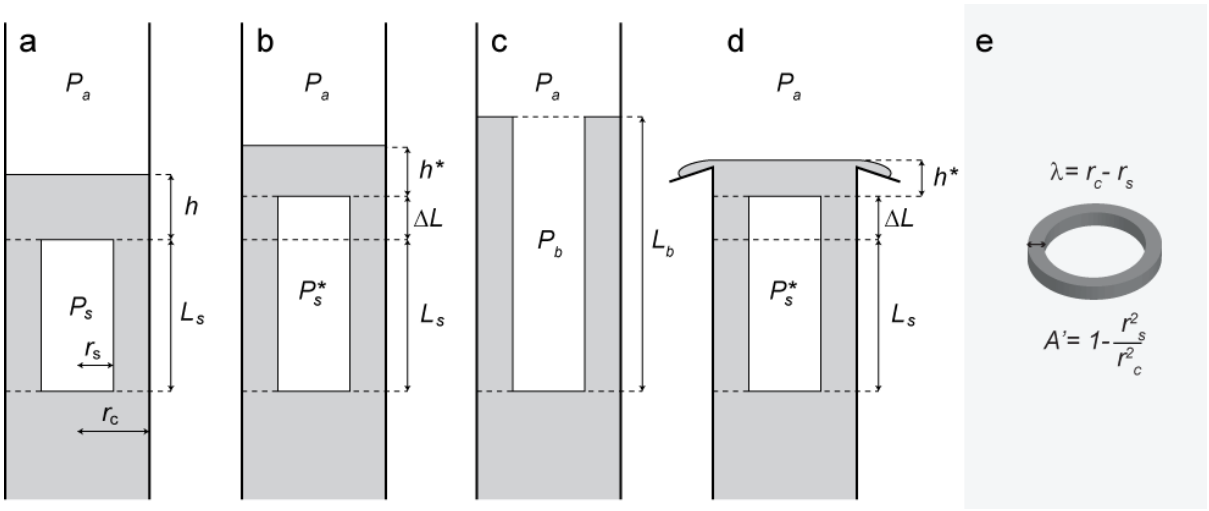

Figure 3-1. Theoretical model of a cylindrical slug of radius r_s and length L_s bursting at the top of an idealized conduit of radius r_c. a) Initially, gas pressure in the slug (P_s) is in equilibrium with the magmastatic (ρgh) plus atmospheric pressure (P_a) as the slug rises. b) When a perturbation causes the slug to lengthen by a small amount (ΔL) the magmastatic head decreases to h^* ($h^* < h$) and both the pressure within the slug (now P_s^*) and the magmastatic pressure (ρg h^*) decrease. c) If magmastatic pressure drops below the slug pressure, the perturbation grows, causing the slug to burst with a pressure P_b and length L_b. d) If magma is allowed to erupt from the conduit during slug ascent (overflow model, section 3.1.2), the height of the column of magma above the slug during perturbation is smaller than in case b). e) Cross-section of a conduit occupied by a gas slug, illustrating schematically the thickness (λ) of the liquid film and the dimensionless parameter A'.

James et al. [2009] have demonstrated that, although simplified, the static model is in good agreement with data from experiments involving only relatively modest slug expansion, implying that, for these conditions, the contribution of viscous and inertial effects on dynamic expansion can be neglected. For larger, more rapid slug expansion, viscous and inertial effects become more important and act to increase slug overpressure; in this case our model can be considered a lower limit for overpressure at burst.

As the slug rises from depth (Figure 3-1a), the pressure P_s of the gas within the slug is in equilibrium with the magmastatic pressure P_h due to the column of liquid above the slug, which is given by:

$$P_h = \rho g h + P_a \,, \tag{3-1}$$

where ρ is the magma density, g is the gravitational acceleration, h is the height of the column of liquid above the slug and P_a is the ambient pressure at the top of the conduit. As the slug rises, it expands in response to decreasing P_h. Since thermal effects and non-ideal gas behavior are shown to be secondary processes and can be neglected [*Seyfried and Freundt*, 200; *James et al.*, 2008], we assume that the gas within the slug behaves isothermally; hence, $P_s L_s$ = const. It is useful to define a reference slug length, L_a, which is the length that the slug would have at atmospheric pressure P_a, hence:

$$P_s L_s = P_a L_a . \tag{3-2}$$

The mass of gas in the slug is assumed to be constant (i.e., there is no diffusion of volatiles from the surrounding melt and no coalescence with other bubbles during ascent, as supported by gas-melt chemistry data [*Burton et al.*, 2007a; *Allard et al.*, 2010]); hence, the size of the slug can be related to the number of moles of gas n that it contains, assuming the ideal gas law:

$$P_a L_a \pi r_s^2 = nRT \,, \tag{3-3}$$

where R is the ideal gas constant and T is the absolute temperature of the gas.

James et al [2009] consider the stability of the equilibrium between the pressure in the slug, and the magmastatic pressure above the slug in response to a perturbation which

increases the slug length by a small amount ΔL, and during which the base of the slug is stationary (Figure 3-1b). The perturbation causes a change in both the pressure within the slug, and the magmastatic pressure above the slug. The pressure within the slug decreases according to equation 3-2; hence, the perturbed pressure in the slug P_s^* becomes:

$$P_s^* = \frac{P_a L_a}{L_s + \Delta L}. \qquad (3\text{-}4)$$

The perturbation also causes magma to flow from the head region into the falling film around the slug. Conservation of magma volume gives the perturbed height of the magma column above the slug $h^* r_c^2 = h r_c^2 - \Delta L(r_c^2 - r_s^2)$; hence, the perturbed magmastatic pressure above the slug P_h^* also decreases, becoming (from equation 3-1):

$$P_h^* = \rho g(h - A' \Delta L) + P_a; \qquad (3\text{-}5)$$

where A' is the fraction of the cross-sectional area of the conduit that is occupied by the falling film in the slug region (Figure 3-1e):

$$A' = 1 - \frac{r_s^2}{r_c^2}. \qquad (3\text{-}6)$$

The competition between these two pressure changes determines whether the perturbation grows ($P_s^* > P_h^*$) or decays ($P_h^* > P_s^*$). If, in the limit $\Delta L \rightarrow 0$, the perturbation decays (i.e. the decrease in slug pressure is larger than the decrease in magmastatic pressure), then the slug is *'stable'*. Conversely, for an *'unstable'* slug, the slug pressure decrease is not balanced by the decreasing magmastatic pressure; hence, the perturbation grows, and the slug continues to lengthen until all the liquid above it

has moved to the annulus around the growing slug, at which point the slug has burst (Figure 3-1c). Note that, in this context, 'unstable' refers to the loss of equilibrium between magmastatic pressure and slug pressure, and does not imply that the slug will break up.

James et al [2009] demonstrate that some slugs rise to the surface without becoming unstable, whilst others become unstable at a finite depth *h*. By considering the limiting case $P_s^* = P_h^*$, they find that such a slug becomes unstable when its pressure drops below a limiting pressure (P_{slim}) given by:

$$P_{slim} \equiv \sqrt{\rho g A' P_a L_a} \,. \qquad (3\text{-}7)$$

By setting $P_{slim} = P_a$ we can determine the maximum size for a slug that can rise to the surface without becoming unstable, expressed as its equivalent length at atmospheric pressure:

$$L_{alim} = \frac{P_a}{\rho g A'} \,. \qquad (3\text{-}8)$$

If $L_a \leq L_{alim}$ then the slug is sufficiently small that the equilibrium $P_s = P_h$ is maintained throughout the slug's journey to the surface, where it releases its gas passively. If, by contrast, $L_a > L_{alim}$ then the slug will become unstable before it reaches the surface, and will burst with an overpressure. We suggest that equation 8 represents a more intuitive criterion for the transition between passive degassing and Strombolian eruption than that presented by *James et al* [2009].

The depth at which a slug becomes unstable (h_{lim}) can be determined by setting $P_s > P_{slim}$ in equation 3-1, yielding:

$$h_{lim} = \frac{P_{slim} - P_a}{\rho g}, \tag{3-9}$$

which is equivalent to equation 12 in *James et al* [2009]. We define the beginning of the burst process, for an unstable slug, as the point when it reaches depth h_{lim}. The burst process is completed when the magmastatic head approaches zero (i.e. when the slug nose reaches the surface); at this point, all of the liquid that was above the slug when it became unstable, has moved into the annular falling-film around the slug. We assume that the velocity of the slug nose is rapid during the burst process compared with the velocity of the slug base during burst; hence, we treat the slug base as stationary throughout the burst process (Figure 3-1c). Conservation of liquid volume in the system dictates that the length of the slug at burst is given by $L_b = L_{slim} + h_{lim}/A'$, where L_{slim} is the length of the slug when it becomes unstable; hence, the pressure in the slug when the slug nose reaches the magma surface is given by:

$$P_b = \frac{A' P_a L_a}{A' L_{slim} + h_{lim}} = \frac{\rho g A' P_a L_a}{2\sqrt{\rho g A' P_a L_a} - P_a}. \tag{3-10}$$

3.1.2 Development of slug overpressure during effusion of lava (overflow model)

The standard model outlined in the previous section follows the assumption of *James et al.* [2009] that the magma above the slug remains confined to the volcanic conduit as it is pushed upwards by the expanding slug. This is consistent with observations of normal Strombolian eruptions, for which very little magma is erupted (*Chouet et al.*

[1974] report a volume ratio of erupted gas to erupted magma of 10^4–10^5). It also implies that the magma surface must be sufficiently far below the vent in the interval between slug arrivals, so that magma does not overflow during slug ascent and burst. This is supported at Stromboli by the delay time between seismic and acoustic signals recorded during normal explosions, which indicates that the surface of an approximately stagnant magma column resides at a depth of around 100- 200 m below the craters [*Ripepe et al.,* 2002 and reference therein].

The assumption is not, however, consistent with some observations of paroxysmal eruptions. *Calvari et al.,* [2011] collate observational data from paroxysmal eruptions at Stromboli in 2003 and 2007 and conclude that paroxysmal eruptions may occur during periods of lava effusion, as a consequence of magma depressurization. We note that the hypothesis of *Calvari et al.* [2011] is based on a small number of recent events and that it is possible that paroxysmal eruptions may have occurred during periods without lava effusion. However, simultaneous effusive/explosive activity is not an uncommon process at basaltic volcanoes, and has been observed, e.g., at Stromboli crater terrace in November 2010, and during 2001 and 2002-2003 scoria cone-building eruptions at Etna. In this case, the standard model must be modified to account for magma overflow during slug ascent. Figure 3-1d illustrates the effect of perturbation on a slug ascending a conduit from which magma is effusing. Due to the overflow of magma during perturbation, the perturbed height of the magma column above the slug is smaller than is the case for the standard model; consequently, equation 3-5 becomes:

$$P_h^* = \rho g(h - \Delta L) + P_a . \qquad (3\text{-}11)$$

This is identical to equation 3-5 except that A' no longer appears because the volume of magma in the head region above the slug is no longer conserved, due to overflow. This modification propagates through the analysis presented in the previous section. We term this case the overflow model to distinguish it from the standard model set out in section 3.1.1. New equations for P_{slim}, L_{alim} and P_b relevant to the overflow case can be recovered by removing A' from equations 3-7, 3-8 and 3-10 respectively.

3.1.3 Model non-dimensionalization

To non-dimensionalize the above set of equations we choose P_a as the characteristic pressure and $P_a/\rho g$ as the characteristic length-scale. The slug length can then be represented as a dimensionless quantity (indicated by a tick):

$$L_a^{'} = L_a \frac{\rho g}{P_a}. \qquad (3\text{-}12)$$

Other quantities are non-dimensionalized as follows: $P_{s\,lim}^{'} = \frac{P_{slim}}{P_a}$, $h_{lim}^{'} = h_{lim}\frac{\rho g}{P_a}$, $P_b^{'} = \frac{P_b}{P_a}$, $L_b^{'} = L_b \frac{\rho g}{P_a}$, (where $P_{slim}^{'}$ is the same as $P_{s\,lim}^{*}$ in equation 13 and Figure 5 of *James et al* [2009]. From equation 3-8, we can see that the product of A' and $L_a^{'}$ gives the ratio of the slug length to the critical slug length L_{alim} (i.e. it describes how much bigger this slug is than the smallest slug that will burst with an overpressure); we call this ratio the stability index, γ:

$$\gamma = A^{'} L^{'}_{a} = \frac{L_a}{L_{alim}}. \qquad (3\text{-}13)$$

Applying the non-dimensionalization to the system of equations developed in section 3.1.1 reveals that γ is the key parameter describing the burst process. The slug pressure at the onset of bursting (equation 3-7) becomes:

$$P_{s\,lim}^{'} = \sqrt{\gamma}\,, \tag{3-14}$$

the depth at which the burst process begins (equation 3-9) becomes (for γ>1):

$$h_{lim}^{'} = \sqrt{\gamma} - 1, \tag{3-15}$$

and the slug pressure at burst (equation 3-10) becomes (for γ>1):

$$P_b^{'} = \frac{\gamma}{2\sqrt{\gamma} - 1}. \tag{3-16}$$

Since $P_b^{'} L_b^{'} = P_a^{'} L_a^{'}$, where $P_a^{'} > 1$ and the dimensionless slug length at burst is $L_b^{'} = L_b \frac{\rho g}{P_a}$

, we can also write:

$$\frac{L_b^{'}}{L_a^{'}} = \frac{1}{P_b^{'}} = \frac{2\sqrt{\gamma} - 1}{\gamma}, \tag{3-17}$$

this latter parameter will be used later to determine the slug length at burst. The burst process can, therefore, be described entirely by the parameter γ. If $\gamma \leq 1$ the slug is stable throughout its journey to the surface. Note that, for stable slugs, equation 3-15 gives negative values for burst depth and neither equation 3-15 nor equation 3-16 are physically-meaningful. If $\gamma > 1$ the slug becomes unstable at a depth indicated by equation 3-15 and subsequently bursts with an overpressure as given by equation 3-16, and with a final length expressed by equation 3-17. The larger the value of γ, the greater the burst overpressure; as a corollary, the slug expands less during the burst process for

larger γ. This non-dimensionalization is valid both for the standard (section 3.1.1) and the overflow model (section 3.1.2); in the overflow case, A' does not appear in equation 3-8; hence (from equation 3-13), $\gamma = L_a^{'}$.

3.2 Model behavior

The dependence of the depth of burst onset, the burst overpressure, and the length of the slug at burst, on the stability index γ is shown in Figure 3-2. For values of $\gamma < 1$, the pressure in the slug never exceeds local magmastatic pressure and the slug reaches the surface in equilibrium with atmospheric pressure. For large values of γ (i.e. when the slug is much larger than the critical slug size, $L_a >> L_{a\,lim}$) the slug burst overpressure is approximately given by $P_b^{'} \approx \sqrt{\gamma}/2$, and the length of the slug at burst is given by the ratio $L_b^{'}/L_a^{'} \approx 2/\sqrt{\gamma}$.

In order to set the above analysis in a more realistic volcano monitoring context, we demonstrate how the value of the stability index γ (equation 3-13) may be determined from field observations. Equation 3-13 relates the stability index to the slug length; however, the volume of gas released by a slug burst V_a is a more practical quantity since it may be determined by various, established monitoring techniques (see section 1.4.2.3). We define the dimensionless slug volume $V_a^{'}$ as the volume of an erupted gas slug $V_{a,}$ normalized by the characteristic volume $\pi r_c^2 P_a / \rho g$ (which is the product of the cross-sectional area of the conduit and the characteristic length-scale):

$$V_a^{'} = V_a \frac{\rho g}{\pi r_c^2 P_a}. \qquad (3\text{-}18)$$

From equations 3-12 and 3-18, and noting that $V_a = L_a \pi r_s^2$ we find:

$$V_a' = (1 - A')L_a'. \qquad (3\text{-}19)$$

This relationship between the dimensionless length and volume of the slug applies to both the standard model and the overflow model; i.e., A' does not vanish from equation 3-19 for the case when magma overflows form the conduit during slug ascent.

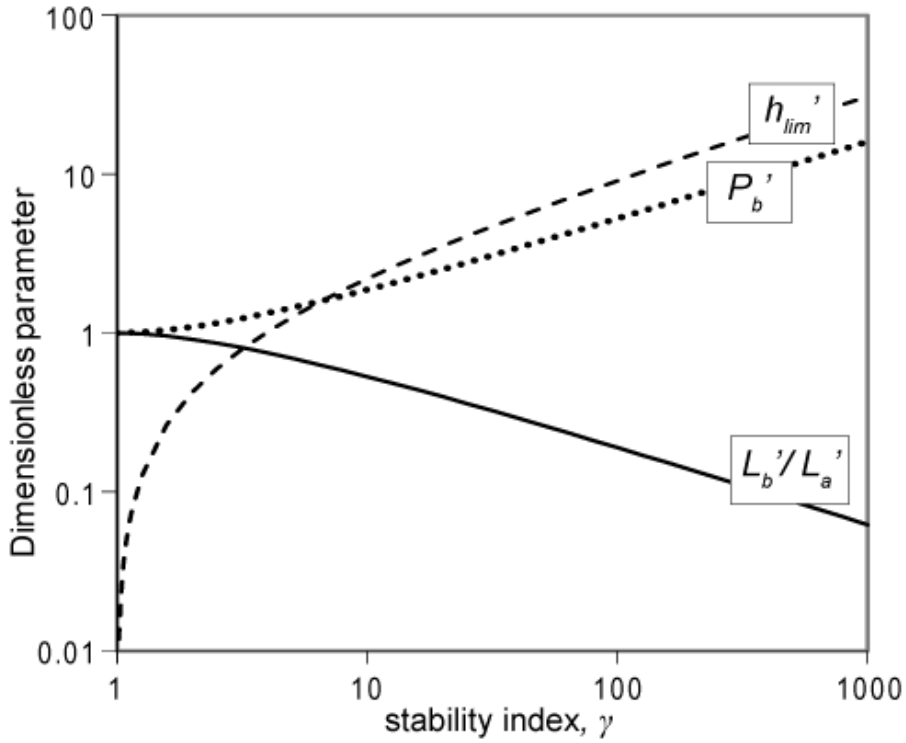

Figure 3-2. Dimensionless depth of burst onset (h'_{lim}, equation 3-15, dashed line), dimensionless burst overpressure (P_b', equation 3-16, dotted line), and ratio of slug expansion (L'_b / L'_a, equation 3-17, solid line) as functions of the dimensionless stability index (γ, equation 3-13), which describes how much bigger a slug is than the smallest slug that will burst with an overpressure.

Using this result, the stability index can be recast in terms of the dimensionless slug volume. For the standard model, $\gamma = A' L_a'$ (Equation 3-13); hence, from equation 3-19:

$$\gamma = \frac{V_a' A'}{1 - A'}\ ; \qquad (3\text{-}20)$$

whereas, for the overflow model, $\gamma = L_a'$; hence:

$$\gamma = \frac{V_a'}{1 - A'}\ . \qquad (3\text{-}21)$$

Equations 3-20 and 3-21 allow us to plot the burst overpressure as a function of dimensionless slug volume (Figure 3-3). This plot demonstrates the key role that the dimensionless film cross section, *A'*, plays in determining slug burst behavior; the controls on this parameter are discussed in detail in the next section. It also shows that the burst overpressures expected when magma overflows from the conduit during slug ascent (as in the case of the paroxysmal eruptions of 5th April 2003 and 15th March 2007) are higher than when magma is confined to the conduit during slug ascent. This increase in burst overpressure is more pronounced for thin falling films (small A') than for thick falling films.

The equations presented here allow one to calculate various parameters of practical interest, including the slug overpressure at burst, slug length at burst and the depth at which the slug becomes unstable. These quantities can be calculated for specific slug burst events if the parameters ρ, g, P_a, r_c, V_a, and A' can be calculated, measured or estimated from field data. A dimensional, worked example is presented in Appendix C.

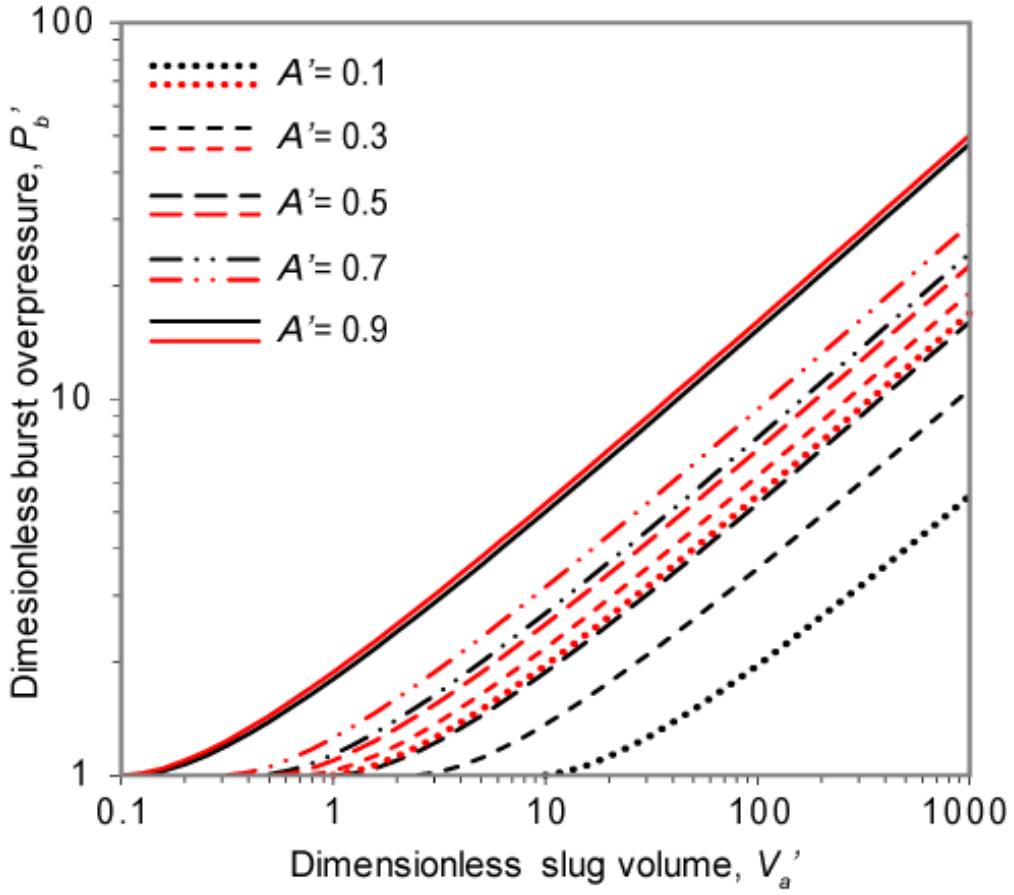

Figure 3-3. Dimensionless burst overpressure P_b' as a function of dimensionless slug volume V_a' (equation 3-18 and 3-19) for various values of parameter A' (equation 3-6), which represents the fraction of the conduit's cross-sectional area occupied by the liquid film draining around the slug (larger A' represents a thicker film). Black and red curves represent model outputs for the standard model (section 3.1.1) and the overflow model section 3.1.2).

3.3 Model results for the Stromboli case

The non-dimensional approach developed in section 3.1.3 allows the model to be applied to any system involving bursting of slugs of gas. Geological examples include, for example, geysers, hydrothermal eruptions, mud volcanoes, and multiphase borehole flows, as well as basaltic volcanoes. In this section we apply the model to the specific case of Stromboli volcano. Stromboli provides the ideal test case because its eruptions

have been so well characterized (section 1.4). The model we present allows several parameters of volcanological interest to be calculated such as i) the maximum size for a stable slug, or, if the size of a slug can be measured, estimated or (for hypothetical cases) assumed ii) the gas pressure within the slug at busting; iii) the slug length at bursting; and iv) the depth at which the slug becomes unstable. In Appendix C, we illustrate the practical application of the system of equations through a worked example.

In this section, we use the model to explore the role played by the various physical properties of the slug–conduit system in controlling eruption parameters for the case of Stromboli volcano. We explore the input parameter space defined by the values reported in Table 1-1, keeping conduit radius fixed at 1.5m.

As already illustrated by experimental results in section 2.2, magma viscosity exerts a strong control on slug behavior, through its influence on the thickness of the falling film of magma around the gas slug. Figure 3-4 illustrates the relationship between magma viscosity and the maximum stable slug size (i.e. the amount of gas that a slug can contain – expressed as the volume the slug would have at atmospheric pressure – above which the slug will burst with an overpressure). The Figure shows that, when viscosity is low (thin film), a slug must contain more gas in order to burst with an overpressure, than when viscosity is high (thick film). For Stromboli, when the magma is bubble free and has viscosity 10^4 Pas, the standard model predicts that a slug will burst with an overpressure when it contains at least an amount of gas equivalent to a volume of 24 m^3 at atmospheric pressure; if the magma viscosity is only 10 Pas, then the threshold volume is 130 m^3. Magma density also plays an important role; the equivalent thresholds for magma with 50% vesicularity are 46 m^3 and 229 m^3 respectively.

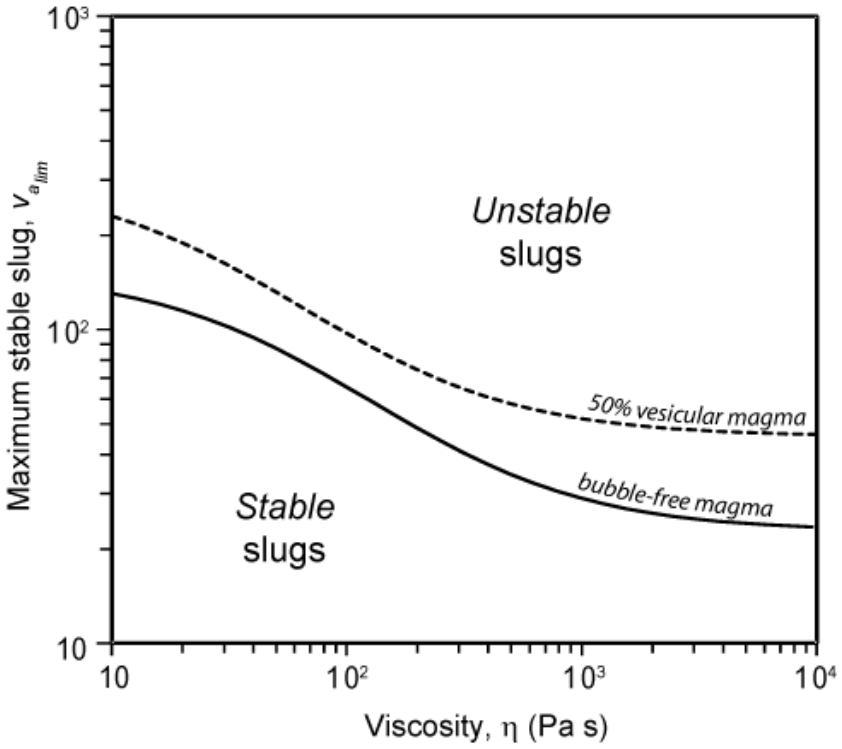

Figure 3-4. Maximum size of a slug (expressed as its equivalent volume at atmospheric pressure, $V_{a\,lim}$) that can rise to the surface in equilibrium with magmastatic pressure, as a function of magma viscosity η, for plausible conditions at Stromboli volcano (Table 1-1 and Table 1-2). Solid and dashed lines represent bubble-free magma and 50% vesicular magma, respectively. The curves mark the transition between slugs that reach the surface in pressure equilibrium (stable slugs), and slugs that reach the surface with an overpressure (unstable slugs).

Figure 3-5 summarizes the three main model outputs (slug pressure and length at bursting and depth at which the slug becomes unstable) over the broad range of Stromboli conditions described in 1.4.2, for both the standard and overflow models. The amount of gas in the slug, expressed as the equivalent slug volume at atmospheric pressure (V_a), has the strongest control, shifting by orders of magnitude all calculated output parameters as it ranges from 10^2 to 10^6 m^3. Bursting pressure (P_b) (Figure 3-5a) ranges 1 - 10^2 bars over this slug volume range, and increases non-linearly with

increasing viscosity. Notably, although the model considers only geometrical and magmastatic factors, significant overpressures are predicted to develop.

Slug length at bursting (L_b) (Figure 3-5b) ranges 10 - 5 x 10^3 m over the same range of slug volumes, but decreases as viscosity increases. This very large range of slug lengths has important implications for model applicability, which are discussed later in section 3.4.2. The depth at which the slug becomes unstable (h_{lim}) (Figure 3-5c) ranges 0 - 10^3 m below magma free surface, and depends more strongly on magma viscosity for smaller slug size.

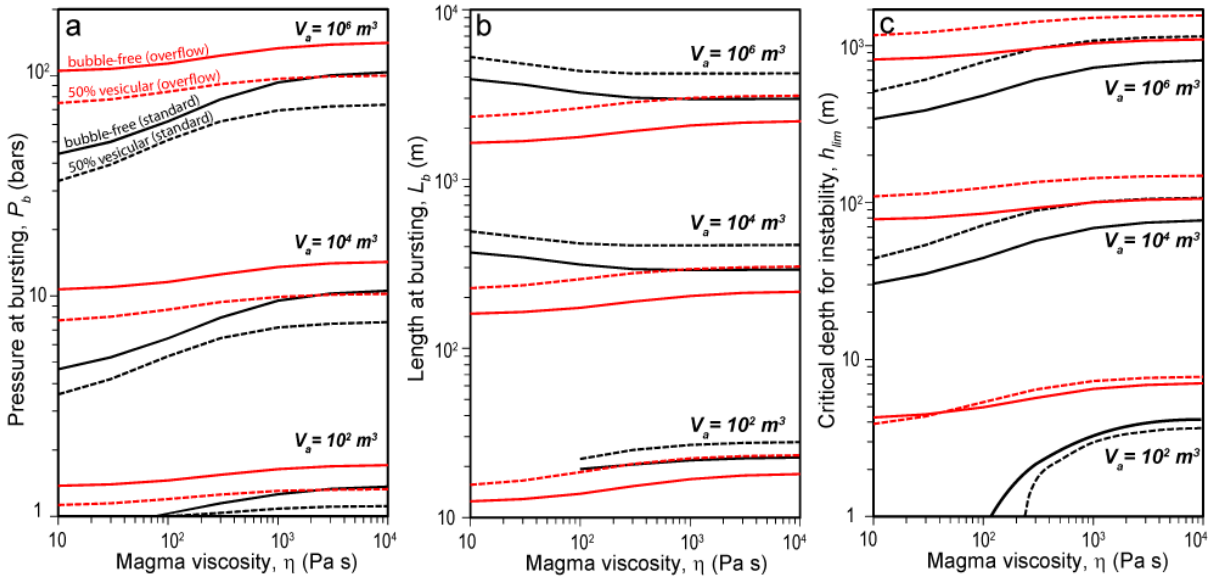

Figure 3-5. Effect of viscosity (η) and slug gas volume (V_a) on a) bursting pressure (P_b), b) length at bursting (L_b), and c) depth of slug instability (h_{lim}) at Stromboli. Solid and dashed lines represent bubble-free magma and 50% vesicular magma, respectively. Black and red curves represent the standard and the overflow model, respectively. Parameter values are taken from Table 1-1.

At Stromboli, variations in magma density play a more minor role in controlling output parameters than variations in magma viscosity and slug volume, mainly because of the relatively small range of plausible densities. Halving the magma density (i.e. assuming

50% vesicularity) leads to lower slug pressure and longer slug length at burst. For most conditions of interest, lower density also corresponds to greater depth of instability, although we note the inverse for the overflow model when slugs are small and viscosity is low (Figure 3-5c). In general, the overflow model predicts higher slug pressure, and shorter slug length at bursting, than the standard model. Furthermore, the influence of viscosity on results is greatly reduced for the overflow model compared with the standard model.

The relationship of greatest practical interest – i.e., more directly linked to field measurable quantities – is that between slug volume and bursting pressure. This relationship is illustrated in Figure 3-6, echoing the dimensionless results presented in Figure 3-3. The results for both the standard (Figure 3-6a) and the overflow (Figure 3-6b) models illustrate the strong dependence of P_b on V_a. For slug volumes $V_a > 10^3$, we find the approximate relationship $P_b \propto \sqrt{V_a}$. Comparing Figure 3-6a and b we observe, again, the reduced influence of viscosity, and enhanced bursting pressure, for the overflow case.

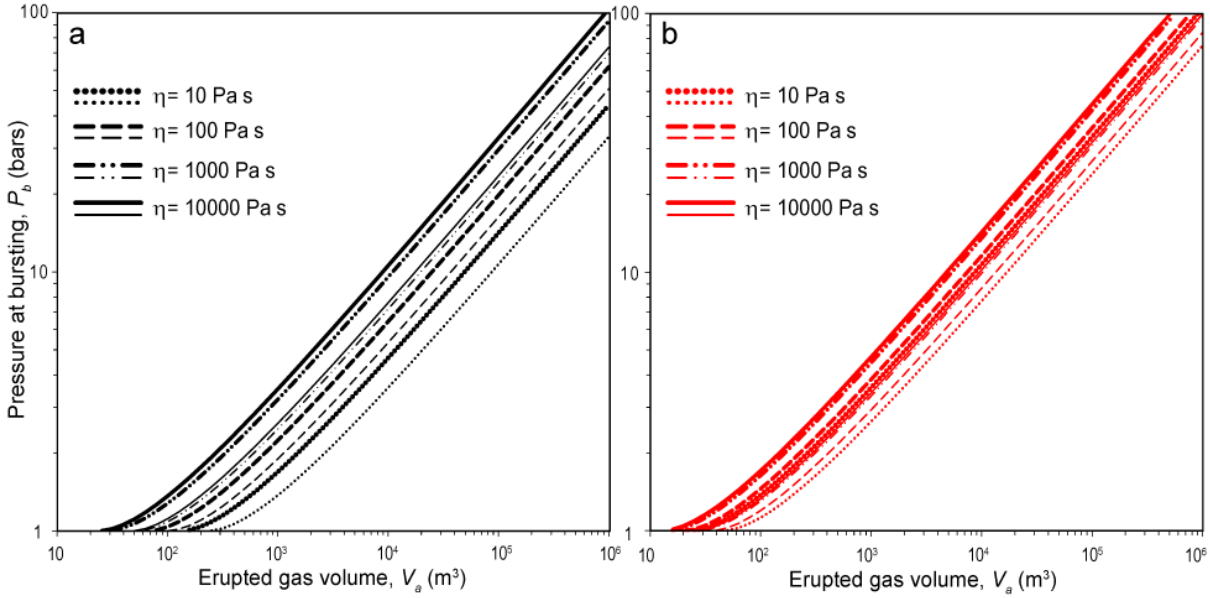

Figure 3-6. Bursting pressure of an erupting gas slug (P_b) at Stromboli as a function of slug size (expressed as equivalent volume at atmospheric pressure, V_a), for (a) the standard and (b) the overflow model. Different curves represent model output calculated for the range of A' values corresponding to magma viscosities 10-10^4 Pa s. Thick and thin lines represent bubble-free magma and 50% vesicular magma, respectively.

3.4 Discussion

3.4.1 Model assumptions and limitations

A key outcome of the analysis presented here is that the gas volume and explosion pressure of a slug – key quantities that can be related to field-based measurements – are linked in a straightforward way through the parameter A', which is related to magma viscosity and conduit geometry. The model given here provides a first order approximation of the gas overpressure that develops during Strombolian eruptions. This value for the slug pressure at burst can be considered a minimum bound for four reasons. Firstly, it is assumed that the slug base is stationary during the burst process; in reality, it will continue to rise, shortening the slug and increasing the pressure of the

gas within it. Secondly the thickness of the film of magma falling around the slug it assumed to remain constant throughout the burst process. Evidence from laboratory analogue experiments indicates that the slug nose actually becomes more pointed as it accelerates towards the surface during bursting, leading to a thicker falling film (Figure 2 of *James et al.* [2008], and pages 182-185 of *Corder* [2008]). Consequently, the slug is shorter when it bursts than is predicted under the assumption of constant film thickness, implying a higher burst pressure. Thirdly, inertia and viscosity in the accelerating body of magma above the expanding slug are neglected; in reality, these will act to retard slug growth, hence increasing overpressure. Finally, the fact that Strombolian eruptions eject magma (albeit a modest volume) implies that the slug bursts while the head region of magma above the slug still has finite thickness. Consequently, the overpressure within the slug is higher than predicted by the model presented here, which assumes that bursting occurs when $h \to 0$.

James et al. [2008] developed a 1D model that includes viscosity and inertia in the magma above the expanding slug, in addition to magmastatic effects. When compared with the results of their model (which uses a magma viscosity of 500 Pa s, a range of conduit radius of 2, 1.5 and 1 m, a slug base ascent velocity 1.71 m/s), our simplified model underestimates overpressure by about 35% in the worst case.

The assumption of a cylindrical conduit of constant diameter is clearly an oversimplification. Very long period seismic signals from Strombolian explosions at Stromboli are best fit by a source model incorporating a transition from a cylindrical shallow conduit, to an inclined dyke-like structure at a depth $\sim$ 200-300 m below the craters [*Chouet et al.*, 2003]. Whilst overpressure model does not account for such complex geometries, the effect of a shallow widening of the conduit can be assessed

qualitatively by assuming a wider conduit than the 1.5m radius used in previous sections (Figure 3-7). A further complexity in the natural system is that direct observation shows that three vent groups are persistently active at Stromboli with different outlet diameters, fed by shallow conduits connected at some depth [e.g., *Rosi et al.*, 2000 and references therein]. The observed variations in intensity and duration of Strombolian explosions from the different vents [e.g., *Chouet et al.*, 1974; *Ripepe and Marchetti*, 2002; *Patrick et al.*, 2007] may be linked, according to our model, to different conduit diameters above the branching depth. For instance, during 2009 the central vent group produced mainly puffing and showed a larger diameter at the surface, which would agree well with model predictions that, other factors being equal, a wider conduit results in reduced overpressure (Figure 3-7).

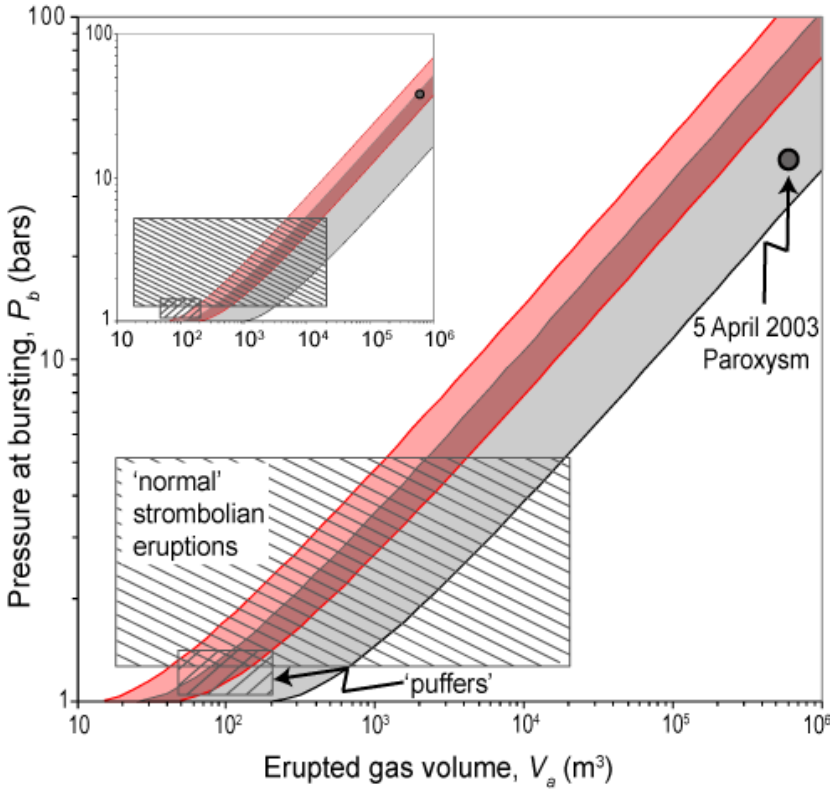

Figure 3-7. Application of overpressure model to explosive activity at Stromboli. The grey and red shaded areas represent bursting pressure P_b as a function of slug gas volume (V_a)

in the standard and overflow cases respectively, as per Figure 3-6. Literature estimates for burst pressures and volumes for a range of eruption styles at Stromboli are shown (puffers, [Ripepe et al., 2002; Harris and Ripepe, 2007a], normal Strombolian eruptions [Vergniolle and Brandeis, 1996; Ripepe and Marchetti, 2002], and for 5 April 2003 paroxysmal eruption [Ripepe and Harris, 2008]). The inset illustrates model results for a conduit radius (r_c) of 3 meters.

Besides conduit geometry, overpressure model does not take into account spatial heterogeneities in magma properties present within the Stromboli conduit. It has been proposed that the magma in Stromboli's plumbing system is vertically zoned, with a relatively evolved, crystal-rich and gas-poor magma occupying the upper few kilometres of the conduit, overlying, and mixing variably with, a crystal-poor and gas-rich magma [e.g., *Landi et al.*, 2004; *Métrich et al.,* 2010]. At very shallow level, the crystal-rich end-member shows horizontal variations in density and rheology caused by the presence of a less vesicular magma at the conduit margins [e.g., *Lautze and Houghton*, 2005], and there are slight, but significant, chemical differences from one crater to the other [e.g., *Landi et al*., 2011].

The vertical heterogeneity is likely only to impact on paroxysmal eruptions, since model results are insensitive of the slug ascent history below h_{lim}, which is in the order of hundreds of meters below magma surface for Strombolian explosions, and only reaches kilometers in depth for paroxysmal explosions. Conversely, the horizontal heterogeneities may have strong implications for slug geometry and consequent overpressure at burst. For instance, *Lautze and Houghton*, [2005] report textural evidences suggesting horizontal magma zoning within the conduit, with a more viscous, degassed magma lining conduit margins. As shown in Figure 3-4, variation in viscosity can determine the transition from a stable to an unstable slug because of its influence

on the parameter A'. Lateral variations in magma viscosity could be incorporated into the model by choosing an appropriate value for A' to account for the rheological transition between the two magmas.

Finally, the analysis presented here should also apply if the gas phase rises in the conduit as a bubble raft rather than a slug. Experimental observation as those presented in section 2 suggests similar behavior between bubble clusters and slugs in a liquid-filled cylindrical conduit: the variation in film thickness along individual bubbles is negligible compared to the conduit radius, and the assumption of constant liquid film around the slug should still hold. Moreover, expansion during final ascent causes rapid coalescence of bubbles in the cluster, resulting in the burst of one or few large slugs. This is also in agreement with field evidences of multiple bubbles bursting during a single eruption at Stromboli [*Taddeucci et al.,* in press].

3.4.2 Implications for explosive activity at Stromboli volcano

In Figure 3-7 model results are compared with existing estimates of eruptive gas budget and burst overpressure determined from field measurements of puffers [*Ripepe et al.,* 2002; *Harris and Ripepe,* 2007a], normal Strombolian eruptions [*Vergniolle and Brandeis,* 1996; *Ripepe and Marchetti,* 2002], and for the 5th April 2003 paroxysmal eruption at Stromboli [*Ripepe and Harris,* 2008]. In general, the trend in burst overpressure with erupted gas volume agrees well with field-based estimates. In particular, the fact that all three types of eruption follow the predicted trend indicates that approach presented, based on magma-static and geometrical considerations alone, is sufficient to account for observed eruptive overpressures across the spectrum of

eruptive activity at Stromboli, from low energy puffing, through normal Strombolian eruptions, up to paroxysmal explosions.

Very good agreement between the model and data is obtained for puffer activity. If we use the 50-190 m^3 range for the volume of released gas, estimated by *Harris and Ripepe* [2007a], as input to the model, we calculate pressure at bursting of 1.11 - 1.73 bars and 1.33 - 2.23 bars for the standard and overflow models, respectively. These values are in good agreement with the 1.1 – 1.4 bars range obtained from the oscillating gas bubble model of *Vergniolle and Brandeis* [1996]. Our model predicts that the slugs that cause puffing are a few meters to tens of meters long when they burst, and that they become unstable (i.e., the burst process begins) when the slug nose is a few meters below the magma surface (Figure 3-5).

Whilst there is considerable overlap between the model and field data for normal Strombolian eruptions, the range of burst overpressures estimated from field observations (1.3 - 5 bars, *Vergniolle and Brandeis* [1996]; *Ripepe and Marchetti* [2002]) is rather smaller than predicted (1 to 20 bars) if volume estimates of 20 m^3 - 2 x 10^4 m^3 are assumed as input for the model. This discrepancy probably reflects uncertainties both in field estimates and in our model assumptions. (For example, the upper predicted value of 20 bars is based upon the assumption of a slug of volume 2 x 10^4 m^3 bursting through highly viscous magma (10^4 Pa s) during overflow; if, instead, the same slug is assumed to burst through low viscosity (10 Pa s), low density (1300 kg/m^3) magma which is confined to the conduit, as is likely for normal Strombolian activity, a burst pressure of 4.9 bar in obtained, which is in much closer agreement with field observations.) Further, the model predicts that bursting starts no deeper than 150 m below the magma surface and that the length of the slugs at burst is between a few

metres and a few hundred metres (Figure 3-5). *Vergniolle and Brandeis* [1996] report rather shorter slug lengths of 0.7-33 m, based on a model fit to their acoustic measurements; however, it must be noted that these values are for slugs with volumes of the order of 100 m^3, comparable with volumes reported for puffers [*Harris and Ripepe,* 2007a]. By contrast, *Chouet et al.* [1974] report that the length of the resonator during Strombolian explosions, which could include the length of the slug plus the overlying conduit, is in the range 280-400 m. New observations and modeling based on high-speed videography and shock-tube experiments suggest slug length at Stromboli in the order of 100-200 m [*Taddeucci et al*., 2011].

Puffing and Strombolian activity are usually distinguished on the basis of bursting pressure. *Colò et al.* [2010] relate the amplitude of infrasonic signals to bursting overpressure, and indicate that, for puffers, infrasonic amplitude is <5 Pa, whilst for 'explosive' events it is >5 Pa. *James et al.,* [2009] used the variation of measured signals in experimental modeling of slug burst to place the limit between passive degassing and bursting at $1 > P'_{slim} > 3$. The model demonstrates that, whilst slug volume exerts the strongest control on burst overpressure, magma properties and conduit geometry also have a role to play, mainly through their influence on the parameter A'. Figure 3-7 shows that the volume of gas erupted during puffing events falls within the range for normal Strombolian activity, suggesting that variations in gas volume are not primarily responsible for determining whether puffing or Strombolian eruption occurs; rather, that the distinction is a result of different magma properties or conduit radius. For instance, for V_a equal to 100 m^3 and a bubble free magma, only slugs ascending in a magma with a viscosity higher than 1000 Pa s are predicted to erupt 'explosively' whereas only puffing is expected, regardless of viscosity, for magma with 50%

vesicularity (Figure 3-5). This implies that modest variations in magma vesicularity or crystallinity, as have been reported for Stromboli by, e.g., *Lautze and Houghton* [2007], could dictate whether puffing or Strombolian eruption occurs.

Concerning paroxysmal explosions, the only relevant field data were collected for the 5th April 2003 by *Ripepe and Harris* [2008], who used thermal and seismic data to infer a volume of gas of 5.7×10^5 m^3 released during the main 'peak' event, at a pressure of 38 bars. Using their volume estimate as input, the standard and overflow models predict a bursting pressure in the range 25-78 and 57-106 bars, respectively (Figure 3-7). The standard model cannot be applied to this case because it predicts that the length of the slug at burst is in the range 2-4 km, which is inconsistent with the assumption that the magma above the slug is confined to the conduit. This supports the assertion of *Calvari et al.* [2011], that paroxysmal eruptions are associated with magma effusion.

Whilst the great slug length at burst may appear surprising, it is consistent with the observations that: 1) paroxysmal explosions typically erupt a more primitive and gas-rich magma of deeper origin [*Bertagnini et al.*, 2003; *Métrich et al.*, 2010]; 2) the slugs which drive paroxysmal eruptions may have their origins as deep as 4 km below the vents, as suggested by geochemical composition of gas plume during both 5th April 2003 [*Allard,* 2010] and 15th March 2007 [*Aiuppa et al.,* 2010]; and 3) the relatively long duration (6 minutes for the 5th April 2003 event [*Ripepe and Harris*, 2008]) of the observed paroxysmal eruptions.

The overflow model prediction of the slug burst pressure is greater than the field estimate for the 5th April 2003 by roughly a factor of 2. The agreement is improved if a conduit radius of 3 m is used, rather than the usual estimate of 1.5 m (inset in Figure 3-7), however, this change gives a worse agreement between field estimates and model

results for puffers and normal Strombolian eruptions. This may be reconciled in the hypothesis that the conduit is wider at depth than in the shallow subsurface, since this would reduce the predicted overpressure for paroxysms, where the onset of slug burst may be as deep as 1.2 km, but not for small slugs associated with puffing and normal Strombolian activity, which begin to burst at much shallower depths. Slug burst is predicted to begin when the slug nose is 600-1200 m below the surface (Figure 3-5), which is rather deeper than the 80-150 m reported by *Ripepe and Harris* [2008] for the magma fragmentation level.

Overall, the proposed model of slug-driven eruption, in which only magmastatic force balance and slug geometry are considered, can account for the wide range of gas bursting pressures occurring in a real volcanic scenario. This range at Stromboli encompasses puffing, Strombolian activity, and paroxysmal explosions. The good agreement between field-based estimates and model results (Figure 3-7) strongly suggests that the bursting of overpressured slugs can be envisaged as a general mechanism to explain the entire spectrum of eruptive dynamics at Stromboli [as previously proposed by *Allard*, 2010].

4. Modeling slug-related geophysical signals in laboratory-scale conduits

The aim of this section is to explore the effect of processes related to gas slug expansion on explosive behavior and geophysical signals in a volcanic conduit. The problem is approached by performing analogue laboratory simulations that are scaled to conditions appropriate for a low-viscosity magma volcanic system.

As already pointed out in section 1.3.4, in a previous series of works, *James et al.* [2004] and [*Corder*, 2008] attempted to examine pressure changes related to slugs ascending and expanding in vertical and inclined tubes. They used the same analogue experimental facility adopted in this work to carry out experiments aimed at exploring the effect of different geometrical features on fluid flow oscillations in the conduit. So far, these experiments have considered the simplest scenario of a slug ascending in a closed-base and open-vent pipe boundary conditions, simulating a stagnant and homogeneous column of magma. Though far from a realistic representation of nature, their models allowed to capture the first-order features that revealed simpler in terms of understanding fluid motions and matched the numerical simulations directly.

The experimental simulations presented here investigate the expansion and bursting of a slug, and its implications on the oscillatory processes generated in the slug-conduit system, by considering the additional aspect, not covered in the previous simulations, of changing boundary conditions. Two different suites of experiments are conducted in order to investigate the limiting scenarios of 'open' vs. 'closed' boundary conditions both at the base and at the top of the conduit:

1) Closed base experiments. In this first suite, experiments are conducted in a constant volume of liquid to simulate closed conduit conditions at the base (as in previous experiments); these are referred as 'closed base experiments' in the following sections and are marked with the letter (c).

2) Open base experiments. In this second suite, the pipe is connected to a reservoir buffering pressure at the base, to simulate an open conduit in connection with a constant pressure magma chamber; these are referred as 'open base experiments' in the following sections and are marked by a (o).

For both series, experiments are initially conducted in a homogeneous liquid. Secondly, a variable thickness h_i of liquid of contrasting (higher) viscosity (i) of is placed at the top of the liquid column to simulate the presence of a cooling, near-solid portion of magma, partially obstructing the uppermost portion of the conduit. As reported in section 1.4.2.1, at Stromboli a degassed, highly viscous and partially crystallized magma resides in the upper portion of the conduit, partially clogging the vents down to some depth below which a low-density, volatile-rich magma resides, and eventually mixes with the former. These two types of magmas have contrasting viscosities, in the order of $\sim 10\text{-}10^2$ Pa s versus $\sim 10^4$ Pa s, and densities of 2500 versus 2700 kg/m^3, respectively. [*Landi et al.*, 2004 and reference therein; *Metrich et al.*, 2001]. The uppermost portion could be partially or completely solidified - behaving as rigid-like plug - in response to their crystal and volatile content. In both cases, as slug rises beneath the viscous impedance, it would: i) reach the viscous plug at the top of the conduit in almost closed vent conditions, presumably with a reduced degree of expansion, and ii) push the degassed magma back down the conduit, as suggested by analytical constant base pressure models of gas slugs ascending in open versus plugged vent conditions [*Llewellin et al.*, 2010].

As previously done by *Corder* [2008] and *James et al.* [2008; 2009], the experiments are scaled in terms of the potential expansion, P^* (see section 1.3.4) by reducing the

ambient pressure at a fixed P_{surf} = 30 mbar (~ 3000 Pa) with the aid of a vacuum pump. The results of our experiments are validated by comparing our 'test' simulations, carried out in closed conduit conditions and constant viscosity liquid, both at ambient and at reduced pressure, with those previously carried out by *Corder* [2008] at the same reduced pressure.

4.1 Materials and methods

4.1.1 Experimental set up

Closed base experiments are performed using an experimental apparatus equivalent to that defined in *Corder* [2008], as illustrated in Figure 4-1. It consists of a transparent borosilicate glass tube (2.0 m length and internal diameter 25.7 mm, as accurately determined *Corder* [2008]), that is connected by flanges to an upper and a lower 0.3 m-long and 25.7 mm-wide sections. The tube is filled with liquid up to a fixed height h_0 ~1.7m. The top section is equipped with two differential pressure transducers (named here *P163-1* and *P163-2,* details in section 4.1.2) placed before a junction linking the pipe to a wider, 0.12 m – long section (D = 80 mm), that is in turn attached to a flexible tube connecting the apparatus to a liquid trap and to the vacuum pumping system. In case an excess amount of gas in the system causes accidental spillage of liquid from the pipe to the flexible tube, the trap prevents it from reaching the vacuum system. This latter comprises a vacuum chamber and a rotary vane pump, allowing pressure above the liquid surface in the pipe to be reduced to up to 5×10^{-3} mbar (~0.5 Pa).

The bottom end of the pipe is connected to a 10 cm-long, 80 mm-wide section to allow sufficient room for an efficient gas injection. A steel plate mounted at the base of the

pipe contains a displacement transducer (here named *VertDispl*, details in section 4.1.2), an active strain gauge pressure transducer (named Base ASG details in section 4.1.2), and provides vertical stability to the pipe system, that is hanged to the walls by means of 2 springs.

Air is injected at the base of the pipe with a syringe of maximum capacity 10 ml (or 50 ml for the largest volumes considered). The tampon is drilled with a series of equally interspaced holes corresponding to a 2 ml volume, allowing the required volume to be fixed by inserting a pin in the corresponding hole. The syringe is connected to the pipe with a hose to which a one-way valve is attached to prevent oil from draining back. Before each experiment, the vacuum pump is activated to equilibrate the system to the required experimental pressure. Gas is then drawn into the pipe by simply pulling the pin out.

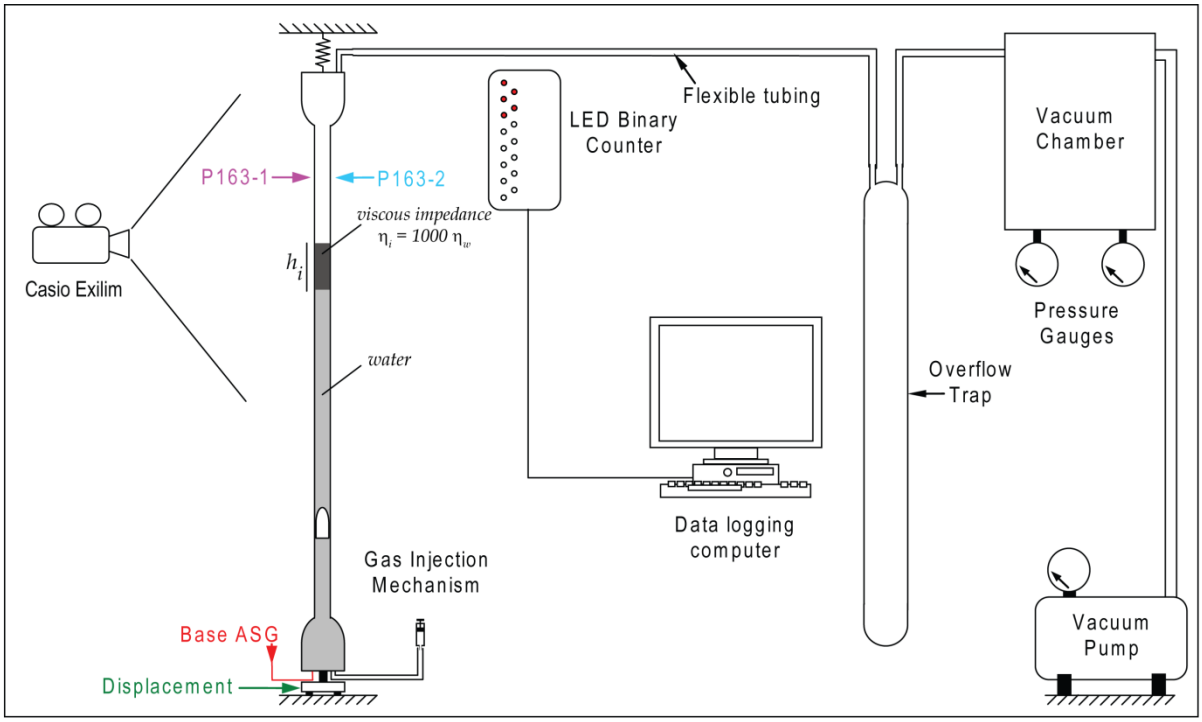

Figure 4-1. Experimental apparatus used for 'closed base' experiments.

Open base experiments are performed by modifying the previous apparatus as illustrated in Figure 4-2. A second 'manometer' tube section of 2.2 m length and internal diameter 40 mm is mounted parallel to the 2 m long, 25.7 mm wide, main section. This is linked, through two 40 mm-wide elbow section attached to T-type pipe junctions, to the principal section of the pipe. The two-pipe system is filled with experimental liquid up to a thickness of ~1.7m. When the slug is injected in the 25.7 mm section, hydrostatic pressure reduction is experienced at the base of the pipe, due to an amount of liquid remaining suspended around the ascending slug. This decompression causes liquid to flow from the 'manometer' pipe to the main pipe setting an almost constant pressure conditions at the base. Possible torque forces may be imparted in the system as a consequence of the geometrical configuration of the apparatus. Since it was not possible to quantify how these forces directly affect vertical displacement, the displacement transducer was not employed in open base experiments.

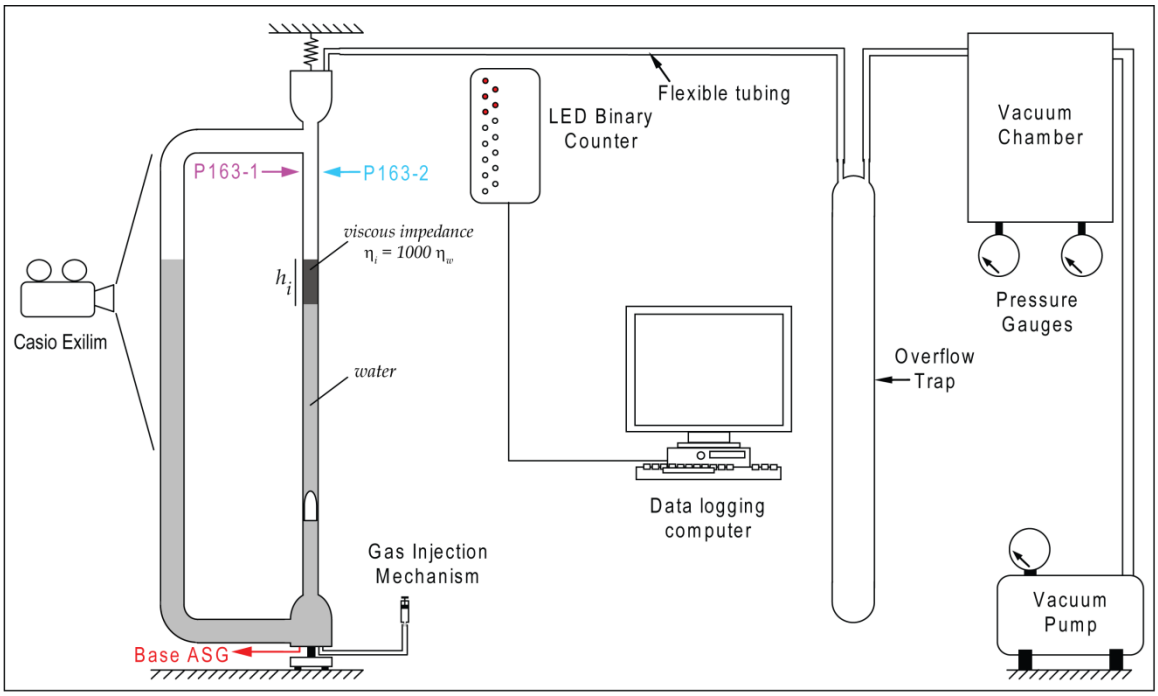

Figure 4-2. Experimental apparatus used for 'open base' experiments.

4.1.2 Data acquisition systems

The set-up is equipped with different acquisition systems to record the following synchronized data: i) pressure and displacement variations imparted on the apparatus by the ascending slug; ii) position and expansion of the slug in time, iii) bursting dynamics and other fluid flow processes in relation to the signals recorded.

The relevant characteristics of the measuring devices employed during the experiments are summarized as follows:

Absolute pressure transducers (*ASG*). An Active Strain Gauge with a pressure range of 1000 mbar (BOC Edwards A.S.G.1000) is used to detect pressure oscillations at the base of the system (ASGBase). This has a response speed of 5 ms a and frequency response of 0 - 200 Hz. The calibration function applied for conversion from measured voltage to absolute pressure (in Pa) is Pa = 10102*volts. An Active Strain Gauge with a pressure range of 2000 mbar (BOC Edwards A.S.G.2000) is employed within the vacuum chamber (Cham ASG). The calibration function applied is Pa = 20205*volts -833.62

Differential pressure transducers (*s163*). Two differential pressure transducers (Honeywell 163PC01D75) are mounted in the section of the pipe above the liquid surface to record changes in pressure above the liquid surface and during the bursting process. They have a quoted pressure range of i ± 2.5 inches H_2O, equivalent to ± 623 Pa. The calibration function applied for conversion from measured voltage to absolute pressure (in Pa) is Pa = 0.0254*9.81*volts.

Vertical displacement sensor (*VertDisp*, for closed base experiments only). A load cell for strain measurement (S100 50 N) is mounted on a steel platform where the base of the apparatus is positioned. The sensor is adjusted until under a compression equal to

approximately half of its full scale deflection. A positive signal is recorded when an downward displacement of the apparatus is detected, and vice versa, hence voltage recorded during the measurement is calibrated for vertical displacement using the calibration value of 47.9 μm V^{-1} reported in [*James et al.*, 2006], additionally multiplied by -1, in order to obtain a direct correspondence between measured signals and actual displacements.

Digital Camcorder. A Casio Exilim FX1 digital camcorder was employed for measuring the positions of the slug base, slug nose and liquid surface during each experimental run. A 512*384 pixel resolution and an image sampling rate of 300 frames per second was used to capture the later stages of the ascent of the gas slug and to fully analyze the dynamic of rapid expansion an bursting. Since a higher frame rate required the camera to operate at a limited pixel resolution, the field of view was restricted to the upper portion of the conduit to obtain a good image quality, and the resulting video provided positional data for the liquid surface and for the slug nose. The camera was mounted on a support fixed at a height of ~10 cm above the liquid surface in order to minimize parallax. A 24 LED binary counter was mounted in the field of view to allow images to be synchronized with the data in the data logger. On/off frequency is dictated by the sampling frequency (10000 Hz) of the data logger. For open base experiments, the camera also operated at a frame rate of ~30 f.p.s. and at a full image quality (640*480 pixel resolution) and was used to record images of the full ascent process and to measure the position of the slug base. In this case the camera was mounted on a tripod, placed as far as possible from the tube to cover a field of view including the entire pipe section. LED counter synchronization was not performed in these runs and the images

were manually synchronized with the logged data during the processing stage of the imagery.

4.1.3 Data processing

Following data acquisition, the output voltages from the transducers are calibrated for their actual magnitudes using their respective calibration functions in *Matlab*. A specifically created *Matlab*® interface, developed by Dr. Michael James at Lancaster University, provided a visual representation of the LEDs on the binary counter appearing in each frame of the avi files recorded with the camera, allowing the conversion of the lit LEDs to the corresponding point recorded by the data logging software. LED counter processing allowed to correlate digital frames of the LED counter to the sensor data with an accuracy of ±10 data points (1 ms).

A video processing utility (*MtrackJ* plug in) from the free software package *imageJ* was then used to determine the positions of the gas slug base, nose and the liquid surface when visible. The time versus position data obtained from the synchronized video were saved as text files for direct comparison with sensor data. For those video where the binary counter was not in the field of view of the camera, it was necessary to manually adjust for the correct time by adding a time shift to the original positional data. This Δt is the difference between the time corresponding to the maximum observed peak of the s163 sensor and the time of the last measured point in positional sequence (i.e., the frame capturing the liquid surface just before disruption as a continuum, or the rupture of the gas slug meniscus). All data obtained for each experimental run were then plotted onto a single graph.

4.1.4 Experimental procedure

For all experiments the system is filled with tap water, and the vacuum system is kept switched on for around 10 minutes in order to let the system pressure to slowly set to experimental pressure, and to let the liquid degas until eventual trapped bubbles are removed. For experiments carried out with a viscous impedance *i*, this process is repeated after the volume of liquid corresponding to the fixed thickness h_i, is poured in the top section of the tube and left to settle for a 12-24 hours. After this procedure, the syringe is set to the desired volume and the pump system is switched on until the experimental pressure is achieved. For experiments carried out at 'namely' ambient pressure, the system pressure is set to ~0.5 bar in order to achieve liquid degassing. The pressure is read on a multimeter that is connected to the vacuum pump and calibrated with an active strain gauge pressure transducer located in the vacuum chamber. The signal from this transducer is also logged in the computer during each experimental run, in order to check for pressure leaks. The pump is then switched off to prevent vibrations being recorded by the transducers. The binary LED counter is reset to zero prior to each run, and the data logging acquisition system is set for recording. After the Casio camera is started, the gas slug is then injected into the system. The recording time for the data logger is set to 25 seconds, with a sampling frequency of 1000 Hz, and resultant 25000 collected data points.

To test the reproducibility of the experiments, each experimental series was entirely repeated for each volume explored. For open base series, a third control run was performed for collection of the high-definition videos executed at 30 fps.

4.1.5 Analogue materials and scaling

Tap water is employed as analogue for low viscosity magma (Newtonian viscosity at 20°C, $\mu_w \sim 0.001$ Pa s; density, $\rho \sim 1000$ kg/m^3; surface tension $\sigma \sim 0.07$ N/m), as previously done with this experimental set up [*James et al.*, 2004; 2006]. The upper solidified magma portion (impedance layer *i*) is modeled using a transparent Newtonian liquids with contrasting viscosity (castor oil, viscosity at 20°C, $\mu_i \sim 1$ Pa s; density, $\rho \sim 961$ kg/m^3; surface tension $\sigma \sim 0.03$ N/m) giving a required liquid viscosity contrast $\mu_i/\mu_w = 10^3$, consistently with expected viscosity contrast at Stromboli (see section 1.4.2.1).

Material properties and scaling relationships for this experimental set-up are reported in Table 4-1, together with those for Strombolian volcanic slugs (see also Table 1-1 and1-2). Analogue material properties are given at 20°C, as reported by the manufacturer, while conditions reported for a basaltic magma are referred to a temperature of T=$\sim$ 1150° C. As already illustrated in section 1.2.2, *Mo*, *Eo*, *Nf*, *Fr*, and *Re* are typical dimensionless quantities required for scaling to volcanic flow. Material properties for a basaltic magma at 1150°C are such that surface tension plays a negligible role for volcanic slugs, hence their morphology and ascent velocity are predominantly controlled by inertial and viscous forces [*Seyfried and Freundt*, 2000]. Given an overall 10% conservative relative error of the nominal value of rheological properties due to experimental complications such as, e.g., a change in room temperature, or to a progressively increasing amount of bubbles remaining entrapped as experiments progressed over, the relative uncertainty in the estimate of dimensionless parameters is, after error propagation, 30% for *Mo* and 20% for all other dimensionless parameters.

Physical Property	Laboratory –scale		Volcano-scale
	water	castor oil	
μ (Pa s)	0.0012±0.0001	1.00	10-10000
ρ (kg m^{-3})	999.7±100	961.0	1300-2600
σ (N m^{-1})	0.073±0.0073	0.03	0.07
$Mo = \frac{g\eta^4}{\rho\sigma^3}$	5.23 ± 1.57 x 10^{-11}	3.63±1.09 x 10^{2}	5.9×10^{2} - 1.2×10^{15}
$Eo = \frac{4\rho g r_c^2}{\sigma}$	8.87 ± 1.77 x 10^{1}	2.08±0.42 x 10^{2}	2.9×10^{5} - 2.3×10^{6}
$N_f = \frac{\rho}{\eta}\sqrt{8gr_c^3}$	1.08 ± 0.21 x 10^{4}	1.24±0.25 x 10^{1}	2.1 - 1.2×10^{4}
$Fr = \frac{v_s}{\sqrt{2gr_c}}$	3.00 ± 0.60 x 10^{-1}	9.87±1.97 x 10^{-2}	0.02 - 0.34
$Re = N_f Fr$	3.22±0.65 x 10^{3}	1.22±0.25	0.04 – 4×10^{3}

Table 4-1. Dimensionless parameters for scaling system behavior. Laboratory scale conditions are referred to ambient temperature (T=20°). Volcano-scale conditions are referred to magmatic temperature T=1150°C.

Notably, as the diameter of our laboratory-scale pipe results in much smaller *Eo* numbers than in basaltic systems, surface effects will be relatively enhanced in our experiments. However, as shown in section 1.2.2, for *Eo* > 40 surface tension plays little role in slug ascent so that this difference should not represent a controlling factor. The reported inverse viscosity imply that experiments cover a range of investigated conditions going from viscously-controlled (N_f < 2) up to purely inertia-dominated regimes.

4.1.6 Experimental data grid

The details of the experimental conditions and the investigated variables for each experimental run are reported in this section.

For each data series a first pilot experiment is conducted at fixed pressure conditions above surface (P_{surf}) close to atmospheric pressure (50 kPa~500 mbar). All other experiments are conducted at a fixed nominal ambient pressures 3 kPa (30 mbar, P* = 7). This pressure provides large potential expansion of the gas (see section 1.3.4), but avoids oil/water boiling point to be overcome. The thickness of the viscous impedance layer h_i was varied in the experiments in order to obtain a length ratio (normalized to conduit diameter, h_i/D) ranging from a minimum of 0.5 to a maximum of 9. For each selected impedance thickness, a series of experiments was carried out for a range of injection volumes from 2 ml to 10 ml, or occasionally, up to 49 ml.

127 experiments were executed in total, of which 35 provided un-synchronized high definition imagery for selected runs. The remaining 92 runs provided synchronized data for transducer signals and imagery. Of these, 8 were discarded due to errors in injection/ascent operations or in data acquisition.

A comprehensive table of the complete experimental dataset is reported in Appendix D. For each experiment we report i) name of data logger file ii) condition at the base (C = closed, O = open), iii) impedance layer versus water viscosity ratio (μ_i/μ_w), iv) impedance layer thickness, normalised to pipe diameter (h_i/D), v) nominal gas volume injected (V_0, ml), vi) nominal reduced surface pressure (P_{surf}, mbar), vii) name of the video file, vii) outcome of the experiment, and viii) notes.

4.2 Results

In this section we report salient diagrams of selected experiments showing the variation of transducers signals with i) pressure ii) volume injection, iii) and boundary conditions at the base (open versus closed), and at the top (impedance thickness), respectively. In Appendix E a graphical representation of both position and transducers data is reported for the complete dataset of experiments performed. For simplifying reading the values of the conditions fixed for each plot are defined as follows from now on: V_0 = nominal injection volume *o* =open base, *c*= closed base, h_i/D = impedance thickness ratio. The signals voltage variation in time for the base ASG (ASGBase, red), vertical displacement (VertDisp, black), and differential pressure transducers (s163-1 in cyan, and s163-2 in purple) sensors is reported, together with slug nose, base, and liquid surface position (blue dots) relative to the initial position of the liquid surface (h_0). The overall experiment is reported in the top section of the figure, while the bottom left and bottom right sides of the figure zoom into the injection region and the final stage of slug expansion/rupture of the liquid meniscus, respectively.

4.2.1 Effect of pressure variation

The pilot experiments conducted at nominal atmospheric pressure (P_{surf} = 500 mbar) and volume V_0 = 10 ml in open base conditions (Figure 4-3), provided results in agreement (within measurement errors) with corresponding previous experiments performed in closed base conditions at low potential expansions [Figure 6-5 in *Corder et al.*, 2008]. The video data show that the expansion of the gas slug is limited compared to reduced pressure experiments, as expected, and recorded signals are characterized by low amplitude oscillations.

For the investigated range of h_i/D (0, 5, and 9, Figure 4-3, Figure 4-4, Figure 4-5) the injection of the slug into the apparatus causes an upward displacement of the liquid surface, and is marked by a sudden increase in ASGBase s163 pressure, which is followed by oscillations with frequency ~10 Hz that is typical of an oscillating bubble frequency with length L, $f_L = 1/2\pi \sqrt{\gamma P_0/\rho L h_0}$, where $\gamma = 1.41$ is the ratio of specific heat capacity, P_0 is the pressure in the slug assumed as the liquid column static pressure plus ambient pressure, ρ and h_0 are liquid density and height, respectively; [*Vergniolle et al,* .1996]. Maximum amplitude of the signal is inversely proportional to h_i/D. Viscous damping of the system causes the signal amplitudes to decay until pressure equilibrium is restored.

Following initial upward displacement, the liquid surface remains stationary until the slug has reached sufficient expansion to displace the overlying viscous cap up to an approximately constant height. The time interval between slug injection and the beginning of the upward displacement appears to correlate with the increased thickness of the viscous impedance (~6.8, 2.3, 1.3 s for h_i/D = 0, 5, and 9, respectively). As the slug approaches the impedance interface, it causes the interface to dome upwards. Passing of the slug into the viscous layer causes its length to increase in response to a change in the thickness of the liquid film draining around the slug. The liquid free surface remains more or less stationary during the final stages of the ascent, causing forced drainage of liquid back down the conduit until a thin meniscus of liquid remains at the surface, and ultimately breaks. Meniscus rupture is undetected by the pressure transducers.

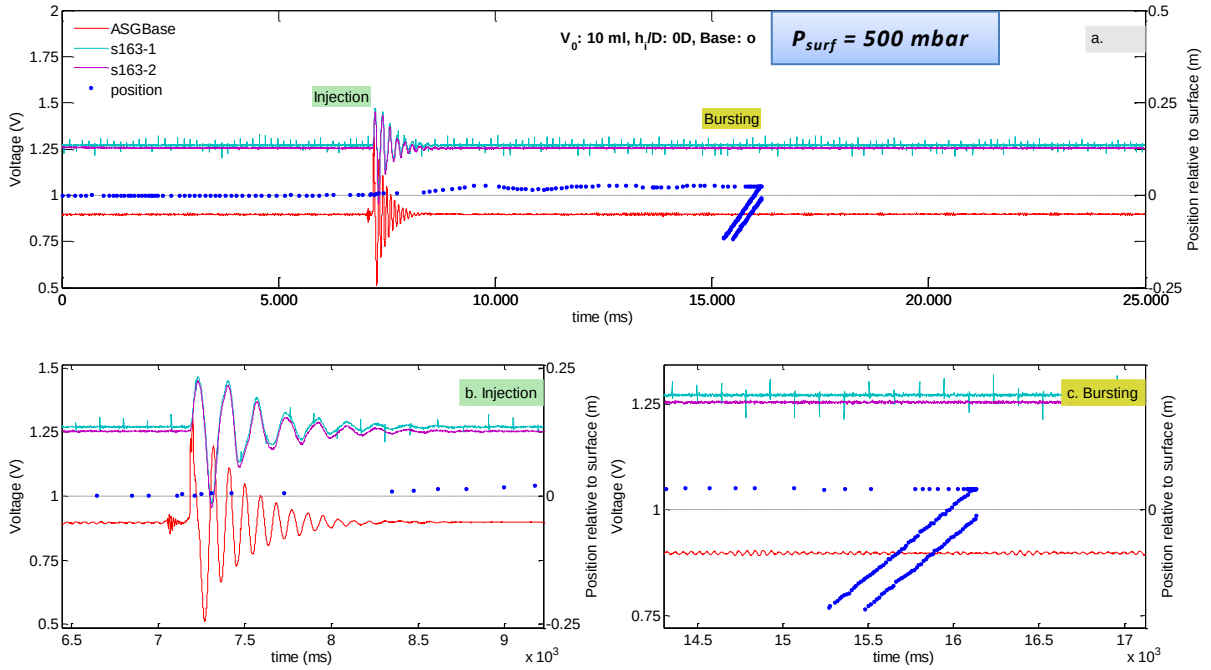

Figure 4-3. Transducers and slug position data for a 10 ml slug, open base conditions, and thickness h_i/D= 0, at surface pressure of 500 mbar (~0.5 atm).

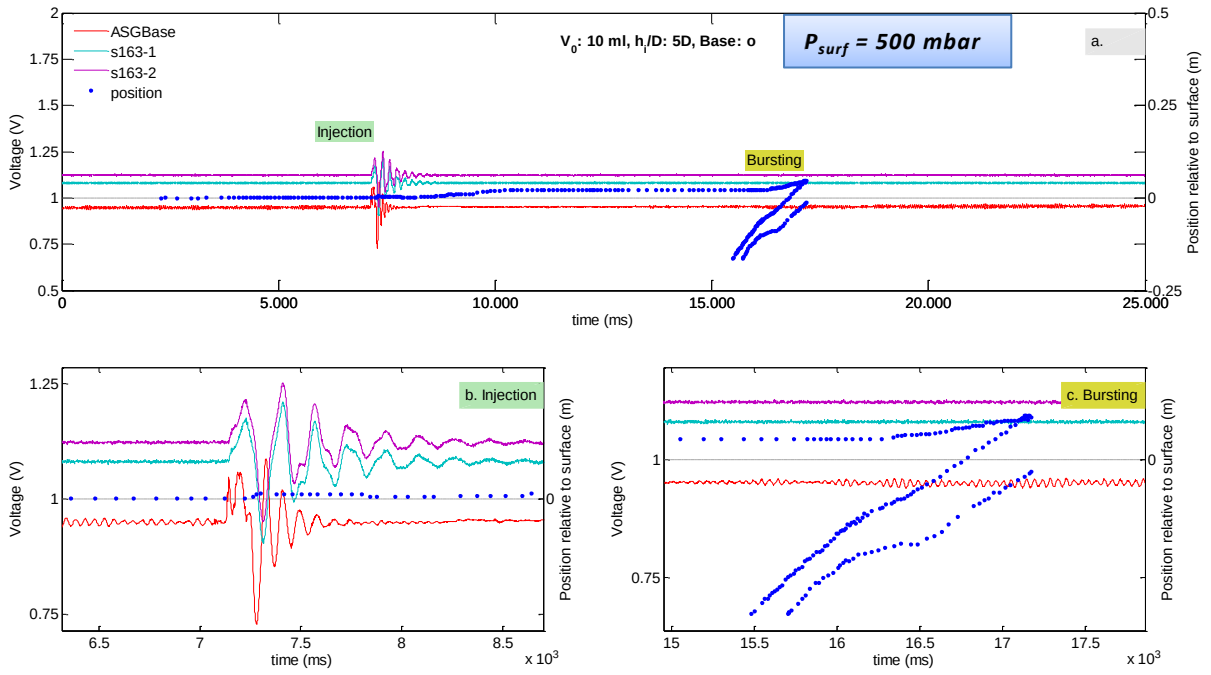

Figure 4-4. Transducers and slug position data for a 10 ml slug, open base conditions, and thickness h_i/D= 5, at surface pressure of 500 mbar (~0.5 atm).

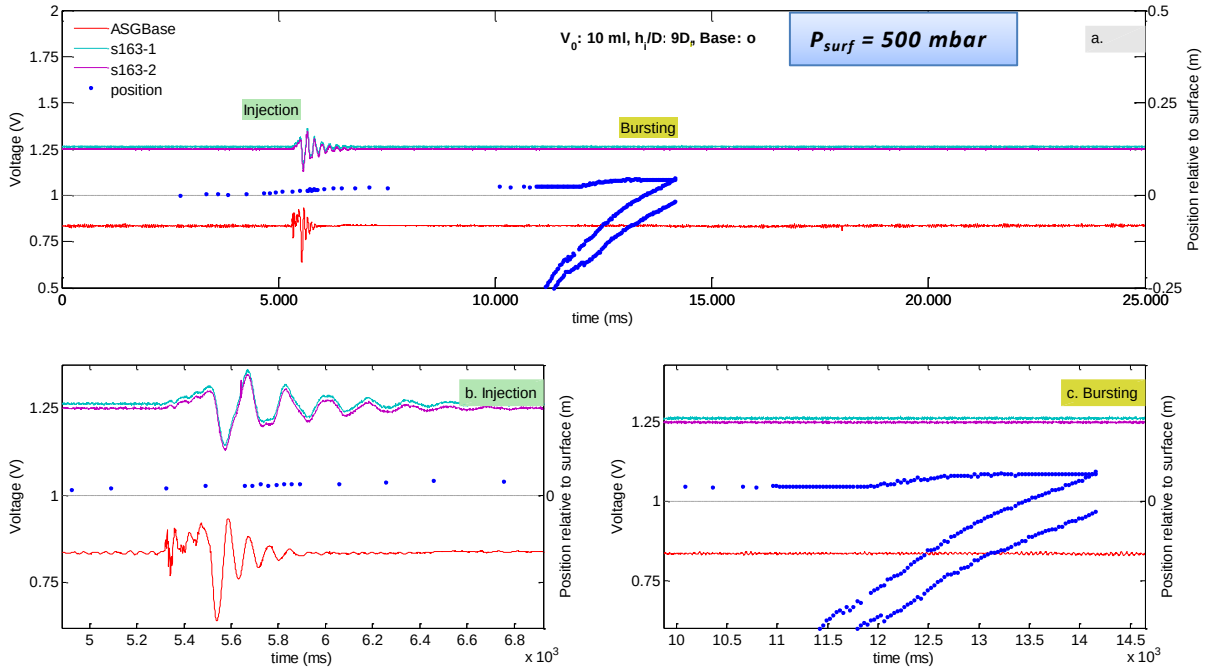

Figure 4-5. Transducers and slug position data for a 10 ml slug, open base conditions, and thickness h_i/D= 9, at surface pressure of 500 mbar (~0.5 atm).

The experiments conducted at reduced ambient pressure (P_s = 30 mbar) produced significant differences from those performed at low potential expansions, other conditions being equal (Figure 4-6, Figure 4-7). For instance, for the maximum impedance considered for closed and open base suites (h_i/D = 7 and 9, respectively) and a slug volume V_0 = 10 ml, the expansion of the slug is more pronounced, reaching a maximum length of ~ 0.5 m before disruption of liquid in a spray, compared to ~0.063 m maximum expansion at atmospheric pressure (Figure 4-5), and the bursting is strongly controlled by rapid expansion of the slug and subsequent acceleration of the overlying liquid surface.

Further, at slug injection, ASGBase signal shows a low amplitude pressure oscillation, and s-163 transducers show no change in voltage. This is due to the lower density of the air above the liquid surface. After injection, pressure start to slightly increase until a

maximum (this is not observed in absence of the impedance layer). The viscous cap at the top forces some water to be drained back until the slug reaches the base of the oil cap; at that point the slug has sufficient pressure to push water through oil. This phase corresponds to the relatively rapid decrease in pressure at the base until 'bursting', marked by a transient minimum pressure. After gas liberation, a slower re-pressurization follows due to drainage of the more viscous liquid film surrounding the expanding slug. For a particular case illustrated in Figure 4-6 (h_i/D = 7) the equilibrium pressure is not completely recovered until the end of recording. This is linked with the liquid upward drag forces acting on the tube walls. After gas liberation the liquid falls back into the conduit, re-establishing pressure equilibrium. The velocity of this process is related to the viscosity of the liquid, the more viscous the liquid, the longer the time to drain along the tube walls (i.e., the liquid is supported by the tube walls, and does not contribute to the head of liquid).

The s-163 signals record a rapid pressure propagation in the air occupying the top section of the pipe in response to a rapid upward movement of the liquid piston ahead of the gas slug. At the same time, the experiments performed in closed base show that the displacement transducer (Figure 4-6) detects the upward movement of the apparatus caused by the net upward force resulting from the viscous shear of the liquid piston on the tube wall. The first transient peak, corresponding to an upward motion of the tube is consistent with ASGBase and s-163 sensors, and corresponds, as shown by image analysis, to meniscus rupture time.

The video data also show that at injection, while the liquid surface remains stationary, the interface at the base of the viscous layer suddenly starts to dome up. As the slug ascends, it pushes the interface upwards, until it enters the viscous cap and changes its

shape becoming narrower and longer. The rupture mechanism contrasts markedly from that observed at ambient pressure, with rapid acceleration of the liquid (reaching speeds up to 3 m/s in the last phase) and disruption into a dispersed spray.

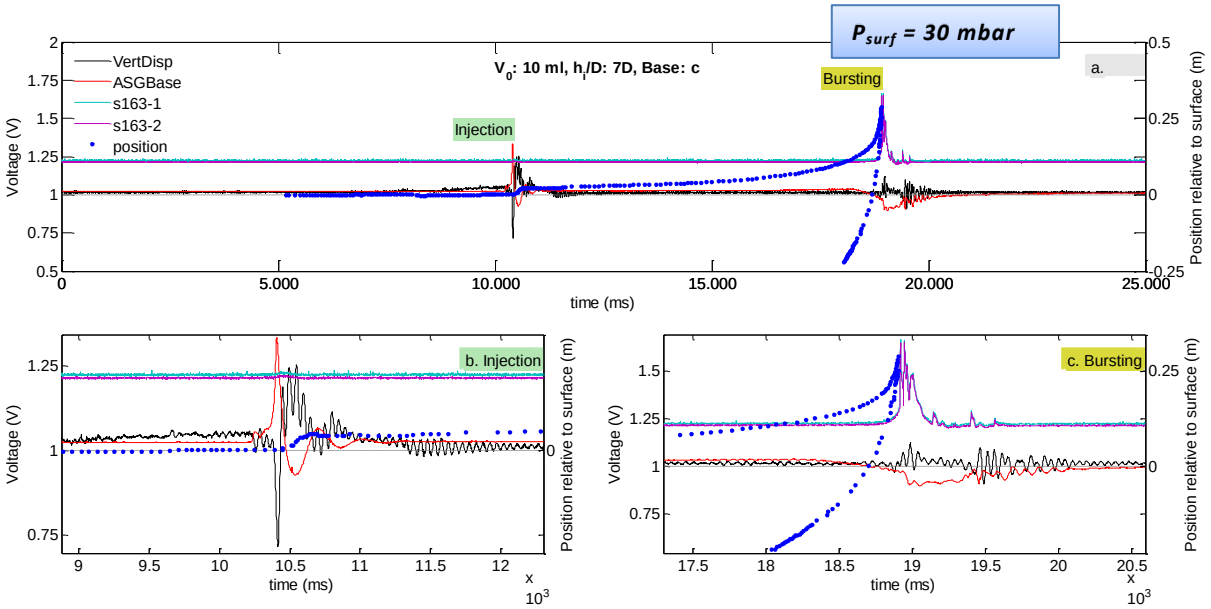

Figure 4-6. Transducers and slug position data for a 10 ml slug, closed base conditions, and maximum explored thickness h_i/D= 7, at a surface pressure of 30 mbar.

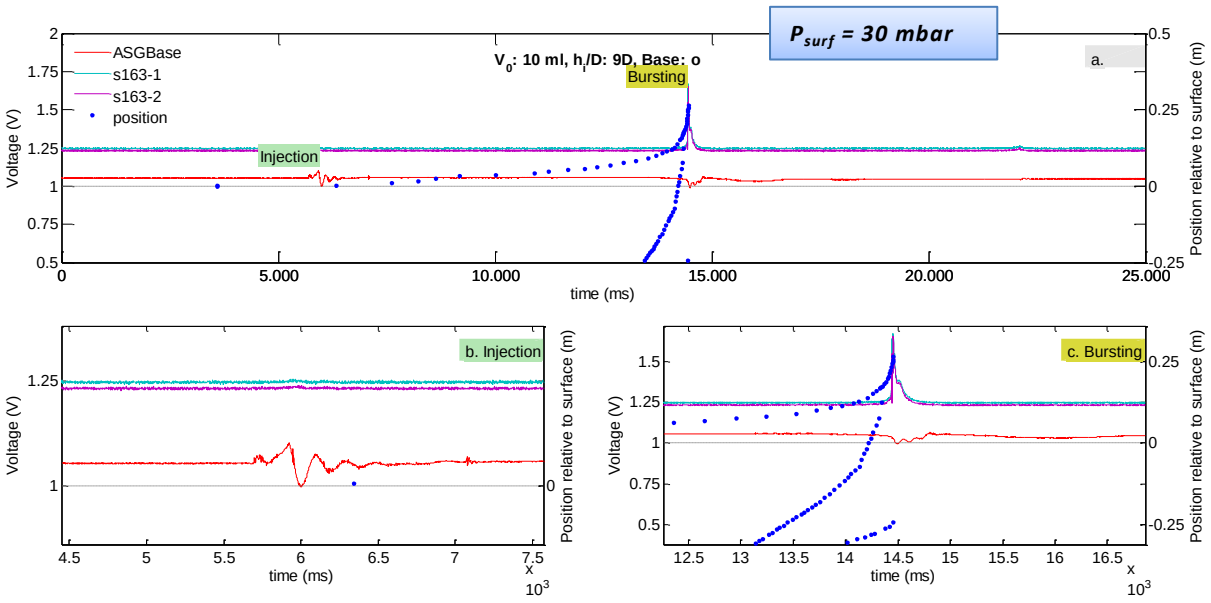

Figure 4-7. Transducers and slug position data for a 10 ml slug, open base conditions, and maximum explored thickness h_i/D= 9, at a surface pressure of 30 mbar.

4.2.2 Effect of volume variation

We describe here the effect of initial slug volume variation V_0 focusing on the two end-member conditions at the top of the conduit, i) hi/D = 0, (i.e, for a homogenous liquid), and ii) hi/D = 7 or 9 (the maximum explored for 'closed' and 'open' base experimental suites, respectively). Since there is no significant variation in the signal at the injection apart from its systematic increase in amplitude, the interpretation of the results presented here focuses on the analysis of pressure oscillations in the final stage of slug expansion and liquid surface disruption.

For the experiments performed in a homogenous liquid (hi/D = 0) we observe the following features. For closed base conditions, at low injection volume, the ASGBase signal show a low amplitude pressure drop, resulting from the expansion of gas slug (Figure 4-8a). The following pressure recovery is caused by the drainage of liquid film accumulated on the tube walls. As the injection volume increases, the magnitude of pressure drop increases and the time interval from injection to bursting is reduced, correlating well with the increased expansion capability of larger volume-slugs. A second transient positive pressure peak, followed by a high frequency oscillation coincides with the impact of the liquid film draining back into the conduit on the liquid free surface. The magnitude of this transient peak is also related to the injected volume. A significant reduction in amplitude characterizes runs performed in open base conditions (Figure 4-8b).

Figure 4-9 illustrates the same conditions reported in Figure 4-8b, but when a fixed thickness of the impedance layer is considered (the highest explored in the data set, i.e., $h_i/D=7$ and 9 for closed and open base conditions, respectively). This shows that the

magnitude of pressure drop recorded by ASGBase signals is increased with respect to the homogenous viscosity case, other conditions being equal. This occurs both in closed (Figure 4-9a) and in open base conditions, though the effect is markedly reduced for the open base case (Figure 4-9b). The rate of decrease in pressure before 'bursting' is dependent on the rate of slug expansion. When $h_i/D = 0$, expansion is slower than the case when $h_i/D > 0$. In that latter case, expansion process is hindered by the viscous cap until the slug starts rising through the impedance layer, where it undergoes rapid acceleration and sudden expansion. A low frequency oscillation is observed after 'bursting' of the slug in closed base conditions (Figure 4-9a). This appears to correlate with inertial fluctuations of the liquid surface in response to the oscillation between the two pipes.

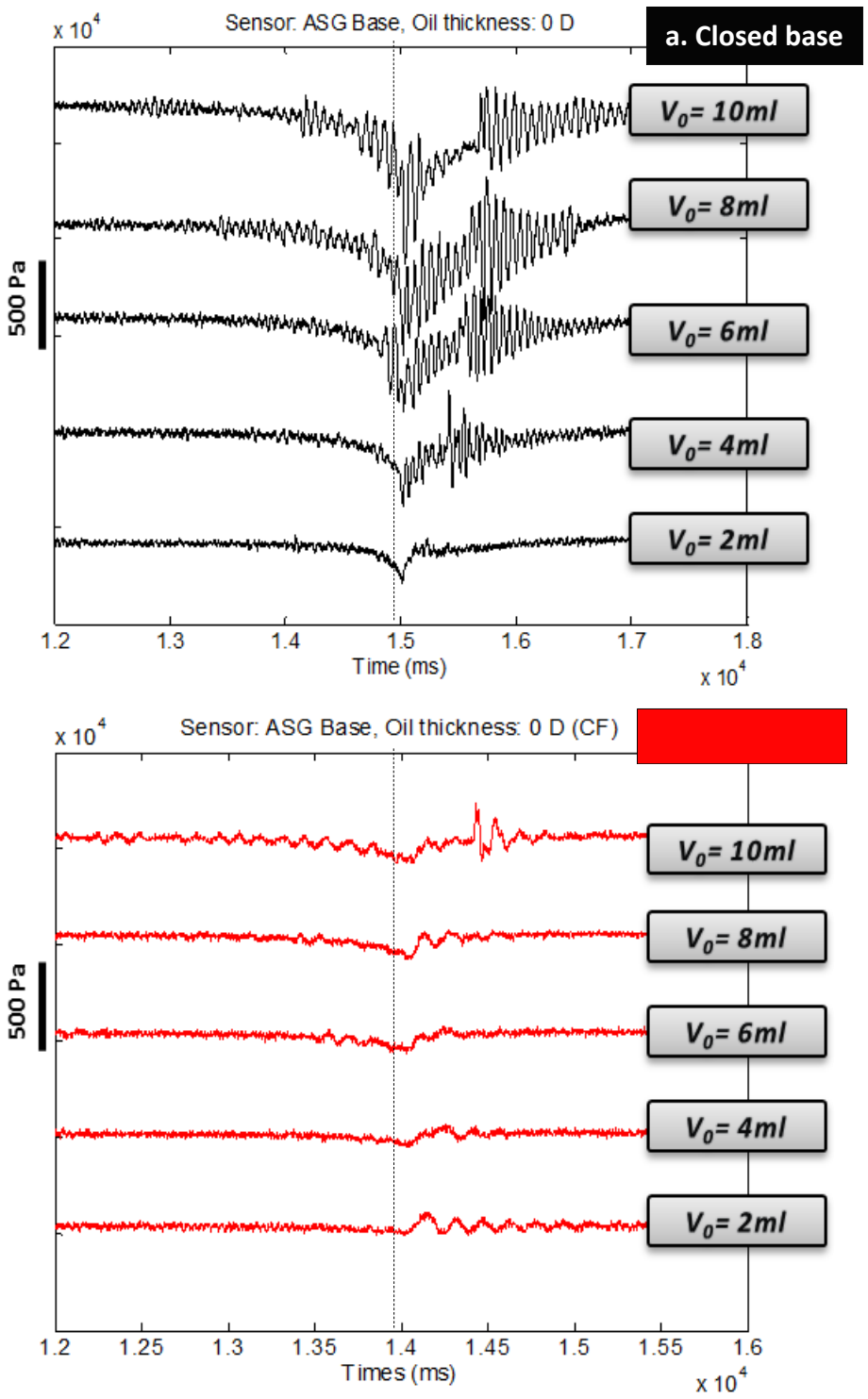

Figure 4-8. ASGBase signal variations for experiments carried out at P_{surf} = 30 mbar, in a homogenous liquid (hi/D= 0), in closed (a) and open base conditions (b), respectively. Initial injection volumes V_0 vary from 2 to 10 ml. Signals are time-adjusted to coincide at 'bursting spike' (marked with the vertical dashed line).

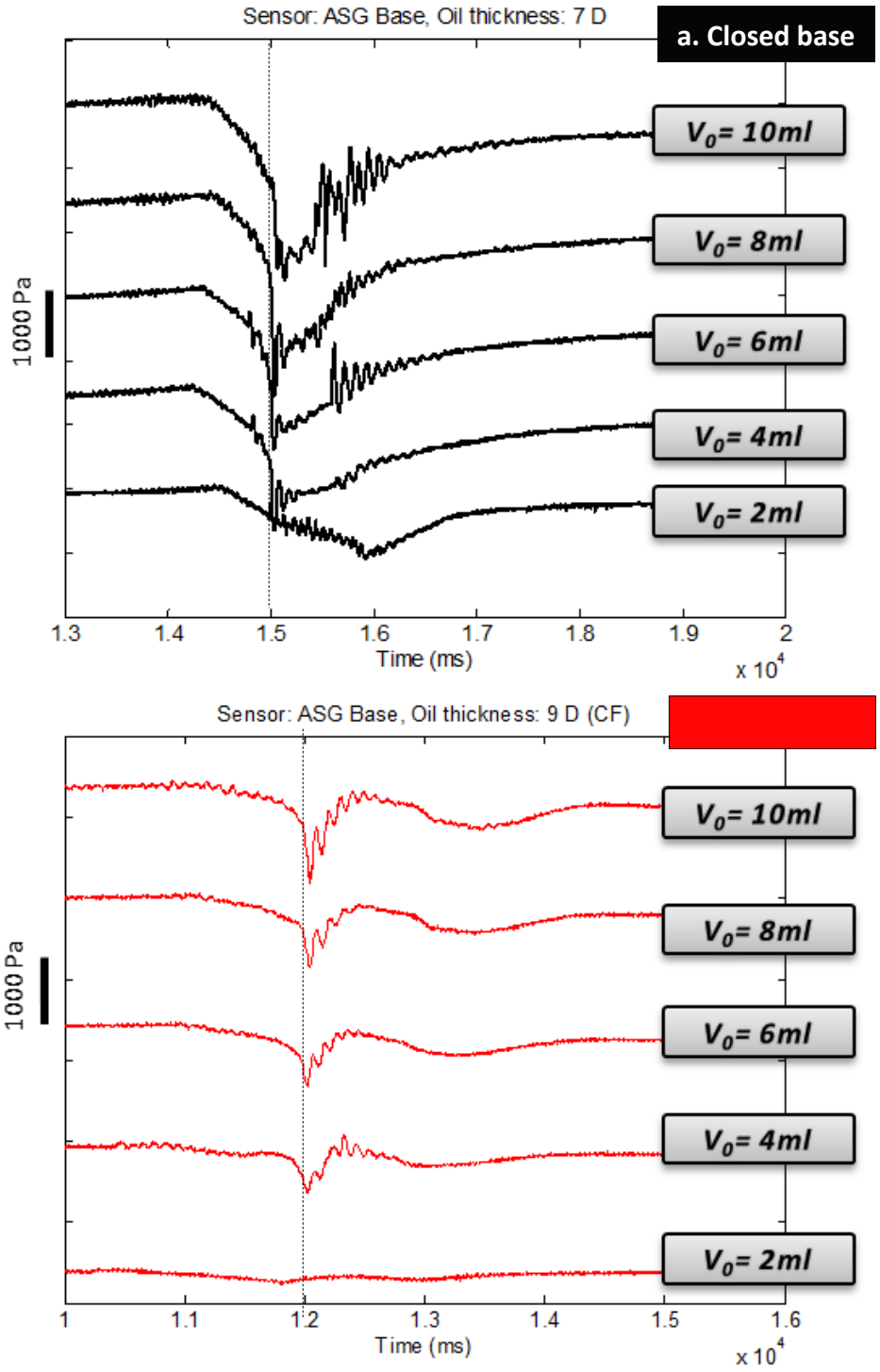

Figure 4-9. ASGBase signal variations for experiments carried out at P_{surf} = 30 mbar, in closed base conditions and for a impedance thickness h_i/D= 7 (a), and in open base conditions and h_i/D= 9 (b), respectively. Initial injection volumes V_0 vary from 2 to 10 ml. Signals are time-adjusted to coincide at 'bursting spike' (vertical dashed line).

The differential pressure transducer s-163 signals show that there is a direct correlation between amplitude of the pressure transients and injected volume both in a homogenous liquid (Figure 4-10), and when a viscous cap is placed at the top (Figure 4-11). For closed base conditions and h_i/D = 0, slug burst generates a pressure transient for the entire range of volumes explored, with the largest peak (V_0= 10 ml) having a maximum amplitude of ~150 Pa (Figure 4-10a). In open base conditions (Figure 4-10b), no clearly discernible transient is observed for V_0≤6 ml, and general damping of the signals is observed as for ASGBase. The largest peak (V_0= 10 ml) in the suite has a maximum amplitude ~25 Pa. The same features are shown when h_i/D >0 (Figure 4-11), except that a general increase of the magnitude of the transients is recorded, other factors being equal (maximum amplitudes recorded for a V_0= 10 ml slug are ~190 Pa and 70 Pa for closed and open base, respectively).

All the s-163 signals, regardless of the amount of volume injected, have a similar form that is related to the dynamic of bursting process (Figure 4-12). Prior to burst, the differential pressure transducers first detect a gradual pressure increase driven by the accelerated liquid surface pressurizing the air above it. As volume increases, pressure increases more abruptly due to faster expansion of the slug. On bursting, a first maximum amplitude peak is recorded, and a secondary peak is present for V_0 > 2 ml (with the exception of closed base, h_i/D = 0 case). The observation of synchronized video data show that the first peak is attributable to the acceleration of liquid surface, and the second peak is associated with meniscus rupture and subsequent release of air from within the over-pressured gas slug. For V_0 < 2 ml, the bursting process remains undetected by the pressure transducers. Given the small injection volume, the pressurization of the slug is not sufficient to accelerate the liquid surface and the release

of air within the slug in the tube takes place through meniscus rupture. Therefore the process of burst of the gas slug is phenomenologically different according to the initial injected volume.

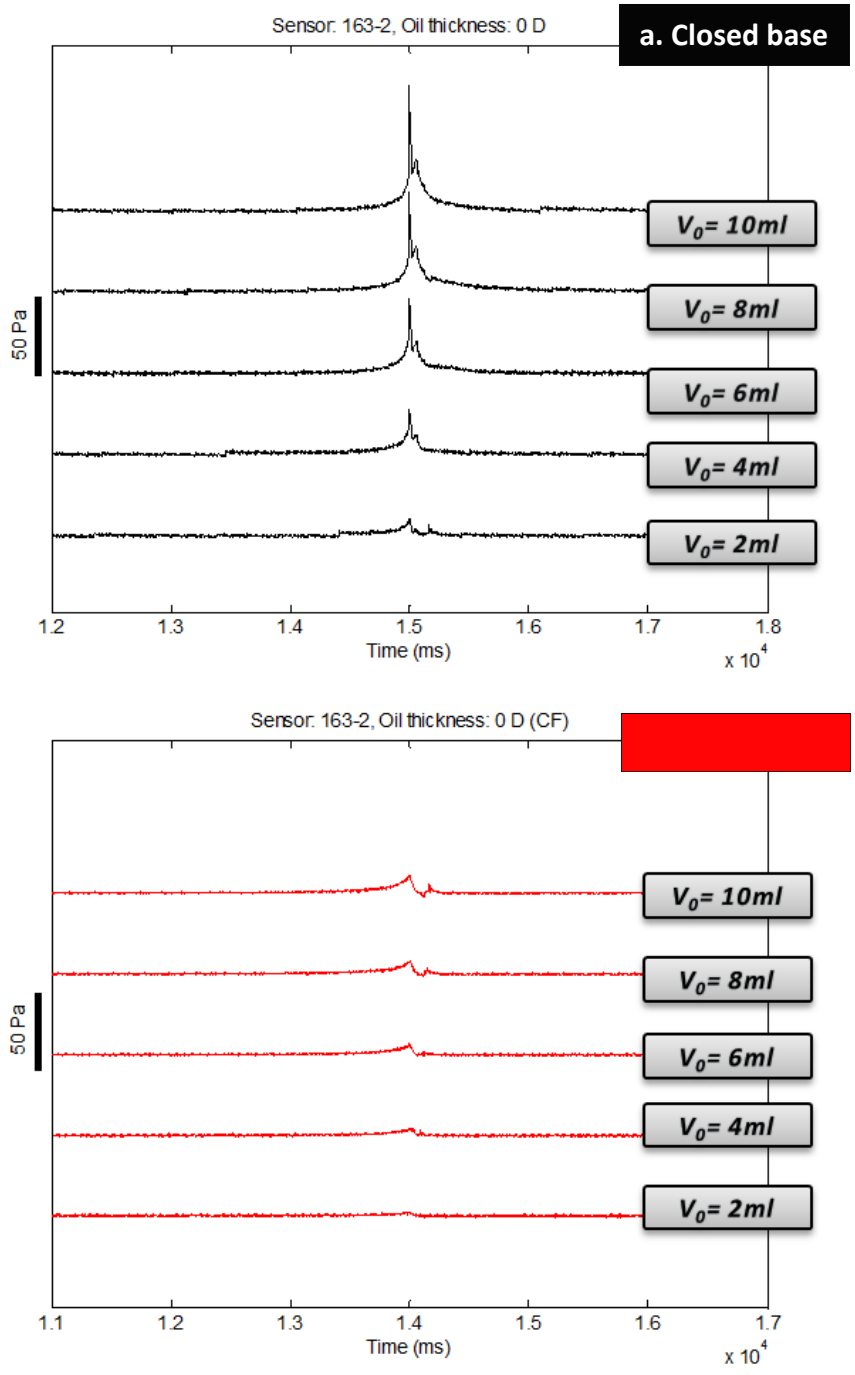

Figure 4-10. s-163_2 signal variations for experiments carried out at P_{surf} = 30 mbar, and for homogenous liquid (h_i/D= 0) in closed base (a), and in open base conditions (b),

respectively. Initial injection volumes V_0 vary from 2 to 10 ml. Signals are time-adjusted to coincide at 'bursting spike.

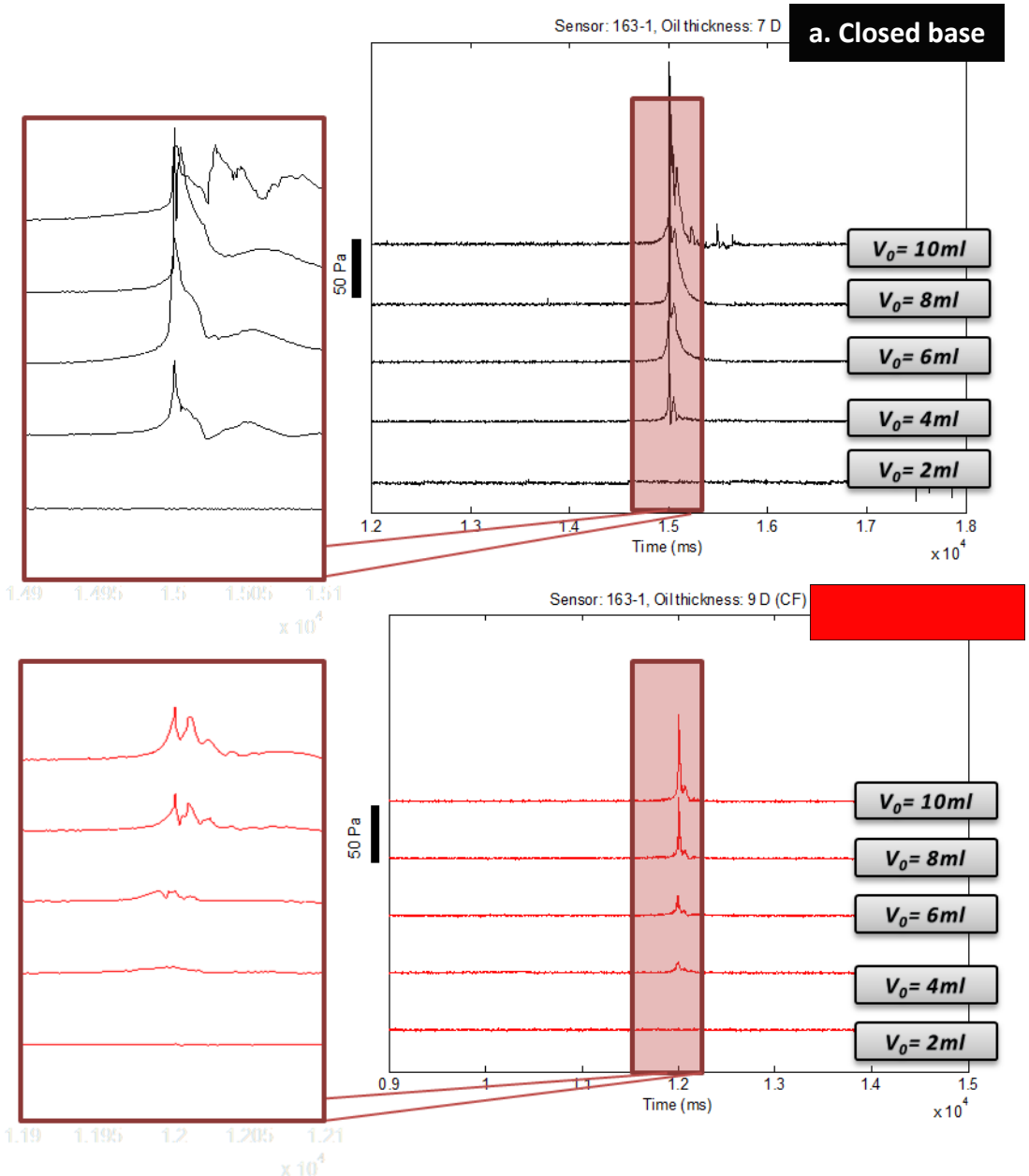

Figure 4-11. s-163_2 signal variations for experiments carried out at P_{surf} = 30 mbar, in closed base conditions and for a impedance thickness h_i/D= 7 (a), and in open base conditions and h_i/D= 9 (b), respectively. Initial injection volumes V_0 vary from 2 to 10 ml. Signals are time-adjusted to coincide at 'bursting spike.

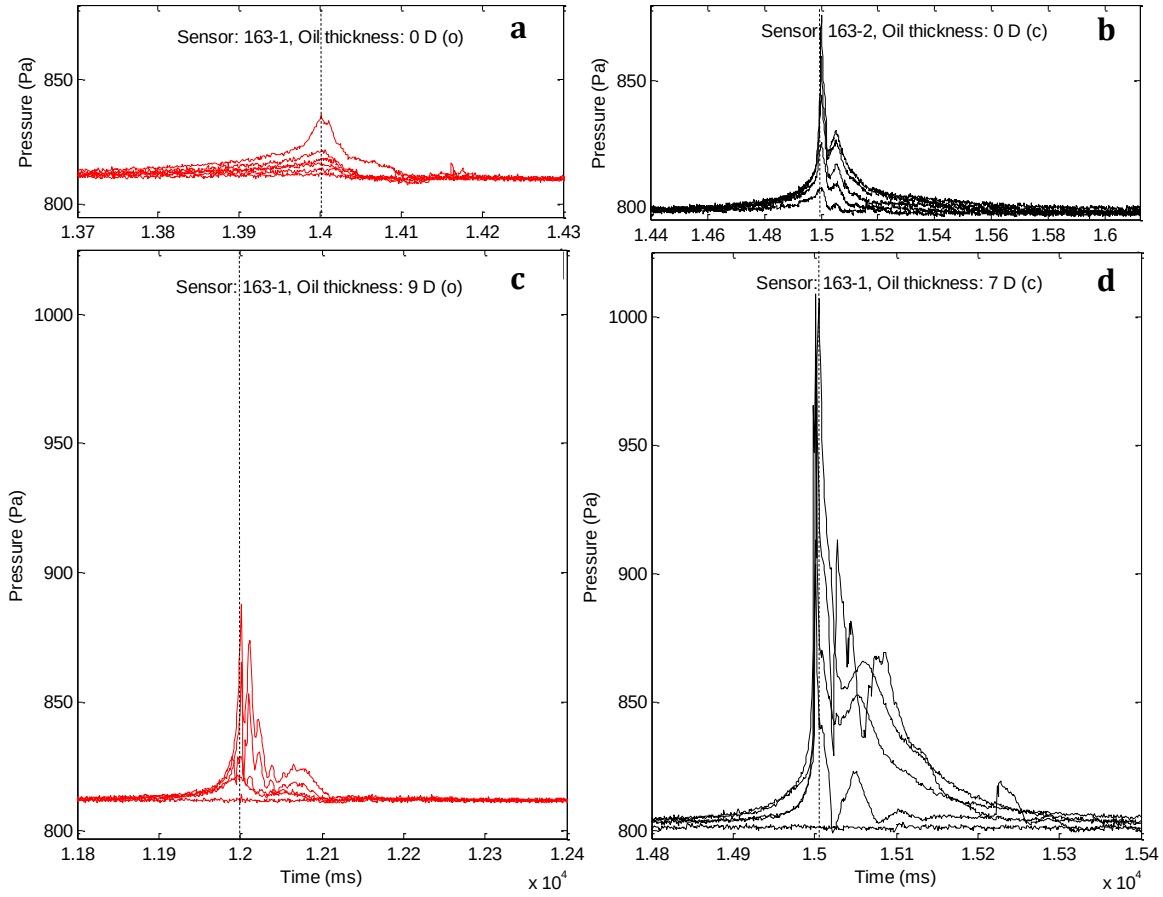

Figure 4-12. Bursting time interval for s-163_2 signal variations for all the experiments carried out at P_{surf} = 30 mbar and injection volumes 2ml< V_0<10ml . a) Open base , h_i/D = 0; b) closed base , h_i/D = 0; c) open base , h_i/D = 9; d) closed base , h_i/D = 7; Note the secondary peaks following the maximum on both of the s-163 transducer signals. The black vertical dashed line corresponds to the point of slug burs, as identified from synchronized video data.

For closed base experiments, the behavior of the displacement transducer signal is also shown (Figure 4-13). Small volumes cause only a slight perturbation to the natural oscillation of the system (~20 Hz). The amplitude of the oscillation is proportional to the slug volume, i.e. a larger injection results in a larger apparatus upward displacement. The upward displacements are then followed by a decaying resonant oscillation after bursting of the gas slug.

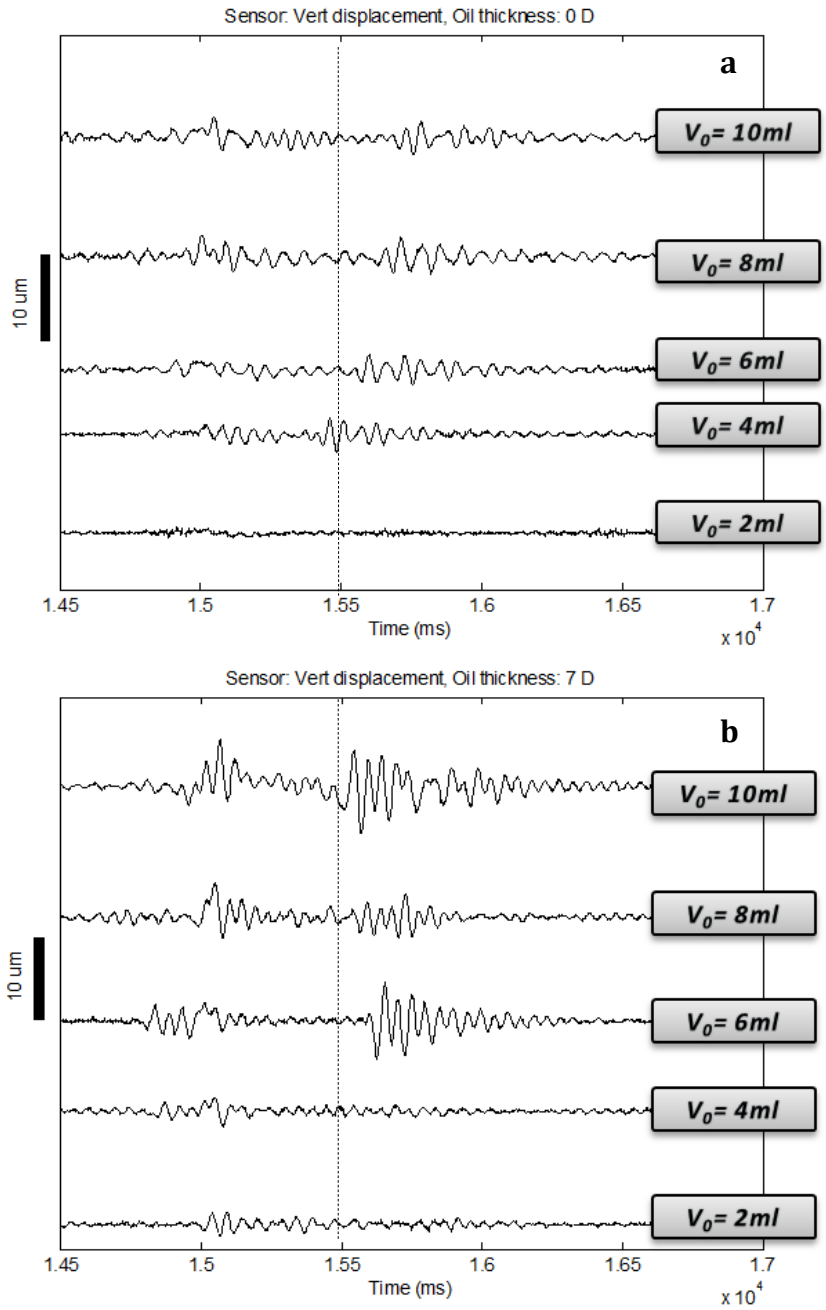

Figure 4-13. VertDispl sensor displacement for experiments carried out at P_{surf} = 30 mbar, in closed base conditions and for a impedance thickness h_i/D= 0 (a), and h_i/D= 7 (b), respectively. Initial injection volumes V_0 vary from 2 to 10 ml. Signals are time-adjusted to coincide at 'bursting spike' (vertical dashed line marks bursting time).

4.2.3 Effect of changing boundary conditions

The results presented in previous section suggest that a distinct change in meniscus rupture dynamics occurs for increasing slug volumes. Now we illustrate the features identified in the experiments carried out for systematic variation of the high-viscosity liquid layer thickness for both closed base ($0 \leq h_i/D \leq 7$) and open base conditions ($0 \leq h_i/D \leq 9$).

The magnitude of pressure transients for the suite of experiments carried out using variable thickness of the viscous layer at an ambient pressure of 30 mbar are reported as a function of volume in Figure 4-14a. For experiments conducted in closed base conditions we also report the maximum vertical displacement recorded (Figure 4-14b). Overall, an increase in s-163 pressure transients occurs with increasing volume of gas injected and increasing thickness of the viscous cap. However for open base conditions the magnitude of the transients is remarkably reduced, and the amplitude variation does not appears to have a proportional correlation with increasing thickness. For the case h*i*/D=0 (i.e., in a homogenous liquid), very small transients are recorded for all the range of investigated injection volumes. Conversely, above a given thickness of the viscous layer ($0 < h_i/D < 5$), an abrupt increase is recorded for injection volumes $V_0 \geq 4$ ml, indicating that the gas slugs become dynamically over-pressured at burst.. For small injection volumes pressure transients are very small, indicating that the gas slug is not over-pressured. Note that a few experiments give some outliers in the plots, resulting from the malfunction of the transducers s-163 caused by clogging of the transducer by sprayed water/oil. A significant decrease of AGSBase pressure transients at bursting is recorded for increasing thickness of the viscous cap for closed base experiments, with a minimum pressure transient of ~17 kPa recorded immediately before bursting of a 10

ml slug and h_i/D= 7. As for the s-163 signals, the same threshold behavior is observed at a thickness between 0 < h_i/D < 5 for experiments carried out in open base conditions, together with a general decrease in magnitude of transients. Here, the minimum recorded transient value (~19 kPa) is much higher than that measured for the same injected volume in closed base, indicating that the expansion of the gas slug is strongly inhibited in these particular conditions. Maximum vertical displacement for the experiments carried in closed base conditions (Figure 4-14b) show a general correlation with thickness, though a positive trend is clear just for the maximum thickness suite (h_i/D= 7). In all instances, the apparatus is displaced in an upward direction, indicating an upward directed vertical force, with the maximum displacement obtained of 16 μm. Little or no variations is observed for thickness 0 < h_i/D < 2 indicating that the release of gas from the slug is not abrupt.

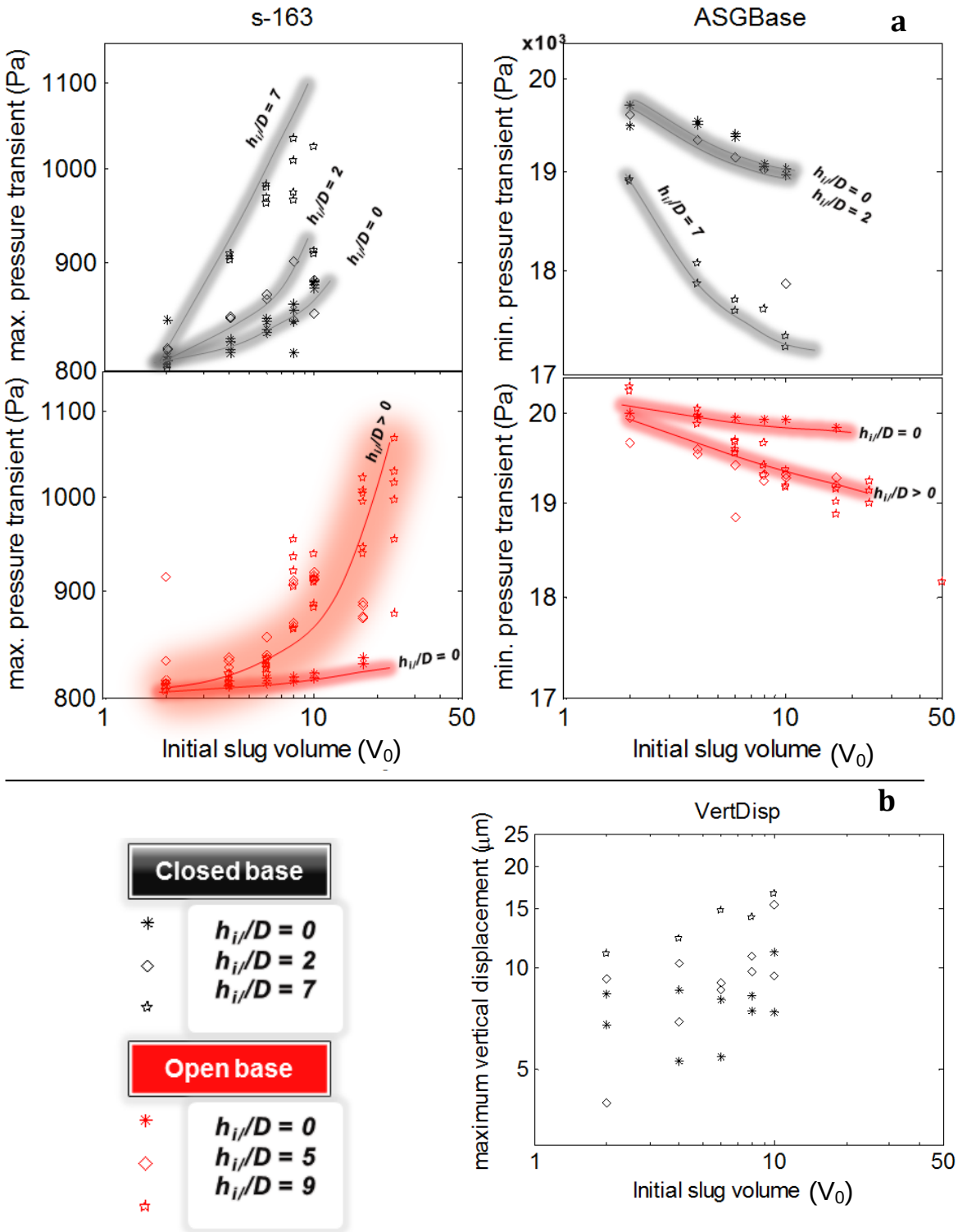

Figure 4-14. Magnitude of pressure transients recorded by s-163 and ASGBase pressure transducers (a) and maximum vertical displacement recorded for the closed base suite (b), for varied injection volumes of gas and thickness of viscous layer at 30 mbar. Lines are only to catch the eye.

4.3 Expansion – bursting dynamics from video

In the previous section we illustrated that a change in boundary conditions in the conduit concur to affect the expansion and burst dynamic of the slug. The observation of video data allows interpreting transducers signals and to better constrain the dynamic of slug expansion in relation with the change in boundary conditions.

4.3.1 Open versus closed base

First of all, the analysis of transducers signals showed that the presence of an upward flux at the base of the conduit (i.e. in open base conditions) is correlated with a general attenuation of the magnitude of the pressure transients: for the simplest case of a slug bursting in a homogenous liquid (h_i/D = 0) s-163 maximum transient pressure is lower, and ASGBase minimum pressure is higher with respect to the experiment carried out in closed base conditions, other factors being equal.

Analysis of video data show that in open base conditions the rate of ascent of the liquid surface is smaller compared to the rate of ascent in closed base condition. In Figure 4-15, slug expansion dynamic for a 10 ml slug ascending in a closed base conduit is compared with that of a same slug in an open base conduit. The simplest case of a homogenous liquid is reported (h_i/D = 0) to exclude the effect of the viscous impedance on slug expansion. Slug nose, base, and liquid surface position (Figure 4-15a), together with slug length (Figure 4-15b) are reported against time after injection. Since the video data for closed base conditions didn't capture the slug base position, this is extrapolated by calculating the length of the ascending slug L_s assuming conservation of liquid volume before and after injection, $\pi\, r_c^2 h_0 = \pi\, r_c^2\, (h - L_s) \;+\; \pi\, (r_c^2 - r_s^2)\, L_s$, where h_0 is

the height of the liquid cylinder before injection of the slug, and h is the height of the liquid surface after injection (as measured from video data). From this expression we obtain $L_s = h - h_0 \frac{r_c^2}{r_s^2}$, with the quantity r_c^2/r_s^2 derived using the expression for A' (equation 2-2) reported in section 2. As a test, L_s was also calculated for open base conditions and compared with the slug length measured from video, obtaining a satisfactory fit to measured data.

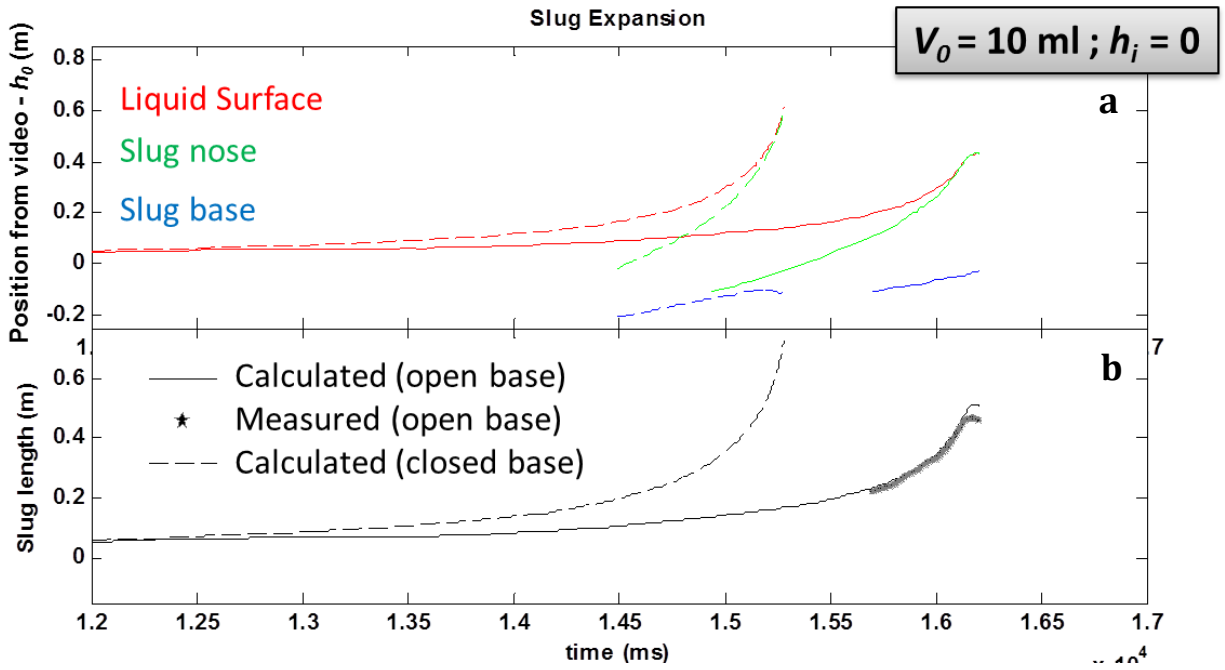

Figure 4-15. Expansion dynamic of a 10 ml slug ascending in a homogenous liquid (h_i/D=0) and in closed base (dashed line) and open base (solid line) conditions. a) Measured vertical position of the slug nose, slug base and liquid surface is reported with respect to initial liquid surface h_0. In b) we plot calculated slug length against time. Measured data for open base conditions are also plotted (stars), to attest good fit of the model. Note that slug length (and so the position of the slug base in closed base reported in a) is calculated assuming conservation of liquid volume before and after injection (see details in text). Time is adjusted to coincide at injection time.

In open base conditions, the liquid surface rises a shorter distance in the tube before it is intercepted by the slug nose. The bursting process occurs at larger distance with respect to the s-163 sensor position, and the gas is released deeper in the pipe, resulting in a lower pressure recorded by the transducers. The reduced acceleration of the liquid surface can be explained in terms of some counter flow effect induced by liquid flowing in/out of the base. This should effectively contrast the ascent of the liquid, causing a resultant reduced upward acceleration. Consequently, a reduced pressure increase would be detected by the differential pressure transducers.

The rate of decrease in pressure at the base (ASGBase transducers) can be explained in terms of a reduced expansion capability of the slug (i.e., the smaller the slug, the lesser the material suspended along the tube walls and the smaller the potential pressure drop below it). The extent of expansion correlates again with the reduced acceleration of the liquid free surface. For injection of a volume of gas of 10 ml (Figure 4-15), at bursting, a slug will be of shorter length (0.5 m) in an open base conduit than in a closed base one (0.8 m), because counter flow will cause less liquid to remain ahead of the gas slug. Consequently, the slug will intercept the liquid surface with a reduced degree of expansion, being not able to propagate further due to earlier run out of liquid.

4.3.2 Rheologically plugged conduits

As previously shown in Figure 4-14, the presence of a viscous impedance placed at the top of the conduit is correlated with a general increase in magnitude of the pressure transients. For both closed and open base experiments, a transitional thickness is identified, above which s-163 maximum pressure transients increase abruptly, ASGBase

minimum pressure transients decrease, and (for closed base conditions only) vertical displacements of the tube are higher.

Below the transitional thickness (h_i/D < 2 and h_i/D < 5 for closed and open base experiments, respectively), oil thickness is insufficient to behave as impedance. This is confirmed by video data, showing an amount of water proportional to the injected volume being pushed through oil before the slug actually ascends through it. Above the transitional thickness, oil thickness effectively act as a 'plug'. If we compare positional data for the case h_i/D = 0 and h_i/D =9 (Figure 4-16), i.e., the two end-member conditions for the open base case, we observe that the presence of an impedance at the top of the conduit significantly reduces expansion capability of the slug, other factors being equal.

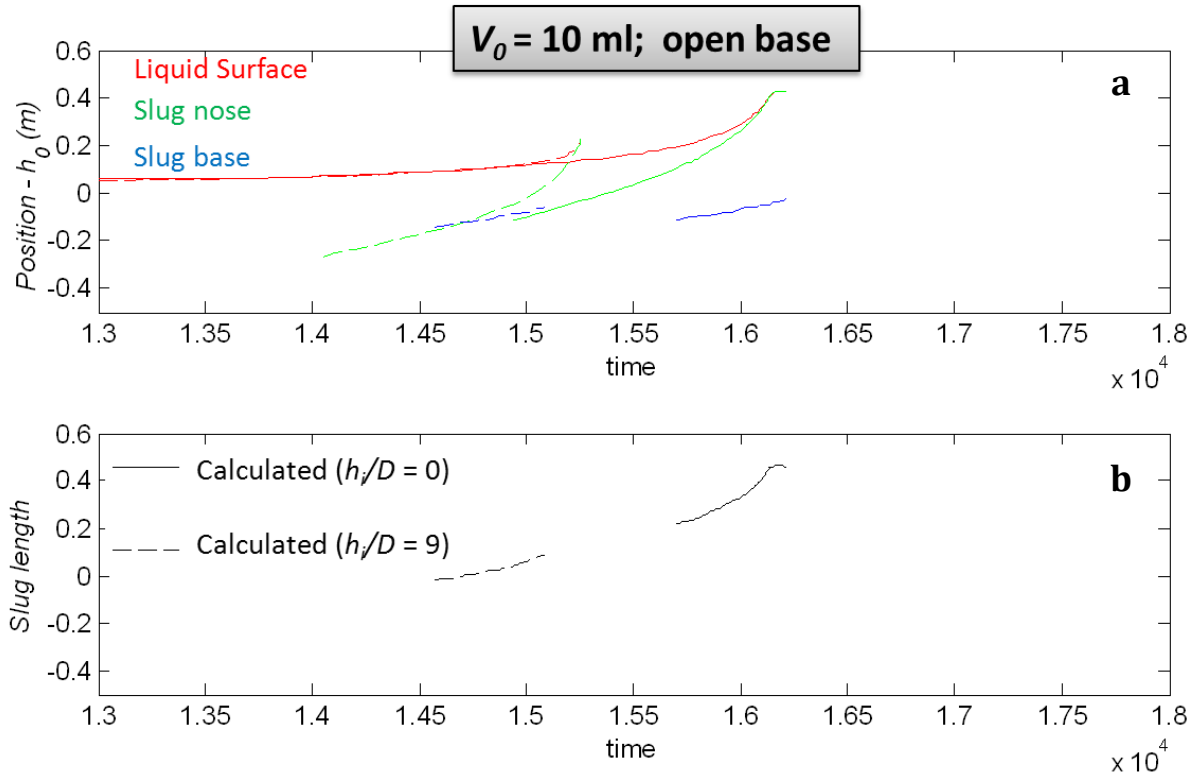

Figure 4-16. Expansion dynamic of a 10 ml slug ascending in a homogenous liquid (h_i/D=0, solid line) and in a liquid with an overlying viscous impedance (h_i/D=9, solid line) in open

base conditions. a) Measured vertical position of the slug nose, slug base and liquid surface is reported with respect to initial liquid surface h_0. In b) measured slug length is plotted against time. Time is adjusted to coincide at injection time.

For a 10 ml volume, a slug bursting in a rheologically impeded conduit ($h_i/D = 9$) will be of much shorter length (~0.1 m) then a slug bursting a in a homogenous liquid (~0.5 m). Liquid surface is relatively stationary until the slug reaches the bottom of the viscous impedance, and slug expansion develops in a 'downward' direction, i.e., ascent velocity of the slug base decreases. Before that point, energy not is dissipated in the acceleration of the liquid head above it, and consequently the degree of pressurization inside the slug increase. Once the slug has sufficient energy to push its way through the viscous layer, a sudden acceleration to the liquid mass is imparted, that is associated to the large amplitude of the observed s-163 transients.

4.4 Implications for Strombolian eruptions

The overall suite of experiments carried out with variable boundary conditions show a number of characteristic features that are relevant to the nature of the change in gas slug decompression history and final burst process in a real volcanic scenario.

The first direct implication of our experiments is that at a volcano, expansion of a gas slug is strongly controlled by of i) the flow conditions inside the volcanic conduit, and ii) the extent of the viscous transition obstructing the top of a volcanic conduit. The degree of the expansion correlates with the magnitude of the oscillatory signals recorded by the displacement, base ASG and P163 differential pressure transducers.

During slug ascent and expansion, the liquid ahead of the rising gas slug enters the region between the gas slug and the tube wall, it accelerates, imparting a downward directed viscous shear at the tube wall. In closed base conditions, i.e. (when the volume liquid is maintained constant) this downward directed shear is contrasted by the upward directed viscous shear of the liquid piston ahead of the gas slug; hence before late-stage rapid expansion of the slug, the resultant force and motion imparted to the system is . In open base conditions, i.e., when the liquid is free to flow in and out of the conduit, another mechanism operates. Viscous shear is enhanced, causing significant reduction of the resultant forces. At the volcanic scale, this suggests that pressure oscillations related to the passage of a gas slug in a conduit where a magma is flowing are likely to produce weak signals or remain undetected. However, the laboratory experiments describe the situation for a gas slug rising in a liquid-filled tube with a perfectly cylindrical geometry, where almost no shear is encountered at the tube walls. Further, at both scales, there are many factors that have uncertainties that we cannot constrain sufficiently, as, for instance, the magnitude and the direction of flow along the conduit height. Moreover, during the late stage of ascent, the near-surface, rapid-expansion of the slug is reduced, with a resulting decrease in the magnitude of pressure reduction at the base. Very low acceleration of the liquid mass ahead of the slug causes small variation in pressure into the overlying atmosphere, and consequently very weak acoustic pressures signals are recorded by infrasonic arrays.

A viscous transition in the top-most region conduit changes dramatically the magnitude of the observed pressure transients, favoring a sudden, and more energetic pressure release into the overlying atmosphere. Variation of the s-163 pressure transducers show a highly repeatable waveform characterized by an initial higher amplitude peak

resulting from the compression of the air above the liquid surface followed by a lower amplitude, secondary peak attributed to the burst of the gas slug. The highest the volume and the thickness of the impedance, the larger the magnitude of the pressure peaks. The video data indicates that there is a change in the style of meniscus rupture, from a more passive process at a thin viscous cap/low injection volumes, to a more energetic process at a thick viscous cap/high injection volumes.

This suggest that for instance, at Stromboli, when a slug ascends in a plugged, or partially solidified conduit the associated acoustic signals are larger than those expected if a slug were rising a homogenous magma. In previous works, the magnitude of acoustic pressure transients obtained from acoustic and seismo-acoustic studies at Stromboli is generally associated with the discrete volume of the gas slug involved in an eruption [e.g., *Vergniolle and Brandeis,* 1996; *Ripepe et and Marchetti*, 2001; *Harris and Ripepe*, 2007; *Colò et al*., 2010]. Our results suggest that there may be a similar correlation between acoustic signals recorded at Stromboli and the extent of the rheological impedance at the top of the vent. Consequently, the observed transition between passive bursting, in which gas bubbles are not overpressured, and overpressured slug burst regimes observed at Stromboli [*Marchetti et al.* 2006*, Harris and Ripepe*, 2007; *Colò et al.,* 2010], could be interpreted as resulting from multiple effects in the conduit, and not necessarily through a variation in the amount of discrete gas erupted. In section 3.4.2 we already highlighted the possibility that different factors affecting the shape of the slug (e.g., viscosity and conduit diameter) prior bursting are crucial for the pressurization and resultant behavior at bursting. Here we further stress that different explosions at Stromboli may be driven by rheological variations localized at the single vent. For instance, at Stromboli, a same eruptive style can persist at the

same vent for relatively long periods of time [e.g., *Patrick et al.*, 2007]. The observed variations from at different vents may be linked, according to our model, to different clogging conditions of the uppermost portion of the conduits.

5. Conclusive remarks

The aim of this thesis was to study how explosive behavior and geophysical signals in a volcanic conduit are related to the development of overpressure in slug-driven eruptions.

Experimental data presented here demonstrate that, in the case where interfacial tension can be ignored ($Eo > 40$), the thickness of the film of liquid that falls around a rising Taylor bubble is a function of the inverse viscosity only (N_f). The experiments show that the dimensionless film thickness, expressed as dimensionless cross sectional area of the conduit occupied by the film (A'), has a sigmoidal dependence on N_f (figure 4). For $N_f < 10$, the dimensionless film thickness is independent of N_f with value $A' \approx 0.55$; in the interval $10 < N_f < 104$, A' decreases with increasing N_f ; for $N_f < 10^4$, film thickness is, independent of N_f with value $A' \approx 0.15$. Therefore, at the volcanic scale this parameter is simply dependent from the magma properties and geometrical parameters of the conduit, hence the value of the parameter A' can be computed if the density and viscosity of the magma, and the size of the conduit are known.

Based on experimental results an analytical model is developed for the rise and burst of gas slugs in a volcanic conduit. The model explores the physical controls on slug burst overpressure, and hence explosion intensity; and conclude that the overpressure is determined by the amount of gas in the slug, and by the thickness of the film of magma falling around the slug. The model neglects inertia and viscosity at the conduit scale, and shows that significant overpressures can develop from geometric and magmastatic considerations alone. Non-dimensionalization of the model facilitates its application to any system in which gas slugs rise up a conduit or pipe (e.g., Strombolian and hydrothermal eruptions on Earth and other planets, geysers, mud volcanoes, and engineering applications).

When applied to volcanic scenarios, the model predicts that explosion overpressure in slug-driven basaltic eruptions should vary dramatically in response to variations in slug size (*V'*), magma viscosity and density, and conduit diameter. As a case study, eruptions at Stromboli volcano (Aeolian Islands) are modelled. Overpressure predicted by the model is in good agreement with previous field estimates for eruptions at Stromboli over its entire spectrum of explosive activity, from low energy puffing, through normal Strombolian eruptions, up to paroxysmal explosions. This wide-ranging agreement suggests that it is plausible to envisage a common, slug-driven mechanism for all eruptive styles at Stromboli, providing further support to a slug-related origin of paroxysmal eruption.

Various geometrical and physical parameters for volcanic slugs can be calculated using the model, including slug size and radius, the thickness of the surrounding magma layer, depth of burst onset, and the evolution of pressure within the slug during ascent. At Stromboli, we find that the transition from passive degassing to explosive bursting occurs for slugs with volume greater than 24-230 m^3, depending on magma viscosity and conduit diameter, and that at burst, a typical Strombolian slug (with volume 100–1000 m^3) has an internal gas pressure of 1–5 bars and a length of 13–120 m. These model outputs can be used as input parameters for more sophisticated eruption models and can be combined with geophysical monitoring information to better assess eruptive dynamics and associated hazards at basaltic volcanoes worldwide.

Finally, our experiments suggest that bursting of gas slugs at a volcano is strongly controlled by of i) the flow conditions inside the volcanic conduit, and ii) the extent of the viscous transition obstructing the top of a volcanic conduit. When the slug is ascending in a non-stagnating magma column, an overall reduction in the magnitude of

the observed signals is postulated with respect to stagnant conditions. Very low acceleration of the liquid mass ahead of the slug causes small variation in pressure into the overlying atmosphere, and consequently very weak acoustic pressures signals are recorded by infrasonic arrays.

When the vent is either constricted, or filled at the top with a liquid possessing a higher viscosity stress, the ascending and expanding gas slug causes the liquid beneath it to flow back down the conduit and re-enter the subsurface reservoir. The dynamic of slug pressurization is dramatically increased by rheological stiffening of the magma at the top, and so are the magnitudes of pressure transients associated with the bursting of pressurized gas slugs.

6. Reference list

Aiuppa, A., M. Burton, T. Caltabiano, G. Giudice, S. Guerrieri, M. Liuzzo, F. Murè, and G. Salerno, (2010), Unusually large magmatic CO2 gas emissions prior to a basaltic paroxysm, *Geophys. Res. Lett.*, 37, L17303, doi: 10.1029/2010GL043837.

Alatorre-Ibarguengoitia, M.A., B. Scheu, D.B. Dingwell, H. Delgado-Granados, and J. Taddeucci (2010), Energy consumption by magmatic fragmentation and pyroclast ejection during Vulcanian eruptions, ***Earth Planet. Sci. Lett.,* 291 (1-4),** 60-69, doi: 10.1016/j.epsl.2009.12.051.

Allard, P., A. Aiuppa, M. Burton, T. Caltabiano, C. Federico, G. Salerno, and A. La Spina (2008), Crater gas emissions and the magma feeding system of Stromboli volcano, In: S. Calvari, S. Inguaggiato, G. Puglisi, M. Ripepe, M. Rosi (Eds.), *Learning from Stromboli volcano: insights from the 2002-2003 eruption*, AGU Geophys. Monograph. Series, vol. 182, Washington DC, Chap. 1.5, 65-80.

Allard, P. (2010), A CO_2-rich gas trigger of explosive paroxysms at Stromboli basaltic volcano, Italy, *J. Volcanol. Geotherm. Res.*, 189 (3-4), 363–374, doi: 10.1016/j.jvolgeores.2009.11.018.

Allard, P., J. Carbonnelle, N. Métrich, H. Loyer, and P. Zettwoog (1994), Sulfur output and magma degassing budget of Stromboli volcano, ***Nature,* 368 (6469)**, 326-330.

Anderson, A.T., (1995), CO_2 and the eruptibility of picrite and komatiite, *Lithos*, 34, p. 19-25.

Andronico, D., A. Cristaldi, P. Del Carlo, and J. Taddeucci (2009), Shifting styles of basaltic explosive activity during the 2002–03 eruption of Mt. Etna, Italy, *J. Volcanol. Geotherm. Res.*, 180 (2-4), 110–122, doi: 10.1016/j.jvolgeores.2008.07.026.

Barberi, F., M. Rosi, and A. Sodi (1993), Volcanic hazard assessment at Stromboli based on review of historical data, *Acta Vulcanol*., 3, 173–187.

Barberi, F., L. Civetta, M. Rosi, and R. Scandone (2009), Chronology of the 2007 eruption of Stromboli and the activity of the Scientific Synthesis Group, *J. Volcanol. Geotherm. Res.*, 182 (3-4), 123-130, doi: 10.1016/j.jvolgeores.2008.09.019.

Batchelor, G. K. (1967), *An Introduction to Fluid Dynamics*, Cambridge Univ. Press, Cambridge, U. K.

Bertagnini, A., N. Métrich, P. Landi, and M. Rosi (2003), Stromboli volcano (Aeolian Archipelago, Italy): An open window on the deep-feeding system of a steady state basaltic volcano, *J. Geophys. Res.*, 108(B7), 2336, doi:10.1029/2002JB002146.

Bertagnini, A., N. Métrich, L. Francalanci, P. Landi, S. Tommasini, and S. Conticelli (2008), Volcanology and magma geochemistry of the present-day activity: constraints on the feeding system, in: Calvari, S., Inguaggiato, S., Ripepe, M., Rosi, M. (Eds.), The *Stromboli Volcano: An Integrated Study of the 2002–2003 Eruption: AGU Geophys. Monograph. Series*, Washington DC, vol. 182, pp. 19–37.

Blackburn, E. A., L. Wilson, and R. S. J. Sparks (1976), Mechanisms and dynamics of Strombolian activity, *J. Geol. Soc. London*, 132, 429–440, doi:10.1144/gsjgs.132.4.0429.

Bottinga, Y. and M. Javoy, (1989), MORB degassing: Evolution of CO2, *Earth Planet. Sci. Lett*. 95, p. 215-225.

Bottinga, Y. and M. Javoy, (1990), MORB degassing: Bubble growth and ascent, *Chem. Geol.*, 81, p. 255-270.

Bottinga, Y. and M. Javoy, (1991), The degassing of Hawaiian tholeiite, *Bull. Volcanol*., 53, p.73-85.

Brown, R.A.S. (1965), The mechanics of large gas bubbles in tubes I. Bubble velocities in stagnant liquids. *Can. J. Chem. Eng*., 43 (5), 217–223, doi: 10.1002/cjce.5450430501.

Bugg, J. D., K. Mack, and K. S. Rezkallah (1998), A numerical model of Taylor bubbles rising through stagnant liquids in vertical tubes, *Int J Multiphas Flow*, *24*(2), 271-281.

Burton, M., P. Allard, F. Mure, and A. La Spina (2007a), Magmatic gas composition reveals the source depth of slug-driven Strombolian explosive activity, *Science*, 317 (5835), 227-230, doi: 10.1126/science.1141900.

Burton, M.R., H.M. Mader, and M. Polacci (2007b), The role of gas percolation in quiescent degassing of persistently active basaltic volcanoes, ***Earth Planet. Sci. Lett,*** 264 (1-2), 46-60, doi: 10.1016/j.epsl.2007.08.028.

Calvari, S., L. Spampinato, A. Bonaccorso, C. Oppenheimer, E. Rivalta, and E. Boschi (2011), Lava effusion - A slow fuse for paroxysms at Stromboli volcano?, ***Earth Planet. Sci. Lett,*** 301, 317-323, doi: 10.1016/j.epsl.2010.11.015.

Campos, J. B. L. M., and J. R. F. Guedes de Carvalho (1988), An experimental study of the wake of gas slugs rising in liquids. *J. Fluid Mech.* 196, 27–37, doi:10.1017/S0022112088002599.

Cimarelli, C., F. Di Traglia, and J. Taddeucci (2010), Basaltic scoria textures from a zoned conduit as precursors to violent Strombolian activity, *Geology*, 38 (5), 439–442, doi: 10.1130/G30720.1.

Chouet, B. (2003), Volcano seismology, *Pure Appl. Geophys.*, 160 (3-4), 739 – 788, doi: 10.1007/PL00012556.

Chouet, B., N. Hamisevicz, and T. R. McGetchin (1974), Photoballistics of Volcanic Jet Activity at Stromboli, Italy, *J. Geophys. Res.*, 79 (32), 4961 – 4976, doi:10.1029/JB079i032p04961.

Chouet, B., P. Dawson, T. Ohminato, M. Martini, G. Saccorotti, F. Giudicepietro, G. De Luca, G. Milana, and R. Scarpa, (2003), Source mechanisms of explosions at Stromboli Volcano, Italy, determined from moment-tensor inversions of very-long-period data, *J. Geophys. Res.*, 108 (B1), 219, doi:108 10.1029/2002JB001919.

Chouet, B. A., P. B. Dawson, and M. Martini (2008), Shallow-conduit dynamics at Stromboli Volcano,Italy, imaged from waveform inversions, .), *Fluid motion in volcanic conduits: A source of seismic and acoustic signals*, Geological Society Special Publications, London, v. 307; p. 57-84

Chouet, B. A., P. B. Dawson, M. James, and S. Lane (2010), Seismic source mechanism of degassing bursts at Kilauea: Results from waveform inversion in the 10 - 50 s band, *J. Geophys. Res.*, 115 B09311, doi: 10.1029/2009JB006661.

Colò, L., M. Ripepe, D.R. Baker, and M. Polacci (2010), Magma vesiculation and infrasonic activity at Stromboli open conduit volcano, *Earth Planet. Sci. Lett.*, 292, 274-280, doi: 10.1016/j.epsl.2010.01.018.

Corder, S.B. (2008), The near-surface expansion of gas slugs: Insights into eruptive activity at low magma viscosity volcanoes, PhD Thesis, Lancaster Environmental Centre, Lancaster University, Lancaster, UK.

De Lauro, E., S. De Martino, M. Falanga, and M. Palo (2009), Modelling the macroscopic behavior of Strombolian explosions at Erebus volcano, *Phys. Earth Planet. In.*, 176 (3-4), 174-186, doi: 10.1016/j.pepi.2009.05.003.

D'auria, L. (2006), Numerical modelling of gas slugs rising in basaltic volcanic conduits: inferences on Very-Long-Period event generation, presented at International Workshop: The Physics of Fluid Oscillations in Volcanic Systems I, Lancaster, U.K. http:// www.es.lancs.ac.uk/seismicflow/.

Edmonds M., and T.M. Gerlach (2007), Vapor segregation and loss in basaltic melts, *Geology*, 35(8), 751-754, doi: 10.1130/G23464A.1

Feng, J. Q. (2008), Buoyancy-driven motion of a gas bubble through viscous liquid in a round tube, *J Fluid Mech*, *609*, 377-410.

Gerst, A., M. Hort, P. R. Kyle, and M. Voge (2008), 4D velocity of Strombolian eruptions and man-made explosions derived from multiple Doppler radar instruments, *J. Volcanol. Geotherm. Res.*, 117 (3), 648-660, doi: 10.1016/j.jvolgeores.2008.05.022.

Gresta, S., M. Ripepe, E. Marchetti, S. D'Amico, M. Coltelli, A. L. J. Harris, and E. Privitera (2004), Seismoacoustic measurements during the July-August 2001 eruption of Mt. Etna volcano, Italy, *J Volcanol Geoth Res*, 137(1-3), 219-230.

Harris, A., and M. Ripepe (2007a), Temperature and dynamics of degassing at Stromboli, *J. Geophys. Res*., 112, B03205, doi: 10.1029/2006JB004393.

Harris, A., and M. Ripepe (2007b), Synergy of multiple geophysical approaches to unravel explosive eruption conduit and source dynamics - A case study from Stromboli, *Chem. Erde-Geochem*., 67(1), 1-35, doi: 10.1016/j.chemer.2007.01.003.

Houghton, B.F., and H. M. Gonnermann (2008), Basaltic explosive volcanism: Constraints from deposits and models, *Chem. Erde-Geochem*., 68 (2), 117-140, doi: 10.1016/j.chemer.2008.04.002.

Hui, H., and Y. Zhang (2007), Toward a general viscosity equation for natural anhydrous and hydrous silicate melts, *Geochim. Cosmochim. Acta*, 71 (2), 403–416, doi:10.1016/j.gca.2006.09.003.

Ishibashi, H. (2009), Non-Newtonian behavior of plagioclase-bearing basaltic magma: Subliquidus viscosity measurement of the 1707 basalt of Fuji volcano, *J. Volcanol. Geotherm. Res*., 181 (1-2), 78-88, doi: 10.1016/j.jvolgeores.2009.01.004.

James, M.R., S.J. Lane, and B. Chouet (2004), Pressure changes associated with the ascent and bursting of gas slugs in liquid-filled vertical and inclined conduits, *J. Volcanol. Geotherm. Res*., 129 (1-3), 61-82, doi: 10.1016/S0377-0273(03)00232-4.

James M.R., S.J. Lane, and B.A. Chouet (2006), Gas slug ascent through changes in conduit diameter: Laboratory insights into a volcano-seismic source process in low-viscosity magmas, *J. Geophys. Res*., 111(B5), B05201, doi: 10.1029/2005JB003718.

James, M.R., S.J. Lane, and S. B. Corder (2008), Modelling the rapid near-surface expansion of gas slugs in low viscosity magmas, In: Lane, S.J., Gilbert, J.S. (Eds.), *Fluid motion in volcanic conduits: A source of seismic and acoustic signals*, Geological Society Special Publications, London, pp. 147–167.

James, M.R., S.J. Lane, L. Wilson, and S.B. Corder (2009), Degassing at low magma-viscosity volcanoes: Quantifying the transition between passive bubble-burst and Strombolian eruption, *J. Volcanol. Geotherm. Res.*, 180 (2-4), 81–88, doi: 10.1016/j.jvolgeores.2008.09.002.

Jaupart, C., and S. Vergniolle (1988), Laboratory models of Hawaiian and Strombolian eruptions, *Nature,* 331 (6151), 58-60.

Jaupart, C., and S. Vergniolle (1989), The generation and collapse of a foam layer at the roof of a basaltic magma chamber, *J. Fluid Mech*., 203, 347-380.

Jones K.R., J.B. Johnson , R. Aster , P.R. Kyle, and W.C. McIntosh (2008), Infrasonic tracking of large bubble bursts and ash venting at Erebus Volcano, Antarctica, *J. Volcanol. Geotherm. Res*., 177(3), 661-672, doi: 10.1016/j.jvolgeores.2008.02.001.

Kang, C.W., S.P. Quan, and J. Lou (2010), Numerical study of a Taylor bubble rising in stagnant liquids, *Phys. Rev.*, 81, 066308.

Landi, P., N. Métrich, A. Bertagnini, and M. Rosi (2004), Dynamics of magma mixing and degassing recorded in plagioclase at Stromboli (Aeolian Archipelago, Italy), *Contrib. Mineral. Petrol.*, 147 (2), 213–227, doi:10.1007/s00410-004-0555-5.

Landi, P., E. Marchetti, S. La Felice, M. Ripepe, and M. Rosi (2011), Integrated petrochemical and geophysical data reveals thermal distribution of the feeding conduits at Stromboli volcano, Italy, *Geophys. Res. Lett.*, 38, L08305, doi:10.1029/2010GL046296.

Lautze, N.C., and B.F. Houghton (2005), Physical mingling of magma and complex eruption dynamics in the shallow conduit at Stromboli volcano, Italy, *Geology*, 33 (5), 425–428, doi:10.1130/G21325.1.

Lautze, N.C., and B.F. Houghton (2007), Linking variable explosion style and magma textures during 2002 at Stromboli volcano, Italy, *Bull. Volcanol.*, 69, 445-460, doi:10.1007/s00445-006-0086-1.

Llewellin, E.W., H.M. Mader, and S.D.R. Wilson (2002), The constitutive equation and flow dynamics of bubbly magmas, *Geophys. Res. Lett.*, 29 (24), 2170, doi: 10.1029/2002GL015697.

Llewellin, E. W., S. A. Mathias, E. Del Bello, S. J. Lane, J. Taddeucci, and M. R. James (2010), Gas slug rise in open versus plugged basaltic conduits and the transition from Strombolian activity to sustained eruption, paper presented at EGU General Assembly, Vienna (Austria).

Llewellin, E. W., E. Del Bello, J. Taddeucci, P. Scarlato, and S. J. Lane (2011), The thickness of the falling film of liquid around a Taylor bubble, *Proc. R. Soc. A*, doi:10.1098/rspa.2011.0476.

McGetchin, T.R., and B.A. Chouet (1979), Energy budget of the volcano Stromboli, Italy, *Geophys. Res. Lett.,* 6 (4), 317-320.

McGreger, A. D., and J. M. Lees (2004), Vent discrimination at Stromboli Volcano, Italy, *J Volcanol Geoth Res*, 137(1-3), 169-185.

Métrich, N., A. Bertagnini, P. Landi, and M. Rosi (2001), Crystallization driven by decompression and water loss at Stromboli volcano (Aeolian Islands, Italy), *J. Petrol.*, 42 (8), 1471–1490.

Métrich, N., A. Bertagnini, and A. Di Muro (2010), Conditions of magma storage, degassing and ascent at Stromboli: new insights into the volcano plumbing system with inferences on the eruptive dynamics, *J. Petrol.*, 51 (3), 603-626, doi: 10.1093/petrology/egp083.

Misiti, V., F. Vetere, A. Mangiacapra, H. Behrens, A. Cavallo, P. Scarlato, and D. B. Dingwell (2009), Viscosity of high-K basalt from the 5th April 2003 Stromboli paroxysmal explosion, *Chem. Geol.*, 260 (3-4), 278-285, doi: 10.1016/j.chemgeo.2008.12.023.

Mori, T., and M. Burton (2009), Quantification of the gas mass emitted during single explosions on Stromboli with the SO_2 imaging camera, *J. Volcanol. Geotherm. Res*., 188 (4), 395-400, doi: 10.1016/j.jvolgeores.2009.10.005.

Mueller, S., E.W. Llewellin, and H.M. Mader (2010), The rheology of suspensions of solid particles, *Proc. Royal Soc.*, A 466 (2116), 1201-1228, doi: 10.1098/rspa.2009.0445.

Mueller, S., E.W. Llewellin, and H.M. Mader (2011), The effect of particle shape on suspension viscosity and implications for magmatic flows, *Geophys. Res. Lett.*, 38, L13316, doi:10.1029/2011GL047167.

Murase, T., and A.R. McBirney (1973), Properties of some common igneous rocks and their melts at high temperatures, *Geol. Soc. Am. Bull.*, 84, 3563-3592.

Namiki, A., and M. Manga (2008), Transition between fragmentation and permeable outgassing of low viscosity magmas, *J. Volcanol. Geotherm. Res.*, 169 (1-2), 48-60, doi: 10.1016/j.jvolgeores.2007.07.020.

Nogueira, S., M.L. Rietmuler, J.B.L.M. Campos, and A.M.F.R. Pinto (2006), Flow in the nose region and annular film around a Taylor bubble rising through vertical

columns of stagnant and flowing Newtonian liquids, *Chem. Engine. Sci*., 61(2), 845 – 857, doi: 10.1016/j.ces.2005.07.038.

O'Brien, G.S., and C.J. Bean (2008), Seismicity on volcanoes generated by gas slug ascent, *Geophys. Res. Lett.*, 35 (7), L16308, doi:10.1029/2008GL035001.

Parfitt, E. A. (2004), A discussion of the mechanisms of explosive basaltic eruptions, *J. Volcanol. Geotherm. Res.*, 134 (1-2), 77-107, doi: 10.1016/j.jvolgeores.2004.01.002.

Parfitt, E.A., and L. Wilson (1995), Explosive volcanic-eruptions, 9: the transition between Hawaiian-style lava fountaining and Strombolian explosive activity, *Geophys. J. Int*., 121 (1) 226-232.

Patrick, M.R., A. Harris, M. Ripepe, J. Dehn, D.A. Rothery, and S. Calvari (2007), Strombolian explosive styles and source conditions: insights from thermal (FLIR) video, *Bull. Volcanol.*, 69, 769-784, doi:101007/s00445-006-0107-0.

Pino, N.A., R. Moretti, P. Allard, and E. Boschi (2011), Seismic precursors of a basaltic paroxysmal explosion track deep gas accumulation and slug upraise, *J. Geophys. Res.*, 116, B02312, doi: 10.1029/2009JB000826.

Polacci, M., D.R. Baker, L. Mancini, S. Favretto, and R.J. Hill (2009), Vesiculation in magmas from Stromboli and implications for normal Strombolian activity and paroxysmal explosions in basaltic systems, *J. Geophys. Res*., 114, B01206, doi:10.1029/2008JB005672.

Ripepe, M., and E. Gordeev (1999), Gas bubble dynamics model for shallow volcanic tremor at Stromboli, *J. Geophys. Res.*, 104 (B5), 10639-10654.

Ripepe, M., and A.J.L. Harris (2008), Dynamics of the 5 April 2003 explosive paroxysm observed at Stromboli by a near-vent thermal, seismic and infrasonic array, *Geophys. Res. Lett.*, 35 (7), L07306, doi: 10.1029/2007GL032533.

Ripepe, M., and E. Marchetti (2002), Array tracking of infrasonic sources at Stromboli volcano, *Geophys. Res. Lett*., 29(22), 2076, doi: 10.1029/2002GL015452.

Ripepe, M., A.J.L. Harris, and R. Carniel (2002), Thermal, seismic and infrasonic evidences of variable degassing rates at Stromboli volcano, *J. Volcanol. Geotherm. Res*., 118 (3-4), 285-297.

Rosi, M., A. Bertagnini, and P. Landi (2000), Onset of the persistent activity at Stromboli Volcano (Italy), *Bull. Volcanol*., 62 (4-5), 294-300.

Rosi, M., A. Bertagnini, A.J.L. Harris, L. Pioli, M. Pistolesi, and M. Ripepe (2006), A case history of paroxysmal explosion at Stromboli: timing and dynamics of the April 5, 2003 event, *Earth Planet. Sci. Lett.*, 243 (3-4), 594-606, doi: 10.1016/j.epsl.2006.01.035.

Sawyer, G.M., S.A. Carn, V.I. Tsanev, C. Oppenheimer, and M. Burton (2008), Investigation into magma degassing at Nyiragongo volcano, Democratic Republic of the Congo, *Geochem. Geophys. Geosyst.*, 9, Q02017, doi: 10.1029/2007GC001829.

Self, S., L. Wilson, and I.A. Nairn (1979), Vulcanian eruption mechanisms, *Nature*, 277 (5696), 440-443.

Seyfried, R., and A. Freundt (2000), Experiments on conduit flow and eruption behavior of basaltic volcanic eruptions, *J. Geophys. Res.*, 105 (B10), 23727–23740.

Stein D.J., and F.J. Spera (2002), Shear viscosity of rhyolite-vapor emulsions at magmatic temperatures by concentric cylinder rheometry, *J. Volcanol. Geotherm. Res.*, 113 (1-2), 243-258.

Taddeucci, J., M. Pompilio, and P. Scarlato (2004a), Conduit processes during the July-August 2001 explosive activity of Mt. Etna (Italy): Inferences from glass chemistry and crystal size distribution of ash particles, *J. Volcanol. Geotherm. Res.*, 137 (1-3), 33–54, doi: 10.1016/j.jvolgeores.2004.05.011.

Taddeucci, J., O. Spieler, B. Kennedy, M. Pompilio, D.B. Dingwell, and P. Scarlato (2004b), Experimental and analytical modeling of basaltic ash explosions at Mount Etna, Italy, 2001, *J Geophys. Res.*, 109 (B8), B08203, doi: 10.1029/2003JB002952.

Taddeucci J., P. Scarlato, A. Capponi, E. Del Bello, C. Cimarelli, D. Palladino, U. Kueppers, High-speed imaging of Strombolian explosions: the ejection velocity of pyroclasts, Geophysical Research Letters, in press.

Valentine, G.A., D. Krier, F.V. Perry, and G. Heiken (2005), Scoria cone construction mechanisms, Lathrop Wells volcano, southern Nevada, USA, *Geology*, 33 (8), 629–632, doi: 10.1130/G21459.1.

Vergniolle, S., and G. Brandeis (1994), Origin of the sound generated by Strombolian explosions, *Geophys. Res. Lett.*, 21 (18), 1959-1962.

Vergniolle, S., and G. Brandeis (1996), Strombolian explosions .1. A large bubble breaking at the surface of a lava column as a source of sound, *J. Geophys. Res.*, 101 (B9), 20433-20447.

Vergniolle, S., and C. Jaupart (1986), Separated 2-phase flow and basaltic eruptions, *J. Geophys. Res.*, 91 (B1), 2842-2860.

Vergniolle, S., and M. Ripepe (2008), From Strombolian explosions to fire fountains at Etna Volcano (Italy): what do we learn from acoustic measurements? In: Lane, S. J. and Gilbert, J. S. (eds) *Fluid Motions in Volcanic Conduits: A Source of Seismic and Acoustic Signals*, Geological Society, London, Special Publications, 307, 103–124.

Vergniolle, S., G. Brandeis, and J.C. Mareschal (1996), Strombolian explosions .2. Eruption dynamics determined from acoustic measurements, *J. Geophys. Res.*, 101 (B9), 20449-20466.

Vergniolle, S., M. Boichu, and J. Caplan-Auerbach (2004), Acoustic measurements of the 1999 basaltic eruption of Shishaldin volcano, Alaska - 1. Origin of Strombolian activity, *J. Volcanol. Geotherm. Res.* 137 (1-3), 109-134, doi: 10.1016/j.jvolgeores.2004.05.003.

Viana, F., R. Pardo, R. Yanez, J. Trallero, D. Joseph (2003), Universal correlation for the rise velocity of long gas bubbles in round pipes, *J. Fluid Mech.*, 494, 379-398.

Vidal, V., M. Ripepe, T. Divoux, D. Legrand, J.C. Geminard, and F. Melo (2010), Dynamics of soap bubble bursting and its implications to volcano acoustics, *Geophys. Res. Let.*, 37, L07302, doi: 10.1029/2009GL042360.

Vona, A., C. Romano, D.B. Dingwell, D. Giordano (2011), The rheology of crystal-bearing basaltic magmas from Stromboli and Etna, *Geochim. Cosmochim Acta*, 75, 3214–3236, doi:10.1016/j.gca.2011.03.031.

Wallis, G. B. (1969), *One-Dimensional Two-Phase Flow*. McGraw-Hill, New York.

Wilson, L. (1980), Relationships between pressure, volatile content and ejecta velocity, *J. Volcanol. Geotherm Res.*, 8, 297–313.

Woodward, R. P. (2008), Surface tension measurements using the drop shape method. First Ten Angstroms, Pdf available on line at http://www.firsttenangstroms.com/pdfdocs/STPaper.pdf.

7. Appendices

A. Viscosity measurements (section 2)

TAP WATER				SOAP				SEED OIL				33% DILUTED SOAP				25% DILUTED SOAP			
Meas. Pts.	Viscosity [Pa·s]	Shear Rate [1/s]	Shear Stress [Pa]	Meas. Pts.	Viscosity [Pa·s]	Shear Rate [1/s]	Shear Stress [Pa]	Meas. Pts.	Viscosity [Pa·s]	Shear Rate [1/s]	Shear Stress [Pa]	Meas. Pts.	Viscosity [Pa·s]	Shear Rate [1/s]	Shear Stress [Pa]	Meas. Pts.	Viscosity [Pa·s]	Shear Rate [1/s]	Shear Stress [Pa]
2	0.00093	1.18	0.0011	2	0.330	1.02	0.336	2	0.0434	1.02	0.0443	2	0.0137	1.02	0.014	2	0.171	1.02	0.174
3	0.00101	1.39	0.00139	3	0.326	2.04	0.665	3	0.0445	2.04	0.0909	3	0.0144	2.04	0.0293	3	0.168	2.04	0.342
4	0.00103	1.63	0.00168	4	0.324	3.06	0.992	4	0.0456	3.06	0.14	4	0.015	3.06	0.046	4	0.165	3.06	0.504
5	0.00106	1.92	0.00203	5	0.321	4.08	1.31	5	0.0451	4.08	0.184	5	0.0142	4.08	0.0579	5	0.163	4.08	0.664
6	0.00112	2.26	0.00254	6	0.319	5.1	1.63	6	0.0434	5.1	0.221	6	0.0122	5.1	0.0621	6	0.162	5.1	0.825
7	0.00100	2.66	0.00266	7	0.318	6.12	1.95	7	0.0421	6.12	0.258	7	0.0112	6.12	0.0688	7	0.163	6.12	0.998
8	0.00094	3.13	0.00295	8	0.320	7.14	2.28	8	0.0433	7.14	0.309	8	0.0127	7.14	0.0908	8	0.164	7.14	1.17
9	0.00094	3.68	0.00347	9	0.318	8.16	2.6	9	0.044	8.16	0.359	9	0.0133	8.16	0.108	9	0.163	8.16	1.33
10	0.00092	4.34	0.00398	10	0.317	9.18	2.91	10	0.0425	9.18	0.39	10	0.0117	9.18	0.108	10	0.162	9.18	1.49
11	0.00101	5.1	0.00517	11	0.317	10.2	3.24	11	0.0433	10.2	0.442	11	0.0128	10.2	0.131	11	0.163	10.2	1.67
12	0.00112	6.01	0.00672	12	0.315	11.2	3.54	12	0.0431	11.2	0.484	12	0.0124	11.2	0.139	12	0.162	11.2	1.82
13	0.00103	7.07	0.0073	13	0.316	12.2	3.86	13	0.0429	12.2	0.525	13	0.0124	12.2	0.152	13	0.163	12.2	1.99
14	0.00091	8.32	0.00754	14	0.314	13.3	4.17	14	0.0431	13.3	0.572	14	0.0125	13.3	0.166	14	0.162	13.3	2.14
15	0.00108	9.8	0.0106	15	0.314	14.3	4.49	15	0.043	14.3	0.614	15	0.0126	14.3	0.179	15	0.162	14.3	2.32
16	0.00094	11.5	0.0108	16	0.313	15.3	4.79	16	0.0427	15.3	0.654	16	0.0122	15.3	0.186	16	0.161	15.3	2.47
17	0.00107	13.6	0.0146	17	0.313	16.3	5.11	17	0.0433	16.3	0.706	17	0.0128	16.3	0.209	17	0.161	16.3	2.64
18	0.00087	16	0.0138	18	0.312	17.3	5.41	18	0.0427	17.3	0.741	18	0.0123	17.3	0.213	18	0.161	17.3	2.8
19	0.00113	18.8	0.0212	19	0.311	18.4	5.71	19	0.0427	18.4	0.784	19	0.0122	18.4	0.224	19	0.16	18.4	2.95
20	0.00119	22.1	0.0263	20	0.310	19.4	6.02	20	0.0431	19.4	0.835	20	0.0126	19.4	0.245	20	0.16	19.4	3.11
21	0.00119	26	0.031	21	0.310	20.4	6.32	21	0.043	20.4	0.878	21	0.0127	20.4	0.258	21	0.16	20.4	3.27
22	0.00120	30.7	0.0368	22	0.309	21.4	6.62	22	0.0428	21.4	0.916	22	0.0124	21.4	0.266	22	0.16	21.4	3.43
23	0.00093	36.1	0.0336	23	0.308	22.4	6.92	23	0.0426	22.4	0.956	23	0.0122	22.4	0.275	23	0.159	22.4	3.58
24	0.00116	42.5	0.0493	24	0.307	23.5	7.21	24	0.0425	23.5	0.998	24	0.0122	23.5	0.286	24	0.159	23.5	3.73
25	0.00109	50	0.0543	25	0.307	24.5	7.51	25	0.0425	24.5	1.04	25	0.0122	24.5	0.299	25	0.158	24.5	3.88

A. Viscosity measurements (section 2)

1	0.00108	50	0.0538	26	0.306	25.5	7.81	26	0.0425	25.5	1.08	26	0.0122	25.5	0.312	26	0.158	25.5	4.03
2	0.00096	42.5	0.0407	27	0.305	26.5	8.1	27	0.0425	26.5	1.13	27	0.0122	26.5	0.324	27	0.158	26.5	4.19
3	0.00118	36.1	0.0426	28	0.305	27.6	8.4	28	0.0425	27.6	1.17	28	0.0122	27.6	0.337	28	0.157	27.6	4.34
4	0.00109	30.7	0.0335	29	0.304	28.6	8.7	29	0.0425	28.6	1.22	29	0.0123	28.6	0.352	29	0.157	28.6	4.49
5	0.00102	26	0.0267	30	0.304	29.6	8.99	30	0.0426	29.6	1.26	30	0.0125	29.6	0.369	30	0.157	29.6	4.64
6	0.00113	22.1	0.025	31	0.303	30.6	9.28	31	0.0428	30.6	1.31	31	0.0126	30.6	0.385	31	0.156	30.6	4.78
7	0.00113	18.8	0.0213	32	0.302	31.6	9.57	32	0.0427	31.6	1.35	32	0.0125	31.6	0.394	32	0.156	31.6	4.93
8	0.00086	16	0.0137	33	0.302	32.7	9.86	33	0.0424	32.7	1.39	33	0.0123	32.7	0.4	33	0.155	32.7	5.07
9	0.00111	13.6	0.015	34	0.301	33.7	10.2	34	0.0425	33.7	1.43	34	0.0124	33.7	0.418	34	0.155	33.7	5.22
10	0.00087	11.5	0.00999	35	0.301	34.7	10.4	35	0.0427	34.7	1.48	35	0.0125	34.7	0.434	35	0.155	34.7	5.36
11	0.00108	9.8	0.0106	36	0.300	35.7	10.7	36	0.0424	35.7	1.51	36	0.0123	35.7	0.438	36	0.154	35.7	5.5
12	0.00096	8.32	0.00801	37	0.300	36.7	11	37	0.0426	36.7	1.56	37	0.0125	36.7	0.459	37	0.154	36.7	5.65
13	0.00088	7.07	0.00625	38	0.299	37.8	11.3	38	0.0424	37.8	1.6	38	0.0123	37.8	0.466	38	0.153	37.8	5.79
14	0.00100	6.01	0.00603	39	0.299	38.8	11.6	39	0.0425	38.8	1.65	39	0.0125	38.8	0.483	39	0.153	38.8	5.93
15	0.00105	5.1	0.00536	40	0.298	39.8	11.9	40	0.0424	39.8	1.69	40	0.0123	39.8	0.49	40	0.152	39.8	6.07
16	0.00099	4.34	0.00428	41	0.297	40.8	12.1	41	0.0425	40.8	1.74	41	0.0125	40.8	0.51	41	0.152	40.8	6.21
17	0.00099	3.68	0.00364	42	0.297	41.8	12.4	42	0.0423	41.8	1.77	42	0.0123	41.8	0.515	42	0.152	41.8	6.35
18	0.00089	3.13	0.0028	43	0.296	42.9	12.7	43	0.0425	42.9	1.82	43	0.0124	42.9	0.532	43	0.151	42.9	6.48
19	0.00087	2.66	0.00232	44	0.296	43.9	13	44	0.0425	43.9	1.86	44	0.0125	43.9	0.547	44	0.151	43.9	6.62
20	0.00102	2.26	0.00231	45	0.295	44.9	13.2	45	0.0423	44.9	1.9	45	0.0123	44.9	0.554	45	0.15	44.9	6.76
21	0.00097	1.92	0.00186	46	0.294	45.9	13.5	46	0.0424	45.9	1.94	46	0.0124	45.9	0.567	46	0.15	45.9	6.89
22	0.00098	1.63	0.00159	47	0.294	46.9	13.8	47	0.0424	46.9	1.99	47	0.0124	46.9	0.583	47	0.15	46.9	7.02
23	0.00113	1.39	0.00156	48	0.293	48	14.1	48	0.0424	48	2.03	48	0.0124	48	0.596	48	0.149	48	7.16
24	0.00116	1.18	0.00137	49	0.293	49	14.3	49	0.0424	49	2.08	49	0.0124	49	0.608	49	0.149	49	7.29
25	0.00105	1	0.00105	50	0.292	50	14.6	50	0.0424	50	2.12	50	0.0124	50	0.62	50	0.148	50	7.42
				1	0.292	50	14.6	1	0.0423	50	2.12	1	0.0124	50	0.62	1	0.149	50	7.42
				2	0.293	49	14.3	2	0.0423	49	2.07	2	0.0124	49	0.606	2	0.149	49	7.3

A. Viscosity measurements (section 2)

3	0.293	47.9	14	3	0.0423	47.9	2.03	3	0.0123	47.9	0.592	3	0.15	47.9	7.17
4	0.293	46.9	13.8	4	0.0423	46.9	1.98	4	0.0123	46.9	0.579	4	0.15	46.9	7.05
5	0.293	45.9	13.5	5	0.0423	45.9	1.94	5	0.0124	45.9	0.569	5	0.151	45.9	6.92
6	0.294	44.9	13.2	6	0.0423	44.9	1.9	6	0.0124	44.9	0.558	6	0.151	44.9	6.79
7	0.294	43.9	12.9	7	0.0422	43.9	1.85	7	0.0123	43.9	0.54	7	0.152	43.9	6.66
8	0.294	42.9	12.6	8	0.0422	42.9	1.81	8	0.0124	42.9	0.529	8	0.152	42.9	6.53
9	0.295	41.8	12.3	9	0.0423	41.8	1.77	9	0.0124	41.8	0.521	9	0.153	41.8	6.4
10	0.295	40.8	12	10	0.0421	40.8	1.72	10	0.0123	40.8	0.5	10	0.154	40.8	6.27
11	0.295	39.8	11.7	11	0.0423	39.8	1.68	11	0.0125	39.8	0.496	11	0.154	39.8	6.14
12	0.295	38.8	11.4	12	0.0421	38.8	1.63	12	0.0122	38.8	0.475	12	0.155	38.8	6
13	0.296	37.8	11.2	13	0.0423	37.8	1.6	13	0.0125	37.8	0.471	13	0.155	37.8	5.87
14	0.296	36.7	10.9	14	0.0421	36.7	1.55	14	0.0122	36.7	0.449	14	0.156	36.7	5.73
15	0.296	35.7	10.6	15	0.0422	35.7	1.51	15	0.0124	35.7	0.443	15	0.157	35.7	5.6
16	0.296	34.7	10.3	16	0.0422	34.7	1.47	16	0.0124	34.7	0.431	16	0.157	34.7	5.45
17	0.296	33.7	9.98	17	0.042	33.7	1.41	17	0.0122	33.7	0.41	17	0.158	33.7	5.31
18	0.297	32.7	9.69	18	0.0421	32.7	1.38	18	0.0123	32.7	0.402	18	0.159	32.7	5.18
19	0.297	31.6	9.39	19	0.0423	31.6	1.34	19	0.0125	31.6	0.395	19	0.159	31.6	5.03
20	0.297	30.6	9.09	20	0.0422	30.6	1.29	20	0.0124	30.6	0.38	20	0.16	30.6	4.89
21	0.297	29.6	8.79	21	0.0421	29.6	1.25	21	0.0123	29.6	0.363	21	0.16	29.6	4.74
22	0.297	28.6	8.49	22	0.042	28.6	1.2	22	0.0122	28.6	0.348	22	0.161	28.6	4.59
23	0.297	27.6	8.19	23	0.0419	27.6	1.16	23	0.0121	27.6	0.334	23	0.161	27.6	4.45
24	0.298	26.5	7.9	24	0.0419	26.5	1.11	24	0.0121	26.5	0.322	24	0.162	26.5	4.3
25	0.298	25.5	7.6	25	0.0419	25.5	1.07	25	0.0121	25.5	0.309	25	0.163	25.5	4.15
26	0.298	24.5	7.3	26	0.0419	24.5	1.03	26	0.0121	24.5	0.297	26	0.163	24.5	4
27	0.298	23.5	6.99	27	0.042	23.5	0.985	27	0.0122	23.5	0.286	27	0.164	23.5	3.84
28	0.298	22.4	6.7	28	0.0422	22.4	0.946	28	0.0124	22.4	0.278	28	0.164	22.4	3.69
29	0.299	21.4	6.4	29	0.0423	21.4	0.907	29	0.0126	21.4	0.27	29	0.165	21.4	3.54

A. Viscosity measurements (section 2)

		30	0.299	20.4	6.1	30	0.0422	20.4	0.86	30	0.0124	20.4	0.254	30	0.166	20.4	3.39		
		31	0.299	19.4	5.79	31	0.0418	19.4	0.81	31	0.012	19.4	0.233	31	0.166	19.4	3.23		
		32	0.299	18.4	5.49	32	0.042	18.4	0.772	32	0.0122	18.4	0.225	32	0.166	18.4	3.06		
		33	0.299	17.3	5.19	33	0.0423	17.3	0.734	33	0.0127	17.3	0.219	33	0.167	17.3	2.91		
		34	0.299	16.3	4.88	34	0.0417	16.3	0.681	34	0.012	16.3	0.196	34	0.168	16.3	2.74		
		35	0.299	15.3	4.58	35	0.0422	15.3	0.646	35	0.0125	15.3	0.191	35	0.168	15.3	2.57		
		36	0.300	14.3	4.28	36	0.042	14.3	0.6	36	0.0123	14.3	0.176	36	0.169	14.3	2.42		
		37	0.299	13.3	3.97	37	0.0421	13.3	0.558	37	0.0122	13.3	0.162	37	0.169	13.3	2.24		
		38	0.300	12.2	3.67	38	0.0419	12.2	0.513	38	0.0123	12.2	0.15	38	0.17	12.2	2.09		
		39	0.299	11.2	3.36	39	0.0424	11.2	0.475	39	0.0126	11.2	0.141	39	0.17	11.2	1.91		
		40	0.299	10.2	3.05	40	0.0414	10.2	0.423	40	0.0117	10.2	0.119	40	0.171	10.2	1.74		
		41	0.300	9.18	2.76	41	0.0426	9.18	0.392	41	0.0131	9.18	0.12	41	0.172	9.18	1.58		
		42	0.299	8.16	2.44	42	0.0421	8.16	0.344	42	0.0122	8.16	0.0997	42	0.171	8.16	1.39		
		43	0.299	7.14	2.14	43	0.0411	7.14	0.293	43	0.0113	7.14	0.0806	43	0.172	7.14	1.23		
		44	0.301	6.12	1.84	44	0.0421	6.12	0.258	44	0.0126	6.12	0.0773	44	0.174	6.12	1.06		
		45	0.301	5.1	1.53	45	0.0434	5.1	0.221	45	0.0138	5.1	0.0704	45	0.173	5.1	0.884		
		46	0.299	4.08	1.22	46	0.0432	4.08	0.176	46	0.0132	4.08	0.0539	46	0.172	4.08	0.701		
		47	0.297	3.06	0.91	47	0.042	3.06	0.129	47	0.0115	3.06	0.0353	47	0.171	3.06	0.522		
		48	0.295	2.04	0.603	48	0.0399	2.04	0.0815	48	0.00967	2.04	0.0197	48	0.17	2.04	0.348		
		49	0.292	1.02	0.298	49	0.037	1.02	0.0377	49	0.00551	1.02	0.00562	49	0.168	1.02	0.171		
stdv	0.0001	stdv	0.009			stdv	0.0009			stdv	0.0009			stdv	0.007				
% error	9.50997		2.871				2.092				7.4083				4.3294				
max	0.0012	max	0.33			max	0.0456			max	0.015			max	0.174				
min	0.00087	min	0.292			min	0.037			min	0.0055			min	0.148				
mean	0.00103	media	0.302			media	0.0424			media	0.0123			media	0.1598				

A. Viscosity measurements (section 2)

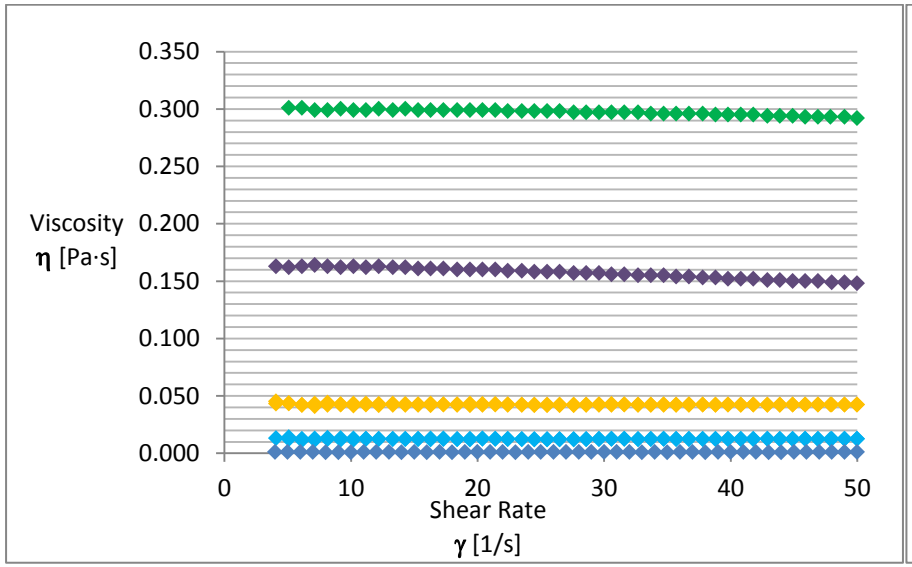

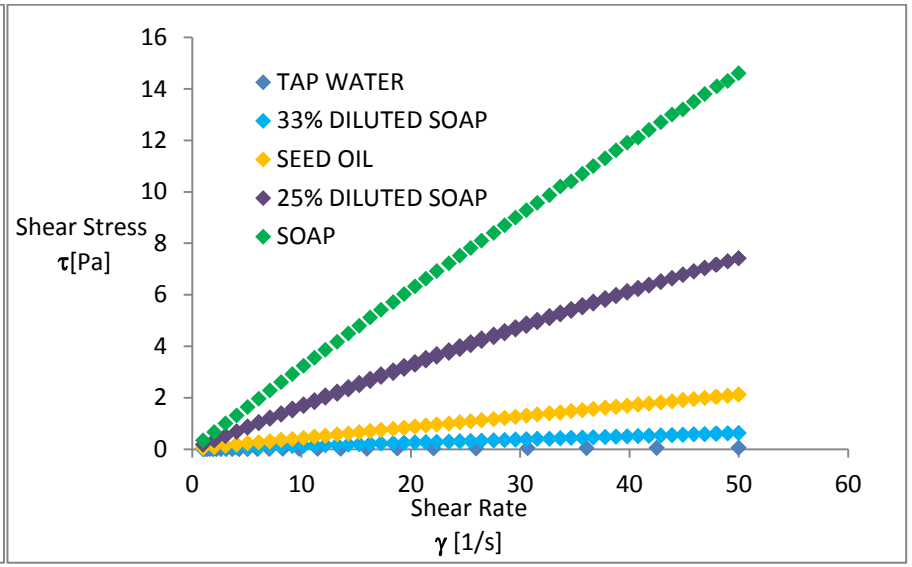

B. Experimental data (section 2)

Lo (m)	x1 (m)	x2 (m)	frame1	Frame2	V (m/s)	L slug	xi	yi	xi^2	yi^2	xi*yi	xi-xb	yi-yb	(xi-xb)^2	(yi-yb)^2	(xi-xb)(yi-yb)	fi	(yi-fi)^2	Linear regression	
0.307	0.2987	0.667	90	126	0.3072	0.3694	0.307	0.369	0.094	0.136	0.113	0.147	0.168	0.0215	0.0282	0.0246	0.3770	5.708E-05	A	1.1970
0.287	0.255	0.65	49	88	0.3042	0.3560	0.287	0.356	0.082	0.127	0.102	0.127	0.154	0.0160	0.0238	0.0195	0.3530	8.916E-06	q	0.0095
0.267	0.316	0.642	1	33	0.3059	0.3310	0.267	0.331	0.071	0.110	0.088	0.107	0.129	0.0113	0.0167	0.0138	0.3291	3.713E-06	R^2	0.9986
0.246	0.028	0.641	46	106	0.3068	0.3040	0.246	0.304	0.061	0.092	0.075	0.086	0.102	0.0073	0.0105	0.0088	0.3039	4.221E-09		
0.230	0.095	0.629	9	62	0.3026	0.2790	0.230	0.279	0.053	0.078	0.064	0.070	0.077	0.0048	0.0060	0.0054	0.2848	3.343E-05	Error analysis	
0.210	0.135	0.631	11	60	0.3040	0.2610	0.210	0.261	0.044	0.068	0.055	0.050	0.059	0.0025	0.0035	0.0029	0.2608	2.518E-08	n	16.0000
0.190	0.13	0.646	1	52	0.3038	0.2370	0.190	0.237	0.036	0.056	0.045	0.030	0.035	0.0009	0.0013	0.0010	0.2369	9.922E-09	A	1.1970
0.171	0.037	0.623	8	66	0.3034	0.2170	0.171	0.217	0.029	0.047	0.037	0.011	0.015	0.0001	0.0002	0.0002	0.2142	8.086E-06	σA	0.0073
0.150	0.333	0.638	1	31	0.3053	0.1950	0.150	0.195	0.023	0.038	0.029	-0.011	-0.007	0.0001	0.0000	0.0001	0.1890	3.578E-05	conf. level (%)	95.0000
0.133	0.096	0.603	11	61	0.3045	0.1740	0.133	0.174	0.018	0.030	0.023	-0.028	-0.028	0.0008	0.0008	0.0008	0.1687	2.842E-05	t value	1.7613
0.112	0.083	0.643	10	65	0.3058	0.1490	0.112	0.149	0.013	0.022	0.017	-0.049	-0.053	0.0024	0.0028	0.0026	0.1435	2.991E-05	ΔA	0.0128
0.092	0.041	0.348	57	87	0.3073	0.1200	0.092	0.120	0.008	0.014	0.011	-0.069	-0.082	0.0047	0.0067	0.0056	0.1196	1.683E-07		
0.072	0.036	0.35	14	45	0.3042	0.0930	0.072	0.093	0.005	0.009	0.007	-0.089	-0.109	0.0078	0.0118	0.0096	0.0956	7.016E-06	A'	0.1646
0.055	0.024	0.35	25	57	0.3059	0.0700	0.055	0.070	0.003	0.005	0.004	-0.106	-0.132	0.0111	0.0173	0.0139	0.0753	2.808E-05	ΔA'+	0.0089
0.033	0.045	0.352	63	93	0.3073	0.0490	0.033	0.049	0.001	0.002	0.002	-0.128	-0.153	0.0163	0.0233	0.0195	0.0490	1.297E-09	ΔA'-	0.0091
0.013	0.047	0.328	84	112	0.3014	0.021	0.013	0.021	0.000	0.000	0.000	-0.148	-0.181	0.0218	0.0326	0.0266	0.0250	1.618E-05		
sum							2.568	3.225	0.541	0.836	0.672			0.1293	0.1855	0.1547		2.568E-04	ΔA'+ (%)	5.3854
mean							0.161	0.202									0.2016		ΔA'- (%)	5.5022

Table B - 1. Water, 80 mm pipe.

B. Experimental data (section 2)

Lo (m)	x1 (m)	x2 (m)	frame1	Frame2	V (m/s)	L slug	xi	yi	xi^2	yi^2	xi*yi	xi-xb	yi-yb	(xi-xb)^2	(yi-yb)^2	(xi-xb)(yi-yb)	fi	(yi-fi)^2	Linear regression	
0.307	0.2987	0.667	90	126	0.3072	0.3694	0.307	0.369	0.094	0.136	0.113	0.147	0.168	0.0215	0.0282	0.0246	0.3770	5.708E-05	A	1.1970
0.287	0.255	0.65	49	88	0.3042	0.3560	0.287	0.356	0.082	0.127	0.102	0.127	0.154	0.0160	0.0238	0.0195	0.3530	8.916E-06	q	0.0095
0.267	0.316	0.642	1	33	0.3059	0.3310	0.267	0.331	0.071	0.110	0.088	0.107	0.129	0.0113	0.0167	0.0138	0.3291	3.713E-06	R^2	0.9986
0.246	0.028	0.641	46	106	0.3068	0.3040	0.246	0.304	0.061	0.092	0.075	0.086	0.102	0.0073	0.0105	0.0088	0.3039	4.221E-09		
0.230	0.095	0.629	9	62	0.3026	0.2790	0.230	0.279	0.053	0.078	0.064	0.070	0.077	0.0048	0.0060	0.0054	0.2848	3.343E-05	Error analysis	
0.210	0.135	0.631	11	60	0.3040	0.2610	0.210	0.261	0.044	0.068	0.055	0.050	0.059	0.0025	0.0035	0.0029	0.2608	2.518E-08	n	16.0000
0.190	0.13	0.646	1	52	0.3038	0.2370	0.190	0.237	0.036	0.056	0.045	0.030	0.035	0.0009	0.0013	0.0010	0.2369	9.922E-09	A	1.1970
0.171	0.037	0.623	8	66	0.3034	0.2170	0.171	0.217	0.029	0.047	0.037	0.011	0.015	0.0001	0.0002	0.0002	0.2142	8.086E-06	σA	0.0073
0.150	0.333	0.638	1	31	0.3053	0.1950	0.150	0.195	0.023	0.038	0.029	-0.011	-0.007	0.0001	0.0000	0.0001	0.1890	3.578E-05	conf. level (%)	95.0000
0.133	0.096	0.603	11	61	0.3045	0.1740	0.133	0.174	0.018	0.030	0.023	-0.028	-0.028	0.0008	0.0008	0.0008	0.1687	2.842E-05	t value	1.7613
0.112	0.083	0.643	10	65	0.3058	0.1490	0.112	0.149	0.013	0.022	0.017	-0.049	-0.053	0.0024	0.0028	0.0026	0.1435	2.991E-05	ΔA	0.0128
0.092	0.041	0.348	57	87	0.3073	0.1200	0.092	0.120	0.008	0.014	0.011	-0.069	-0.082	0.0047	0.0067	0.0056	0.1196	1.683E-07		
0.072	0.036	0.35	14	45	0.3042	0.0930	0.072	0.093	0.005	0.009	0.007	-0.089	-0.109	0.0078	0.0118	0.0096	0.0956	7.016E-06	A'	0.1646
0.055	0.024	0.35	25	57	0.3059	0.0700	0.055	0.070	0.003	0.005	0.004	-0.106	-0.132	0.0111	0.0173	0.0139	0.0753	2.808E-05	ΔA'+	0.0089
0.033	0.045	0.352	63	93	0.3073	0.0490	0.033	0.049	0.001	0.002	0.002	-0.128	-0.153	0.0163	0.0233	0.0195	0.0490	1.297E-09	ΔA'-	0.0091
0.013	0.047	0.328	84	112	0.3014	0.021	0.013	0.021	0.000	0.000	0.000	-0.148	-0.181	0.0218	0.0326	0.0266	0.0250	1.618E-05		
sum							2.568	3.225	0.541	0.836	0.672			0.1293	0.1855	0.1547		2.568E-04	ΔA'+ (%)	5.3854
mean							0.161	0.202									0.2016		ΔA'- (%)	5.5022

Table B - 2. Seed oil, 80 mm pipe.

B. Experimental data (section 2)

Lo (m)	x1 (m)	x2 (m)	frame1	Frame2	V (m/s)	L slug	xi	yi	xi^2	yi^2	xi*yi	xi-xb	yi-yb	(xi-xb)^2	(yi-yb)^2	(xi-xb)(yi-yb)	fi	(yi-fi)^2	Linear regression	
0.262	0.422	0.485	142	148	0.315315	0.372	0.262	0.372	0.069	0.138	0.097	0.107	0.149	0.011	0.022	0.016	0.373	1.95E-06	A	1.4100
0.248	0.2498	0.438	120	138	0.313981	0.352	0.248	0.352	0.062	0.124	0.087	0.093	0.129	0.009	0.017	0.012	0.354	2.74E-06	q	0.0040
0.227	0.208	0.416	112	132	0.312312	0.329	0.227	0.329	0.052	0.108	0.075	0.072	0.106	0.005	0.011	0.008	0.324	2.46E-05	R^2	0.9997
0.203	0.254	0.378	123	135	0.31031	0.29	0.203	0.29	0.041	0.084	0.059	0.048	0.067	0.002	0.005	0.003	0.290	4.2E-08		
0.181	0.182	0.316	107	120	0.30954	0.259	0.181	0.259	0.033	0.067	0.047	0.026	0.036	0.001	0.001	0.001	0.259	3.41E-08	Error analysis	
0.152	0.034	0.231	64	83	0.311364	0.218	0.152	0.218	0.023	0.048	0.033	-0.003	-0.005	0.000	0.000	0.000	0.218	8.67E-08	n	11.0000
0.133	0.02	0.22	90	109	0.316106	0.189	0.133	0.189	0.018	0.036	0.025	-0.022	-0.034	0.000	0.001	0.001	0.192	6.27E-06	A	1.4100
0.112	0.037	0.31	92	118	0.315315	0.162	0.112	0.162	0.013	0.026	0.018	-0.043	-0.061	0.002	0.004	0.003	0.162	1.12E-08	σA	0.0087
0.087	0.052	0.228	102	119	0.310899	0.128	0.087	0.128	0.008	0.016	0.011	-0.068	-0.095	0.005	0.009	0.006	0.127	1.84E-06	conf. level (%)	95.0000
0.063	0.066	0.233	102	118	0.313438	0.092	0.063	0.092	0.004	0.008	0.006	-0.092	-0.131	0.009	0.017	0.012	0.093	6.46E-07	t value	1.8331
0.04	0.055	0.284	106	128	0.312585	0.061	0.04	0.061	0.002	0.004	0.002	-0.115	-0.162	0.013	0.026	0.019	0.060	3.92E-07	ΔA	0.0159
																			A'	0.2908
																			ΔA'+	0.0079
																			ΔA'-	0.0081
sum							1.708	2.452	0.322	0.660	0.461			0.057	0.113	0.080		3.86E-05	ΔA'+ (%)	2.7204
mean							0.155	0.223									0.223		ΔA'- (%)	2.7825

Table B - 3. 25% diluted soap, 80 mm pipe.

B. Experimental data (section 2)

Lo (m)	x1 (m)	x2 (m)	frame1	Frame2	V (m/s)	L slug	xi	yi	xi^2	yi^2	xi*yi	xi-xb	yi-yb	(xi-xb)^2	(yi-yb)^2	(xi-xb)(yi-yb)	fi	(yi-fi)^2	Linear regression	
0.255	0.041	0.741	18	92	0.2841	0.383	0.255	0.383	0.065	0.147	0.098	0.118	0.178	0.014	0.032	0.021	0.382	7.49E-07	A	1.5011
0.232	0.061	0.746	20	92	0.2857	0.351	0.232	0.351	0.054	0.123	0.081	0.095	0.146	0.009	0.021	0.014	0.348	1.15E-05	q	-0.0007
0.213	0.069	0.667	28	91	0.2850	0.32	0.213	0.32	0.045	0.102	0.068	0.076	0.115	0.006	0.013	0.009	0.319	8.34E-07	R^2	0.9991
0.194	0.033	0.407	125	165	0.2808	0.289	0.194	0.289	0.038	0.084	0.056	0.057	0.084	0.003	0.007	0.005	0.291	2.45E-06		
0.178	0.042	0.378	79	114	0.2883	0.263	0.178	0.263	0.032	0.069	0.047	0.041	0.058	0.002	0.003	0.002	0.267	1.26E-05	Error analysis	
0.156	0.049	0.359	70	103	0.2821	0.228	0.156	0.228	0.024	0.052	0.036	0.019	0.023	0.000	0.001	0.000	0.234	3.05E-05	n	13.0000
0.137	0.038	0.36	18	52	0.2844	0.208	0.137	0.208	0.019	0.043	0.028	0.000	0.003	0.000	0.000	0.000	0.205	9E-06	A	1.5011
0.121	0.044	0.37	32	66	0.2879	0.178	0.121	0.178	0.015	0.032	0.022	-0.016	-0.027	0.000	0.001	0.000	0.181	8.89E-06	σA	0.0136
0.099	0.033	0.379	13	49	0.2886	0.153	0.099	0.153	0.010	0.023	0.015	-0.038	-0.052	0.001	0.003	0.002	0.148	2.54E-05	conf. level (%)	95.0000
0.079	0.0249	0.266	91	116	0.2896	0.116	0.079	0.116	0.006	0.013	0.009	-0.058	-0.089	0.003	0.008	0.005	0.118	3.74E-06	t value	1.7959
0.057	0.025	0.252	25	49	0.2840	0.087	0.057	0.087	0.003	0.008	0.005	-0.080	-0.118	0.006	0.014	0.009	0.085	4.37E-06	ΔA	0.0245
0.037	0.035	0.275	59	84	0.2883	0.059	0.037	0.059	0.001	0.003	0.002	-0.100	-0.146	0.010	0.021	0.015	0.055	1.69E-05		
0.019	0.026	0.271	39	65	0.2830	0.024	0.019	0.024	0.000	0.001	0.000	-0.118	-0.181	0.014	0.033	0.021	0.028	1.49E-05	A'	0.3338
																			ΔA'+	0.0107
					0.286														ΔA'-	0.0110
sum							1.777	2.659	0.312	0.700	0.468			0.069	0.157	0.104		0.000142	ΔA'+ (%)	3.2025
mean							0.137	0.205									0.205		ΔA'- (%)	3.3088

Table B - 4. soap, 80 mm pipe.

B. Experimental data (section 2)

Lo (m)	x1 (m)	x2 (m)	frame1	Frame2	V (m/s)	L slug	xi	yi	xi^2	yi^2	xi*yi	xi-xb	yi-yb	(xi-xb)^2	(yi-yb)^2	(xi-xb)(yi-yb)	fi	(yi-fi)^2	Linear regression	
0.312	0.385	0.522	36	50	0.2935	0.375	0.312	0.375	0.0973	0.1406	0.1170	0.1188	0.1254	0.0141	0.0157	0.0149	0.3886	0.000185	A	1.1708
0.287	0.415	0.570	56	72	0.2905	0.356	0.287	0.356	0.0824	0.1267	0.1022	0.0937	0.1064	0.0088	0.0113	0.0100	0.3593	1.12E-05	q	0.0233
0.252	0.270	0.359	52	61	0.2962	0.333	0.252	0.333	0.0635	0.1109	0.0839	0.0588	0.0834	0.0035	0.0070	0.0049	0.3184	0.000214	R^2	0.9913
0.227	0.119	0.337	135	157	0.2972	0.297	0.227	0.297	0.0515	0.0882	0.0674	0.0338	0.0474	0.0011	0.0022	0.0016	0.2891	6.24E-05		
0.213	0.242	0.340	100	110	0.2925	0.28	0.213	0.28	0.0454	0.0784	0.0596	0.0198	0.0304	0.0004	0.0009	0.0006	0.2727	5.32E-05	Error analysis	
0.199	0.110	0.346	74	98	0.2960	0.259	0.199	0.259	0.0396	0.0671	0.0515	0.0057	0.0094	0.0000	0.0001	0.0001	0.2563	7.21E-06	n	12.0000
0.19	0.289	0.457	128	145	0.2963	0.237	0.19	0.237	0.0361	0.0562	0.0450	-0.0033	-0.0126	0.0000	0.0002	0.0000	0.2458	7.71E-05	A	1.1708
0.169	0.178	0.401	114	137	0.2915	0.219	0.169	0.219	0.0286	0.0480	0.0370	-0.0243	-0.0306	0.0006	0.0009	0.0007	0.2212	4.8E-06	σA	0.0347
0.15	0.135	0.426	105	135	0.2912	0.199	0.15	0.199	0.0225	0.0396	0.0299	-0.0433	-0.0506	0.0019	0.0026	0.0022	0.1989	2.97E-09	conf. level (%)	95.0000
0.127	0.177	0.381	115	136	0.2924	0.174	0.127	0.174	0.0161	0.0303	0.0221	-0.0663	-0.0756	0.0044	0.0057	0.0050	0.1720	3.93E-06	t value	1.8125
0.112	0.170	0.307	106	120	0.2938	0.153	0.112	0.153	0.0125	0.0234	0.0171	-0.0813	-0.0966	0.0066	0.0093	0.0078	0.1545	2.12E-06	ΔA	0.0628
0.081	0.099	0.271	98	116	0.2874	0.113	0.081	0.113	0.0066	0.0128	0.0092	-0.1123	-0.1366	0.0126	0.0187	0.0153	0.1182	2.66E-05		
																			A'	0.1459
																			ΔA'+	0.0435
																			ΔA'-	0.0484
sum							2.3190	2.9950	0.5021	0.8221	0.6420			0.0540	0.0746	0.0632		0.0006	ΔA'+ (%)	29.8068
mean							0.1933	0.2496									0.2496		ΔA'- (%)	33.1861

Table B - 5. 33% diluted soap, 80 mm pipe.

B. Experimental data (section 2)

Lo (m)	x1 (m)	x2 (m)	frame1	Frame2	V (m/s)	L slug	xi	yi	xi^2	yi^2	xi*yi	xi-xb	yi-yb	(xi-xb)^2	(yi-yb)^2	(xi-xb)(yi-yb)	fi	(yi-fi)^2	Linear regression	
0.244	0.024	0.297	15	53	0.2157	0.2902	0.2440	0.2902	0.0595	0.0842	0.0708	0.1202	0.1240	0.0145	0.0154	0.0149	0.305	0.000228	A	1.1571
0.223	0.053	0.291	1	34	0.2168	0.2857	0.2230	0.2857	0.0497	0.0816	0.0637	0.0992	0.1195	0.0098	0.0143	0.0119	0.281	2.2E-05	q	0.0230
0.203	0.025	0.293	8	45	0.2169	0.2653	0.2030	0.2653	0.0412	0.0704	0.0539	0.0792	0.0991	0.0063	0.0098	0.0079	0.258	5.53E-05	R^2	0.9962
0.183	0.025	0.301	22	60	0.2178	0.2371	0.1830	0.2371	0.0335	0.0562	0.0434	0.0592	0.0709	0.0035	0.0050	0.0042	0.235	5.66E-06		
0.164	0.047	0.279	1	33	0.2175	0.2171	0.1640	0.2171	0.0269	0.0471	0.0356	0.0402	0.0509	0.0016	0.0026	0.0020	0.213	1.9E-05	Error analysis	
0.145	0.044	0.292	1	36	0.2130	0.1908	0.1450	0.1908	0.0210	0.0364	0.0277	0.0212	0.0246	0.0005	0.0006	0.0005	0.191	2.42E-09	n	13.0000
0.127	0.018	0.173	40	62	0.2110	0.1662	0.1270	0.1662	0.0161	0.0276	0.0211	0.0032	0.0000	0.0000	0.0000	0.0000	0.170	1.39E-05	A	1.1571
0.105	0.019	0.180	30	52	0.2195	0.1472	0.1050	0.1472	0.0110	0.0217	0.0155	-0.0188	-0.0190	0.0004	0.0004	0.0004	0.144	7.47E-06	σA	0.0216
0.084	0.034	0.186	25	46	0.2168	0.1229	0.0840	0.1229	0.0071	0.0151	0.0103	-0.0398	-0.0433	0.0016	0.0019	0.0017	0.120	7.47E-06	conf. level (%)	95.0000
0.063	0.024	0.190	104	127	0.2160	0.0966	0.0630	0.0966	0.0040	0.0093	0.0061	-0.0608	-0.0696	0.0037	0.0048	0.0042	0.096	5.35E-07	t value	1.7959
0.043	0.026	0.184	58	80	0.2155	0.0706	0.0430	0.0706	0.0018	0.0050	0.0030	-0.0808	-0.0956	0.0065	0.0091	0.0077	0.073	4.52E-06	ΔA	0.0388
0.021	0.038	0.182	34	54	0.2162	0.0466	0.0210	0.0466	0.0004	0.0022	0.0010	-0.1028	-0.1196	0.0106	0.0143	0.0123	0.047	4.49E-07		
0.004	0.016	0.175	37	59	0.2166	0.0241	0.0040	0.0241	0.0000	0.0006	0.0001	-0.1198	-0.1421	0.0143	0.0202	0.0170	0.028	1.22E-05	A'	0.1358
																			ΔA'+	0.0281
																			ΔA'-	0.0300
sum							1.6090	2.1604	0.2724	0.4574	0.3521			0.0732	0.0984	0.0847		0.000	ΔA'+ (%)	20.6721
mean							0.1238	0.1662									0.166		ΔA'- (%)	22.1081

Table B - 6. Water, 40 mm pipe.

B. Experimental data (section 2)

Lo (m)	x1 (m)	x2 (m)	frame1	Frame2	V (m/s)	L slug	xi	yi	xi^2	yi^2	xi*yi	xi-xb	yi-yb	(xi-xb)^2	(yi-yb)^2	(xi-xb)(yi-yb)	fi	(yi-fi)^2	Linear regression	
0.238	0.032	0.353	115	157	0.2295	0.304	0.23	0.3102	0.0529	0.0962	0.0713	0.069	0.084	0.0048	0.0071	0.0058	0.3080	4.76E-06	A	1.1858
0.148	0.029	0.342	92	134	0.2238	0.233	0.21	0.2857	0.0441	0.0816	0.0600	0.049	0.0595	0.0024	0.0035	0.0029	0.2843	1.95E-06	q	0.0353
0.218	0.015	0.4	106	157	0.2267	0.294	0.194	0.2653	0.0376	0.0704	0.0515	0.033	0.0391	0.0011	0.0015	0.0013	0.2653	8.98E-10	R^2	0.9977
0.178	0.017	0.393	85	135	0.2258	0.281	0.173	0.2371	0.0299	0.0562	0.0410	0.012	0.0109	0.0001	0.0001	0.0001	0.2404	1.11E-05		
0.104	0.036	0.395	99	147	0.2246	0.156	0.154	0.2171	0.0237	0.0471	0.0334	-0.007	-0.0091	0.0000	0.0001	0.0001	0.2179	6.4E-07	Error analysis	
0.11	0.017	0.381	109	157	0.2277	0.167	0.135	0.1908	0.0182	0.0364	0.0258	-0.026	-0.0354	0.0007	0.0013	0.0009	0.1954	2.09E-05	n	8.0000
0.134	0.019	0.293	124	160	0.2286	0.195	0.107	0.1662	0.0114	0.0276	0.0178	-0.054	-0.06	0.0029	0.0036	0.0032	0.1622	1.62E-05	A	1.1858
0.075	0.033	0.298	83	118	0.2274	0.112	0.085	0.1372	0.0072	0.0188	0.0117	-0.076	-0.089	0.0058	0.0079	0.0068	0.1361	1.25E-06	σA	0.0231
0.04	0.02	0.297	118	155	0.2248	0.065													conf. level (%)	95.0000
																			t value	1.9432
																			ΔA	0.0448
																			A'	0.1567
																			ΔA'+	0.0307
																			ΔA'-	0.0331
sum							1.288	1.810	0.225	0.434	0.312			0.018	0.025	0.021		5.68E-05	ΔA'+ (%)	19.6023
mean							0.161	0.226									0.226		ΔA'- (%)	21.1420

Table B - 7. 33%diluted soap, 40 mm pipe.

B. Experimental data (section 2)

Lo (m)	x1 (m)	x2 (m)	frame1	Frame2	V (m/s)	L slug	xi	yi	xi^2	yi^2	xi*yi	xi-xb	yi-yb	(xi-xb)^2	(yi-yb)^2	(xi-xb)(yi-yb)	fi	(yi-fi)^2	Linear regression	
0.235	0.040	0.429	58	115	0.2047	0.3524	0.235	0.352	0.055	0.124	0.083	0.080	0.111	0.006	0.012	0.0089	0.3539	2.32E-06	A	1.4056
0.216	0.128	0.426	1	45	0.2040	0.3252	0.216	0.325	0.047	0.106	0.070	0.061	0.084	0.004	0.007	0.0052	0.3272	4.07E-06	q	0.0236
0.195	0.041	0.407	11	65	0.2032	0.2887	0.195	0.289	0.038	0.083	0.056	0.040	0.048	0.002	0.002	0.0019	0.2977	8.1E-05	R^2	0.9930
0.174	0.056	0.435	17	72	0.2068	0.2745	0.174	0.275	0.030	0.075	0.048	0.019	0.033	0.000	0.001	0.0006	0.2682	3.99E-05		
0.155	0.056	0.414	37	89	0.2063	0.2543	0.155	0.254	0.024	0.065	0.039	0.000	0.013	0.000	0.000	0.0000	0.2415	0.000164	Error analysis	
0.134	0.035	0.240	54	84	0.2057	0.2105	0.134	0.211	0.018	0.044	0.028	-0.021	-0.031	0.000	0.001	0.0006	0.2120	2.14E-06	n	9.0000
0.114	0.028	0.251	48	80	0.2086	0.1871	0.114	0.187	0.013	0.035	0.021	-0.041	-0.054	0.002	0.003	0.0022	0.1839	1.06E-05	A	1.4056
0.094	0.059	0.244	36	63	0.2053	0.1514	0.094	0.151	0.009	0.023	0.014	-0.061	-0.090	0.004	0.008	0.0054	0.1557	1.88E-05	σA	0.0447
0.075	0.038	0.248	63	93	0.2094	0.125	0.075	0.125	0.006	0.016	0.009	-0.080	-0.116	0.006	0.013	0.0092	0.1290	1.63E-05	conf. level (%)	95.0000
0.054	0.026	0.208	52	78	0.2100	0.0939													t value	1.8946
0.034	0.038	0.246	60	90	0.2083	0.07													ΔA	0.0846
0.017	0.148	0.256	112	128	0.2025	0.0405														
																			A'	0.2885
																			ΔA'+	0.0404
																			ΔA'-	0.0456
sum							1.392	2.169	0.240	0.571	0.370			0.024	0.048	0.034		0.000	ΔA'+ (%)	13.9983
mean							0.155	0.241									0.241		ΔA'- (%)	15.7913

Table B - 8. Seed oil, 40 mm pipe.

B. Experimental data (section 2)

Lo (m)	x1 (m)	x2 (m)	frame1	Frame2	V (m/s)	L slug	xi	yi	xi^2	yi^2	xi*yi	xi-xb	yi-yb	(xi-xb)^2	(yi-yb)^2	(xi-xb)(yi-yb)	fi	(yi-fi)^2	Linear regression	
0.213	0.023	0.419	127	185	0.2050	0.335	0.25	0.450	0.063	0.203	0.113	0.117	0.208	0.014	0.043	0.024	0.436	0.00019	A	1.6634
0.213	0.023	0.421	104	163	0.2026	0.326	0.212	0.366	0.045	0.134	0.078	0.079	0.123	0.006	0.015	0.010	0.373	0.00006	q	0.0206
0.203	0.033	0.423	128	185	0.2055	0.334	0.168	0.295	0.028	0.087	0.050	0.035	0.053	0.001	0.003	0.002	0.300	0.00002	R^2	0.9953
0.184	0.037	0.511	127	197	0.2033	0.310	0.131	0.227	0.017	0.052	0.030	-0.002	-0.015	0.000	0.000	0.000	0.238	0.00013		
0.162	0.046	0.532	134	205	0.2056	0.277	0.11	0.202	0.012	0.041	0.022	-0.023	-0.041	0.001	0.002	0.001	0.204	0.00000	Error analysis	
0.139	0.023	0.325	145	189	0.2061	0.241	0.089	0.171	0.008	0.029	0.015	-0.044	-0.071	0.002	0.005	0.003	0.169	0.00001	n	8.0000
0.116	0.027	0.321	161	204	0.2053	0.206	0.062	0.126	0.004	0.016	0.008	-0.071	-0.117	0.005	0.014	0.008	0.124	0.00000	A	1.6634
0.094	0.022	0.322	140	184	0.2048	0.176	0.045	0.103	0.002	0.011	0.005	-0.088	-0.139	0.008	0.019	0.012	0.095	0.00006	σA	0.0465
0.07	0.02	0.295	140	180	0.2065	0.138													conf. level (%)	95.0000
0.052	0.016	0.297	154	195	0.2058	0.106													t value	1.9432
0.029	0.017	0.3	150	191	0.2073	0.068													ΔA	0.0903
0.011	0.015	0.322	158	203	0.2049	0.040														
0	0.085	0.302	181	222	0.1589	0.018													A'	0.3988
																			ΔA'+	0.0310
																			ΔA'-	0.0345
sum							1.067	1.940	0.179	0.571	0.319			0.036	0.101	0.061		0.00047	ΔA'+ (%)	7.7638
mean							0.133	0.242									0.242		ΔA'- (%)	8.6554

Table B - 9. 25% diluted soap, 40 mm pipe.

B. Experimental data (section 2)

Lo (m)	x1 (m)	x2 (m)	frame1	Frame2	V (m/s)	L slug	xi	yi	xi^2	yi^2	xi*yi	xi-xb	yi-yb	(xi-xb)^2	(yi-yb)^2	(xi-xb)(yi-yb)	fi	(yi-fi)^2	Linear regression	
0.225	0.098	0.397	38	87	0.1827	0.4357	0.225	0.436	0.051	0.190	0.098	0.084	0.163	0.007	0.027	0.014	0.428	5.53E-05	A	1.8548
0.21	0.032	0.432	28	93	0.1847	0.396	0.21	0.396	0.044	0.157	0.083	0.069	0.123	0.005	0.015	0.008	0.400	1.97E-05	q	0.0109
0.19	0.126	0.432	1	50	0.1878	0.3623	0.19	0.362	0.036	0.131	0.069	0.049	0.090	0.002	0.008	0.004	0.363	1.1E-06	R^2	0.9988
0.171	0.030	0.404	102	162	0.1869	0.3258	0.171	0.326	0.029	0.106	0.056	0.030	0.053	0.001	0.003	0.002	0.328	5.32E-06		
0.152	0.014	0.252	49	87	0.1880	0.2906	0.152	0.291	0.023	0.084	0.044	0.011	0.018	0.000	0.000	0.000	0.293	5.14E-06	Error analysis	
0.132	0.025	0.275	77	117	0.1883	0.2535	0.132	0.254	0.017	0.064	0.033	-0.009	-0.019	0.000	0.000	0.000	0.256	5.16E-06	n	10.0000
0.11	0.043	0.292	43	83	0.1873	0.2158	0.11	0.216	0.012	0.047	0.024	-0.031	-0.057	0.001	0.003	0.002	0.215	6.94E-07	A	1.8548
0.09	0.020	0.302	105	150	0.1883	0.1834	0.09	0.183	0.008	0.034	0.017	-0.051	-0.089	0.003	0.008	0.005	0.178	3.06E-05	σA	0.0226
0.076	0.030	0.232	91	123	0.1894	0.1514	0.076	0.151	0.006	0.023	0.012	-0.065	-0.121	0.004	0.015	0.008	0.152	2.55E-07	conf. level (%)	95.0000
0.055	0.035	0.228	61	92	0.1869	0.112	0.055	0.112	0.003	0.013	0.006	-0.086	-0.161	0.007	0.026	0.014	0.113	9.11E-07	t value	1.8595
																			ΔA	0.0419
																			A'	0.4608
																			ΔA'+	0.0119
																			ΔA'-	0.0125
sum							1.411	2.727	0.230	0.848	0.441			0.031	0.105	0.057		0.000124	ΔA'+ (%)	2.5873
mean							0.141	0.273									0.273		ΔA'- (%)	2.7071

Table B - 10. Soap, 40 mm pipe.

B. Experimental data (section 2)

Lo (m)	x1 (m)	x2 (m)	frame1	Frame2	V (m/s)	L slug	xi	yi	xi^2	yi^2	xi*yi	xi-xb	yi-yb	(xi-xb)^2	(yi-yb)^2	(xi-xb)(yi-yb)	fi	(yi-fi)^2	Linear regression	
0.246	0.033	0.283	205	255	0.15021	0.294	0.246	0.294	0.061	0.086	0.072	0.134	0.152	0.018	0.023	0.020	0.299242	2.64E-05	A	1.1655
0.226	0.021	0.320	1	61	0.14950	0.271	0.226	0.271	0.051	0.073	0.061	0.114	0.128	0.013	0.016	0.015	0.275932	2.95E-05	q	0.0125
0.206	0.059	0.325	1	53	0.15344	0.253	0.206	0.253	0.042	0.064	0.052	0.094	0.110	0.009	0.012	0.010	0.252622	1.43E-07	R^2	0.9986
0.187	0.012	0.318	6	67	0.15069	0.231	0.187	0.231	0.035	0.053	0.043	0.075	0.088	0.006	0.008	0.007	0.230478	2.73E-07		
0.166	0.020	0.326	1	62	0.15089	0.210	0.166	0.210	0.028	0.044	0.035	0.054	0.068	0.003	0.005	0.004	0.206003	1.93E-05	Error analysis	
0.147	0.007	0.323	38	101	0.15048	0.187	0.147	0.187	0.022	0.035	0.028	0.035	0.045	0.001	0.002	0.002	0.183858	1.18E-05	n	15.0000
0.128	0.010	0.329	31	95	0.14973	0.165	0.128	0.165	0.016	0.027	0.021	0.016	0.022	0.000	0.000	0.000	0.161714	8.33E-06	A	1.1655
0.108	0.010	0.320	32	95	0.14805	0.141	0.108	0.141	0.012	0.020	0.015	-0.004	-0.002	0.000	0.000	0.000	0.138404	6.23E-06	σA	0.0122
0.087	0.006	0.322	28	92	0.14827	0.117	0.087	0.117	0.008	0.014	0.010	-0.025	-0.026	0.001	0.001	0.001	0.113929	6.61E-06	conf. level (%)	95.0000
0.067	0.009	0.325	15	79	0.14837	0.093	0.067	0.093	0.004	0.009	0.006	-0.045	-0.050	0.002	0.002	0.002	0.090619	4.76E-06	t value	1.7709
0.047	0.011	0.323	22	85	0.14843	0.071	0.047	0.071	0.002	0.005	0.003	-0.065	-0.072	0.004	0.005	0.005	0.067309	1.44E-05	ΔA	0.0216
0.029	0.010	0.325	27	91	0.14776	0.046	0.029	0.046	0.001	0.002	0.001	-0.083	-0.096	0.007	0.009	0.008	0.046331	4.81E-09		
0.015	0.007	0.179	4524	5220	0.14833	0.027	0.015	0.027	0.000	0.001	0.000	-0.097	-0.116	0.009	0.013	0.011	0.030014	1.1E-05	A'	0.1420
0.01	0.014	0.172	306	338	0.14855	0.021	0.01	0.021	0.000	0.000	0.000	-0.102	-0.121	0.010	0.015	0.012	0.024186	7.76E-06	ΔA'+	0.0156
0.005	0.014	0.171	337	369	0.14790	0.012	0.005	0.012	0.000	0.000	0.000	-0.107	-0.130	0.011	0.017	0.014	0.018359	3.67E-05	ΔA'-	0.0162
sum							1.674	2.139	0.282	0.434	0.349			0.095	0.129	0.111		0.000183	ΔA'+ (%)	10.9910
mean							0.112	0.143									0.1426		ΔA'- (%)	11.4059

Table B - 11. Water, 20 mm pipe.

B. Experimental data (section 2)

Lo (m)	x1 (m)	x2 (m)	frame1	Frame2	V (m/s)	L slug	xi	yi	xi^2	yi^2	xi*yi	xi-xb	yi-yb	(xi-xb)^2	(yi-yb)^2	(xi-xb)(yi-yb)	fi	(yi-fi)^2	Linear regression	
0.267	0.014	0.389	139	215	0.1482	0.38	0.267	0.38	0.071	0.144	0.101	0.134	0.189	0.018	0.036	0.025	0.372	6.08E-05	A	1.3598
0.257	0.052	0.392	142	211	0.1480	0.363	0.257	0.363	0.066	0.132	0.093	0.124	0.172	0.015	0.030	0.021	0.359	1.93E-05	q	0.0091
0.242	0.02	0.386	135	209	0.1485	0.344	0.242	0.344	0.059	0.118	0.083	0.109	0.153	0.012	0.024	0.017	0.338	3.36E-05	R^2	0.9982
0.226	0.02	0.382	143	216	0.1489	0.314	0.226	0.314	0.051	0.099	0.071	0.093	0.123	0.009	0.015	0.011	0.316	6E-06		
0.203	0.023	0.352	165	232	0.1475	0.273	0.203	0.273	0.041	0.075	0.055	0.070	0.082	0.005	0.007	0.006	0.285	0.000148	Error analysis	
0.171	0.026	0.333	162	224	0.1487	0.237	0.171	0.237	0.029	0.056	0.041	0.038	0.046	0.001	0.002	0.002	0.242	2.17E-05	n	15.0000
0.147	0.007	0.297	171	230	0.1476	0.203	0.147	0.203	0.022	0.041	0.030	0.014	0.012	0.000	0.000	0.000	0.209	3.63E-05	A	1.3598
0.125	0.033	0.24	186	228	0.1480	0.176	0.125	0.176	0.016	0.031	0.022	-0.008	-0.015	0.000	0.000	0.000	0.179	9.68E-06	σA	0.0159
0.1	0.012	0.16	182	212	0.1481	0.145	0.1	0.145	0.010	0.021	0.015	-0.033	-0.046	0.001	0.002	0.002	0.145	1.36E-08	conf. level (%)	95.0000
0.082	0.013	0.162	177	207	0.1491	0.122	0.082	0.122	0.007	0.015	0.010	-0.051	-0.069	0.003	0.005	0.004	0.121	1.85E-06	t value	1.7709
0.064	0.011	0.105	169	188	0.1486	0.101	0.064	0.101	0.004	0.010	0.006	-0.069	-0.090	0.005	0.008	0.006	0.096	2.34E-05	ΔA	0.0281
0.052	0.008	0.16	175	206	0.1472	0.08	0.052	0.08	0.003	0.006	0.004	-0.081	-0.111	0.007	0.012	0.009	0.080	2.34E-08		
0.036	0.006	0.158	174	205	0.1472	0.058	0.036	0.058	0.001	0.003	0.002	-0.097	-0.133	0.009	0.018	0.013	0.058	8.17E-09	A'	0.2646
0.02	0.014	0.18	209	243	0.1466	0.039	0.02	0.039	0.000	0.002	0.001	-0.113	-0.152	0.013	0.023	0.017	0.036	7.11E-06	ΔA'+	0.0149
0.009	0.02	0.113	213	232	0.1470	0.023	0.009	0.023	0.000	0.001	0.000	-0.124	-0.168	0.015	0.028	0.021	0.021	2.64E-06	ΔA'-	0.0155
sum							2.001	2.858	0.380	0.754	0.535			0.113	0.209	0.154		0.000371	ΔA'+ (%)	5.6330
mean							0.1334	0.190533									0.191		ΔA'- (%)	5.8710

Table B - 12. 33% soap, 20 mm pipe.

B. Experimental data (section 2)

Lo (m)	x1 (m)	x2 (m)	frame1	Frame2	V (m/s)	L slug	xi	yi	xi^2	yi^2	xi*yi	xi-xb	yi-yb	(xi-xb)^2	(yi-yb)^2	(xi-xb)(yi-yb)	fi	(yi-fi)^2	Linear regression	
0.222	0.026	0.442	11	100	0.1404	0.363	0.222	0.363	0.049	0.132	0.081	0.103	0.169	0.011	0.029	0.0174	0.357	3.29E-05	A	1.5886
0.202	0.016	0.39	1	81	0.1404	0.326	0.202	0.326	0.041	0.106	0.066	0.083	0.132	0.007	0.018	0.0110	0.325	2.57E-07	q	0.0046
0.181	0.015	0.277	29	84	0.1431	0.29	0.181	0.29	0.033	0.084	0.052	0.062	0.096	0.004	0.009	0.0060	0.292	4.55E-06	R^2	0.9993
0.156	0.014	0.384	29	108	0.1406	0.247	0.156	0.247	0.024	0.061	0.039	0.037	0.053	0.001	0.003	0.0020	0.252	2.93E-05		
0.136	0.017	0.342	48	117	0.1414	0.22	0.136	0.22	0.018	0.048	0.030	0.017	0.026	0.000	0.001	0.0004	0.221	4.14E-07	Error analysis	
0.117	0.017	0.337	25	92	0.1434	0.19	0.117	0.19	0.014	0.036	0.022	-0.002	-0.004	0.000	0.000	0.0000	0.190	2.11E-07	n	11.0000
0.096	0.028	0.342	36	102	0.1429	0.156	0.096	0.156	0.009	0.024	0.015	-0.023	-0.038	0.001	0.001	0.0009	0.157	1.2E-06	A	1.5886
0.077	0.024	0.271	29	81	0.1426	0.126	0.077	0.126	0.006	0.016	0.010	-0.042	-0.068	0.002	0.005	0.0028	0.127	8.35E-07	σA	0.0140
0.057	0.031	0.277	52	104	0.1421	0.096	0.057	0.096	0.003	0.009	0.005	-0.062	-0.098	0.004	0.010	0.0061	0.095	7.38E-07	conf. level (%)	95.0000
0.037	0.009	0.165	93	126	0.1420	0.066	0.037	0.066	0.001	0.004	0.002	-0.082	-0.128	0.007	0.016	0.0105	0.063	6.93E-06	t value	1.8331
0.028	0.01	0.166	11	44	0.1420	0.05	0.028	0.05	0.001	0.003	0.001	-0.091	-0.144	0.008	0.021	0.0131	0.049	8.64E-07	ΔA	0.0257
																			A'	0.3705
																			ΔA'+	0.0100
																			ΔA'-	0.0104
sum							1.3090	2.1300	0.1999	0.5239	0.3236			0.044146	0.111493	0.070132		7.82E-05	ΔA'+ (%)	2.7064
mean							0.1190	0.1936									0.193636		ΔA'- (%)	2.7955

Table B - 13. Seed oil, 20 mm pipe.

B. Experimental data (section 2)

Lo (m)	x1 (m)	x2 (m)	frame1	Frame2	V (m/s)	L slug	xi	yi	xi^2	yi^2	xi*yi	xi-xb	yi-yb	(xi-xb)^2	(yi-yb)^2	(xi-xb)(yi-yb)	fi	(yi-fi)^2	Linear regression	
0.285	0.009	0.398	177	265	0.1327														A	1.8605
0.215	0.009	0.417	169	261	0.1332	0.419	0.215	0.419	0.0462	0.1756	0.0901	0.1038	0.2022	0.0108	0.0409	0.0210	0.4099	8.31E-05	q	0.0099
0.197	0.026	0.422	169	257	0.1351	0.385	0.197	0.385	0.0388	0.1482	0.0758	0.0858	0.1682	0.0074	0.0283	0.0144	0.3764	7.41E-05	R^2	0.9971
0.18	0.016	0.379	202	282	0.1363	0.346	0.18	0.346	0.0324	0.1197	0.0623	0.0688	0.1292	0.0047	0.0167	0.0089	0.3448	1.53E-06		
0.165	0.025	0.363	183	258	0.1353	0.311	0.165	0.311	0.0272	0.0967	0.0513	0.0538	0.0942	0.0029	0.0089	0.0051	0.3169	3.43E-05	Error analysis	
0.154	0.017	0.293	186	247	0.1359	0.288	0.154	0.288	0.0237	0.0829	0.0444	0.0428	0.0712	0.0018	0.0051	0.0030	0.2964	7.04E-05	n	14.0000
0.137	0.01	0.292	200	262	0.1366	0.261	0.137	0.261	0.0188	0.0681	0.0358	0.0258	0.0442	0.0007	0.0020	0.0011	0.2648	1.41E-05	A	1.8605
0.125	0.016	0.293	210	271	0.1364	0.233	0.125	0.233	0.0156	0.0543	0.0291	0.0138	0.0162	0.0002	0.0003	0.0002	0.2424	8.9E-05	σA	0.0288
0.106	0.011	0.22	187	233	0.1364	0.2	0.106	0.2	0.0112	0.0400	0.0212	-0.0052	-0.0168	0.0000	0.0003	0.0001	0.2071	5.02E-05	conf. level (%)	95.0000
0.087	0.015	0.211	219	262	0.1369	0.17	0.087	0.17	0.0076	0.0289	0.0148	-0.0242	-0.0468	0.0006	0.0022	0.0011	0.1717	3.01E-06	t value	1.7823
0.067	0.006	0.205	241	285	0.1358	0.142	0.067	0.142	0.0045	0.0202	0.0095	-0.0442	-0.0748	0.0020	0.0056	0.0033	0.1345	5.59E-05	ΔA	0.0514
0.054	0.007	0.158	196	229	0.1374	0.114	0.054	0.114	0.0029	0.0130	0.0062	-0.0572	-0.1028	0.0033	0.0106	0.0059	0.1103	1.34E-05		
0.035	0.01	0.161	220	253	0.1374	0.084	0.035	0.084	0.0012	0.0071	0.0029	-0.0762	-0.1328	0.0058	0.0176	0.0101	0.0750	8.12E-05	A'	0.4625
0.024	0.009	0.165	218	252	0.1378	0.054	0.024	0.054	0.0006	0.0029	0.0013	-0.0872	-0.1628	0.0076	0.0265	0.0142	0.0545	2.71E-07	ΔA'+	0.0144
0.011	0.007	0.162	223	257	0.1369	0.028	0.011	0.028	0.0001	0.0008	0.0003	-0.1002	-0.1888	0.0100	0.0356	0.0189	0.0303	5.45E-06	ΔA'-	0.0153
sum							1.557	3.035	0.2309	0.8584	0.4450			0.0577	0.2004	0.1074		0.000576	ΔA'+ (%)	3.1235
mean							0.111	0.217									0.2168		ΔA'- (%)	3.3010

Table B - 14. 25% diluted soap, 20 mm pipe.

B. Experimental data (section 2)

Lo (m)	x1 (m)	x2 (m)	frame1	Frame2	V (m/s)	L slug	xi	yi	xi^2	yi^2	xi*yi	xi-xb	yi-yb	(xi-xb)^2	(yi-yb)^2	(xi-xb)(yi-yb)	fi	(yi-fi)^2	Linear regression	
0.265	0.176	0.556	101	235	0.0852	0.581	0.265	0.581	0.0702	0.3376	0.1540	0.1281	0.2798	0.0164	0.0783	0.0359	0.5664	0.000213	A	2.0696
0.248	0.296	0.655	114	232	0.0914	0.526	0.248	0.526	0.0615	0.2767	0.1304	0.1111	0.2248	0.0124	0.0505	0.0250	0.5312	2.74E-05	q	0.0180
0.225	0.015	0.395	20	142	0.0935	0.473	0.225	0.473	0.0506	0.2237	0.1064	0.0881	0.1718	0.0078	0.0295	0.0151	0.4836	0.000113	R^2	0.9988
0.203	0.185	0.574	1	125	0.0942	0.435	0.203	0.435	0.0412	0.1892	0.0883	0.0661	0.1338	0.0044	0.0179	0.0088	0.4381	9.62E-06		
0.185	0.019	0.397	81	200	0.0954	0.398	0.185	0.398	0.0342	0.1584	0.0736	0.0481	0.0968	0.0023	0.0094	0.0047	0.4008	8.12E-06	Error analysis	
0.165	0.018	0.408	98	222	0.0944	0.357	0.165	0.357	0.0272	0.1274	0.0589	0.0281	0.0558	0.0008	0.0031	0.0016	0.3595	6.04E-06	n	14.0000
0.145	0.033	0.405	98	215	0.0955	0.321	0.145	0.321	0.0210	0.1030	0.0465	0.0081	0.0198	0.0001	0.0004	0.0002	0.3181	8.6E-06	A	2.0696
0.125	0.02	0.404	85	205	0.0961	0.282	0.125	0.282	0.0156	0.0795	0.0353	-0.0119	-0.0192	0.0001	0.0004	0.0002	0.2767	2.84E-05	σA	0.0206
0.107	0.05	0.268	135	204	0.0949	0.239	0.107	0.239	0.0114	0.0571	0.0256	-0.0299	-0.0622	0.0009	0.0039	0.0019	0.2394	1.79E-07	conf. level (%)	95.0000
0.087	0.011	0.261	119	198	0.0950	0.201	0.087	0.201	0.0076	0.0404	0.0175	-0.0499	-0.1002	0.0025	0.0100	0.0050	0.1980	8.82E-06	t value	1.7823
0.067	0.039	0.212	152	206	0.0962	0.159	0.067	0.159	0.0045	0.0253	0.0107	-0.0699	-0.1422	0.0049	0.0202	0.0099	0.1566	5.57E-06	ΔA	0.0367
0.048	0.015	0.212	185	246	0.0970	0.117	0.048	0.117	0.0023	0.0137	0.0056	-0.0889	-0.1842	0.0079	0.0339	0.0164	0.1173	1.01E-07		
0.027	0.01	0.199	170	229	0.0962	0.074	0.027	0.074	0.0007	0.0055	0.0020	-0.1099	-0.2272	0.0121	0.0516	0.0250	0.0739	2.07E-08	A'	0.5168
0.019	0.007	0.227	147	215	0.0972	0.054	0.019	0.054	0.0004	0.0029	0.0010	-0.1179	-0.2472	0.0139	0.0611	0.0291	0.0573	1.09E-05	ΔA'+	0.0084
																			ΔA'-	0.0087
sum							1.916	4.217	0.349	1.640	0.756			0.0863	0.3703	0.1787		0.0004	ΔA'+ (%)	1.6293
mean							0.137	0.301									0.3012		ΔA'- (%)	1.6881

Table B - 15. Soap, 20 mm pipe.

C. Worked example of overpressure model (section 3)

In this section a detailed, worked example of how to apply the models developed in section 3 are given to calculate parameters that are relevant to volcanic slugs. As a case study, the following set of values, which are plausible for a basaltic volcano, are chosen: magma viscosity η = 1,000 Pa s, magma density ρ = 2,600 Kg/m^3; conduit radius r_c = 1.5 m, slug gas volume at atmospheric pressure V_a = 100 m^3. Also, ambient pressure at the surface P_a = 10^5 Pa and gravitational acceleration g = 9.81 m/s^2 are assumed; different values can be chosen for these parameters, if subaqueous, sub-glacial, or extra-terrestrial volcanism is being investigated.

Step 1: calculate inverse viscosity N_f from equation 1-3. This is the key parameter that controls slug ascent and morphology before burst. As it is dimensionless, this parameter scales from laboratory experiments to natural slugs as long as surface tension is negligible. N_f = 42.3 for the given input parameter values. If the slug ascent velocity is required, it can be calculated via the Froude number *Fr* (equations 1-5 and 1-10); in this example, *Fr* = 0.24 and v_s = 1.3 m/s. From equation 1-4 is also possible to calculate slug Reynolds number *Re*, to facilitate comparison with other works that use that parameter (*Re* = 10.1).

Step 2: calculate dimensionless film cross section A' from equation 1-13. In this example, A' = 0.49. From this parameter, film thickness λ and slug radius r_c are derived using equations 1-6 and 1-13 (λ= 0.43 m; r_s = 1.07 m). Film thickness exerts an important control on slug burst behaviour and is also important when inverting geophysical signals, e.g. in acoustic calculations [*Vergniolle et al.,* 2004].

C. Worked example of overpressure model (section 3)

Step 3: calculate the stability index γ. First determine $V_a^{'}$ from equation 3-19 ($V_a^{'}$ = 3.6). The stability index γ can now be calculated using equation 3-20 (for the standard model, in which magma remains confined to the conduit, giving, in this example, γ = 3.4) or equation 3-21 (for the overflow model, in which magma overflows from the conduit during the ascent and burst of the slug, giving, in this example, γ = 7.0). This key quantity allows the stability of the slug, i.e. whether or not it bursts with an overpressure, to be assessed immediately, since slugs are unstable for γ >1.

The following steps 4 and 5 are only applicable if γ > 1.

Step 4: calculate the dimensionless burst pressure $P_b^{'}$ using equation 3-16. This is the pressure within the slug at burst, normalized by the ambient pressure; hence, for sub-aerial eruptions on Earth, it is equal to burst pressure expressed in bars (for the standard model, P_b = 126912 Pa, ~ 1.27 bar; for the overflow model, P_b = 163505 Pa, ~ 1.64 bar). This is the main outcome of the model, having direct implications for geophysical and volcanological observations and interpretations, as well as hazard assessment.

Step 5: calculate the slug length at burst L_b. First, calculate the dimensionless equivalent slug length at atmospheric pressure $L_a^{'}$ via equation 3-19 ($L_a^{'}$ = 7.04), then the dimensionless slug length at burst $L_b^{'}$ via equation 3-17 (respectively $L_b^{'}$ = 5.55 and $L_b^{'}$ = 4.31, for the standard and overflow models), finally multiply by the characteristic length $P_a/\rho g$ to obtain the slug length at burst (respectively L_b = 21.8 m and L_b = 16.9 m).

C. Worked example of overpressure model (section 3)

Determining the length of the slug at burst is critical so that the validity of the standard and overflow models can be assessed, since, by comparing L_b with geophysical/volcanological information [e.g., *Ripepe et al.,* 2002] for the depth of the free magma surface, one can judge whether the magma is likely to remain confined to the conduit during slug ascent and burst, or to overflow. In the present example, the short slug length means that either model may apply. If, instead, we choose V_a = 100,000 m^3, we obtain bursting slug lengths of several hundred meters, which is sufficiently long that magma must overflow, hence the standard model is inappropriate.

D. Experimental data (section 4) -plots

Data logger file #	Base conditions	μ_i/μ_w	h_i/D	V (ml)	P_{surf} (mbar)	Video file #	Result	Notes
110330b	C	-	0	2	30	3188	ok	
110330c	C	-	0	4	30	3189	ok	
110330d	C	-	0	6	30	3190	no	
110330e	C	-	0	6	30	3191	ok	
110330f	C	-	0	8	30	3192	ok	
110330g	C	-	0	10	30	3193	ok	
110330h	C	-	0	2	30	3194	ok	
110330i	C	-	0	4	30	3195	ok	
110330j	C	-	0	6	30	3196	ok	
110330k	C	-	0	8	30	3197	ok	
110330l	C	-	0	10	30	3198	ok	
-	C	10^3	0.5	6	30	3202	ok	test - video only
-	C	10^3	0.5	2	30	3203	ok	test - video only
-	C	10^3	0.5	2	30	3204	ok	test - video only
110331a	C	10^3	0.5	2	30	3205	ok	
110331b	C	10^3	0.5	4	30	3206	no	2 separate slug

D. Experimental data (section 4) -plots

110331c	C	10^3	0.5	8	30	3207	ok	
110331d	C	10^3	0.5	4	30	3208	ok	
110331e	C	10^3	2	2	30	3209	ok	
110331f	C	10^3	2	4	30	3210	ok	
-	C	10^3	2	8	30	3211	ok	video acquired during pumping, small bubbles rising
110331g	C	10^3	2	8	30	3212	ok	
-	C	10^3	2	10	30	3213	ok	test- video only - low expansion experiment (500 mbar)
110331h	C	10^3	2	10	30	3214	ok	
110331i	C	10^3	2	2	30	3215	ok	
-	C	10^3	2	-	30	3216	ok	HD video acquired during pumping, small bubbles rising
-	C	10^3	2	-	30	3217	ok	photo acquired during pumping, small bubbles rising
-	C	10^3	2	-	30	3218	ok	STD video acquired during pumping, small bubbles rising
110331j	C	10^3	2	4	30	3219	ok	
110331k	C	10^3	2	6	30	3220	ok	
110331l	C	10^3	2	8	30	3221	ok	
110331	C	10^3	2	10	30	3222	ok	

D. Experimental data (section 4) -plots

m								
-	C	10^3	2	2	30	3223	ok	STD video acquired of 2 ml slug at 30 mbar
-	C	10^3	2	4	30	3224	ok	STD video acquired of 4 ml slug at 500 mbar opening valve
-	C	10^3	2	-	30	3225	ok	STD video acquired of 4 ml slug pumping down from 500 mbar to 30 mbar
-	C	10^3	2	-	30	3226	ok	STD video acquired of 4 ml slug at 30 mbar
-	C	10^3	2	-	30	3230	ok	STD video acquired of 2 ml slug at 500 mbar
-	C	10^3	2	-	30	3231	ok	STD video acquired of 2 ml slug during pumping to 30 mbar, decompression releted bubbling
110401a	C	10^3	7	2	30	3232	ok	
110401b	C	10^3	7	4	30	3233	ok	
110401c	C	10^3	7	6	30	3234	ok	
110401d	C	10^3	7	8	30	3235	ok	
110401e	C	10^3	7	10	30	3236	ok	
110401f	C	10^3	7	2	30	3237	ok	
110401g	C	10^3	7	4	30	3238	ok	Power supply for counter changed from this. This could have lowered high frequency noise in 163.

D. Experimental data (section 4) -plots

110401h	C	10^3	7	6	30	3239	ok	Power supply for counter changed from this. This could have lowered high frequency noise in 163.
110401i	C	10^3	7	8	30	3240	ok	Power supply for counter changed from this. This could have lowered high frequency noise in 163.
110401j	C	10^3	7	10	30	3241	ok	Power supply for counter changed from this. This could have lowered high frequency noise in 163.
110506a	C	10^7	5	6	30	3350	ok	
110509a	C	10^7	5	6	30	3357	ok	Same conditions as above, silicone left to settle for 3 days.
110517a	O		0	10	500	3375	no	Video waving
110517b	O		0	10	500	3376	ok	
110517c	O		0	10	500	3377	ok	Turned any electronic device off
110517d	O		0	2	30	3378	ok	
110517e	O		0	4	30	3379	ok	
110517f	O		0	6	30	3380	ok	
110517g	O		0	8	30	3381	no	missed one led in the video. Repeated (3382)
110517h	O		0	8	30	3382	ok	ok
110517i	O		0	10	30	3383	ok	2 slugs coalescing before rapid

								expansion, see signals to verify.
110517j	0		0	17	30	3384	ok	
110517k	0		0	17	30	3389	ok	
110517l	0		0	10	30	3391	ok	
110517 m	0		0	8	30	3394	ok	
110517n	0		0	6	30	3395	ok	
110517o	0		0	4	30	3396	ok	
110517p	0		0	2	30	3397	ok	
-	0		0	10	500	3401	ok	%
-	0		0	2	30	3402	ok	%
-	0		0	4	30	3403	ok	%
-	0		0	6	30	3404	ok	%
-	0		0	8	30	3405	ok	%
-	0		0	10	30	3406	no	%, leakage in tube B, repeated (3408)
-	0		0	10	30	3408	ok	%
-	0		0	17	30	3409	ok	%
-	0	10^3	5	-	500	3412	ok	%, acquired during pumping.

-	O	10^3	5	2	500	3413	ok	% FOV, HS
-	O	10^3	5	4	500	3414	ok	%, Large Fov, HD
-	O	10^3	5	4	500	3416	ok	%, Small Fov, HD
-	O	10^3	5	4	500	3417	ok	%, Small Fov, HD, 2 slugs injected consecutively
-	O	10^3	5	6	500	3419	ok	%, Large Fov, HD
-	O	10^3	5	6	500	3420	ok	%, Small Fov, HD
-	O	10^3	5	8	500	3421	ok	%, Large Fov, HD
-	O	10^3	5	8	500	3422	ok	%, Small Fov, HD
-	O	10^3	5	10	500	3423	ok	%, Large Fov, HD
-	O	10^3	5	10	500	3424	ok	%, Small Fov, HD
-	O	10^3	5	17	500	3425	ok	%, Large Fov, HD
-	O	10^3	5	17	500	3426	ok	%, Small Fov, HD
-	O	10^3	5	50	500	3427	ok	%, Large Fov, HD
-	O	10^3	5	50	500	3428	ok	%, Small Fov, HD
-	O	10^3	5	50	500	3429	ok	%, Small Fov, HD, valve opening before slug injection.
-	O	10^3	5	50	500	3430	ok	%, Small Fov, HD, repeat of 3428
110519a	O	10^3	5	10	500	3432	ok	

D. Experimental data (section 4) -plots

110519b	0	10^3	5	2	30	3433	ok	
110519c	0	10^3	5	4	30	3435	ok	
110519d	0	10^3	5	6	30	3436	ok	
110519e	0	10^3	5	8	30	3437	ok	
110519f	0	10^3	5	10	30	3438	ok	
110519g	0	10^3	5	17	30	3439	ok	
110519h	0	10^3	5	17	30	3440	ok	
110519i	0	10^3	5	10	30	3442	ok	
110519j	0	10^3	5	8	30	3443	ok	
110519k	0	10^3	5	6	30	3444	ok	
110519l	0	10^3	5	4	30	3446	ok	
110519 m	0	10^3	5	2	30	3447	ok	
110519n	0	10^3	5	10	500	3448	ok	
-	0	10^3	9	10	500	3457	ok	%, Small FOV, HS
-	0	10^3	9	10	500	3458	ok	% , Small FOV, HD
-	0	10^3	9	10	500	3459	ok	% , Large FOV, HD
110520a	0	10^3	9	10	500	3460	no	% , Large FOV, HD, no led counter

D. Experimental data (section 4) -plots

-	O	10^3	9	-	30	3461	ok	% , Video during pumping to 30 mbars Large FOV, HD
110520b	O	10^3	9	2	30	3462	ok	% , Small FOV, HD
110520c	O	10^3	9	2	30	3463	ok	% , Large FOV, HD
110520d	O	10^3	9	4	30	3464	no	% , Small FOV, HD, expansion out of FOV
-	O	10^3	9	-		3465	ok	% , Video during pumping to 30 mbars Large FOV, HD
110520e	O	10^3	9	4	30	3466	ok	% , Small FOV, HD
110520f	O	10^3	9	4	30	3467	ok	% , Large FOV, HD
110520g	O	10^3	9	6	30	3469	ok	% , Large FOV, HD
110520h	O	10^3	9	6	30	3471	ok	% , Large FOV, HS
110520i	O	10^3	9	8	30	3472	ok	% , Small FOV, HD
110520j	O	10^3	9	8	30	3473	ok	% , Large FOV, HS
110520k	O	10^3	9	10	30	3474	ok	% , Small FOV, HD
110520l	O	10^3	9	10	30	3475	ok	% , Large FOV, HS
110520 m	O	10^3	9	17	30	3476	ok	% , Small FOV, HD
110520n	O	10^3	9	17	30	3477	ok	% , Large FOV, HS
110520o	O	10^3	9	24	30	3478	ok	% , Small FOV, HD

D. Experimental data (section 4) -plots

110520p	0	10^3	9	24	30	3479	ok	% , Large FOV, HS
110524a	0	10^3	9	2	30	3482	ok	
110524b	0	10^3	9	4	30	3483	no	2 separate slugs
110524c	0	10^3	9	4	30	3484	ok	
110524d	0	10^3	9	6	30	3485	ok	
110524e	0	10^3	9	6	30	3486	ok	
110524f	0	10^3	9	8	30	3487	ok	
110524g	0	10^3	9	10	30	3488	ok	
110524h	0	10^3	9	17	30	3489	ok	
110524i	0	10^3	9	24	30	3490	ok	
110524j	0	10^3	9	50	30	3493	ok	163-2 noisy
110524k	0	10^3	9	10	500	3498	no	no signal recorded

E. Experimental data (section 4) – plots

1. C_2D_2ml_30_mbar

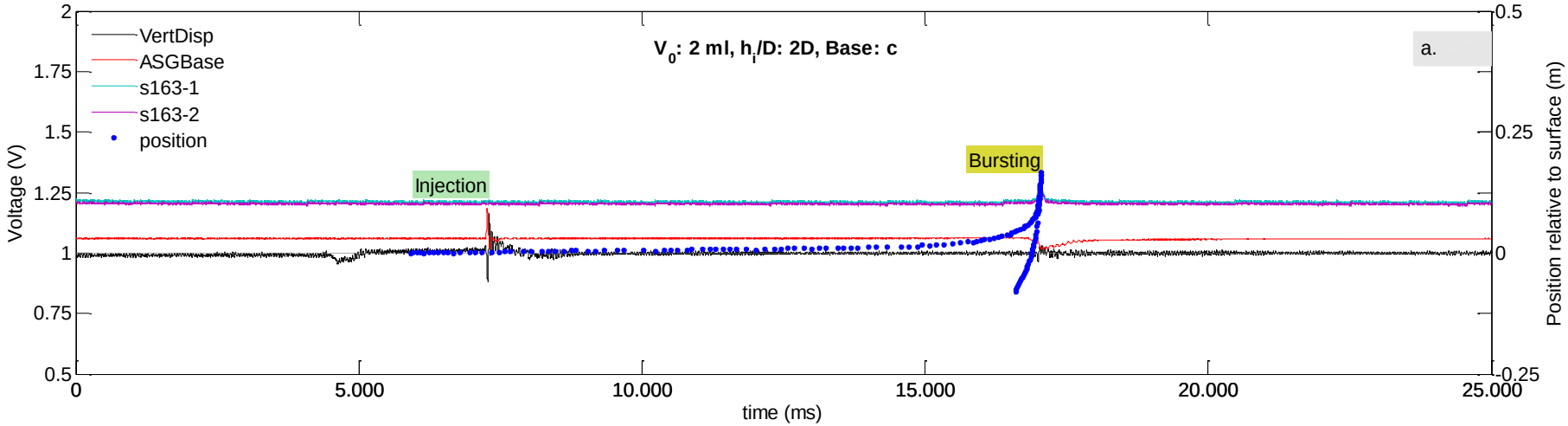

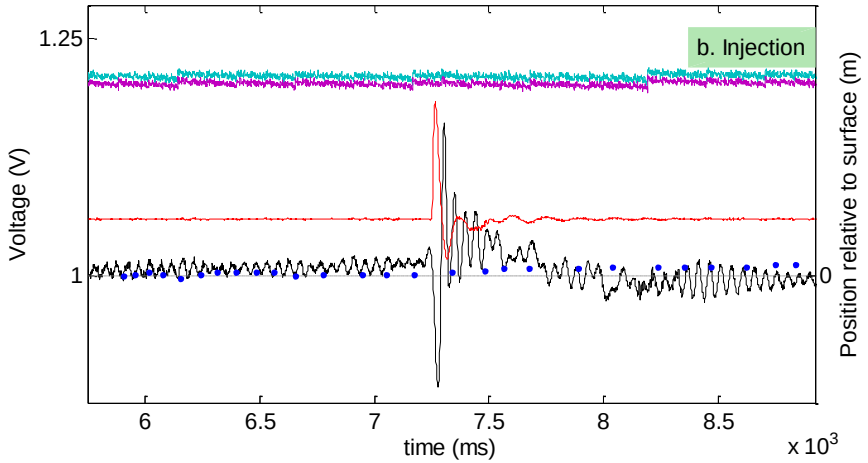

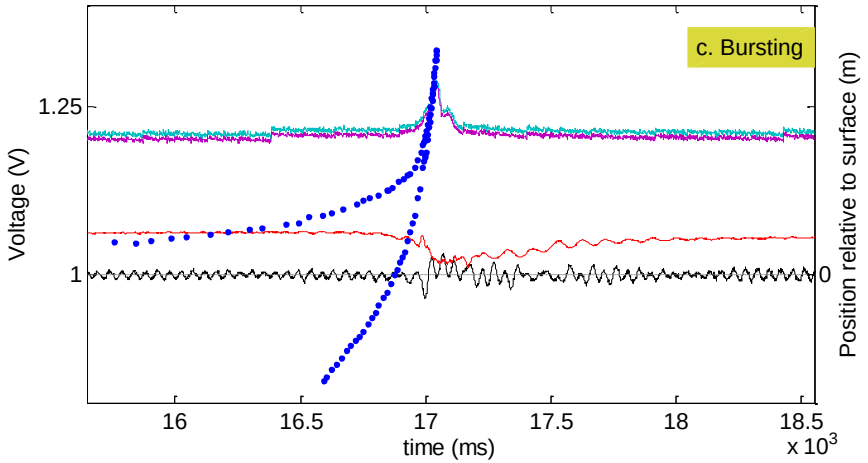

E. Experimental data (section 4) – plots

2. C_0D_4ml_30mbar

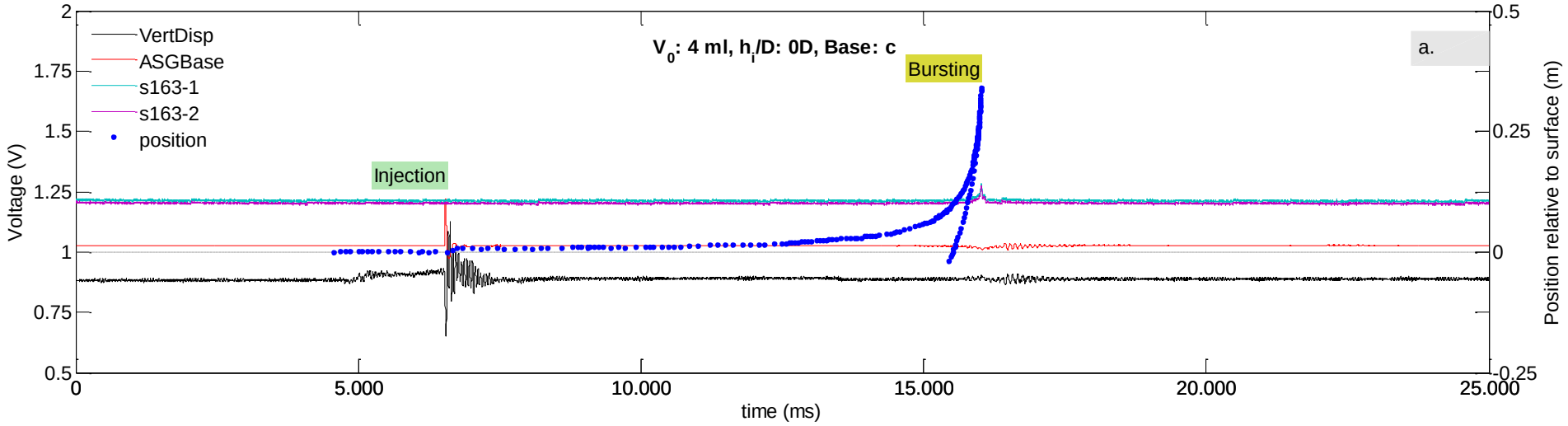

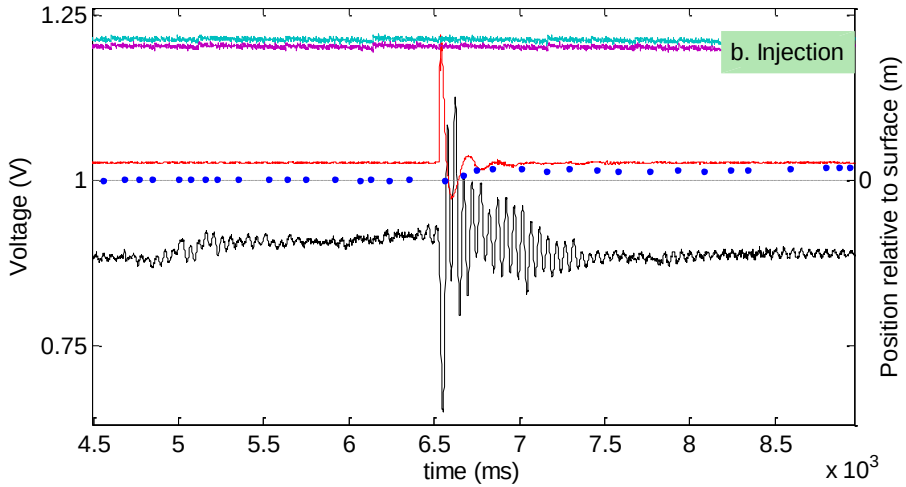

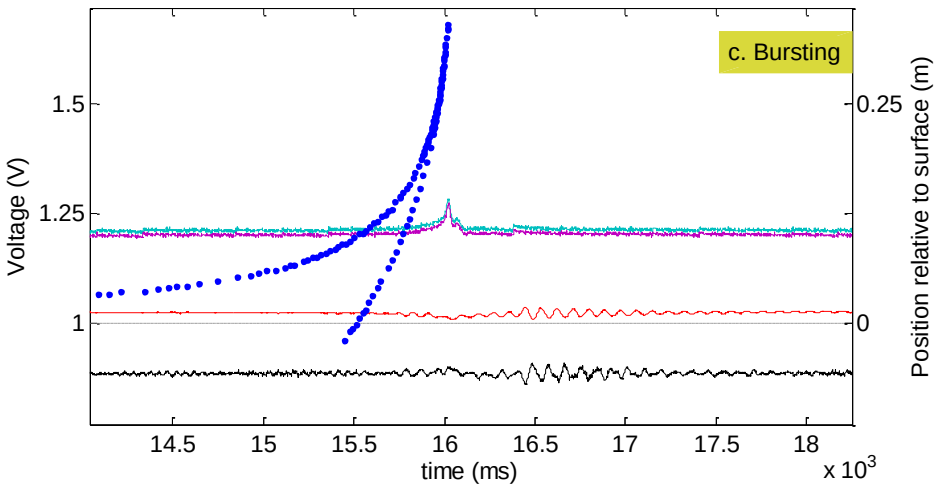

E. Experimental data (section 4) – plots

3. C_0D_6ml_30mbar

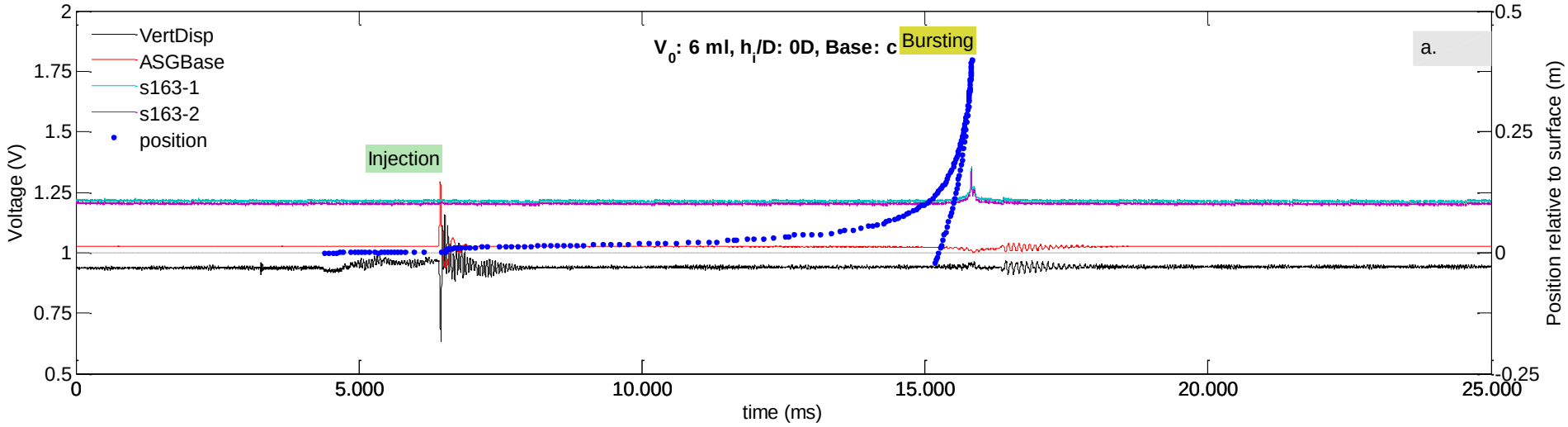

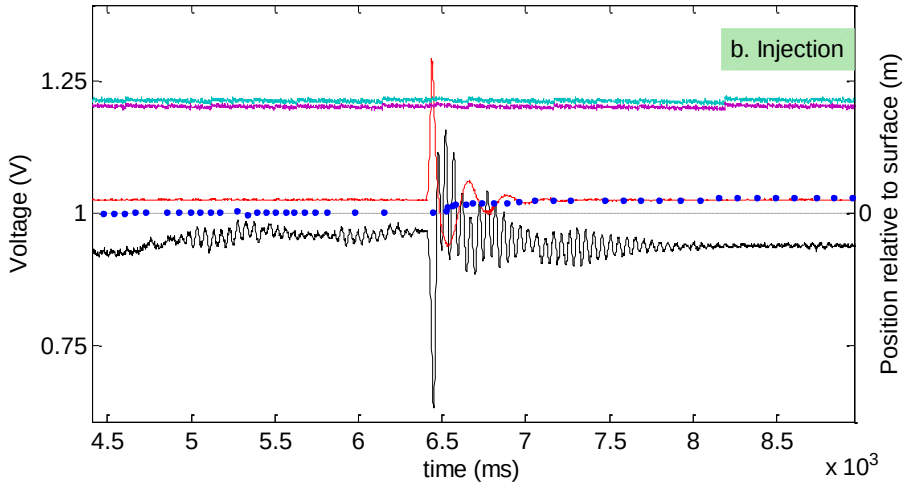

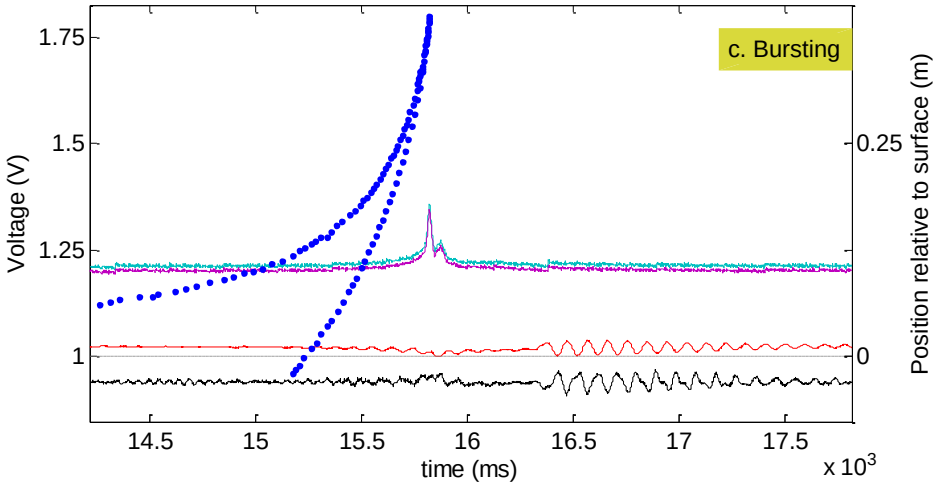

E. Experimental data (section 4) – plots

4. C_0D_8ml_30mbar

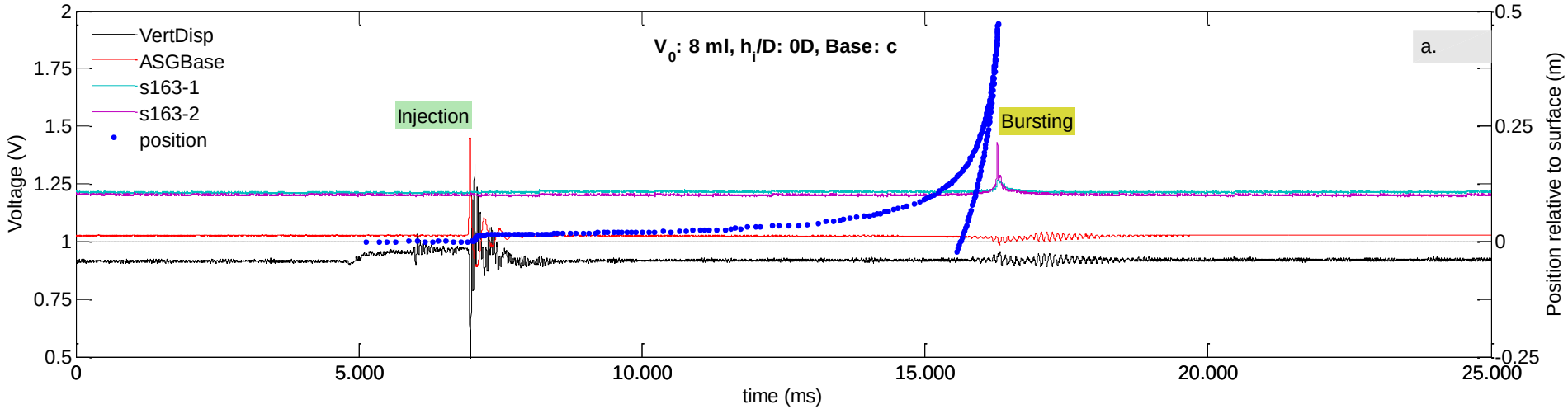

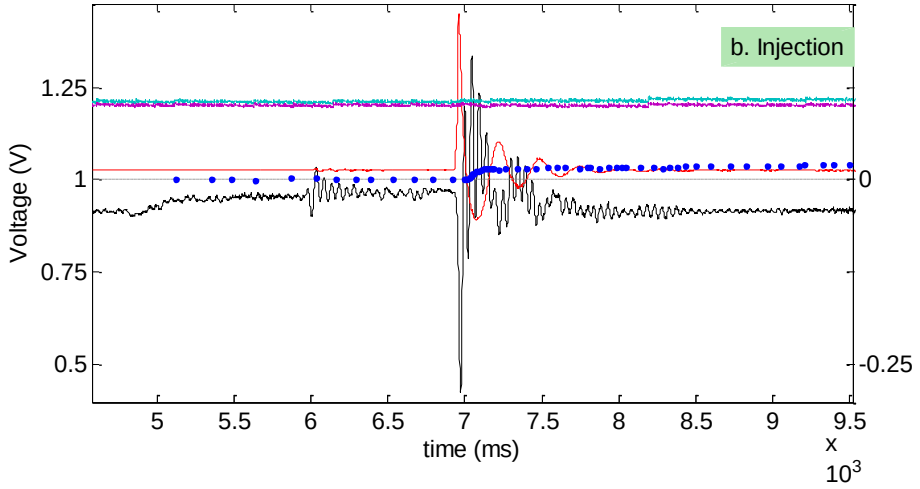

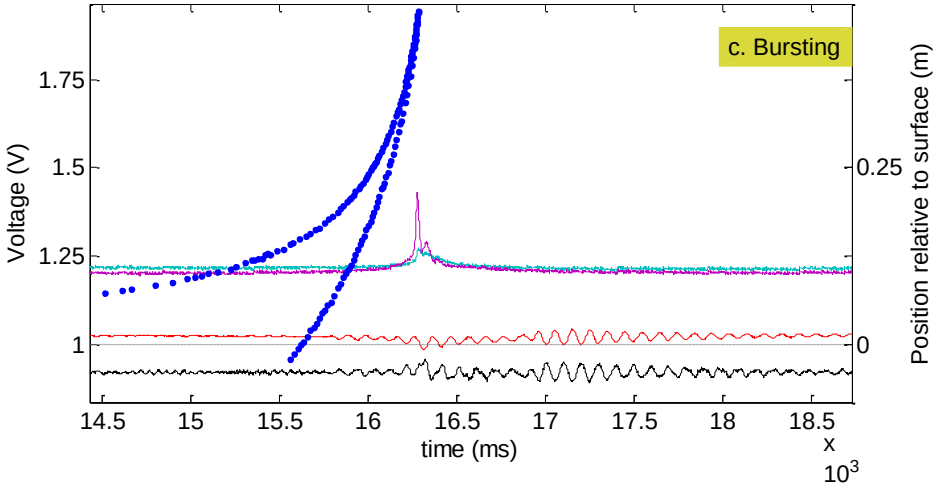

E. Experimental data (section 4) – plots

5. C_0D_10ml_30mbar

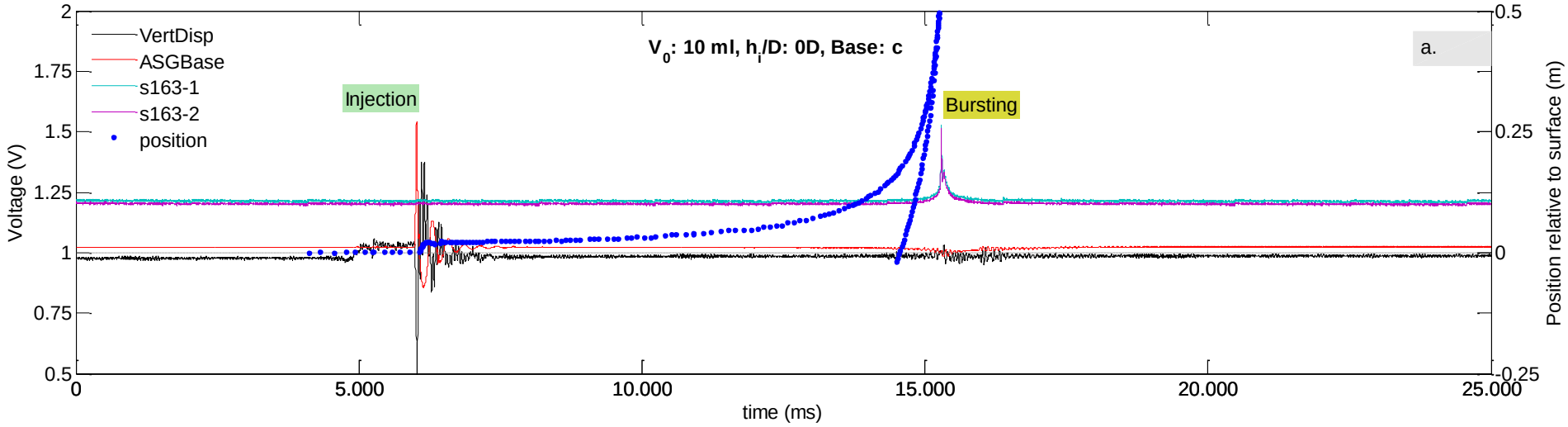

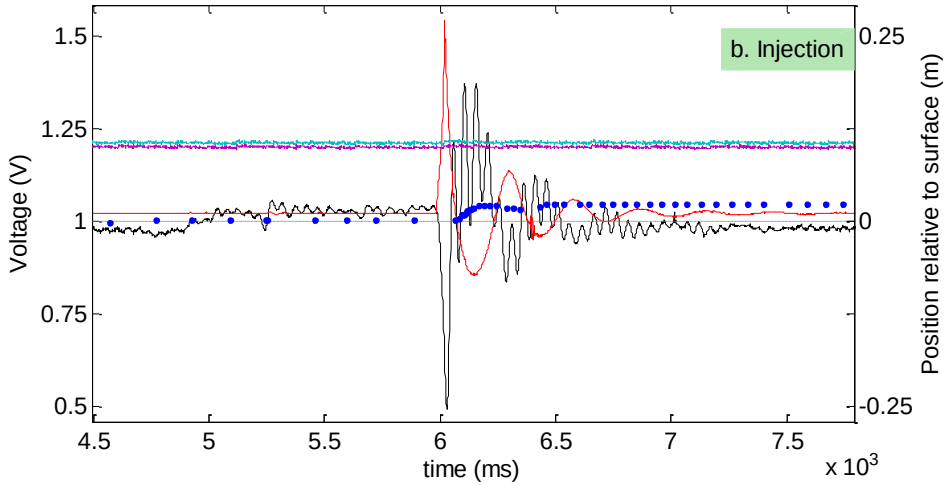

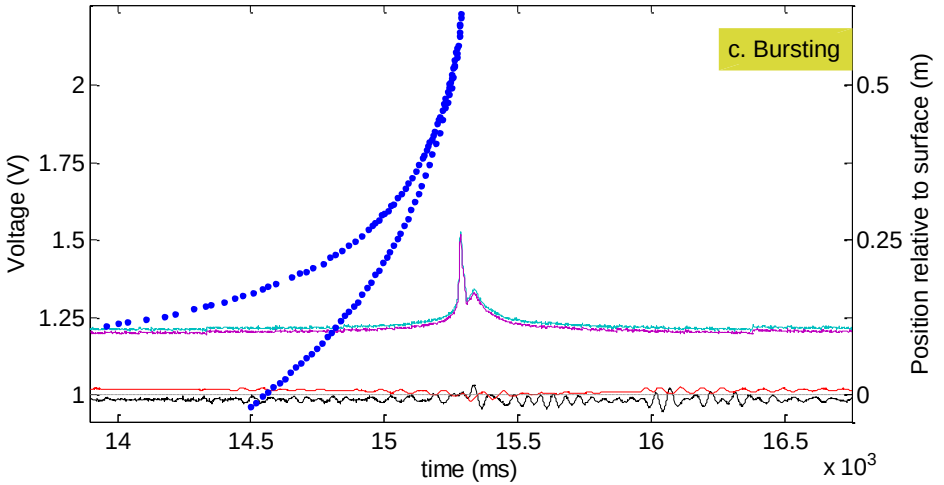

E. Experimental data (section 4) – plots

6. C_2D_2ml_30mbar

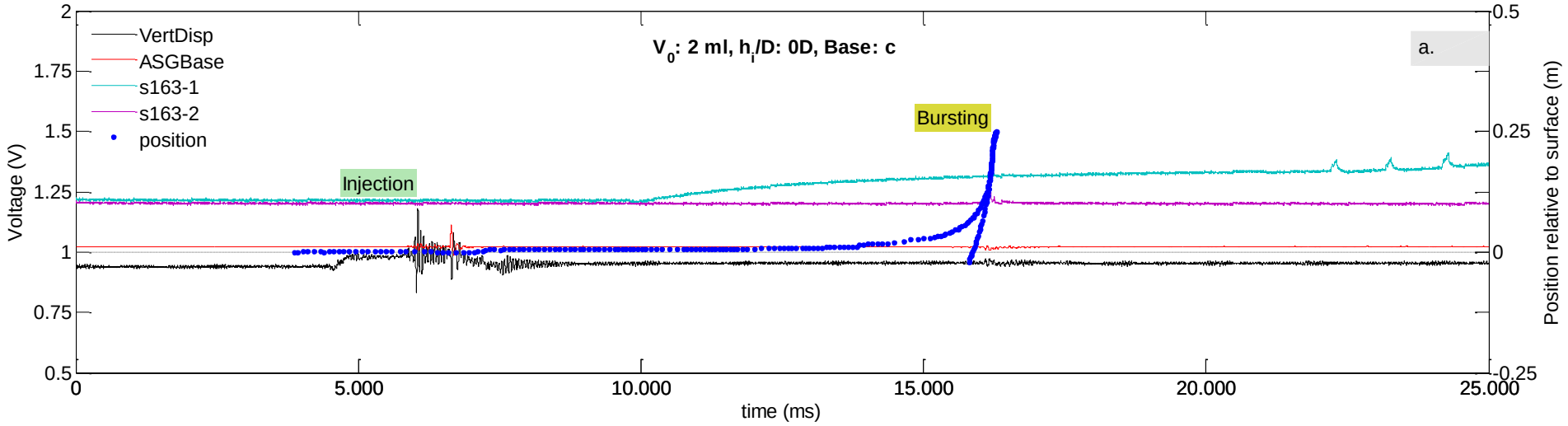

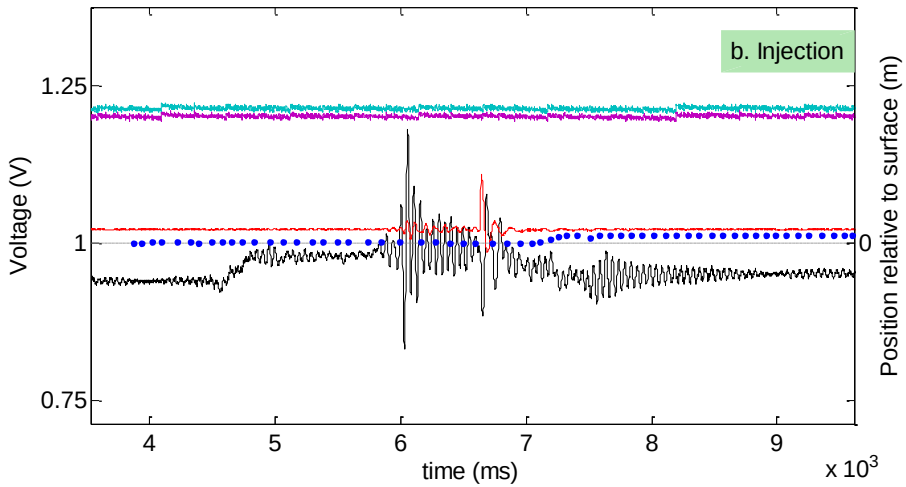

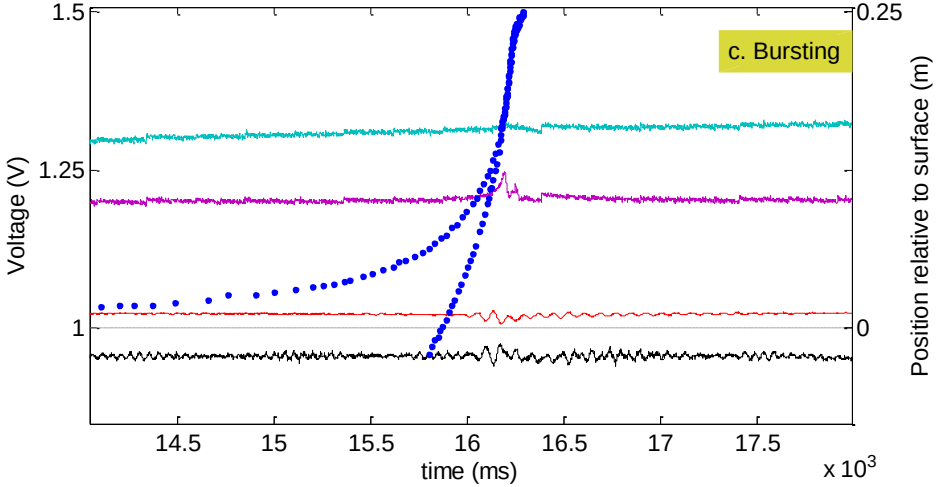

E. Experimental data (section 4) – plots

7. C_2D_4ml_30mbar

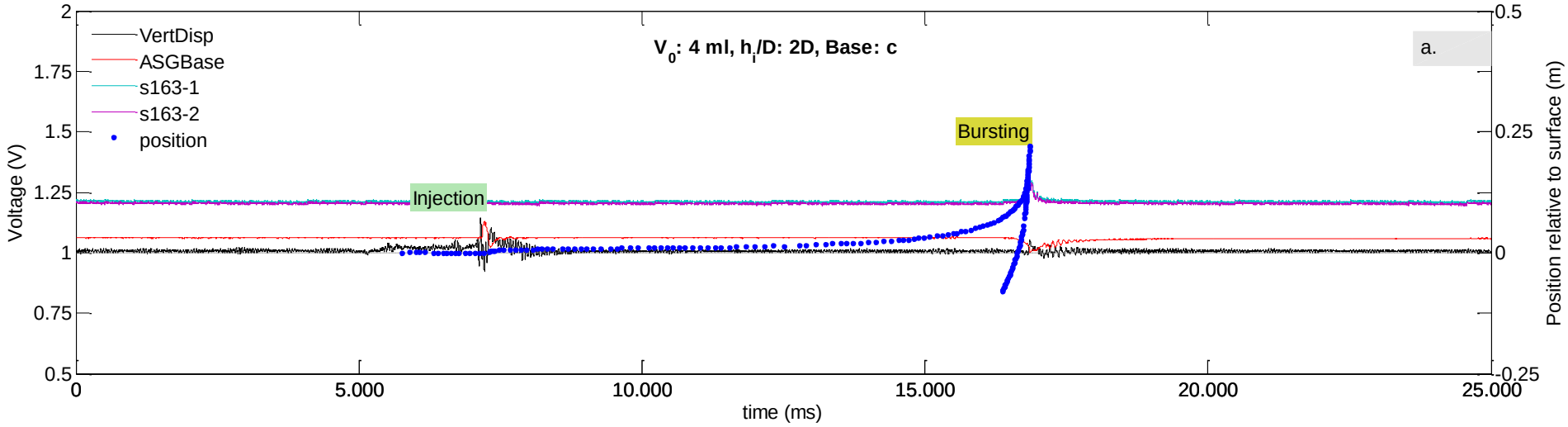

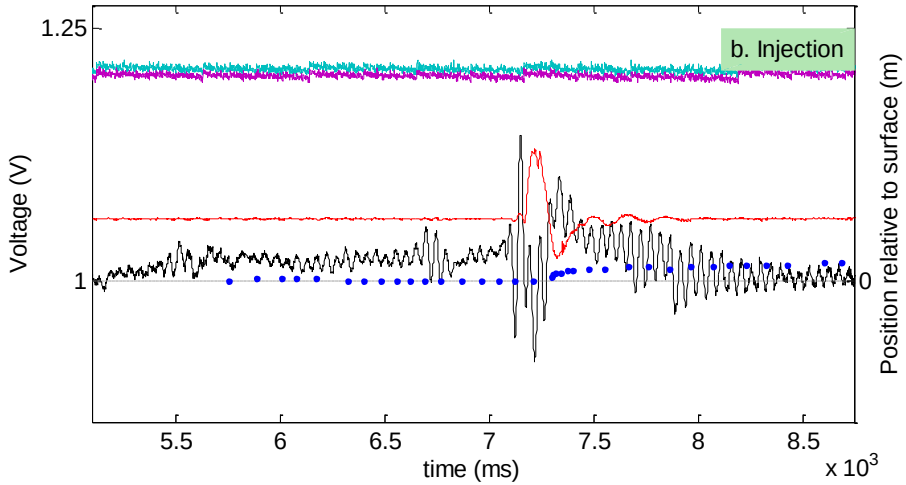

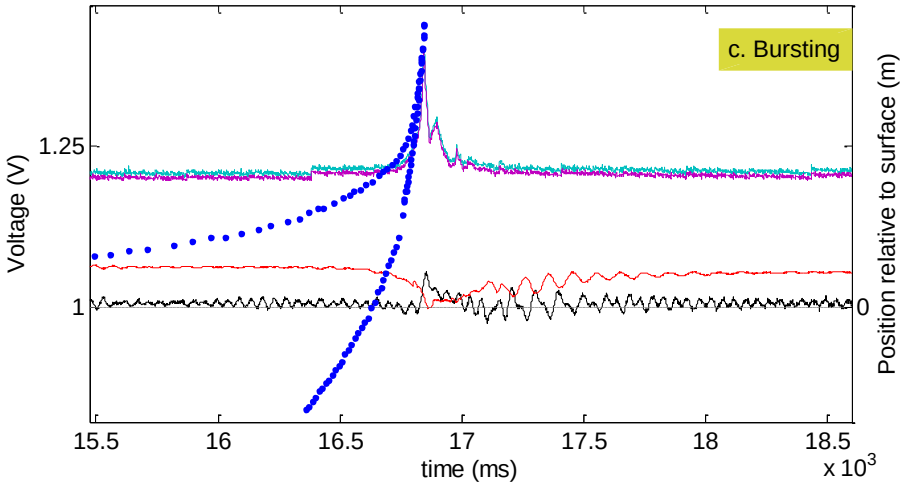

E. Experimental data (section 4) – plots

8. C_2D_6ml_30mbar

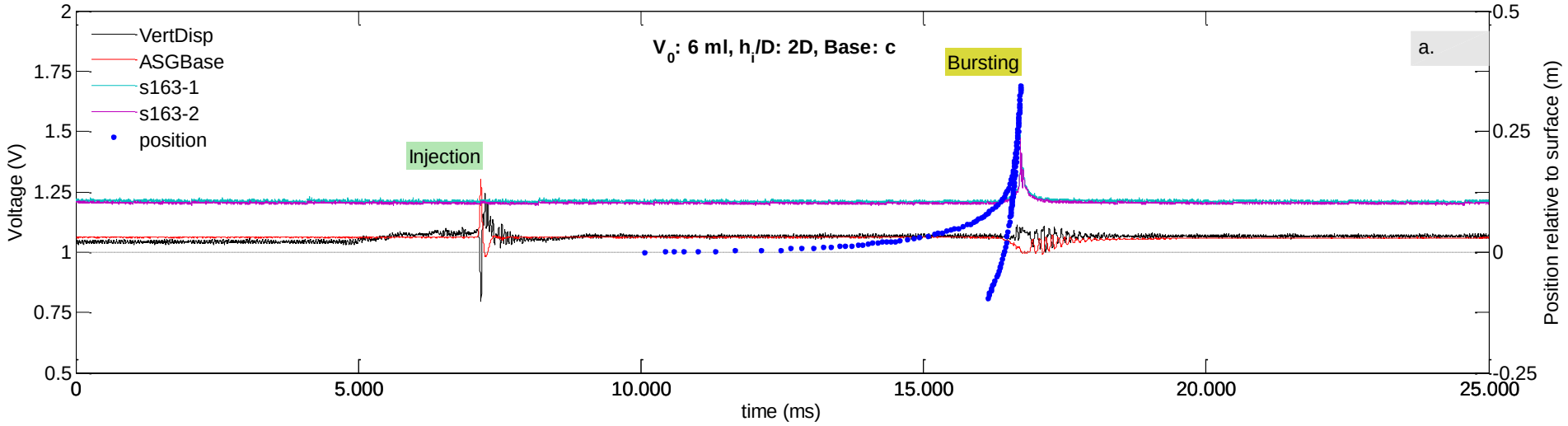

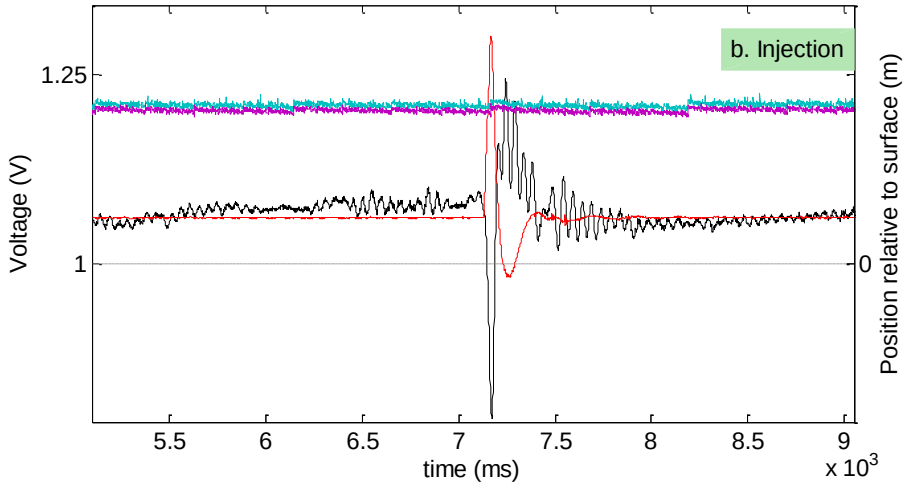

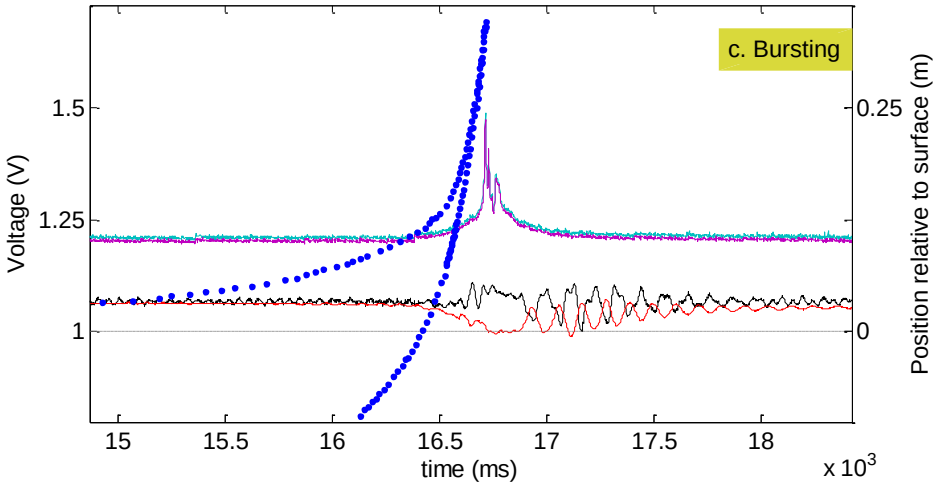

E. Experimental data (section 4) – plots

9. C_2D_8ml_30mbar

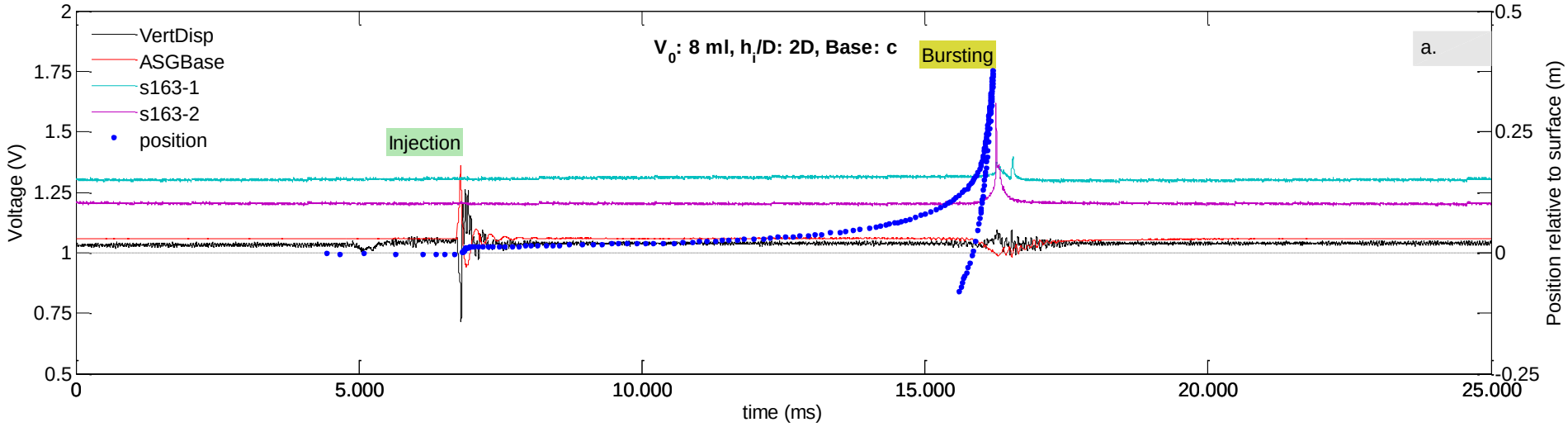

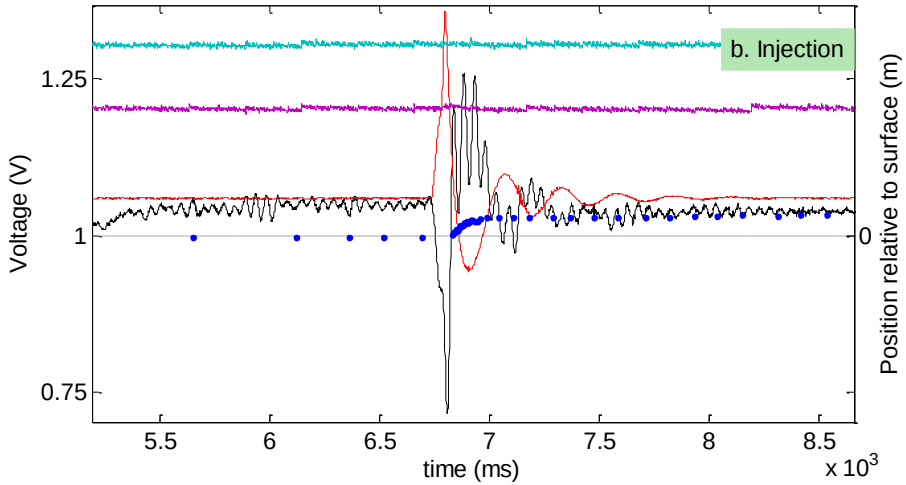

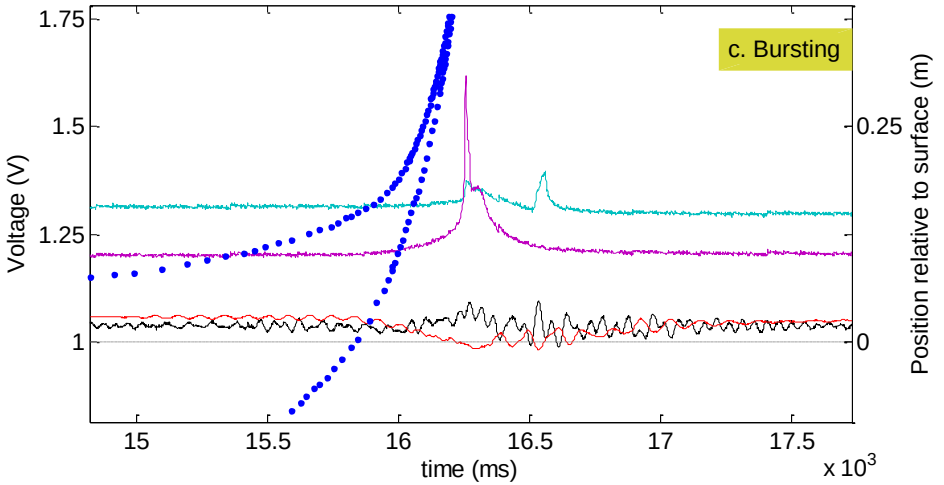

E. Experimental data (section 4) – plots

10. C_2D_10ml_30mbar

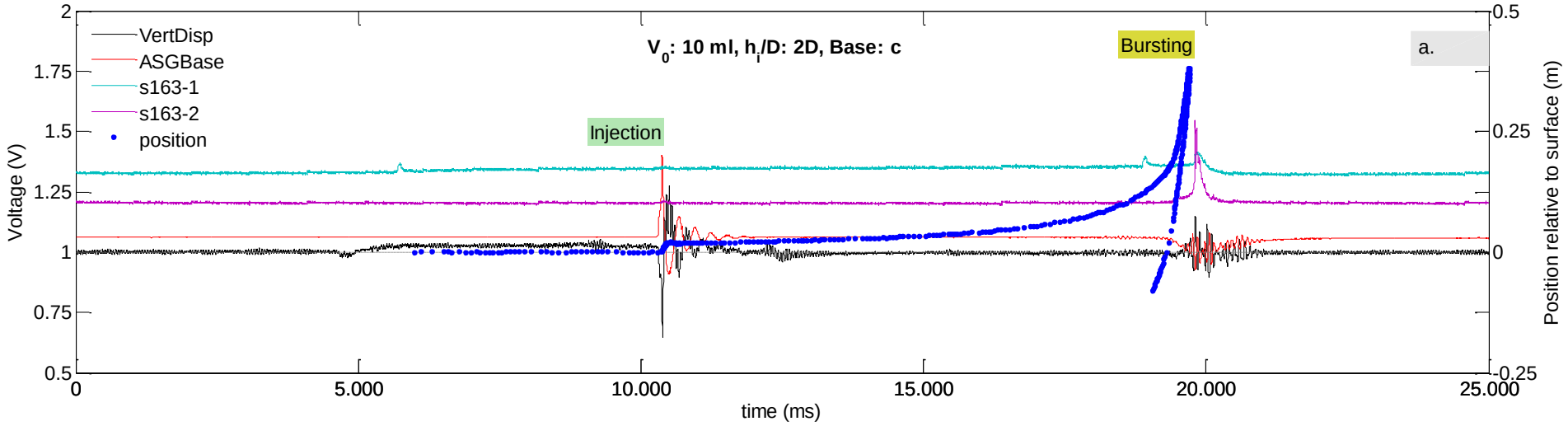

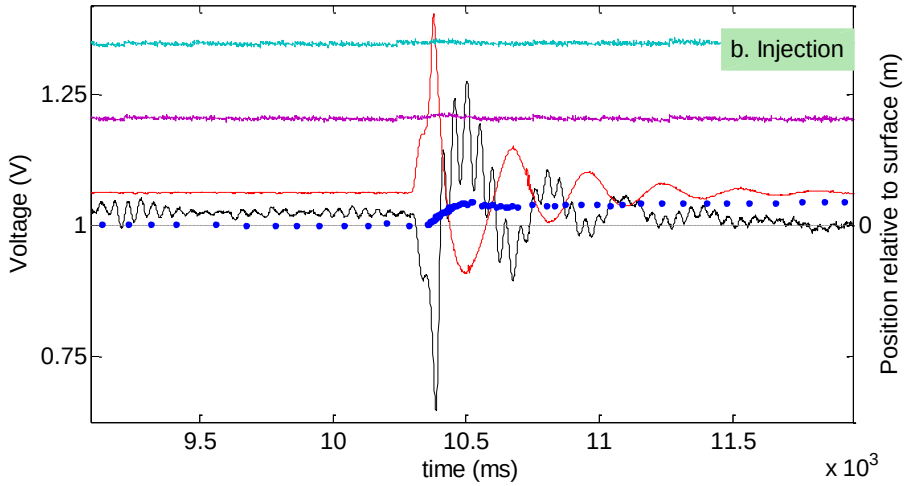

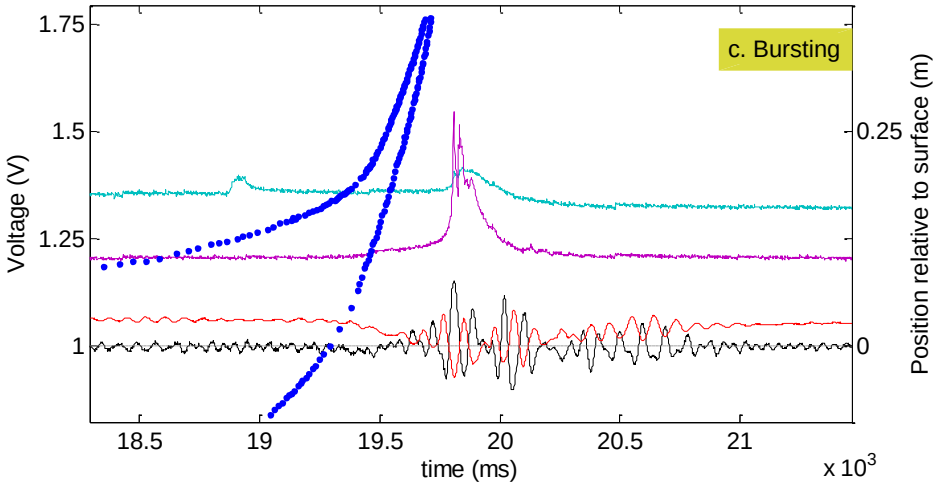

E. Experimental data (section 4) – plots

11. C_7D_2ml_30mbar

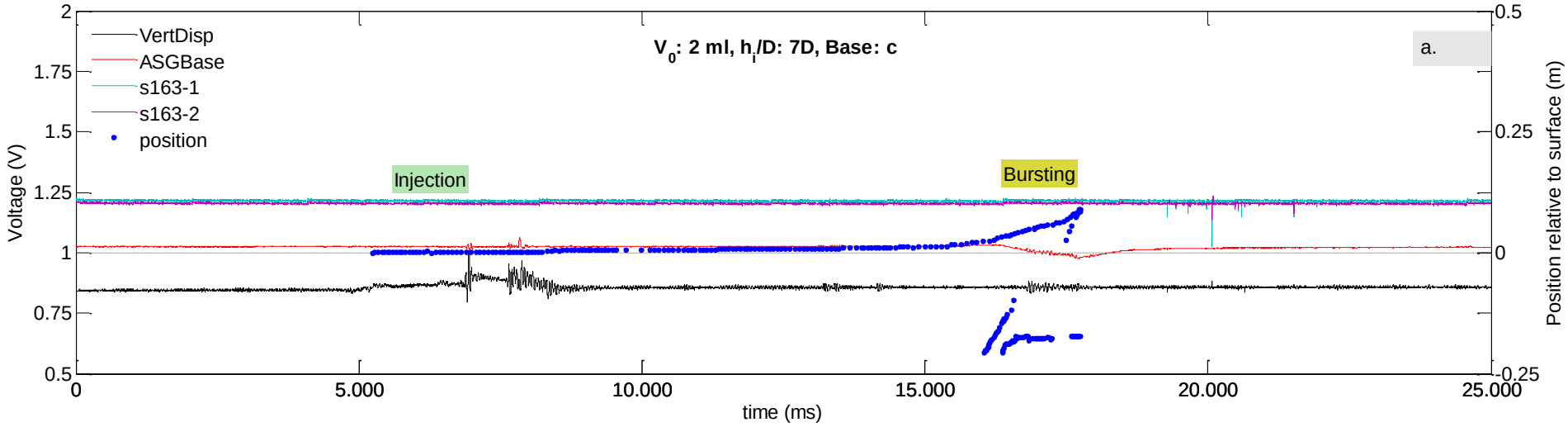

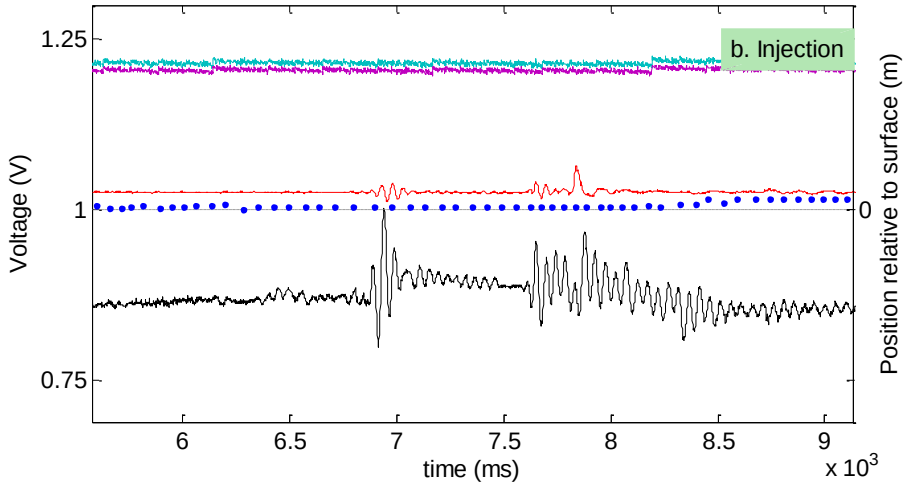

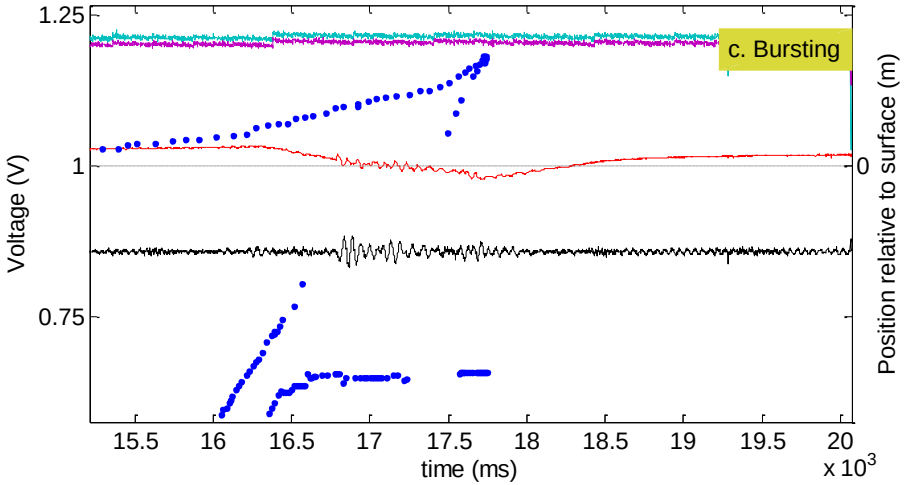

E. Experimental data (section 4) – plots

12. C_7D_4ml_30mbar

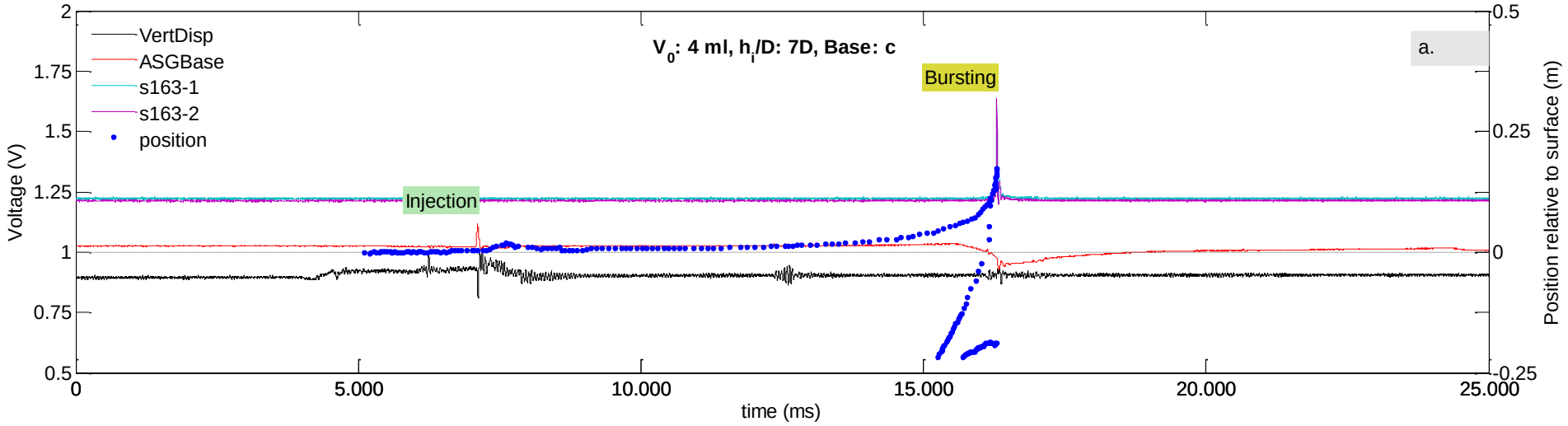

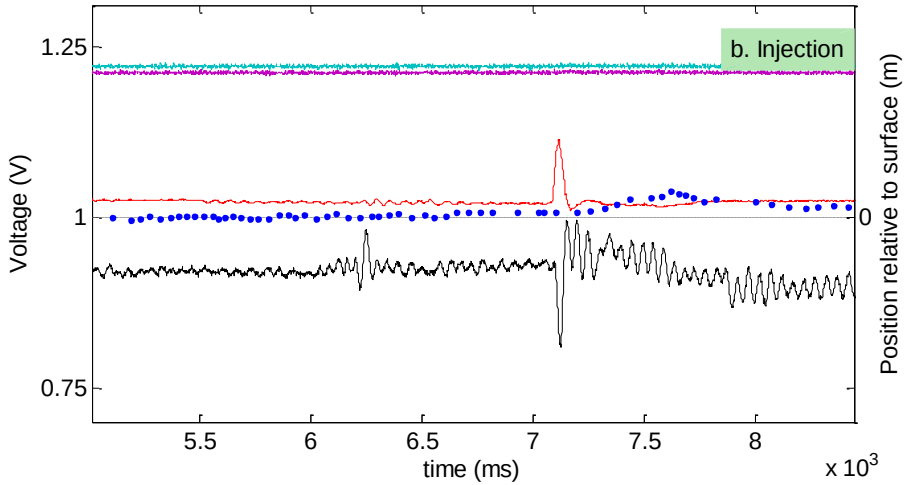

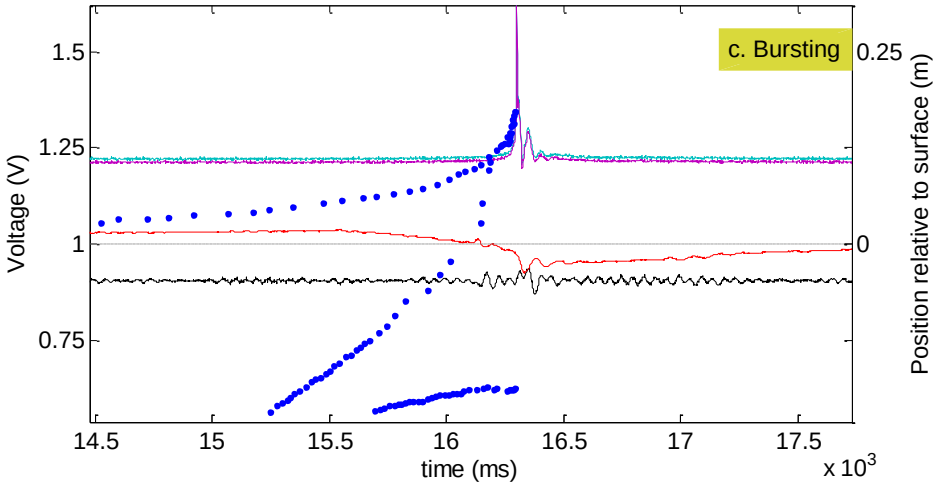

E. Experimental data (section 4) – plots

13. C_7D_6ml_30mbar

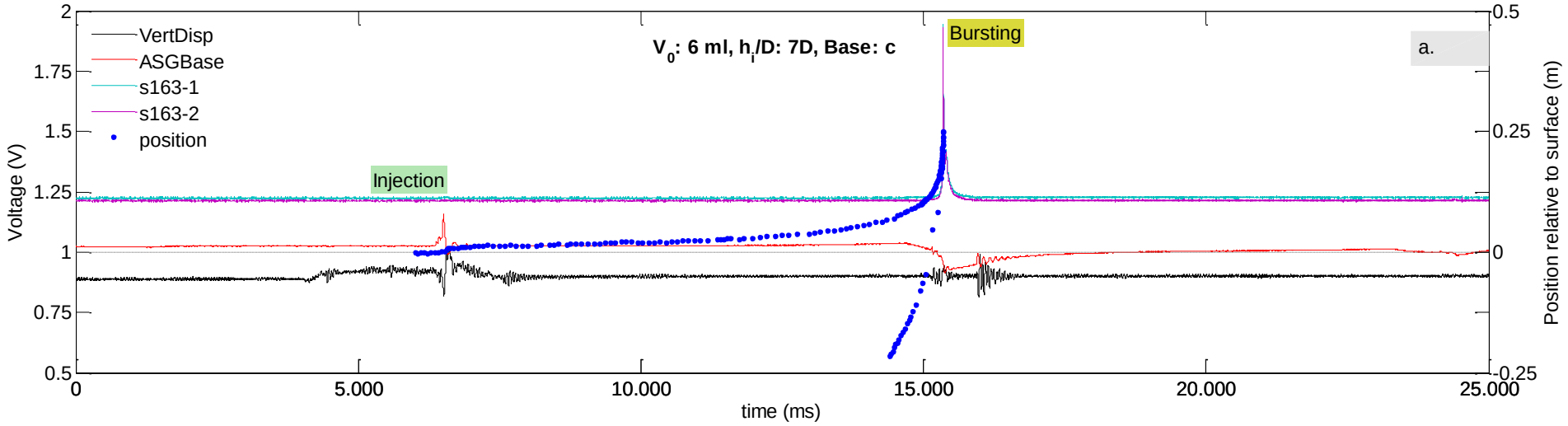

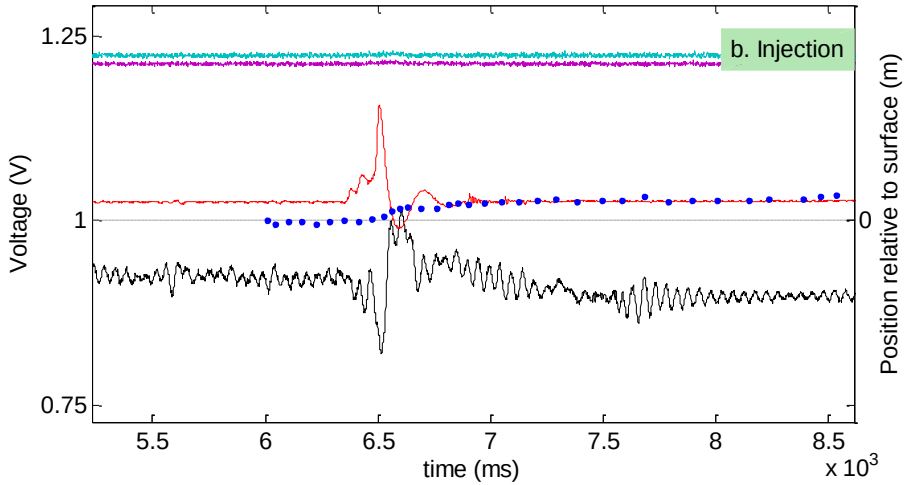

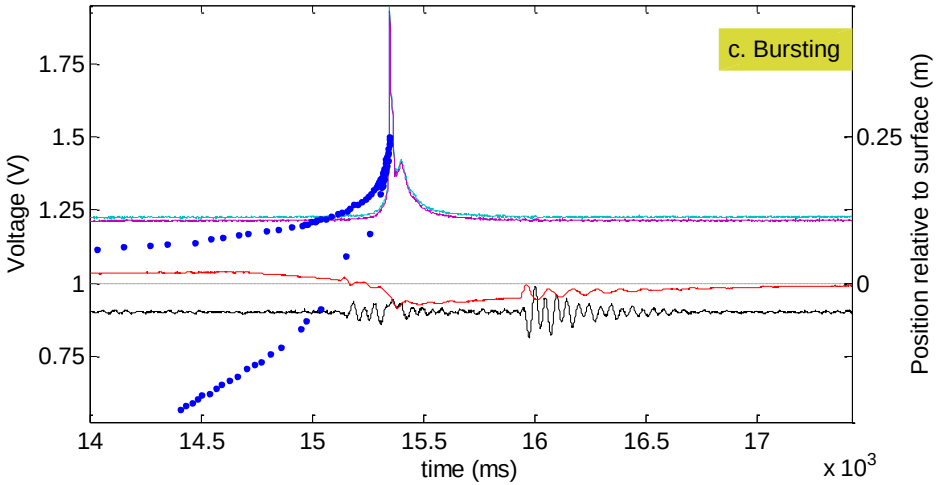

E. Experimental data (section 4) – plots

14. C_7D_8ml_30mbar

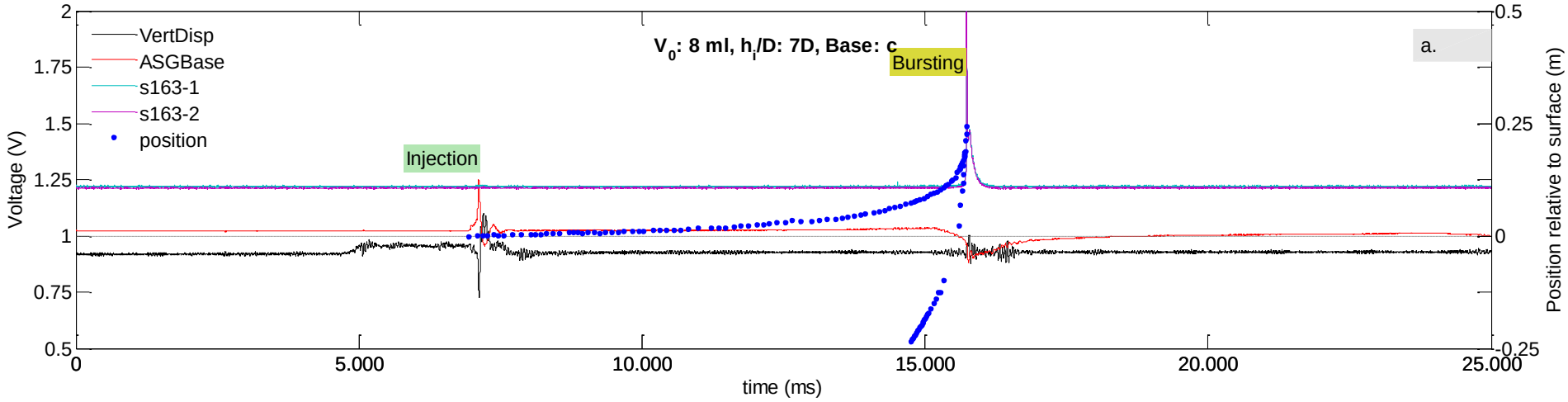

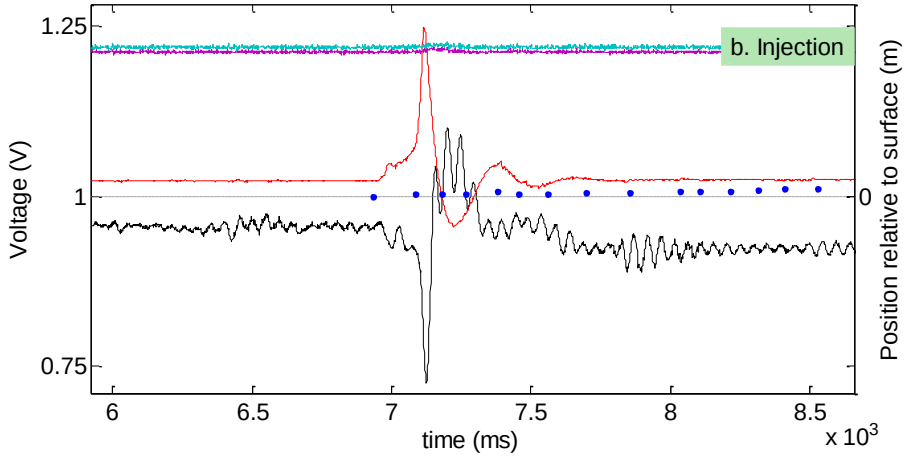

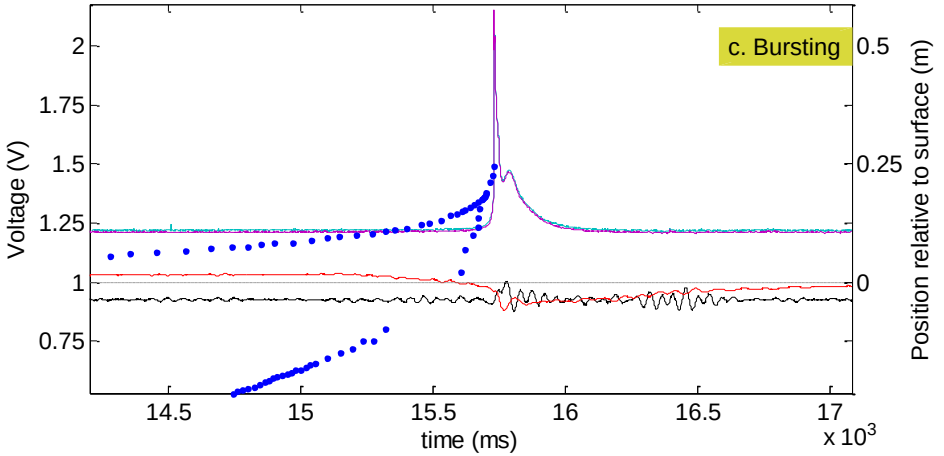

E. Experimental data (section 4) – plots

15. C_7D_10ml_30mbar

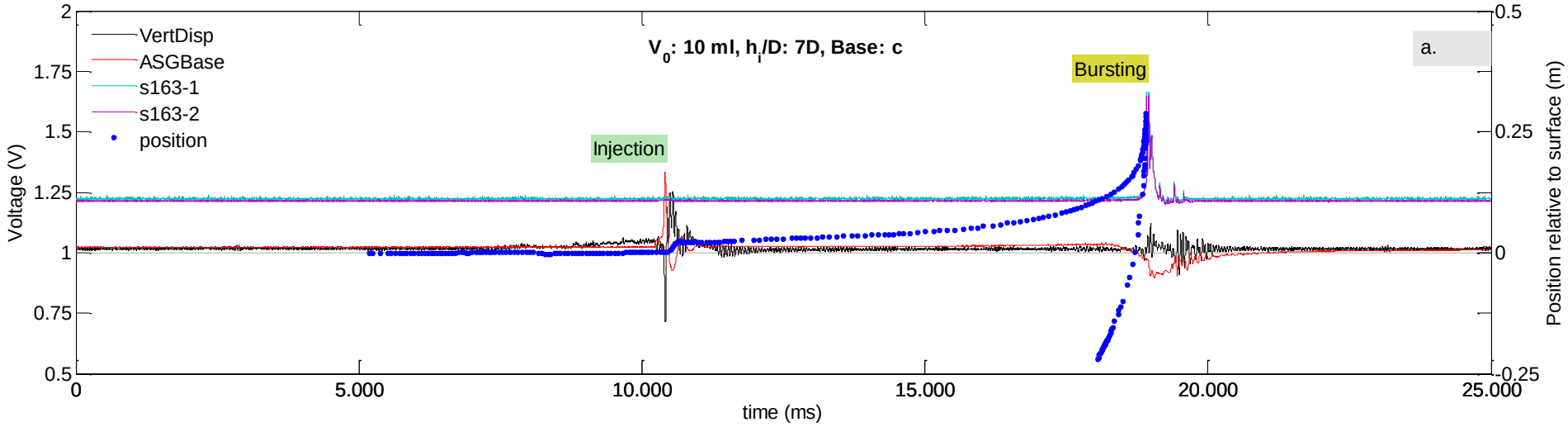

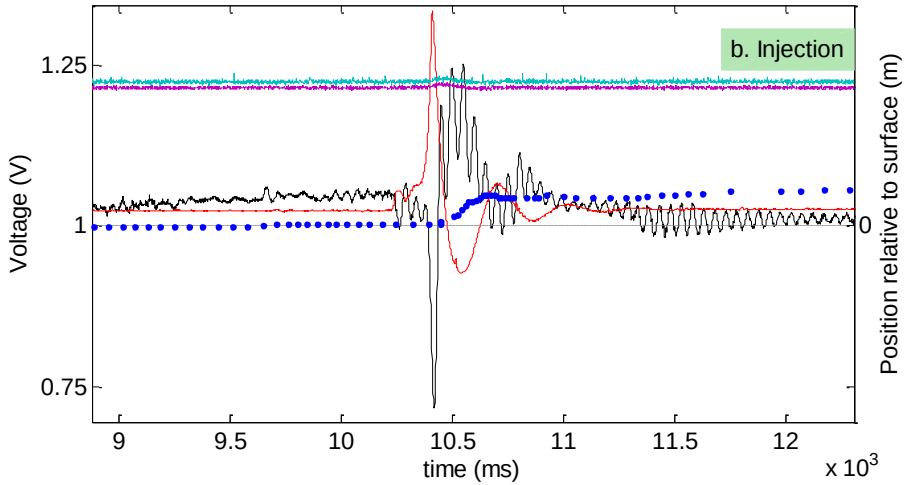

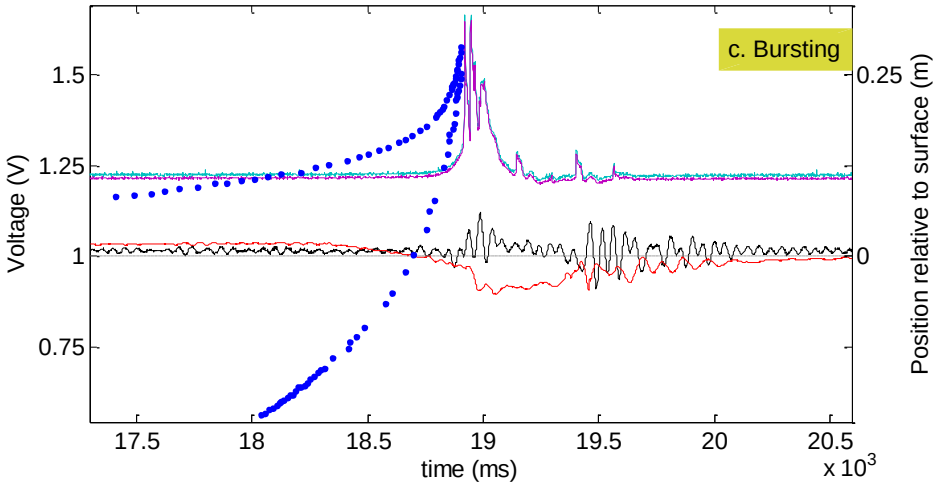

E. Experimental data (section 4) – plots

16. O_0D_10ml_500mbar

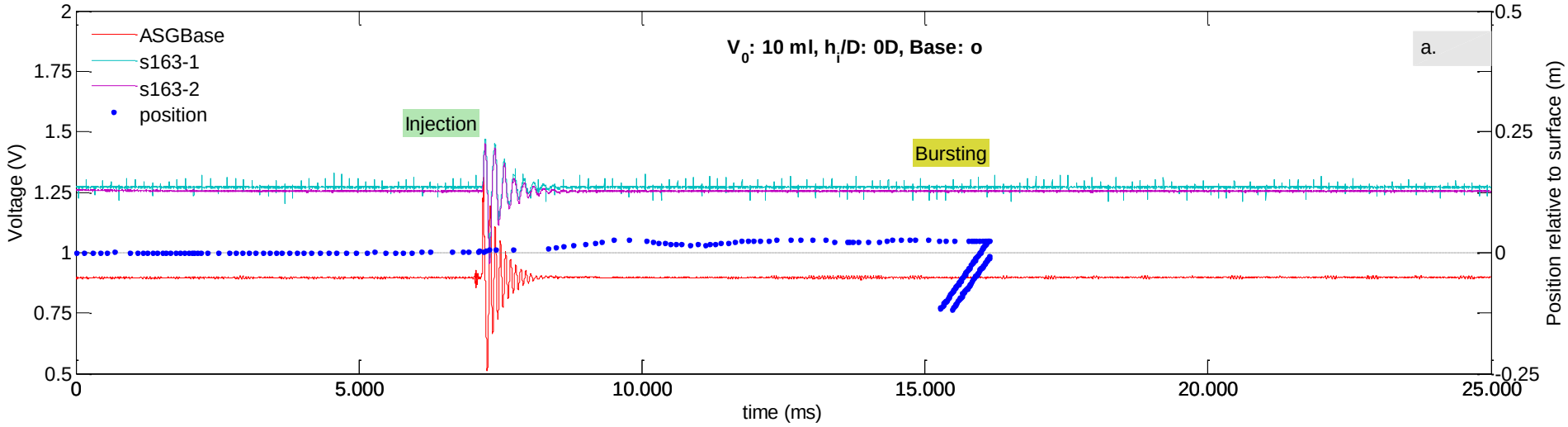

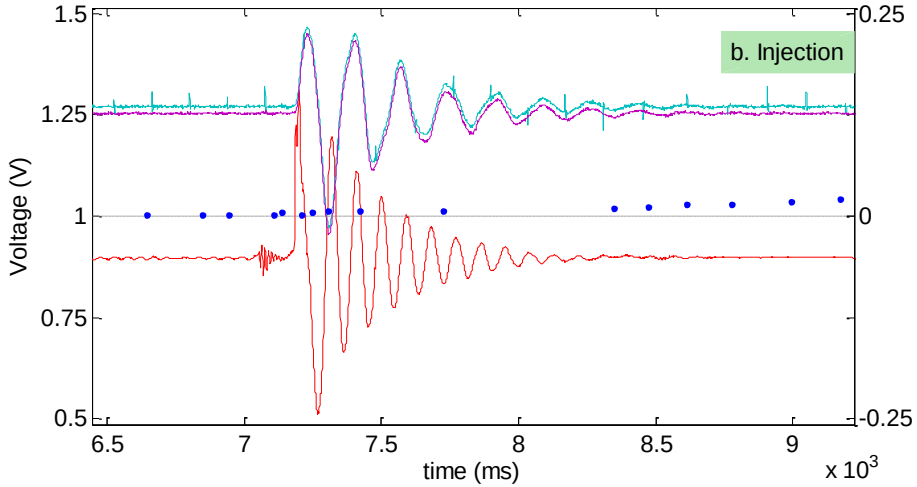

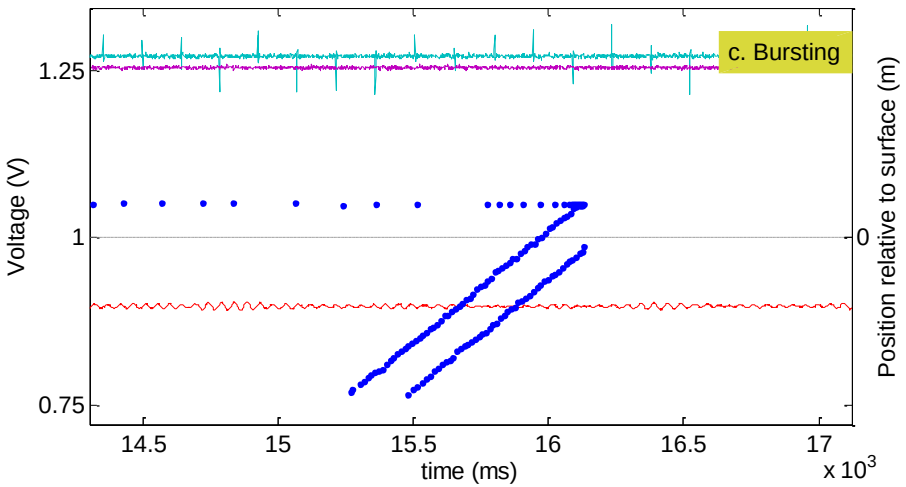

E. Experimental data (section 4) – plots

17. O_5D_10ml_500mbar

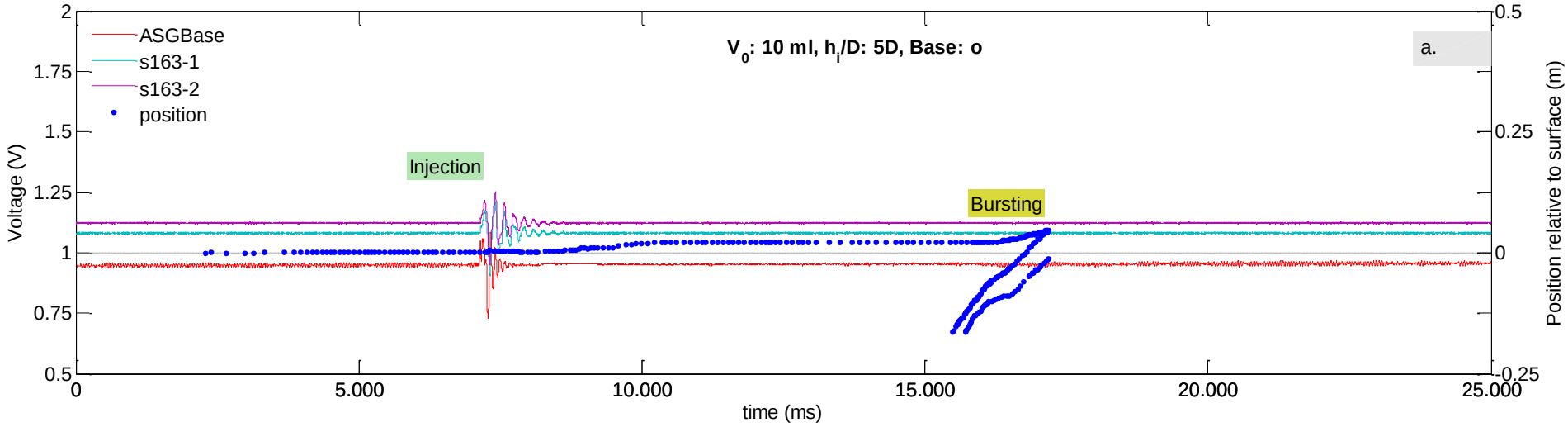

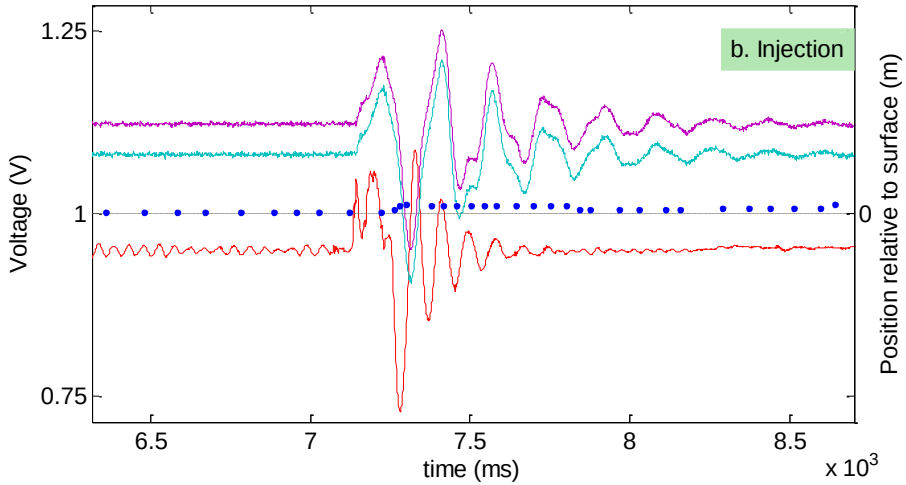

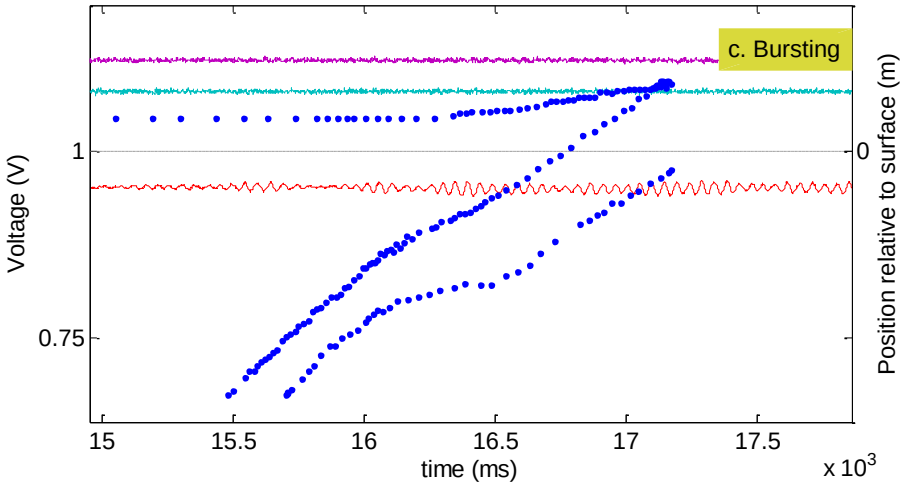

E. Experimental data (section 4) – plots

18. O_9D_10ml_500mbar

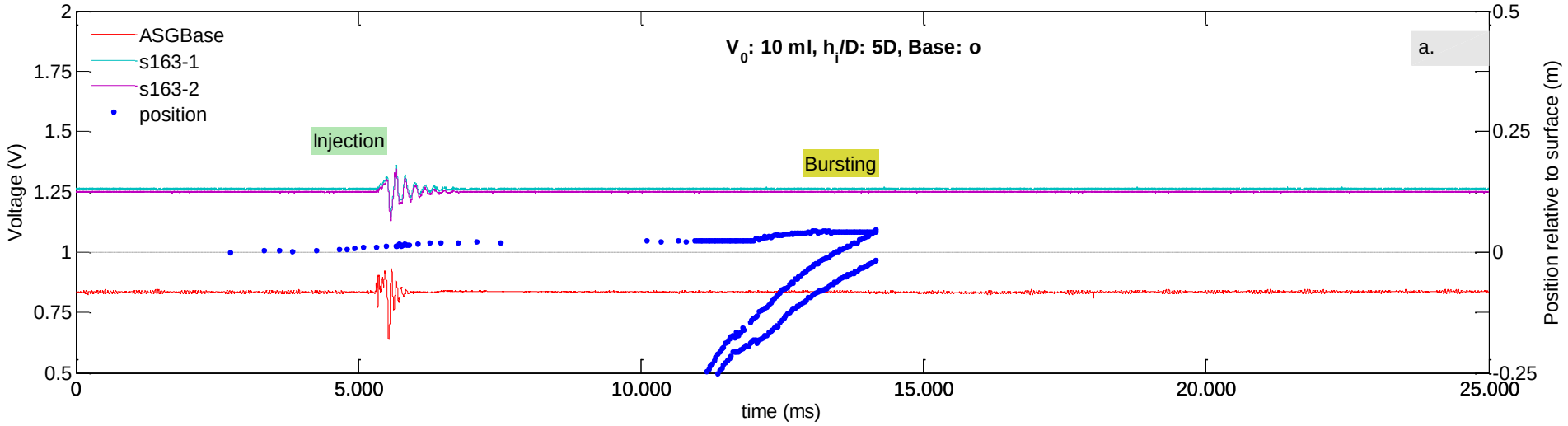

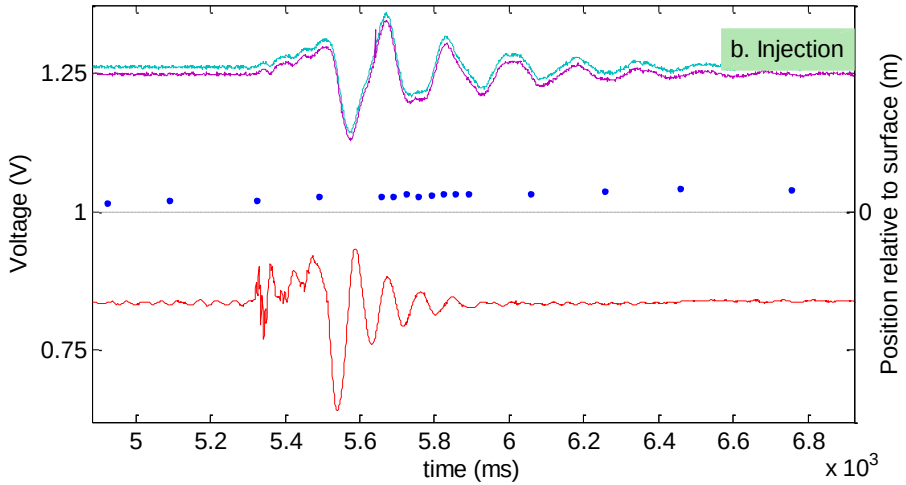

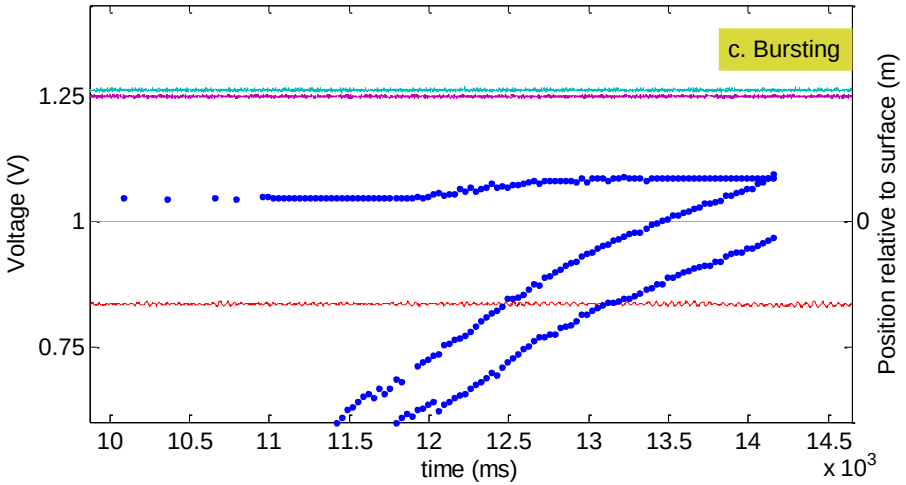

E. Experimental data (section 4) – plots

19. O_0D_2ml_30mbar

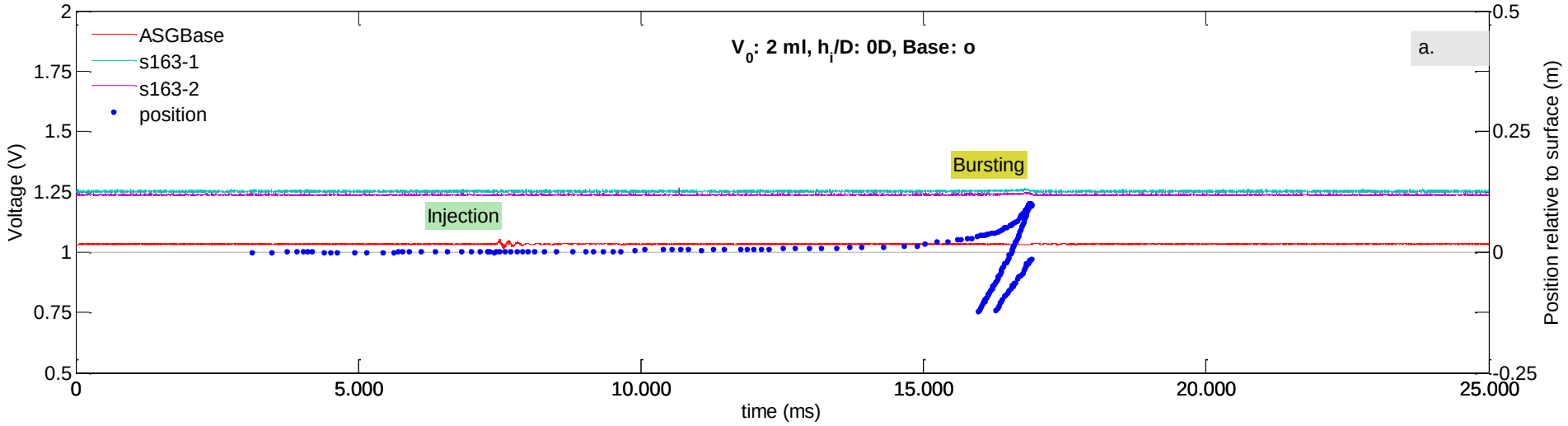

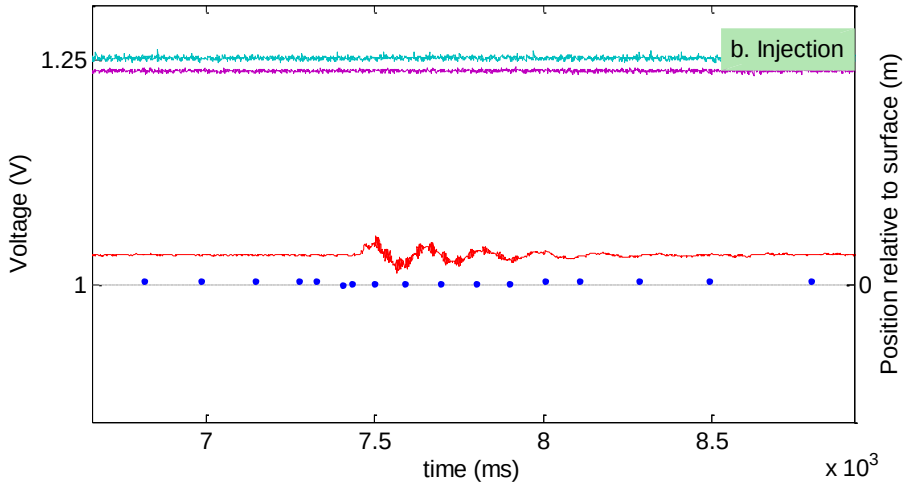

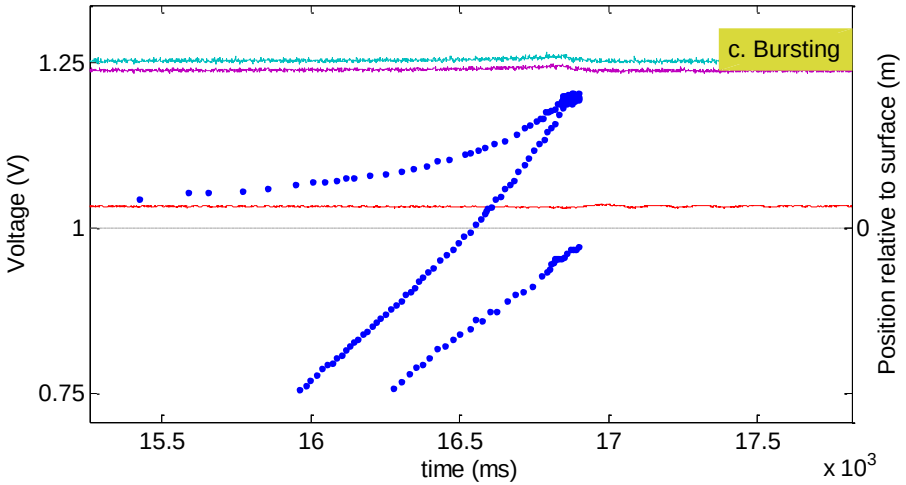

E. Experimental data (section 4) – plots

20. O_0D_4ml_30mbar

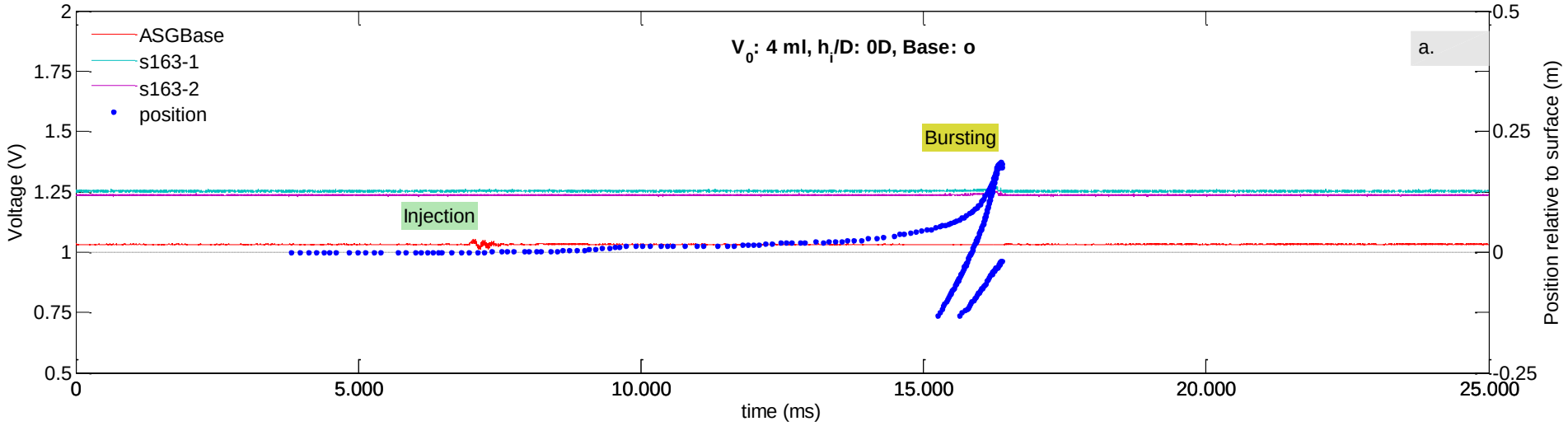

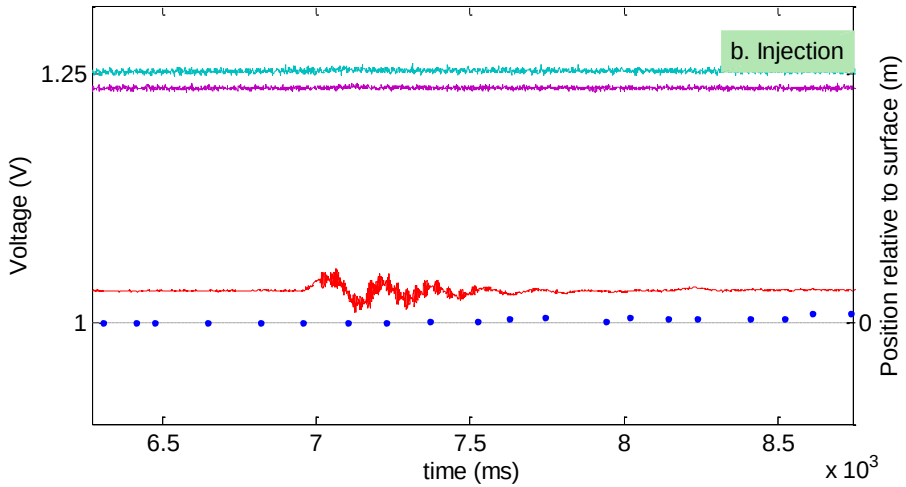

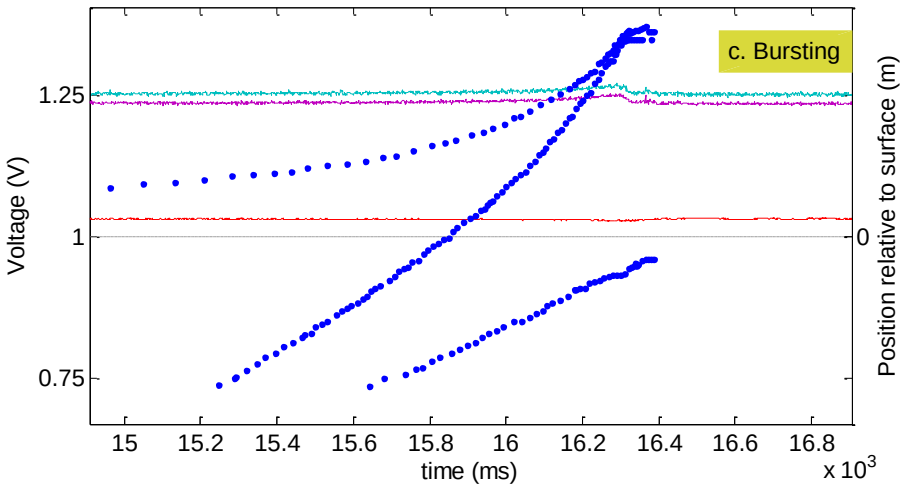

E. Experimental data (section 4) – plots

21. O_0D_6ml_30mbar

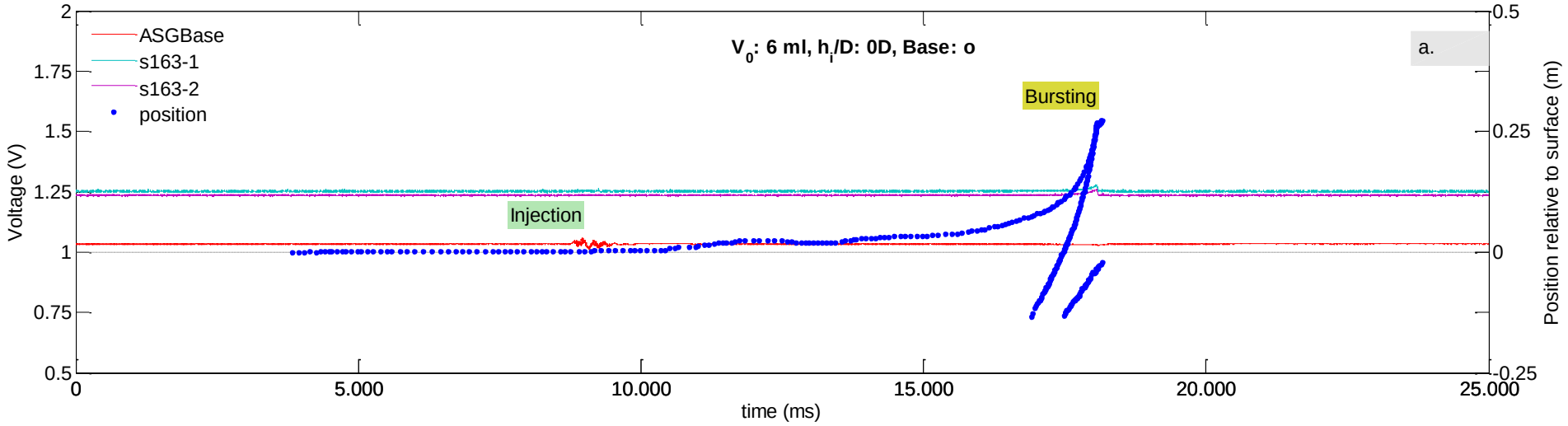

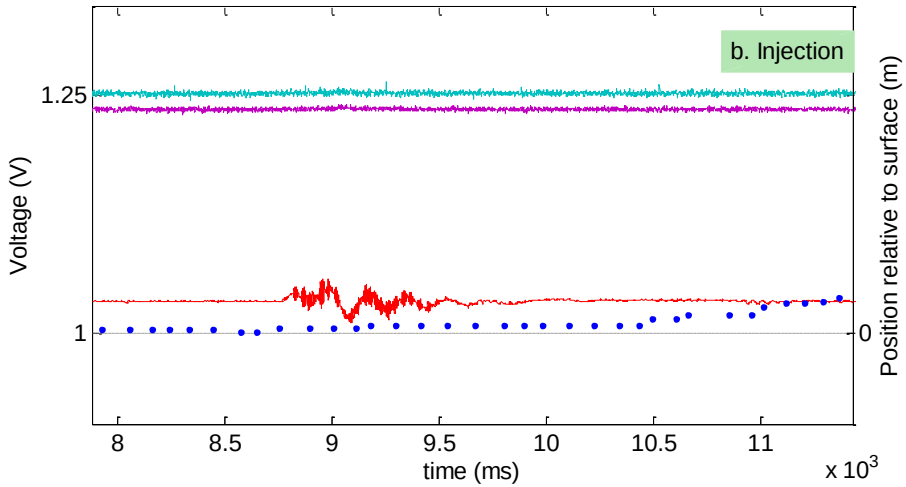

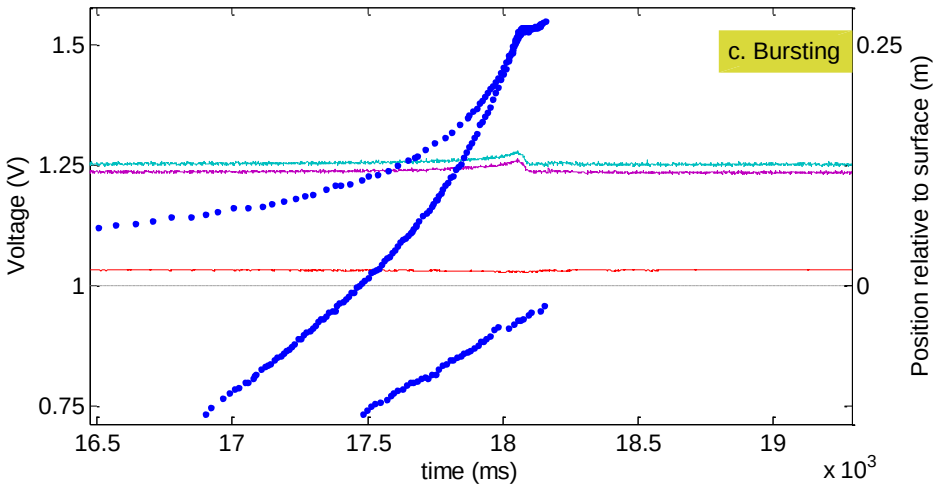

E. Experimental data (section 4) – plots

22. O_0D_8ml_30mbar

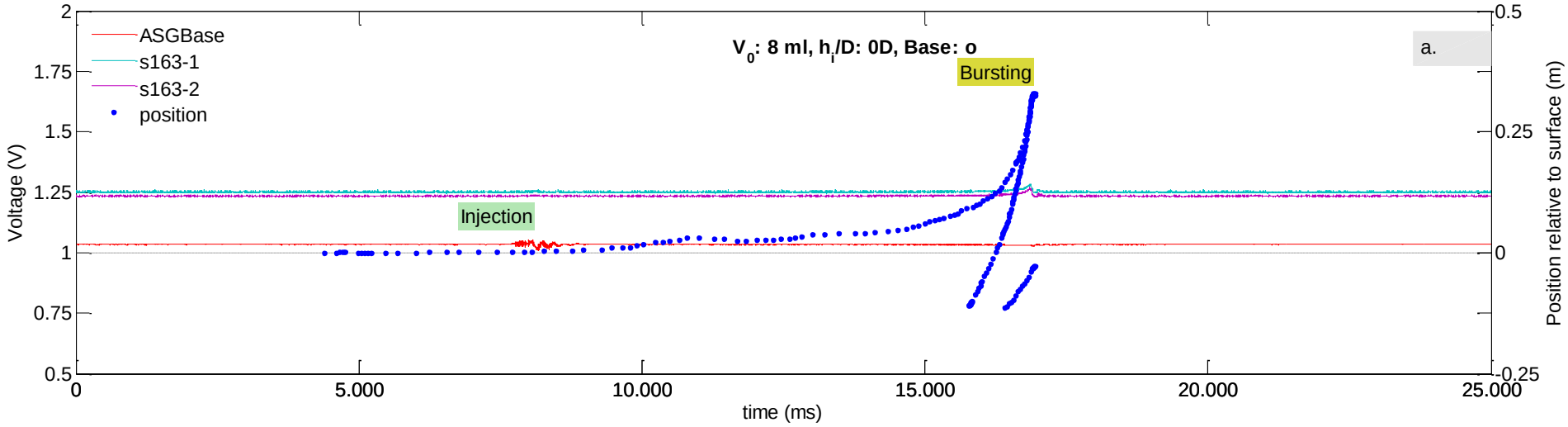

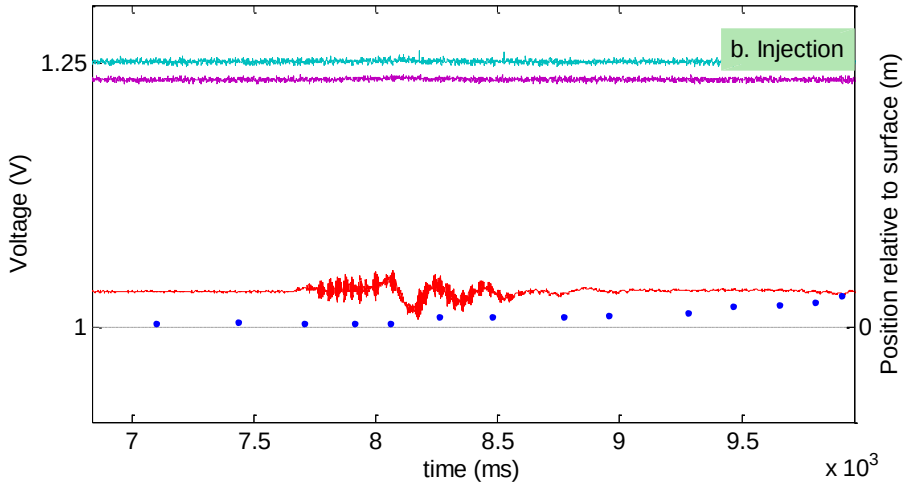

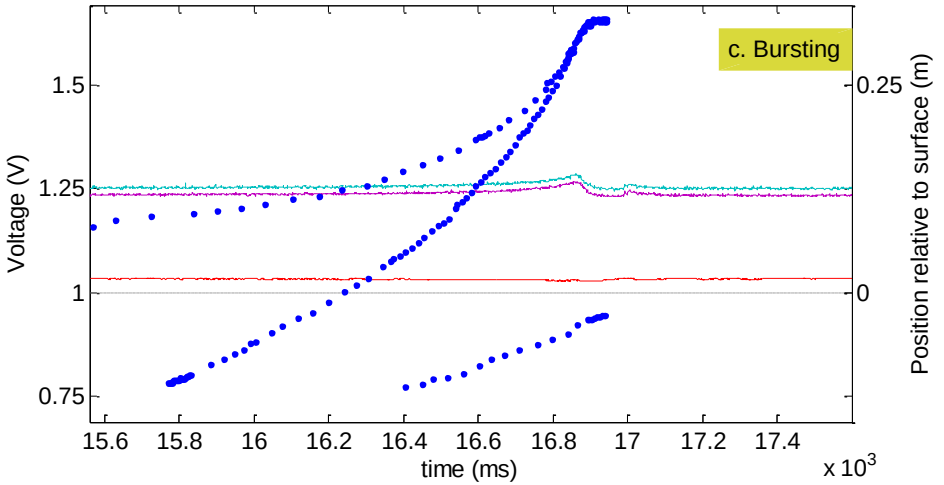

E. Experimental data (section 4) – plots

23. O_0D_10ml_30mbar

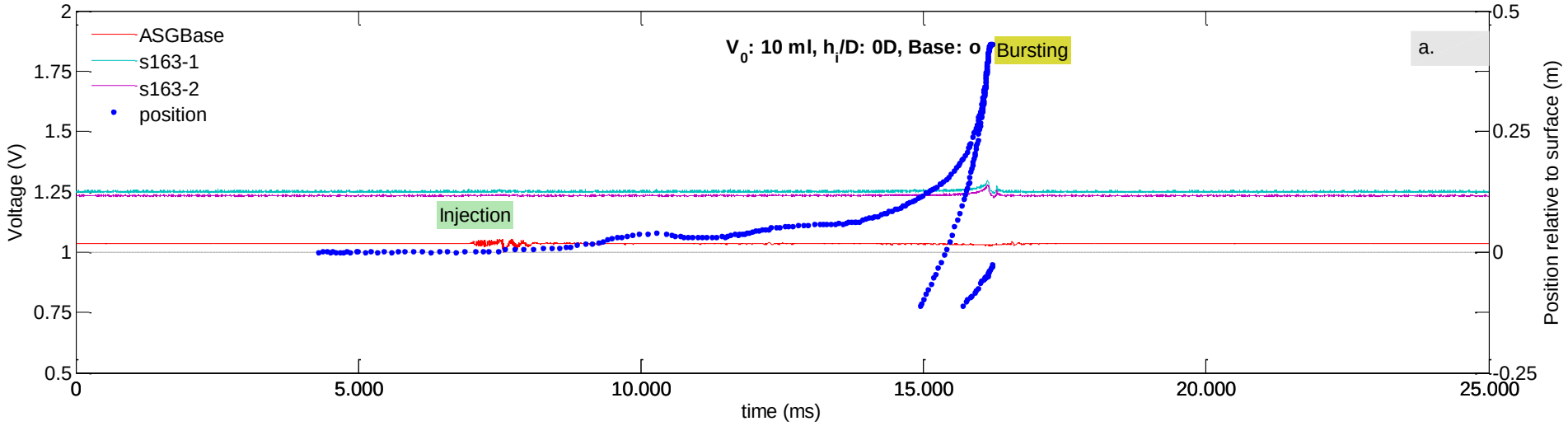

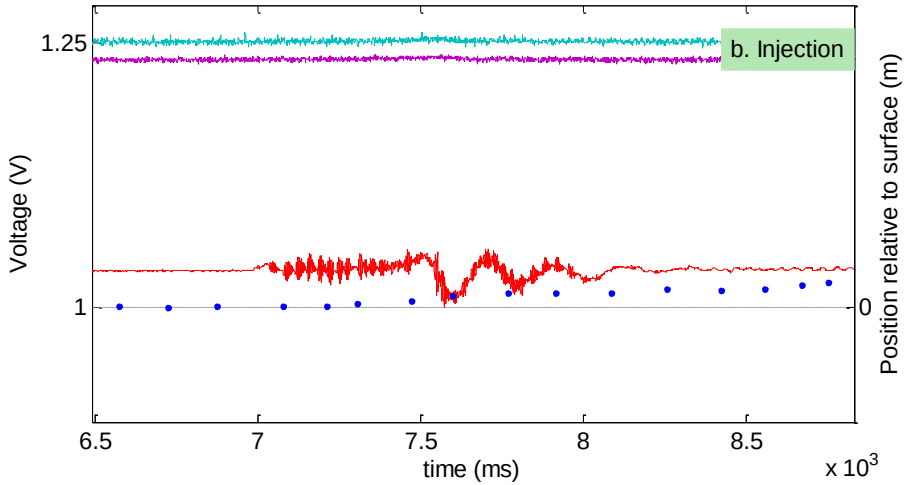

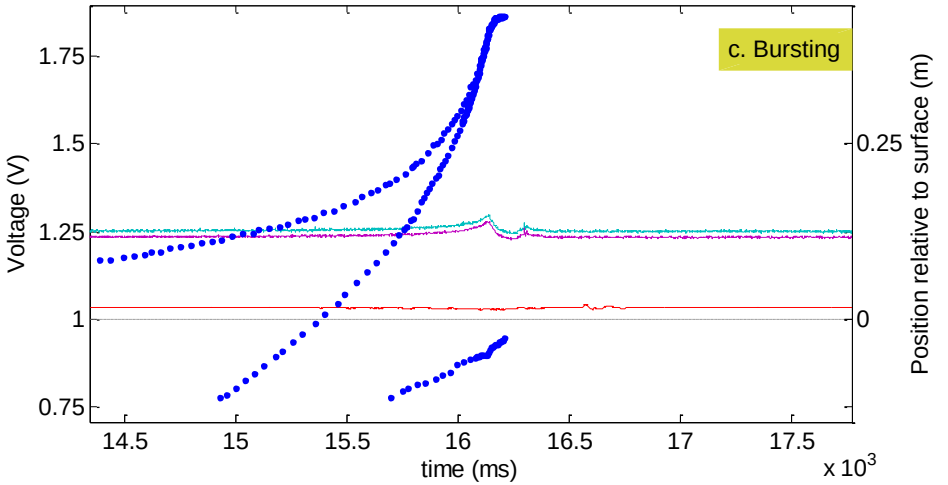

E. Experimental data (section 4) – plots

24. O_0D_17ml_30mbar

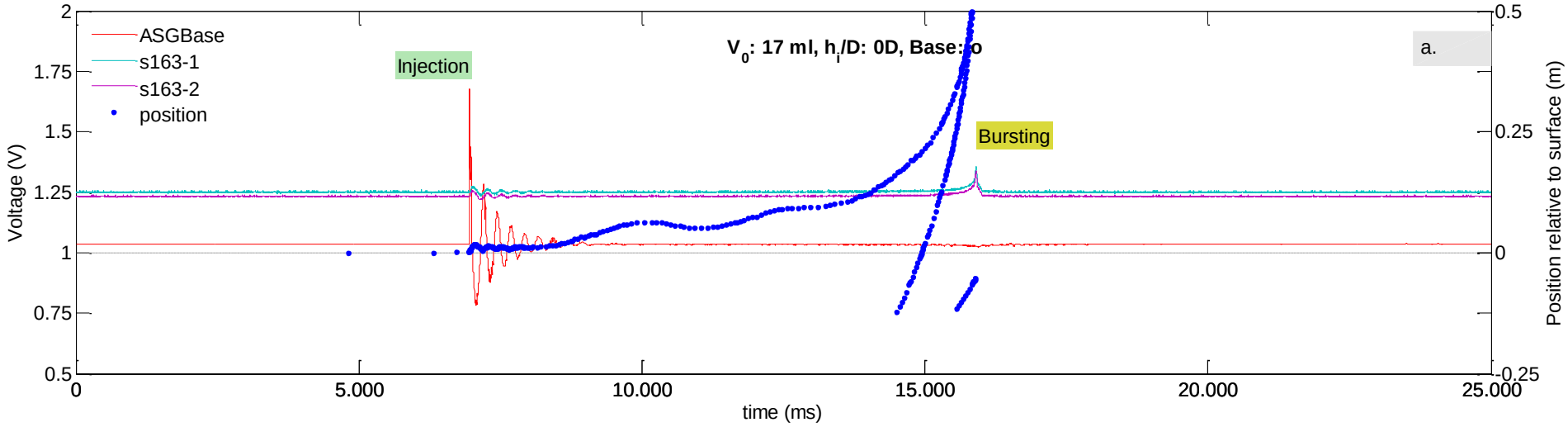

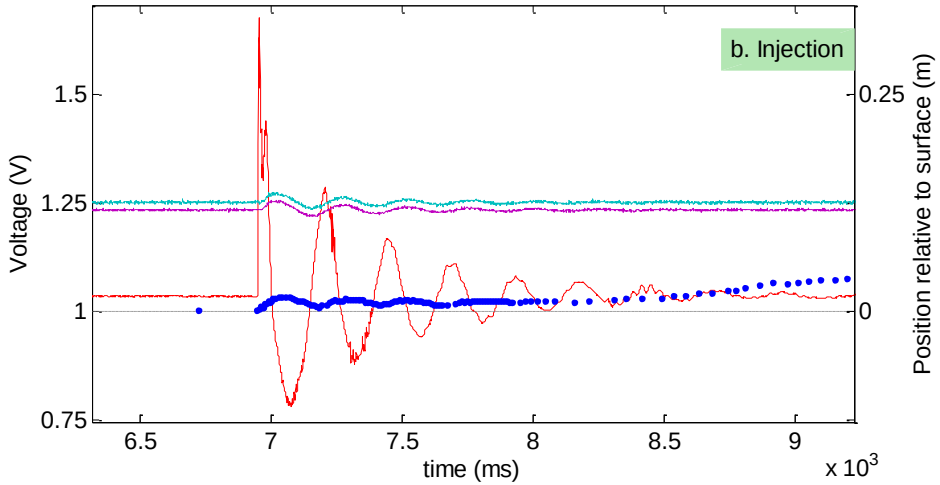

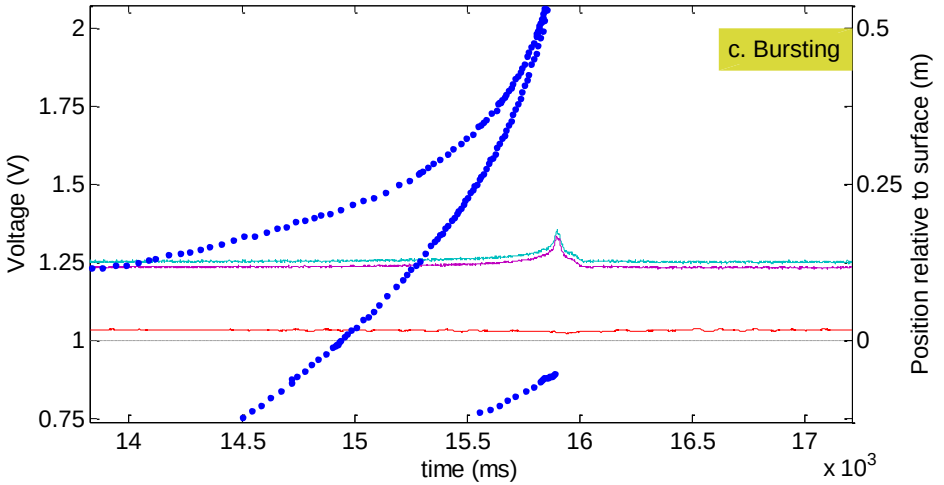

E. Experimental data (section 4) – plots

25. O_5D_2ml_30mbar

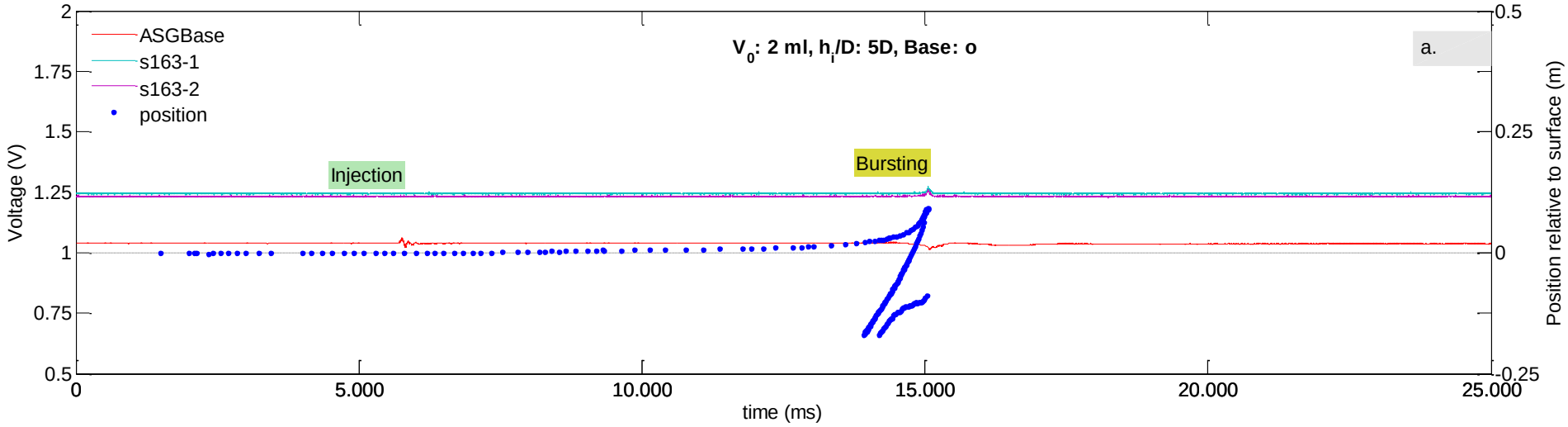

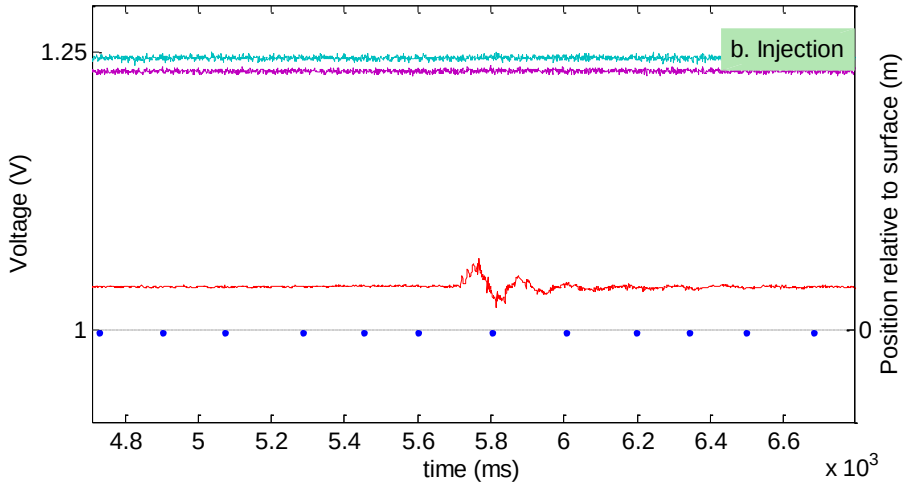

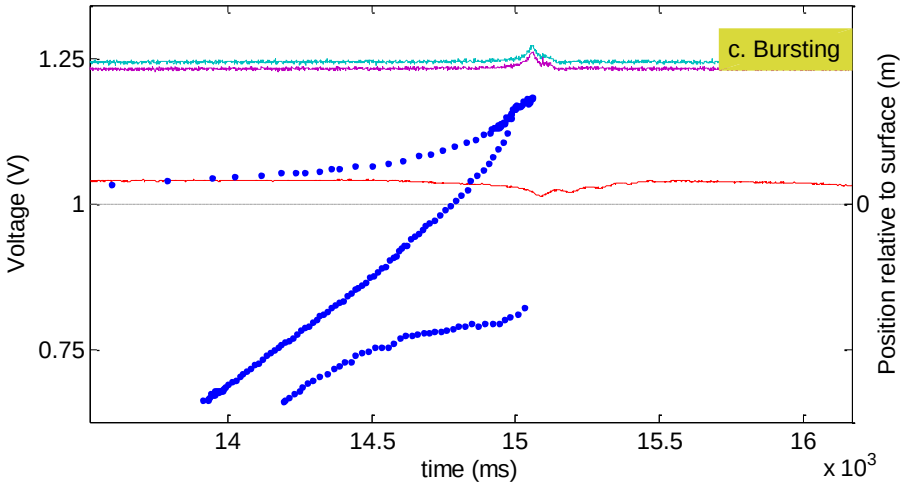

E. Experimental data (section 4) – plots

26. O_5D_4ml_30mbar

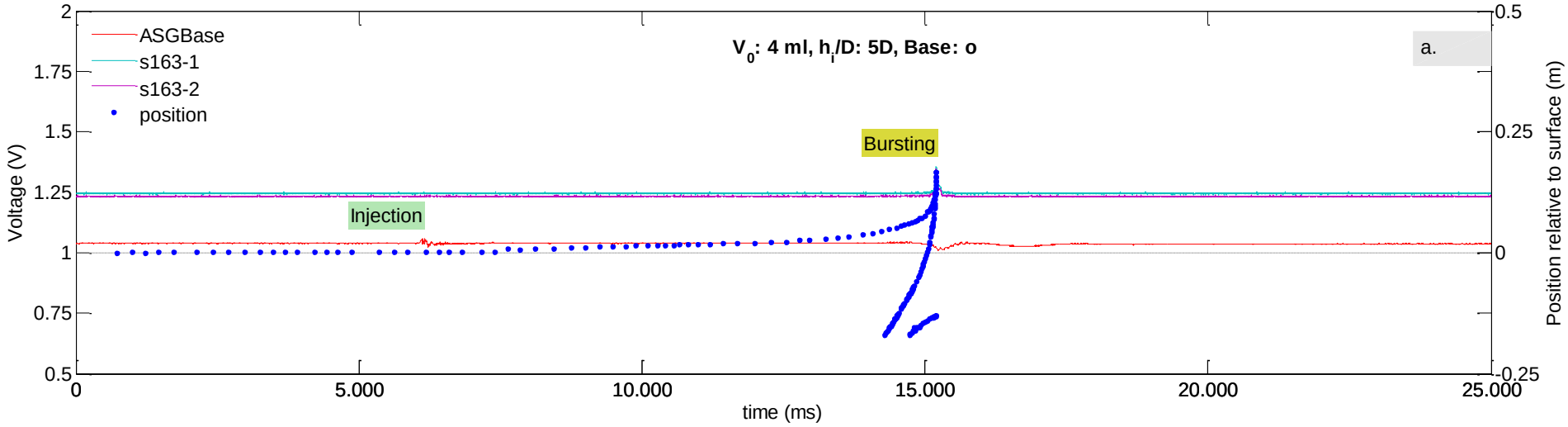

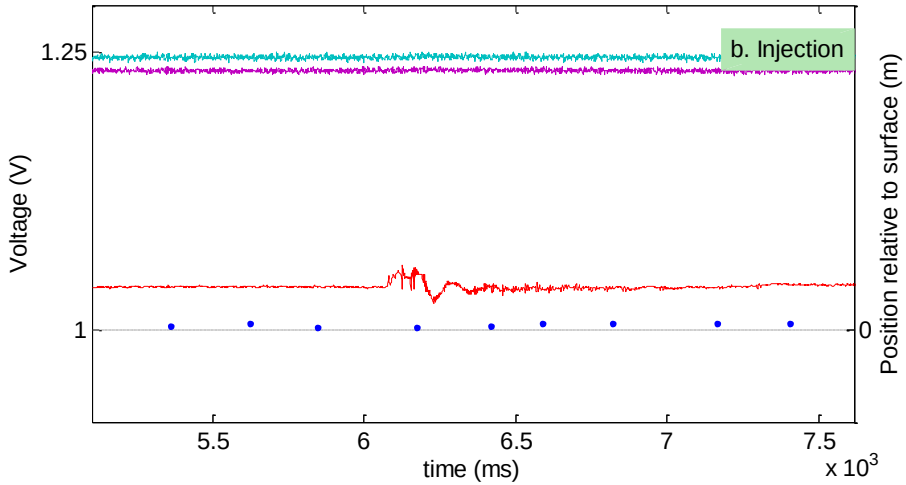

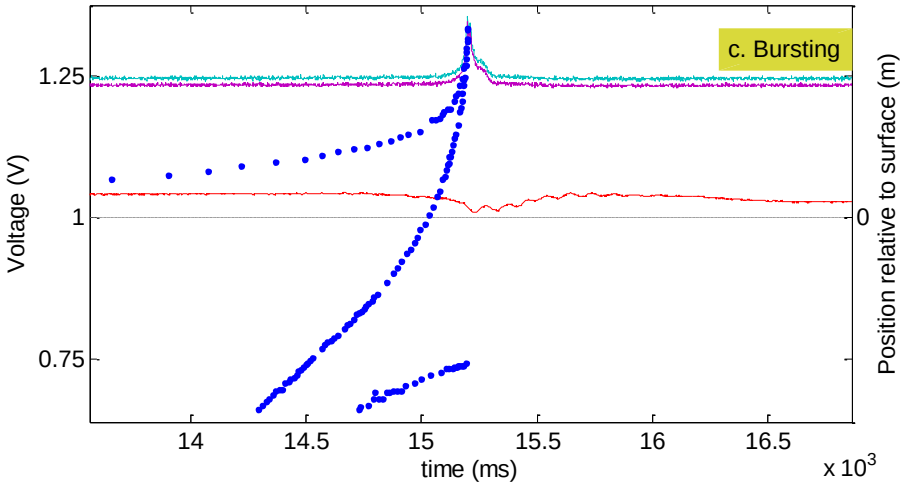

E. Experimental data (section 4) – plots

27. O_5D_6ml_30mbar

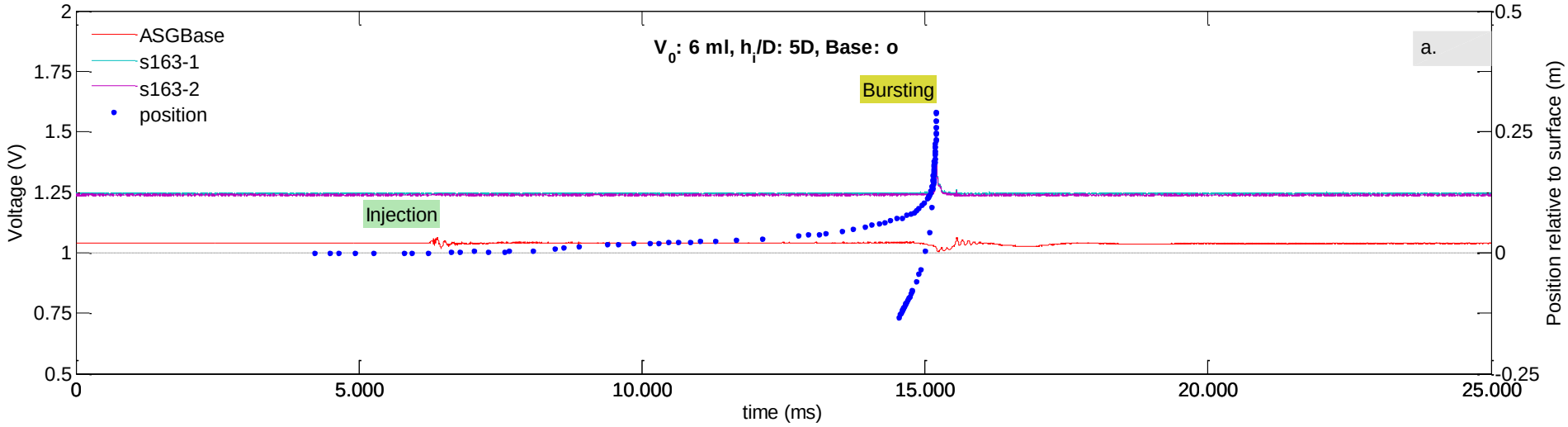

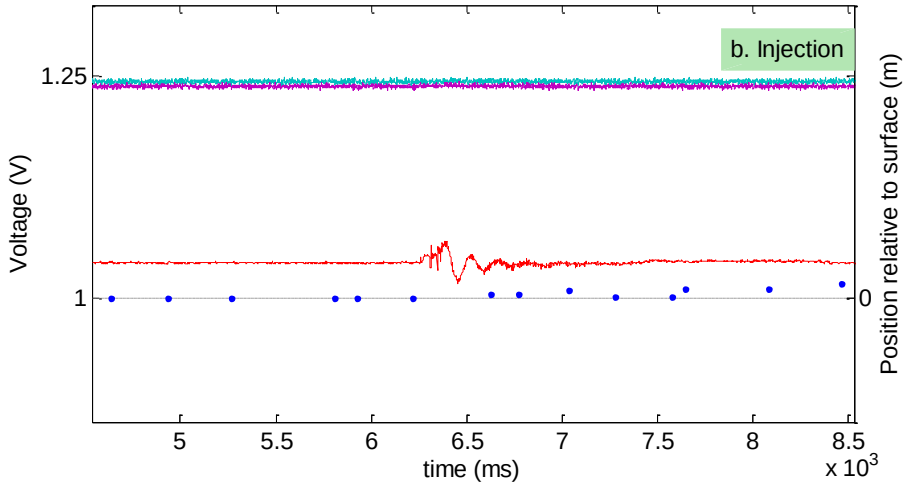

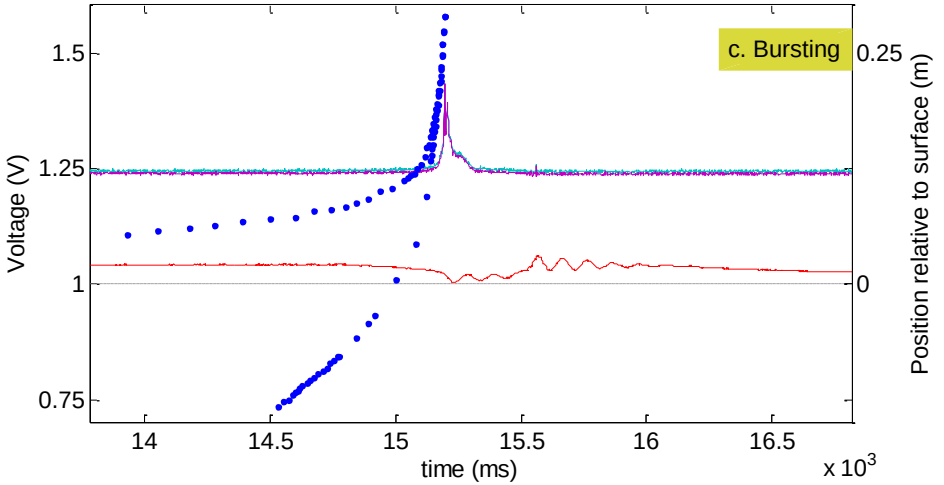

E. Experimental data (section 4) – plots

28. O_5D_8ml_30mbar

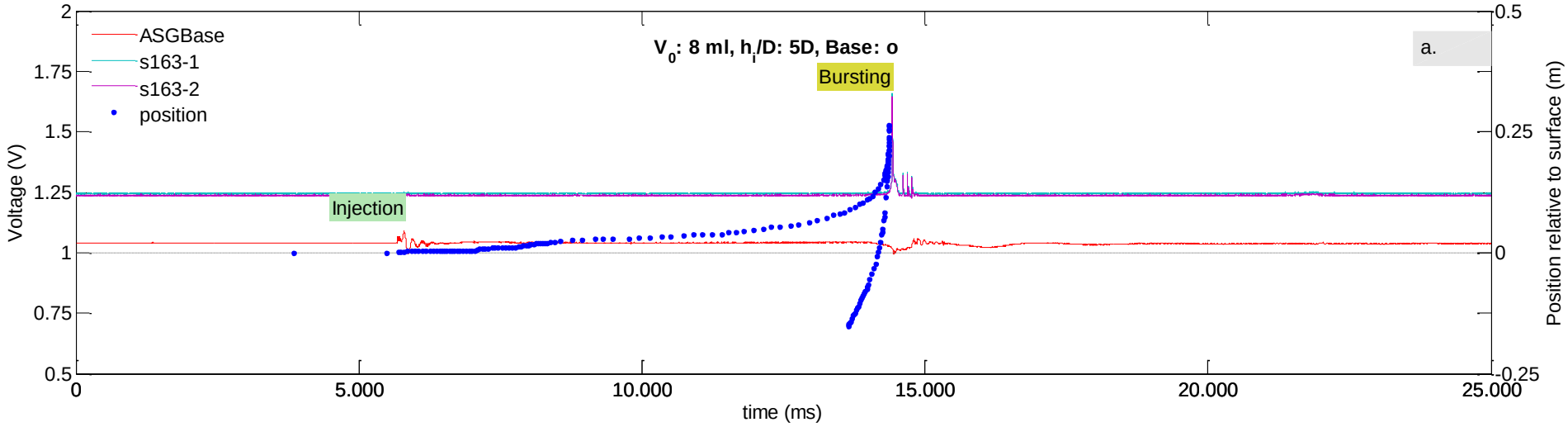

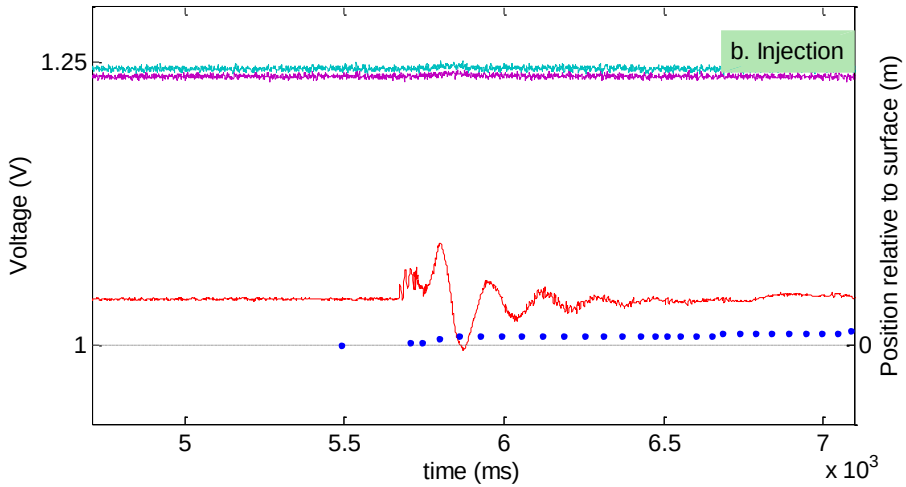

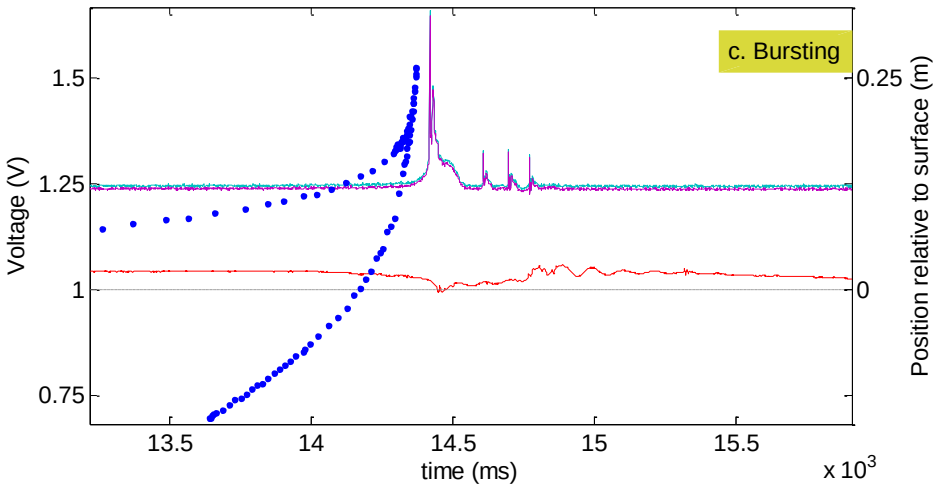

E. Experimental data (section 4) – plots

29. O_5D_10ml_30mbar

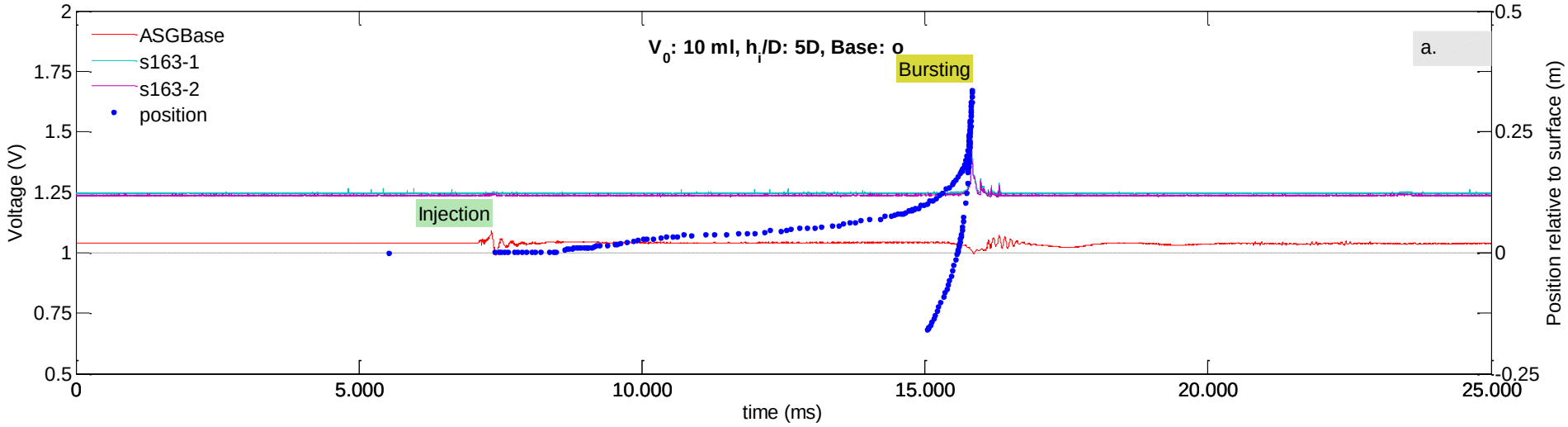

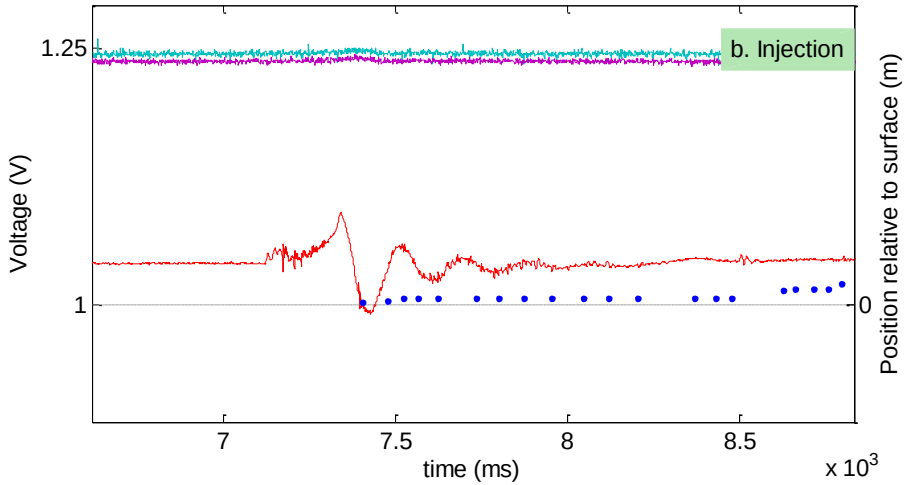

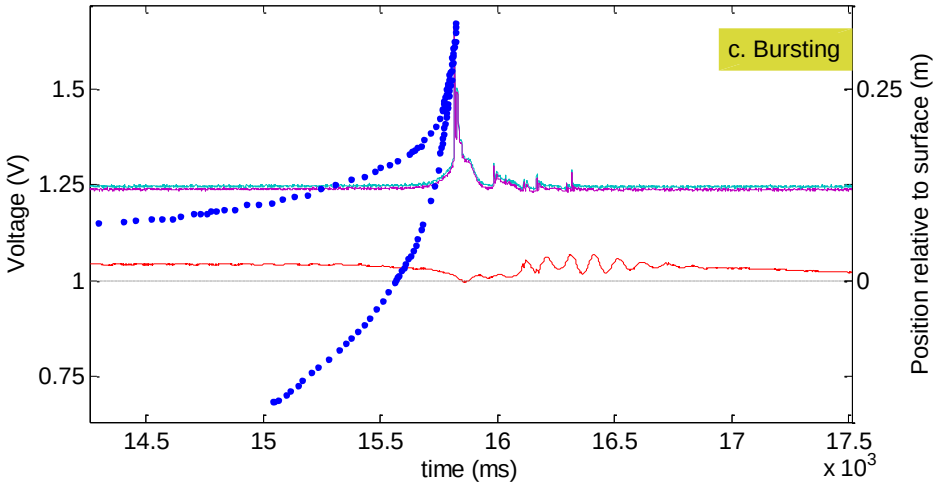

E. Experimental data (section 4) – plots

30. O_5D_17ml_30mbar

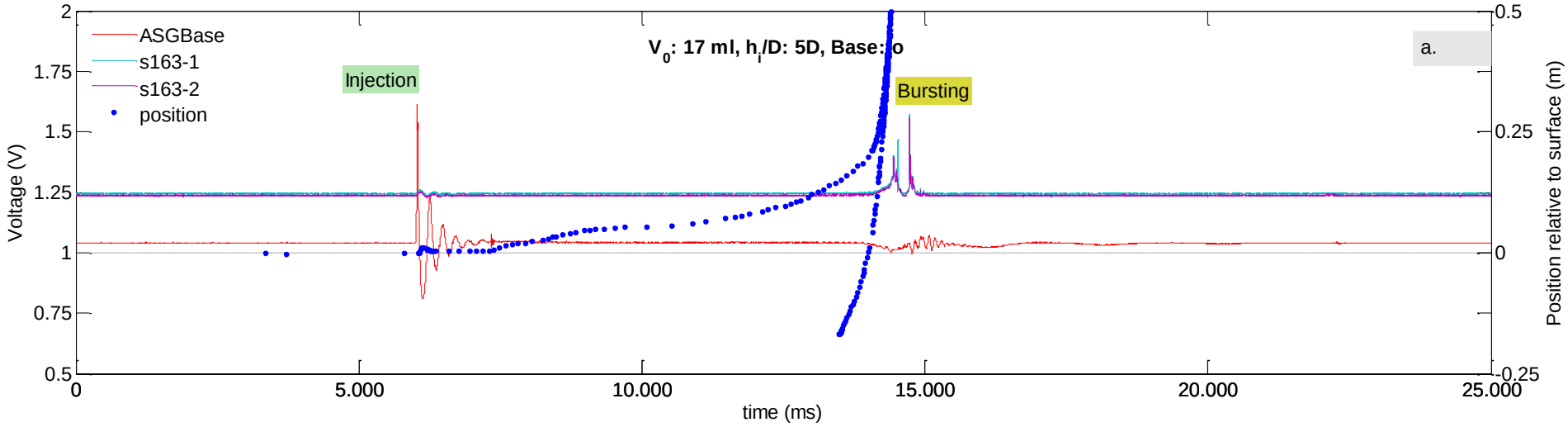

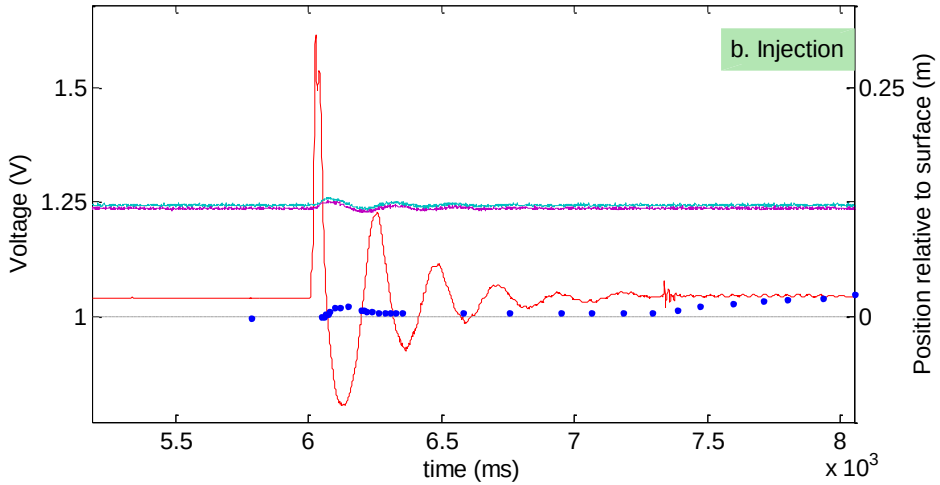

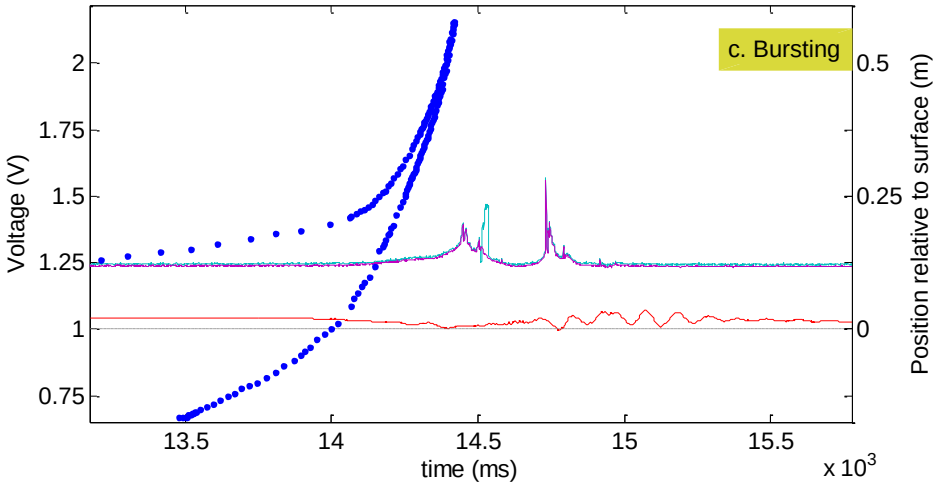

E. Experimental data (section 4) – plots

31. O_9D_2ml_30mbar

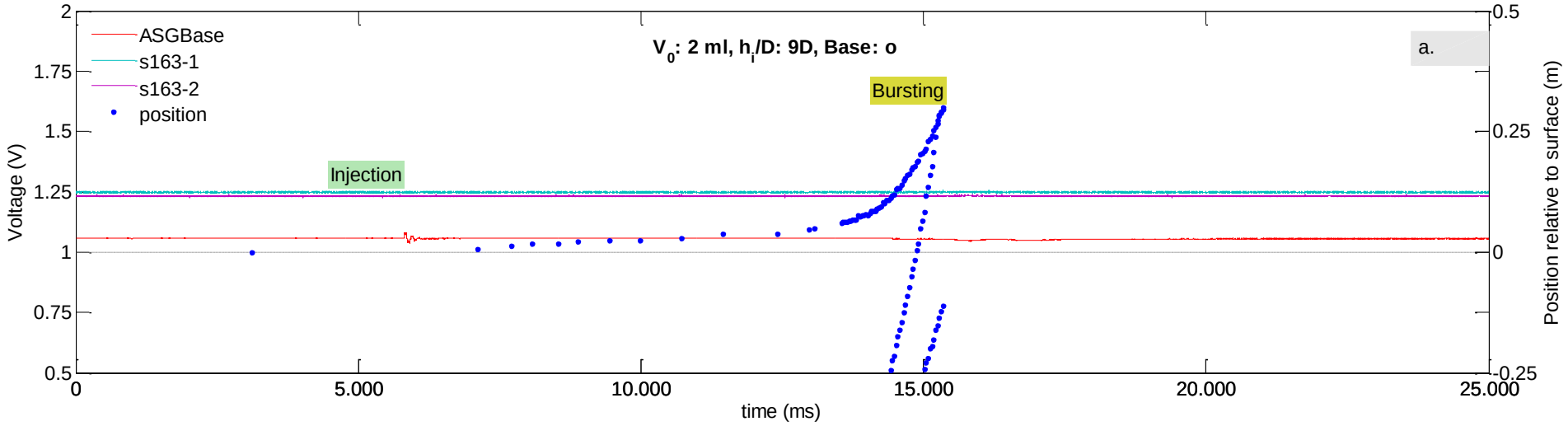

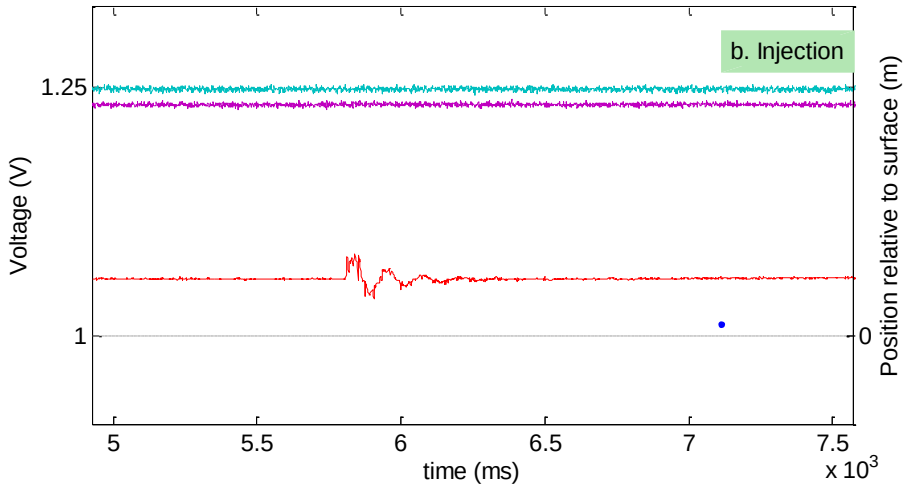

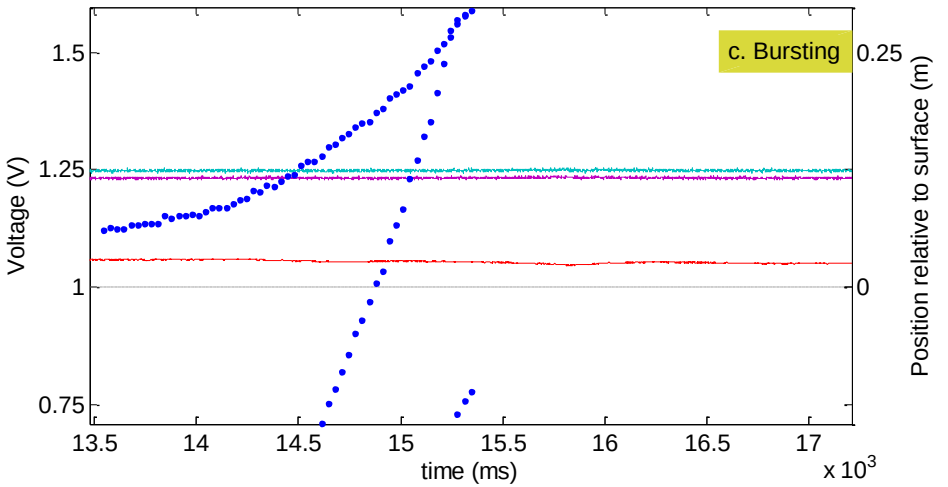

E. Experimental data (section 4) – plots

32. O_9D_4ml_30mbar

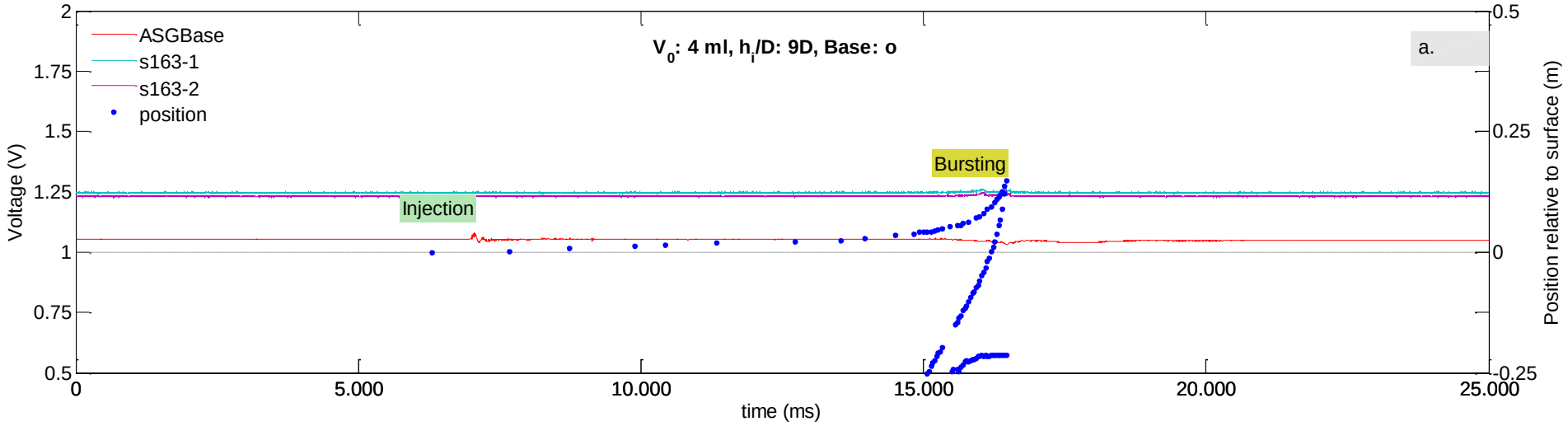

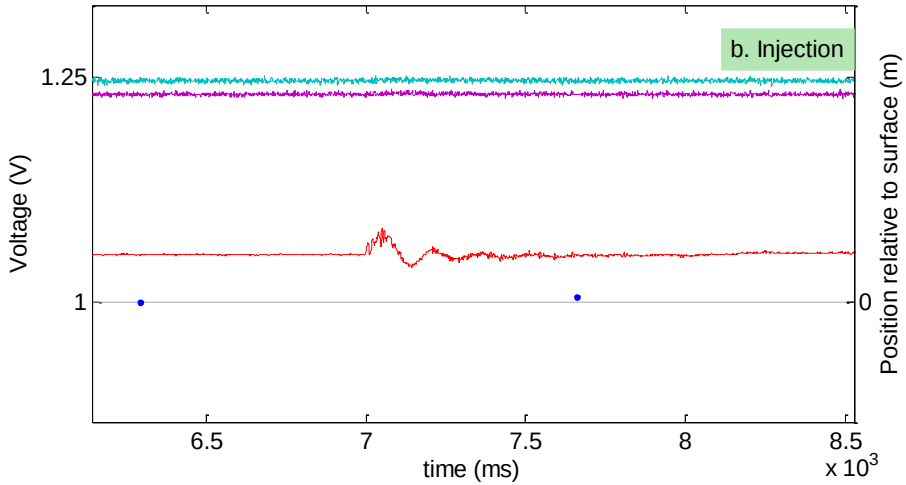

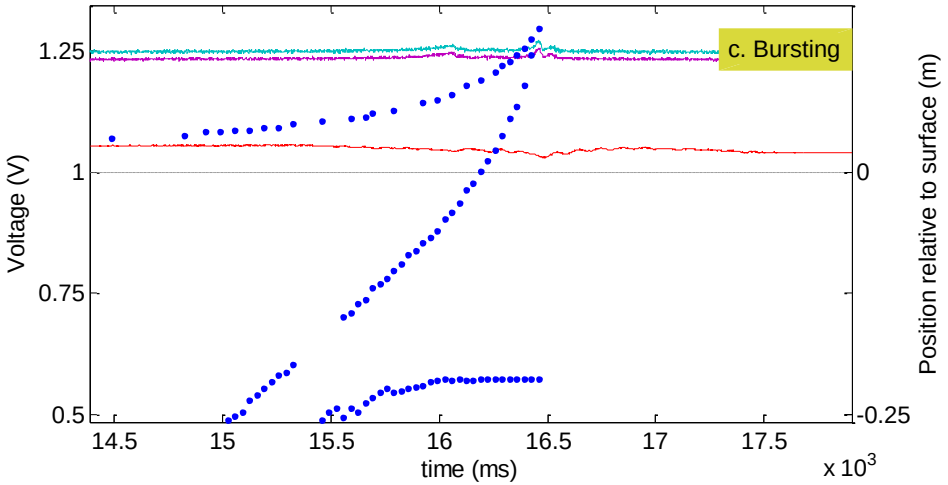

E. Experimental data (section 4) – plots

33. O_9D_6ml_30mbar

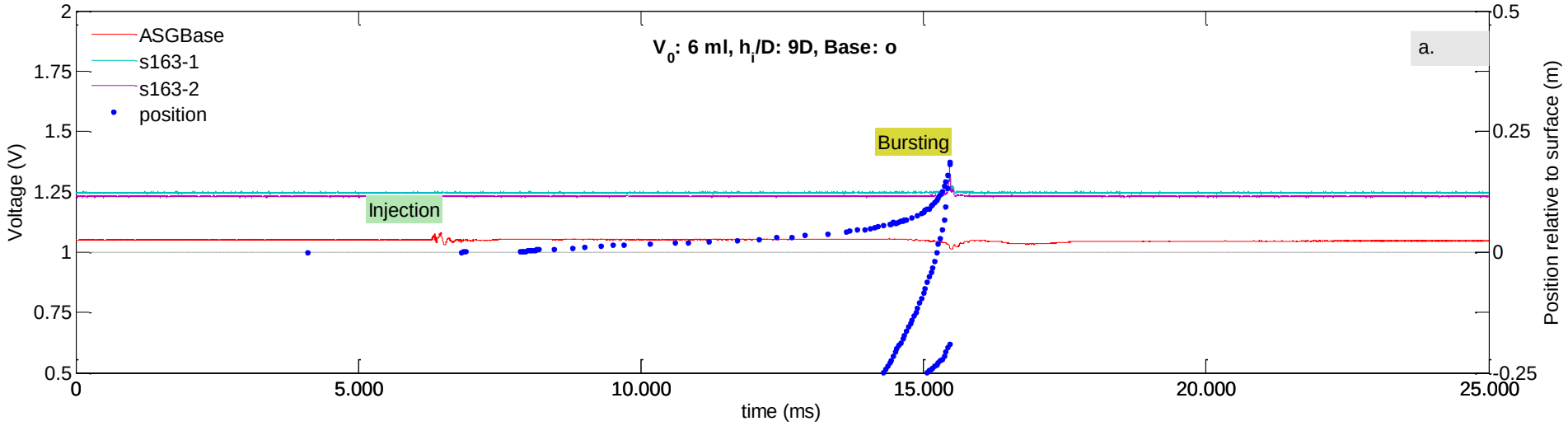

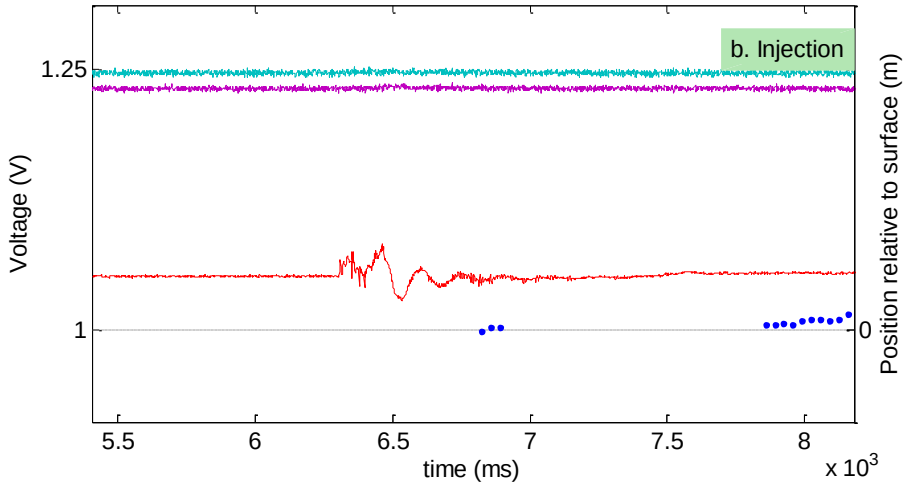

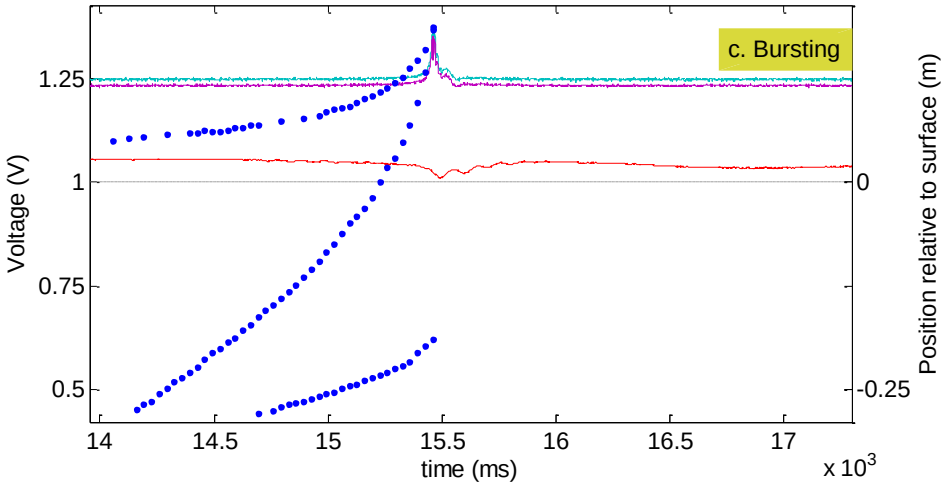

E. Experimental data (section 4) – plots

34. O_9D_8ml_30mbar

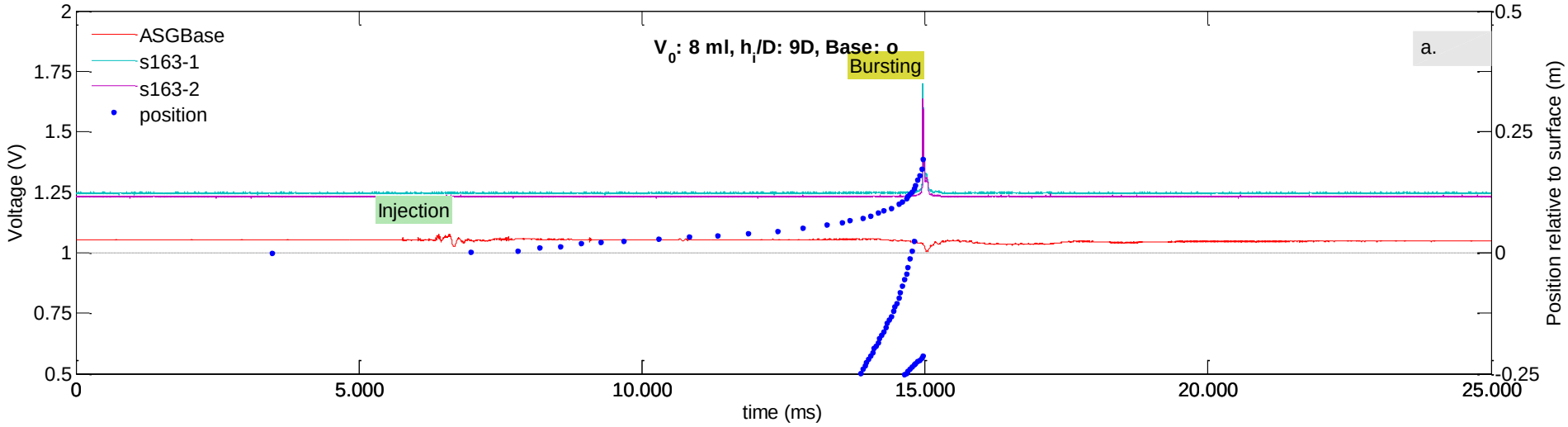

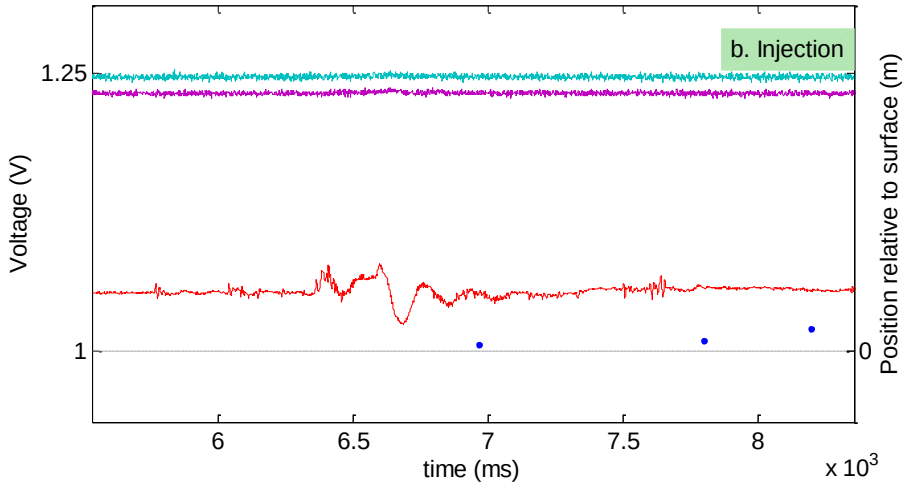

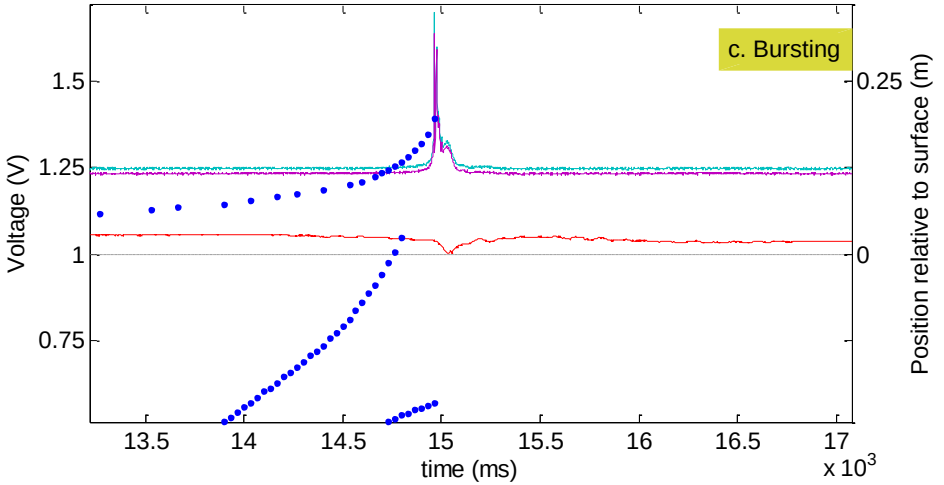

E. Experimental data (section 4) – plots

35. O_9D_10ml_30mbar

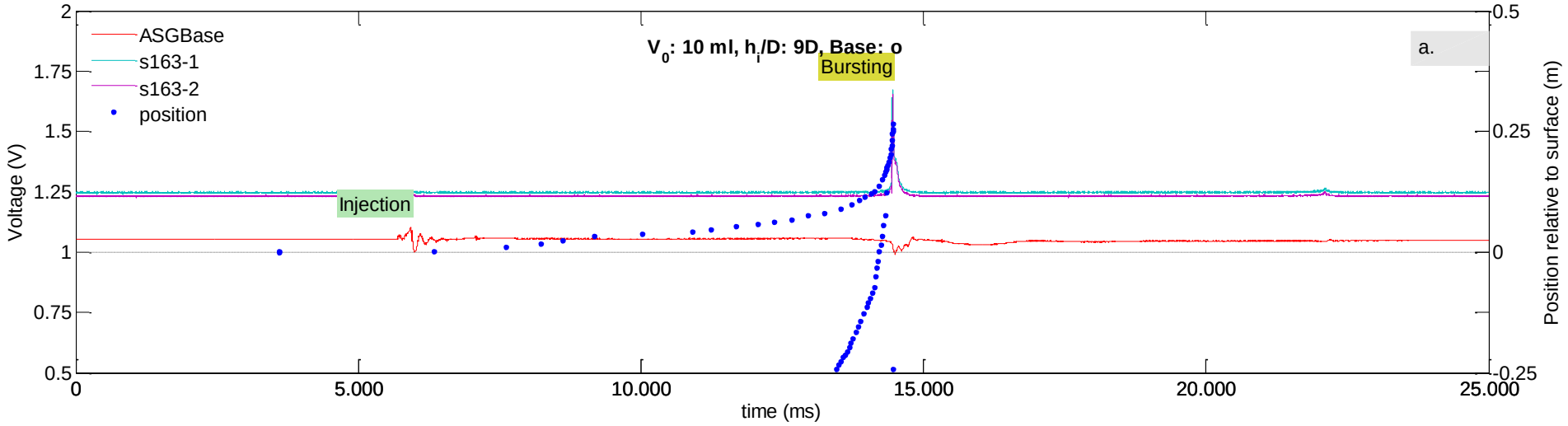

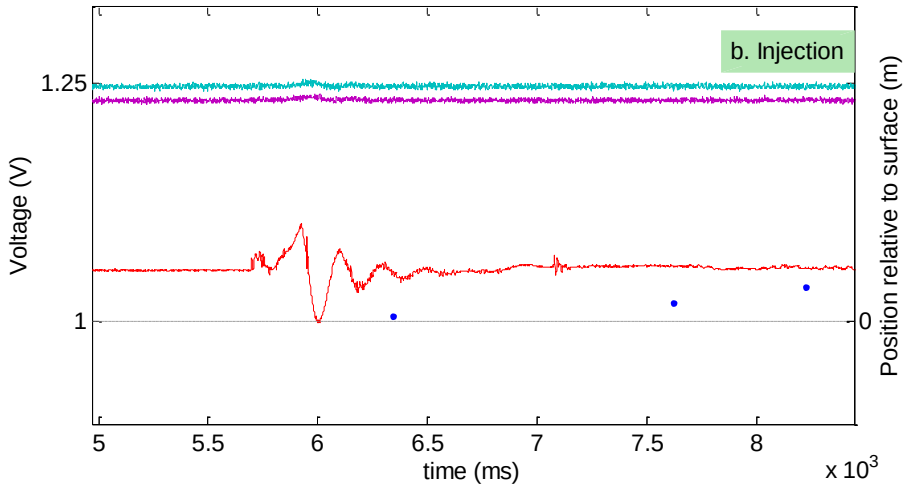

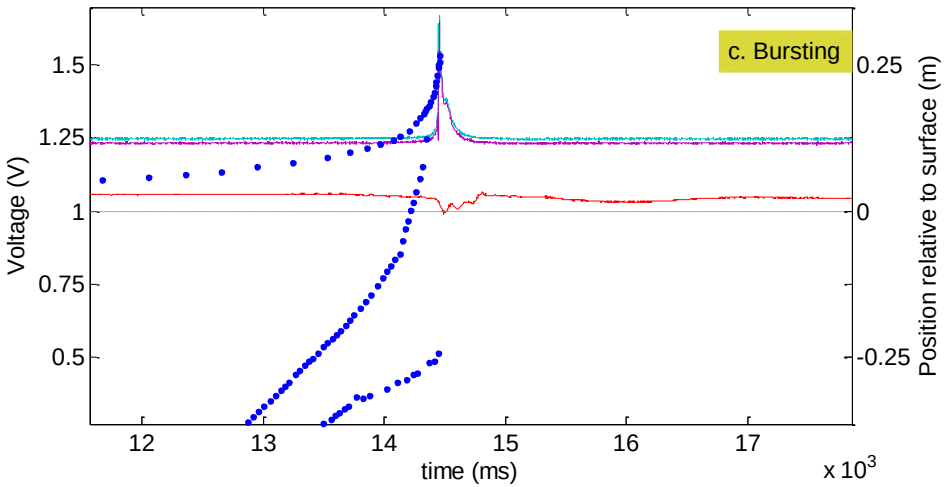

E. Experimental data (section 4) – plots

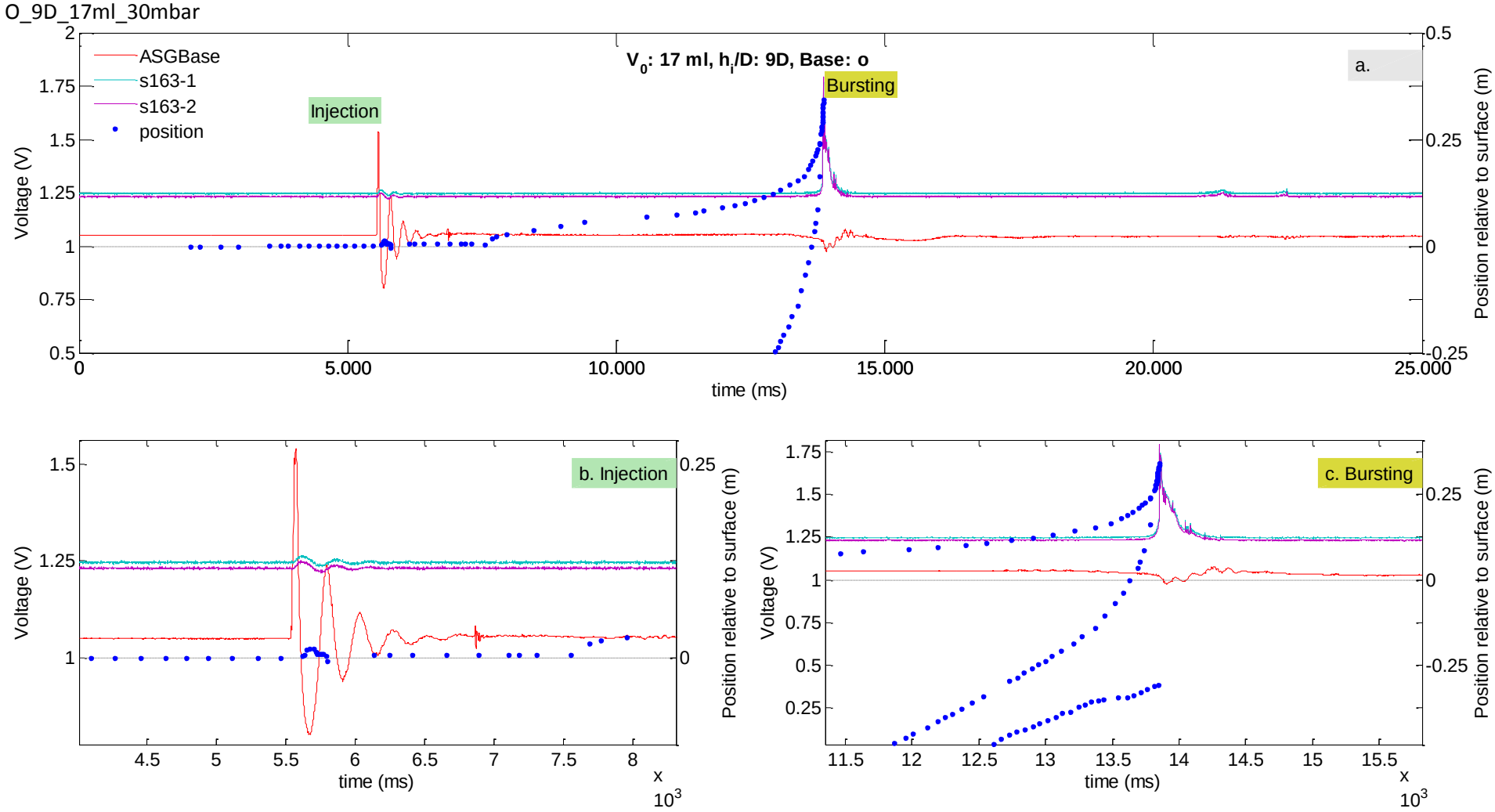

E. Experimental data (section 4) – plots

36. O_9D_24ml_30mbar

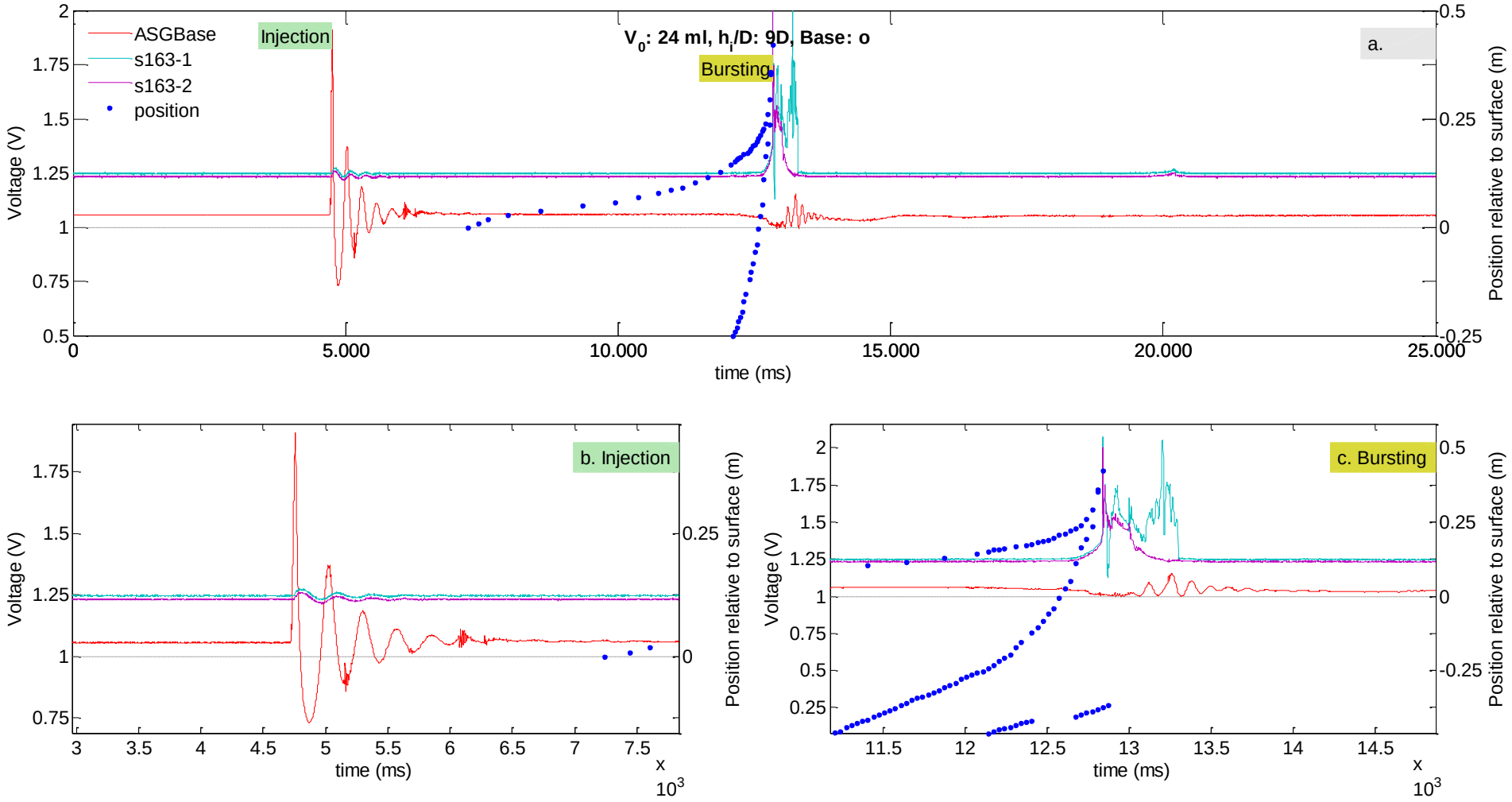

E. Experimental data (section 4) – plots

37. O_9D_50ml_30mbar